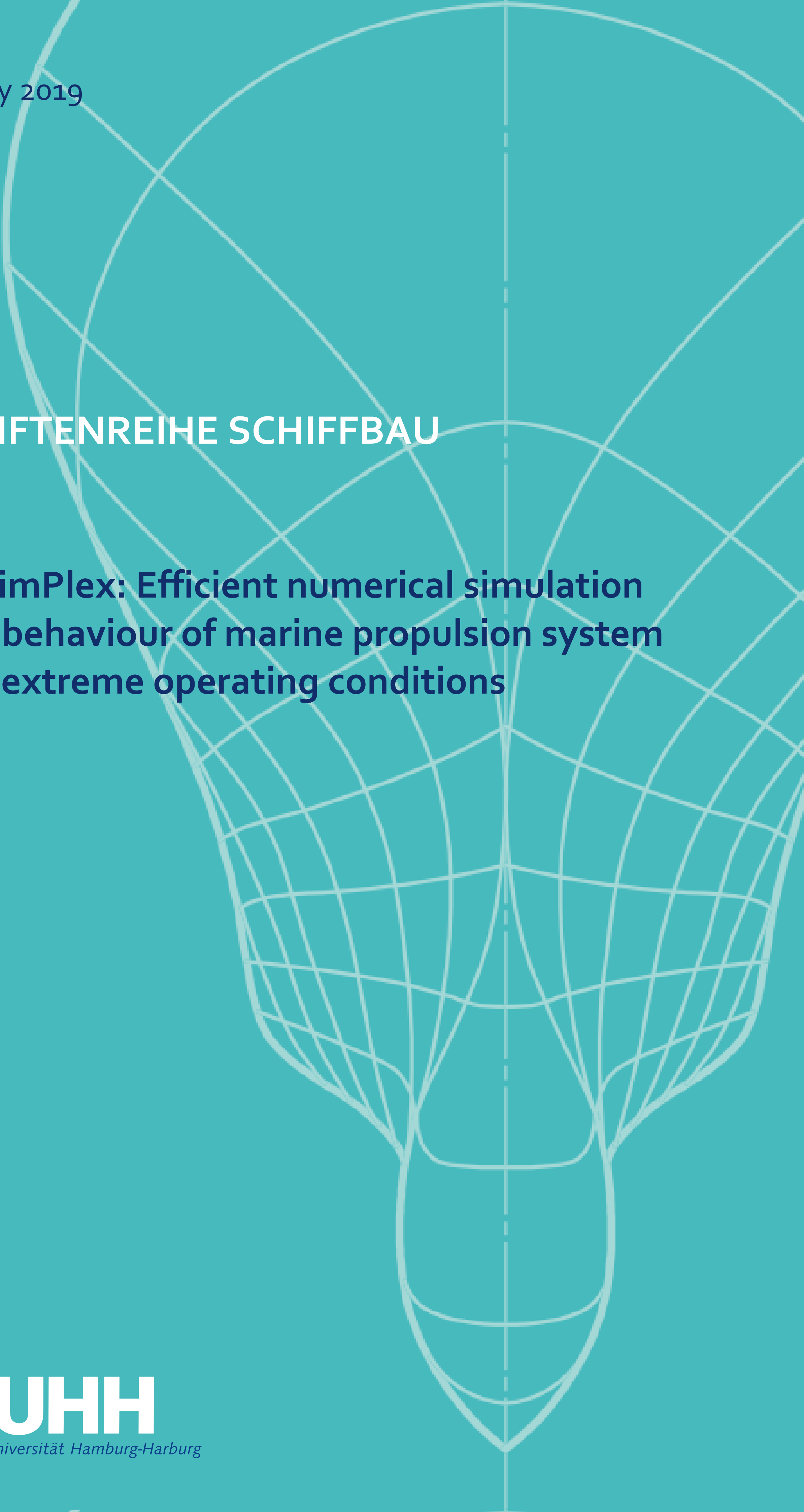

February 2019

SCHRIFTENREIHE SCHIFFBAU

InterSimPlex: Efficient numerical simulation of the behaviour of marine propulsion system under extreme operating conditions

TUHH
Technische Universität Hamburg-Harburg

Kurzdarstellung

Zuwendungsempfänger: Technische Universität Hamburg	Förderkennzeichen: 03SX3958
Vorhabensbezeichnung: Verbundprojekt ERA-NET MARTEC – INTERTHRUST – Untersuchungen zum Einfluss der dynamischen Lasten und Wechselwirkungen auf das Betriebsverhalten von Schiffsantrieben Teilvorhaben SimPlex – Effiziente numerische Simulation des Verhaltens von Schiffsantrieben unter extremen Betriebszuständen Projektleiter: Prof. Dr.-Ing. Moustafa Abdel-Maksoud Wissenschaftliche Mitarbeiter: Dipl.-Ing. Patrick Schiller Dipl.-Ing. Keqi Wang	
Laufzeit des Vorhabens: 01.07.2015 bis 30.06.2018	

Aufgabenstellung

Die Einschätzung der Dynamik der Entwicklung der Märkte für Seetransport und Serviceschiffe einschließlich der erheblichen Veränderungen an den Einsatzprofilen der Schiffe von Beginn des Vorhabens hat sich nicht geändert. Die Auslegung der Haupt- und Hilfsantriebe eines Schiffes in Hinblick auf ihr Einsatzprofil unter Berücksichtigung von kurzfristigen Änderungen wird immer wichtiger. Angesichts dieser unüberschaubaren Zahl möglicher Betriebszustände sahen sich die Zulieferer von Schiffsantrieben nicht in der Lage, den gestiegenen Anforderungen und Erwartungen des aktuellen Marktes zu entsprechen. Ziel war es daher, eine Methodik zu entwickeln, die es erlaubt, mit einer begrenzten Anzahl von numerischen Simulationen die notwendigen Daten über die Belastung der Antriebe bei extremen Einsatzbedingungen bereitzustellen.

Mithilfe von Rechenverfahren für viskose Strömung sollen für Azimuthantriebe sowie Querstrahler zahlreiche extreme Betriebsbedingungen untersucht werden. Dabei sollte für verschiedene Betriebszustände die optimale Kombination von numerischen Modellen für die Simulation von z. B. Turbulenz, Kavitation und relativer Bewegung zwischen den Antriebskomponenten ermittelt werden. Mittels einer Einteilung der Betriebszustände in Gefährdungsklassen können dann die Simulationen auf einen Belastungsfall pro Klasse reduziert werden und somit der Aufwand drastisch reduziert werden. Im Zusammenhang damit wurde als weiteres Ziel die Entwicklung eines parametrischen Modells zur Simulation des Manövrierverhaltens von Schiffen bei verschiedenen Betriebszuständen definiert. Dieses Modell kann in Entwurfsprognosen eingesetzt werden und ermöglicht die Vorhersage des Manövrierverhaltens von Schiffen bei extremen Betriebsbedingungen des Antriebs.

Benutzte Verfahren, Methoden etc.

Am Institut für Fluiddynamik und Schiffstheorie (FDS) werden seit längerem potenzialtheoretische Randelementeverfahren zur Simulation der Umströmung von Propellern entwickelt und eingesetzt. Das Paneelverfahren *pan*MARE als ein hauseigenes Verfahren ist aus diesen Entwicklungen hervorgegangen und wird seitdem ständig weiterentwickelt. Neben der Erfahrung mit der Entwicklung potenzialtheoretischer Verfahren verfügt das FDS über langjährige Kompetenzen in der Weiterentwicklung von RANS-Lösern. Hauptsächlich werden dabei Umströmungen von Schiffsrümpfen und Propellern betrachtet. Im Vorhaben wurde der kommerzielle viskose Strömungslöser ANSYS-CFX eingesetzt, der bei den Partnern ebenfalls verbreitet ist. Für das User-Coding wurde weitgehend auf ANSYS CFX Expression Language (CEL) zurückgegriffen.

Zusammenarbeit

Das Vorhaben hier ist ein Teilprojekt im ERA-NET-MARTEC - Verbundvorhaben ‚InterThrust' und durch eine intensive internationale Zusammenarbeit gekennzeichnet. Daneben hat dieses Projekt eine starke industrielle Komponente. Industrielle Partner im Vorhaben waren Voith Turbo Schneider Propulsion GmbH & Co. KG und Jastram GmbH und Co. KG aus Deutschland sowie Havyard Design and Solutions AS aus Norwegen. Als wissenschaftlicher Partner und zugleich als Koordinator des Vorhabens war SINTEF Ocean (ehemals MARINTEK) aus Norwegen beteiligt.

Die in diesem Vorhaben durchzuführenden Entwicklungen waren ohne die Daten, Ergebnisse und Erfahrungen vor allem der industriellen Partner nicht möglich. Die Zusammenarbeit war sehr intensiv. Gemeinsame Konferenzbeiträge und Veröffentlichungen sind Ausdruck dieser Zusammenarbeit.

Ergebnisse

Der Ablauf und die Ergebnisse des Vorhabens sind im detaillierten Abschlussbericht dargestellt. Der Bericht ist in englischer Sprache verfasst.

Gefördert durch:
Bundesministerium für Wirtschaft und Technologie
aufgrund eines Beschlusses des Deutschen Bundestages

TUHH
Technische Universität Hamburg-Harburg

Fluiddynamik und Schiffstheorie

Final Report

Efficient numerical simulation of the behaviour of marine propulsion system under extreme operating conditions

Acronym: Inter-SimPLex

---

collaborative project

Investigations into the Influence of High Dynamic Loads and Interaction Phenomena on the Performance of Marine Propulsors

Acronym: Inter-Thrust

Authors:

Prof. Dr.-Ing. Moustafa Abdel-Maksoud
Dipl.-Ing. Keqi Wang
Dipl.-Ing. Patrick Schiller

TECHNISCHE UNIVERSITÄT HAMBURG
Submission: November 2018

Nomenclature

x_0, y_0, z_0 : coordinates in earth-fixed coordinate system
x, y, z : coordinates in body-fixed coordinate system
u_0, v_0 : velocity in earth-fixed axis system
u, v : velocity in body-fixed axis system
u', v' : non-dimensionalized velocities in body-fixed axis system
$\vec{T}$: vector combined from forces and moment
ϑ : propeller rotating angle counting from 0 o'clock
ψ : azimuth angle
χ : course angle
β : drift angle
f : azimuth speed
r : radius or yaw velocity
D : propeller diameter
h_G : gap clearance
C_p : pressure coefficient
U : ship speed
ρ : water density
m : ship mass
X : force in body x-axis
Y : force in body y-axis
N : yaw moment in body z-axis
X', Y', N' : non-dimensionalized forces and moment in body-axis system
t : water depth
L_{pp} : ship length between perpendiculars
ω : frequency of the ship
F : force
T : thrust
Q : torque
J : advance velocity
p : pressure
k_t : thrust coefficient
k_q : torque coefficient
k_f : force coefficient
I_{zz} : moment of inertia
A_n, B_n : fourier coefficients
n_p : propeller revolution number

Acronyms

WP : Work Package
TT : Tunnel Thruster
MP : Main Propulsor
HD : Hydrodynamic Derivatives
BM : Bending Moment
ITTC : International Towing Tank Conference
PMM : Planar Motion Mechanism
CFD : Computational Fluid Dynamics
RANSE : Reynolds-Averaged Navier-Stokes Equations
SOLAS : Safety of Life at Sea
PFF : Propeller Free Format
FS : Full Scale
MS : Model Scale
PHV : Propulsion-Hull Vortex

Contents

List of Figures

List of Tables

1 Introduction

Main propulsion and auxiliary devices are usually designed with regard to the contractual design point. Duo to the operational demands on the maritime transport and service vessels, the ships has to be designed for operating under off-design conditions. As consequence, the possibility of the damage caused by extreme loads is growing, which leads to a very costly effect on shipyards and suppliers. Therefore, a development of practical tools is necessary.

The systematic calculations are based on the CFD methods. The optimal combination of numerical models such as turbulence and cavitation will be investigated. Numerical approach using viscous flow are preferred to represent flow phenomena such as flow separation.

Two candidates are involved in the simulation, namely, the podded azimuth propulsor applied as main propulsion (simply ”MP”) and the tunnel thruster (simply ”TT”) used as auxiliary device. On basis of the determined forces and moments caused by the MP, the operating states are divided into different hazard classes. This will enable the suppliers using a small number of numerical simulations to locate the high load range. In view of TT, the loss of thrust due to forward ship speed is well known, which leads to a negative effect on the manoeuvrability of the ship. In this project, a parametric simulation model is developed for estimating performance of MP and TT to predict the manoeuvring behaviour of ships under extreme operating conditions at early design stage.

The Inter-SimPLex project is part of the the Norwegian and German research project called Inter-Thrust. The project is carried out within the framework of MARTEC-II network under the lead of SINTEF and its participants are Havyard Ship Technology, Voith Turbo GmbH, Jastram GmbH and Hamburg University of Technology (TUHH). Following goals will be achieved by Inter-SimPLex:

- Classifying the azimuth thruster operating under off-design conditions.
- Detailed investigation of the flow behaviour by application of viscous numerical methods.
- Prediction of the behaviour of azimuth thruster during the design process by applying a mathematical model deduced from the numerical simulations.
- Development of a manoeuvring model taking into account the influences of MP and TT.

2 Overview of Work Packages

The Inter-SimPLex project consists of six working packages, including project management (WP1), technical working packages (WP2-WP5) and dissemination of project results (WP6). Each WP is divided into a number of subtasks. An overview of the main working packages is listed in Tab. 2.1.

Table 2.1: Main working packages of Inter-SimPLex project

Structure of Inter-SimPLex project	
Working Packages	Description
WP1	Project management
WP2	High dynamic loads on MP
WP3	Design and performance of TT
WP4	Development of design oriented models
WP5	Guidelines for design and performance prediction
WP6	Dissemination

The main tasks of the technical working packages to be fulfilled by TUHH are:

WP2: High dynamic loads on MP

Extreme inflow conditions like oblique flow can lead to high load on the MP. A plenty of numerical calculations is required. Various off-design conditions will be identified.

WP3: Design and performance of TT

The performance of TT integrated in ship depends on the design parameters such as tunnel length, hull frame angle, water line angle and so on. These parameters are very important during the thruster design. At ship manoeuvring, the interaction between ship and thruster slipstream as well as the efficiency loss duo to ship heading speed is of interest. The work of TUHH is focusing on the performance of TT in the turning circle manoeuvre.

WP4: Development of design oriented models

A mathematical model for the estimating performance of TT is required. TUHH participates in contribution of CFD results and provides the manoeuvring model for the cooperation of MP and TT.

WP5: Guidelines for design and performance prediction

The guidelines and recommendations will be issued with connection to the results from working packages WP2. WP3 and WP4.

3 Numerical Method

At this project, all numerical simulations are performed with the commercial CFD code ANSYS CFX, which solves numerically the instantaneous equations of mass and momentum conservation:

$$\frac{\partial p}{\partial t} + \nabla \cdot (\varrho U) = 0 \tag{3.1}$$

$$\frac{\partial(\varrho U)}{\partial t} + \nabla \cdot (\varrho U \otimes U) = -\nabla p + \nabla \cdot \tau + S_M \tag{3.2}$$

Here the stress tensor τ is related to the strain rate by:

$$\tau = \mu \left(\nabla U + (\nabla U)^T - \frac{2}{3} \delta \nabla \cdot U \right) \tag{3.3}$$

S_M stands for the body force and the symbol ⊗ is the outer product.

The ANSYS CFX solver uses a second order numerical scheme by default and is able to work in parallel mode for high performance computing. Different turbulence closure models (e.g. SST, SAS, EARSM, DES and LES) are available. In WP3, all the calculations were performed with the SST-model referred to the research in the previous task WP2, especially in the subtasks T2.1.2 and T2.1.3, showing that the SST-model can provide a sufficient accuracy to predict solutions of engineering problems. In CFX, an available cavitation model based on Rayleigh-Plesset equation (simply ”RPE”) is used as an interface to the mass transfer model. RPE controlled the growth and collapse of the bubble clusters. It should be noted, that the evaporation rate is higher than the condensation rate. Two empirical factors are given separately.

In the case of dynamic simulations (WP2-T2.2 and WP3-T3.3), the solution domain is time-related, the moving boundaries are set according to the chosen parameters such as azimuth speed in WP2 or the motion parameters in WP3. For the detailed mathematical implementation, the CFX modeling guide [6] and the specialist book by Ferziger and Peric [10] are recommended.

The finite volume method solves the flow variables like velocity and pressure at each discrete cell, where the mass and momentum are conserved. Grid cells with sharp angles, which may occur, can result in an insufficient accuracy of the numerical simulation. The big challenge is dealing with the near-wall grid resolution within the boundary layer, which means, the Y^+ value should be less than 1. In order to achieve this requirement, high quality structured meshes are generated by using ANSYS ICEM CFD.

4 Working Package WP2

The high dynamic loads on an azimuth thruster can be caused by thruster azimuth angles, ship drift angle or ocean currents due to the oblique flow. Two kinds of simulations are performed and compared.

The tasks in T2.1 - Loads due to steady oblique inflow – the inclined inflow can lead to a high change of amplitudes of forces and moments as well as flow separation. Subsequently, the cavitation may take place on the pressure side of the blade. It leads to a further deterioration of the propulsion characteristics and an increase of noise level.

For this purpose, various operating conditions with fixed inflow velocities and incident angles are carried out. The numerical investigation includes a grid study and an analysis of different turbulence models, such as SST, k-omega, SAS-SST, BSL-EARSM and DES. Furthermore, the influence of cavitating flow and critical parameter of gap clearance are taken into account.

The tasks in T2.2 - Loads due to unsteady operation conditions - an additional factor is introduced due to the unsteady conditions. The investigation is aimed at the performance of azimuth thruster at different azimuth speeds. This condition is closer to the reality of vessel manoeuvre in crash-back and dynamic positioning situations.

An overview of task WP2 can be found in Tab. 4.1.

Table 4.1.: Sub working tasks of task T2.1 and T2.2

WP2: High dynamic loads on MP	
Work task	Description
T2.1	**Loads due to steady oblique inflow**
T2.1.1	Grid studies at various inflow angles
T2.1.2	Numerical investigation of the flow around azimuth thruster with parallel inflow and at various inflow angles considering isotropic turbulence models
T2.1.3	Numerical investigation of the flow around azimuth thruster with parallel inflow and at various inflow angles considering anisotropic turbulence models
T2.1.4	Numerical investigation of cavitating flow on azimuth thrusters at various inflow angles
T2.1.5	Numerical investigation of the flow around azimuth thruster at different operating points (flow velocity, rotation speed and Azimuth angle)
T2.1.6	Investigation of the influence of critical geometrical parameters such as gap size to the load on the propulsor at selected operating points
T2.2	**Loads due to unsteady operation conditions**
T2.2.1	Simulation of the flow around the propulsor during reversing operation at one given speed, flow velocity and rotation rate for the reversing process
T2.2.2	Simulation of the flow around the propulsor during reversing operation for a second condition at the same rotation rate for the reversing process
T2.2.3	Simulation of the flow around the propulsor during reversing operation for a second rotation rate for the reversing process

4.1. T2.1 - Loads due to steady oblique inflow

Two types of propeller are applied. The first propeller called P-1374 is designed by MARINTEK and applied for the validation tests of grid study (T2.1.1) and turbulence models (T2.1.2 and T2.1.3). For this purpose, four operating conditions (see Tab. 4.2) are chosen, where experimental measurements are available. The second one is the Kaplan propeller with modified skew distribution mainly applied for T2.1.4 to T2.1.6 (see Tab. 4.1). It is very popular for vessels requiring high towing thrust. Both propellers are right-handed propeller.

The housing has a generic geometry designed also by MARINTEK and is manufactured from PVC. The duct called D-136 is a 19A type without diffuser and made from Plexiglas.

The coordinate system as proposed by ITTC is a right-handed, rectangular Cartesian system. The positive X-axis is directed in the forward direction, the Y and Z-axis are positive pointing to the starboard and downwards as shown in Fig. 4.1. For the evaluation of the forces and moments acting on the propulsion system, a thruster-fixed coordinate system has to be defined. Its origin is placed in the rotation axis of the entire thruster on the top of the housing as illustrated on the right side of Fig. 4.1.

Table 4.2: Overview of used flow conditions

case no.	J [-]	n [rps]	azimuth angle ψ [deg]
1	0.0	9	0
2	0.6	11	0
3	0.6	9	-35
4	0.6	9	+35

Fig. 4.1: Definition of coordinate systems

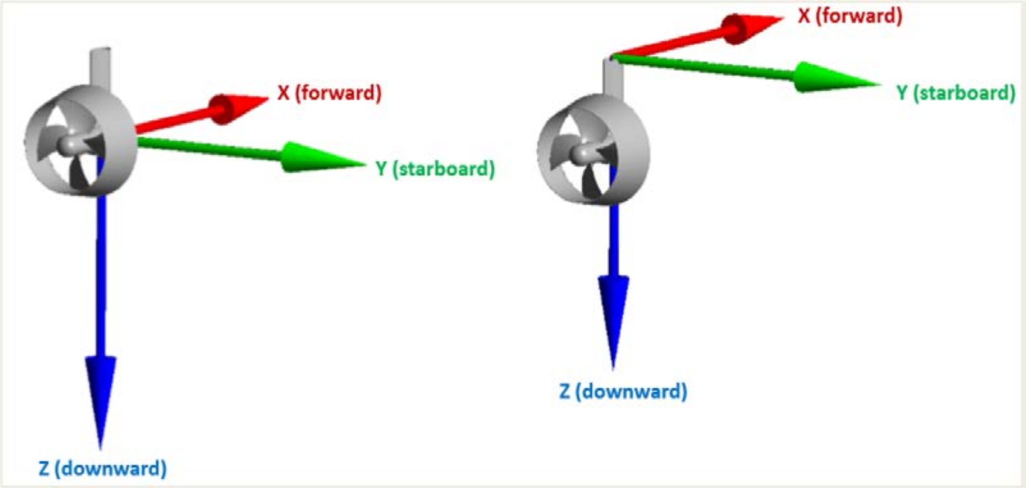

The calculation domain consists of three parts as shown in Fig. 4.2:

- rotating propeller domain,
- thruster domain which includes the whole thruster geometry. The domain has a cylindrical shape and can be rotated around a vertical rotation axis of the thruster,
- exterior domain.

The cylindrical domain has a diameter of 4*D* and a height of 3*D*. The exterior area has a quadratic base of 14*D* x 14*D* and a height of 7*D*. The exterior domain can be rotated for the treatment of the oblique flow. The effect of the free surface is neglected which is defined as slip wall. The velocity and pressure boundary conditions are set for inlet and outlet, respectively. For the side boundaries, opening is applied. The three domains are connected through sliding interfaces.

Fig. 4.2: Computational domain arrangement

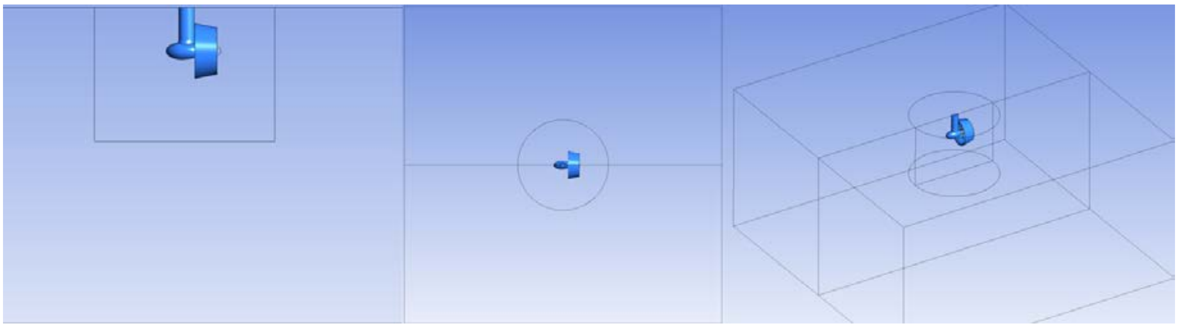

4.1.1. Task T2.1.1 - Grid study

The object of this task is to find out a proper mesh providing more accuracy and less computational effort.

Tab. 4.3 and 4.4 contain the main specifications of the propeller and duct used for the numerical calculations. All the tests are conducted with propeller design pitch of 1.1. The propeller has a cylindrical hub of 50 mm length with additional 14 mm forward elongation. The shape of the propeller cap is a half sphere. The gap between propeller hub and thruster housing is 1 mm. Duct has a length of 125 mm and is centred in agreement with propeller plane. Fig. 4.3 shows the configuration of the model thruster.

Table 4.3: Propeller main specifications

Propeller diameter	250 mm
Hub diameter	60 mm
Design pitch ratio	1.1 at r/R = 0.7
Skew	25 deg
Expanded blade area ratio	0.6
Number of blades	4

Table 4.4: Duct main specifications

Length	125 mm
Inner diameter	252.78
Max. outer diameter	303.96 mm
Leading edge radius	2.78 mm
Trailing edge radius	1.39 mm

Fig. 4.3: Computational domain arrangement

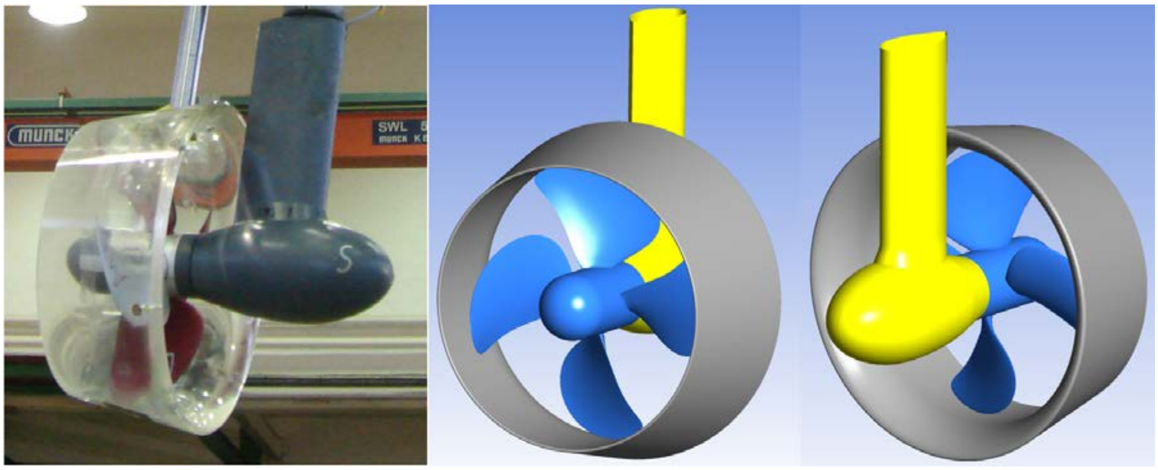

Four meshes are used as shown in Tab. 4.5. The growth of the cell size is followed by a refined factor of $1/\sqrt{2}$ in each spatial direction. The number of cells in the exterior domain remains constant.

Table 4.5: Different mesh resolutions used in the mesh study

mesh no.	number of cells [m.]			
	propeller	cylinder(wo propeller)	exterior	total
1	1.42	0.99	0.29	2.70
2	3.59	2.37	0.29	6.25
3	11.92	7.23	0.29	19.44
4	30.88	21.88	0.29	53.05

Tab. 4.6 to 4.9 show the comparison between calculated and experimental results. The agreement is presented as percentage in the following tables; a value of 100% means an exact match.

In cases 1 and 2 (see Tab. 4.2) the propeller thrust and torque of all meshes fit very well. The maximal deviation is only 2%. In cases 2, 3 and 4 the duct thrust is over-predicted about 12 ~ 16%. The high deviation is caused by the resistance from the duct mounting (see Fig. 4.3, left) which is however not included in the numerical simulation. Due to the small side force of zero azimuth angle, the deviation could be very huge. There is no assessment of the duct side force in this case.

In the presence of oblique flow in cases 3 and 4, the deviation regarding the thrust is in a range of 5%, generally. The largest deviation can be found at the grid with the lowest density. The calculated side forces (duct and total) are under-predicted around 10 ~ 20%. Regardless of the mounting, the predicted accuracy seems to be fine. Clear trend is hardly found for the forces in relation to the mesh resolution.

The steering moment (10M) from case 3 can get a better result with improved mesh resolution. The smallest deviation is only about 9%. In case 4, the results are getting even worse with increased number of nodes. The measured moment must be defective if the measured side force is uncertain.

Table 4.6: Simulation results of grid resolution study for case 1, coefficient values top and percentage of experimental value bottom

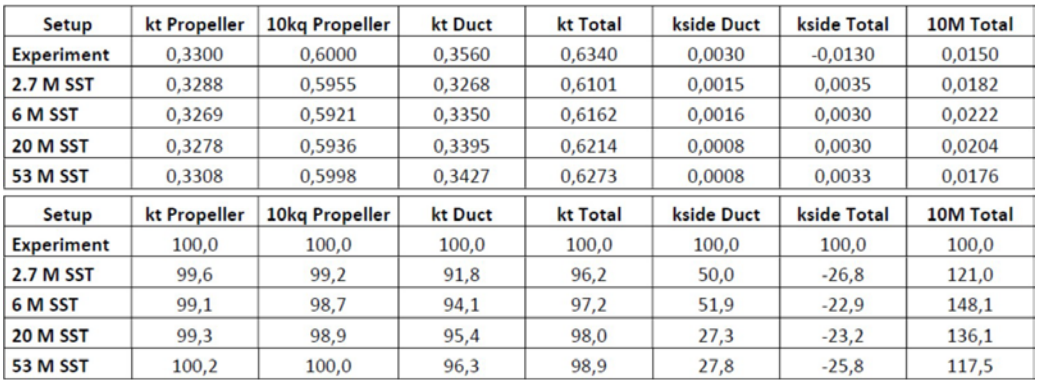

Setup	kt Propeller	10kq Propeller	kt Duct	kt Total	kside Duct	kside Total	10M Total
Experiment	0,3300	0,6000	0,3560	0,6340	0,0030	-0,0130	0,0150
2.7 M SST	0,3288	0,5955	0,3268	0,6101	0,0015	0,0035	0,0182
6 M SST	0,3269	0,5921	0,3350	0,6162	0,0016	0,0030	0,0222
20 M SST	0,3278	0,5936	0,3395	0,6214	0,0008	0,0030	0,0204
53 M SST	0,3308	0,5998	0,3427	0,6273	0,0008	0,0033	0,0176

Setup	kt Propeller	10kq Propeller	kt Duct	kt Total	kside Duct	kside Total	10M Total
Experiment	100,0	100,0	100,0	100,0	100,0	100,0	100,0
2.7 M SST	99,6	99,2	91,8	96,2	50,0	-26,8	121,0
6 M SST	99,1	98,7	94,1	97,2	51,9	-22,9	148,1
20 M SST	99,3	98,9	95,4	98,0	27,3	-23,2	136,1
53 M SST	100,2	100,0	96,3	98,9	27,8	-25,8	117,5

Table 4.7: Simulation results of grid resolution study for case 2, coefficient values top and percentage of experimental value bottom

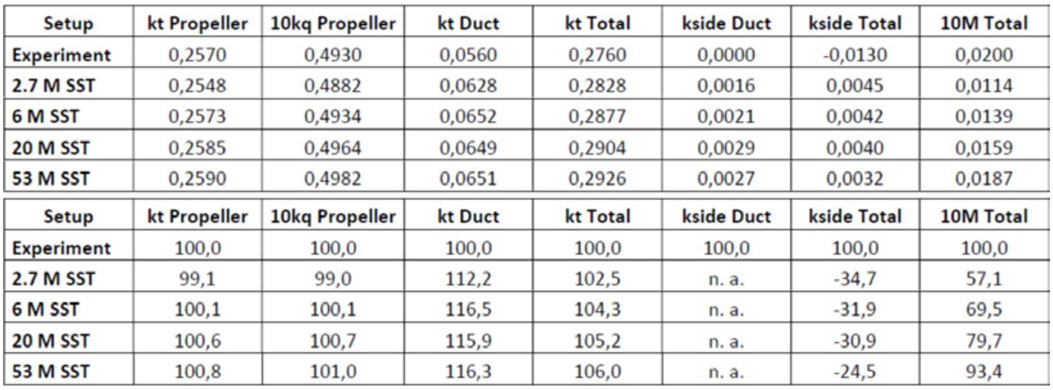

Setup	kt Propeller	10kq Propeller	kt Duct	kt Total	kside Duct	kside Total	10M Total
Experiment	0,2570	0,4930	0,0560	0,2760	0,0000	-0,0130	0,0200
2.7 M SST	0,2548	0,4882	0,0628	0,2828	0,0016	0,0045	0,0114
6 M SST	0,2573	0,4934	0,0652	0,2877	0,0021	0,0042	0,0139
20 M SST	0,2585	0,4964	0,0649	0,2904	0,0029	0,0040	0,0159
53 M SST	0,2590	0,4982	0,0651	0,2926	0,0027	0,0032	0,0187

Setup	kt Propeller	10kq Propeller	kt Duct	kt Total	kside Duct	kside Total	10M Total
Experiment	100,0	100,0	100,0	100,0	100,0	100,0	100,0
2.7 M SST	99,1	99,0	112,2	102,5	n. a.	-34,7	57,1
6 M SST	100,1	100,1	116,5	104,3	n. a.	-31,9	69,5
20 M SST	100,6	100,7	115,9	105,2	n. a.	-30,9	79,7
53 M SST	100,8	101,0	116,3	106,0	n. a.	-24,5	93,4

Table 4.8: Simulation results of grid resolution study for case 3, coefficient values top and percentage of experimental value bottom

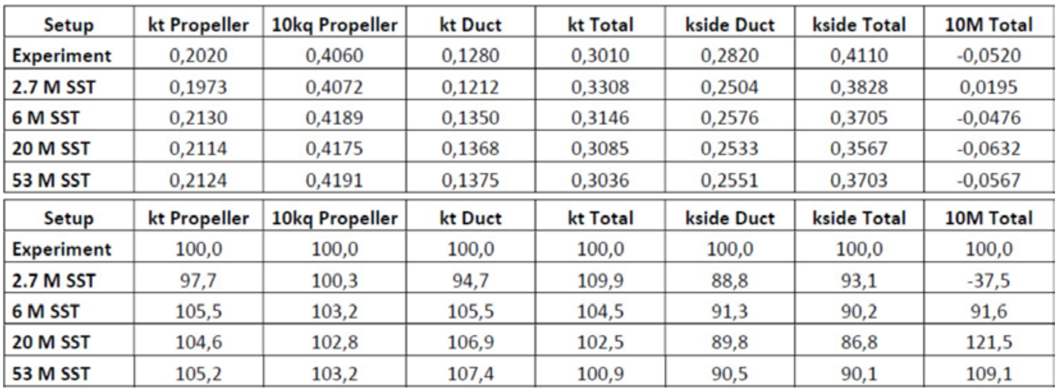

Setup	kt Propeller	10kq Propeller	kt Duct	kt Total	kside Duct	kside Total	10M Total
Experiment	0,2020	0,4060	0,1280	0,3010	0,2820	0,4110	-0,0520
2.7 M SST	0,1973	0,4072	0,1212	0,3308	0,2504	0,3828	0,0195
6 M SST	0,2130	0,4189	0,1350	0,3146	0,2576	0,3705	-0,0476
20 M SST	0,2114	0,4175	0,1368	0,3085	0,2533	0,3567	-0,0632
53 M SST	0,2124	0,4191	0,1375	0,3036	0,2551	0,3703	-0,0567

Setup	kt Propeller	10kq Propeller	kt Duct	kt Total	kside Duct	kside Total	10M Total
Experiment	100,0	100,0	100,0	100,0	100,0	100,0	100,0
2.7 M SST	97,7	100,3	94,7	109,9	88,8	93,1	-37,5
6 M SST	105,5	103,2	105,5	104,5	91,3	90,2	91,6
20 M SST	104,6	102,8	106,9	102,5	89,8	86,8	121,5
53 M SST	105,2	103,2	107,4	100,9	90,5	90,1	109,1

Table 4.9: Simulation results of grid resolution study for case 4, coefficient values top and percentage of experimental value bottom

Setup	kt Propeller	10kq Propeller	kt Duct	kt Total	kside Duct	kside Total	10M Total
Experiment	0,3000	0,5420	0,1640	0,4280	-0,3050	-0,4470	0,0080
2.7 M SST	0,2907	0,5645	0,1553	0,4638	-0,2562	-0,3801	-0,0072
6 M SST	0,2937	0,5489	0,1601	0,4256	-0,2497	-0,3373	0,0525
20 M SST	0,2949	0,5529	0,1684	0,4295	-0,2708	-0,3636	0,0689
53 M SST	0,2992	0,5601	0,1695	0,4312	-0,2692	-0,3646	0,0687

Setup	kt Propeller	10kq Propeller	kt Duct	kt Total	kside Duct	kside Total	10M Total
Experiment	100,0	100,0	100,0	100,0	100,0	100,0	100,0
2.7 M SST	96,9	104,1	94,7	108,4	84,0	85,0	-89,7
6 M SST	97,9	101,3	97,6	99,4	81,9	75,5	655,7
20 M SST	98,3	102,0	102,7	100,4	88,8	81,3	861,0
53 M SST	99,7	103,3	103,3	100,7	88,3	81,6	858,7

Better results can be achieved by using finer meshes. However, after 6M the improvement of the results is very small, thus a mesh size with number of nodes between 6 to 10 million is favoured.

4.1.2. Task T2.1.2-3 - Numerical investigation of the flow around azimuth thruster at various inflow angles considering isotropic and anisotropic turbulence models

Tasks 2.1.2 and 2.1.3 consider simulations with isotropic and anisotropic turbulence models. So for all four operating conditions mentioned in Tab. 4.2 investigations are performed with different turbulence closure models. ANSYS CFX of release 15 has provided following turbulence models:

- k – ω
- SST
- SAS-SST
- BSL-EARSM
- DES

Next, a brief description of turbulence models is introduced (details see CFX modeling guide [6]). The first two models, k-omega and SST, are isotropic models where the eddy viscosity (turbulent viscosity) is equal in all directions. The last three models such as SAS-SST, BSL-EARSM and DES are anisotropic.

4.1.2.1. k–omega model

The k-omega model is a two-equation turbulence model, which solves the two transport equations for the turbulent kinetic energy k and for the turbulent frequency ⍰. One of the advantages of the k-omega formulation is the near wall treatment for low-Reynolds number flow. The model is based on the formulation developed by Wilcox.

4.1.2.2. Shear Stress Transport (SST) model

The SST turbulence model by Menter is a widely used and robust two-equation eddy-viscosity turbulence model. The model combines the k-omega and k-epsilon turbulence model in such a manner that the k-omega model is used in the inner region of the boundary layer and the k-epsilon in the free shear flow.

4.1.2.3. SAS-SST model

The Scale-Adaptive Simulation (SAS) model is an improved URANS formulation, which allows the resolution of the turbulent spectrum under unstable flow conditions. The SAS concept is based on the introduction of the von Karman length-scale into the turbulence scale equation. The information provided by the von Karman length-scale allows SAS models to adjust dynamically to resolved structures in a URANS simulation, which results in a LES-like behavior in unsteady regions of the flow field. At the same time, the model provides standard RANS capabilities in stable flow regions. In this case for stable flows the SST turbulence model is used.

4.1.2.4. Explicit Algebraic Reynolds Stress Models (BSL-EARSM)

The Explicit Algebraic Reynolds Stress Models (EARSM) represents an extension of the standard two-equation model. These are derived from the Reynolds stress transport equations and give a non-linear relation between the Reynolds stresses and the mean strain-rate and vorticity tensors. Due to higher order terms, many flow phenomena are included in the model.

4.1.2.5. Detached Eddy Simulation (DES)

The use of LES in boundary layer flows at high Reynolds numbers is very expensive and therefore not useful for many industrial flow simulations. DES is a combination of RANS and LES formulations in order to arrive a hybrid formulation, where RANS is used inside attached and marginal separated boundary layers. Additionally, LES is applied at massively separated regions.

DES requires a high quality of the grid regarding the cell sizes and aspect ratios. For this purpose, a grid no. 5 needs to be generated additionally. For other models, grid no. 3 (20M cells) is applied (see Tab. 4.10). The result from isotropic turbulence model is used as initialization for the simulations carried out with anisotropic one.

Table 4.10: Meshes used for the variation of turbulence models

mesh no.	number of cells [m.]			
	propeller	thruster	exterior	total
3	11.92	7.23	0.29	19.44
5	11.62	14.11	1.63	27.36

The comparison for case 1 to 4 can be found from Tab. 4.11 to Tab. 4.14, respectively.

Table 4.11: Simulation results of turbulence model variation for case 1, coefficient values top and percentage of experimental value bottom

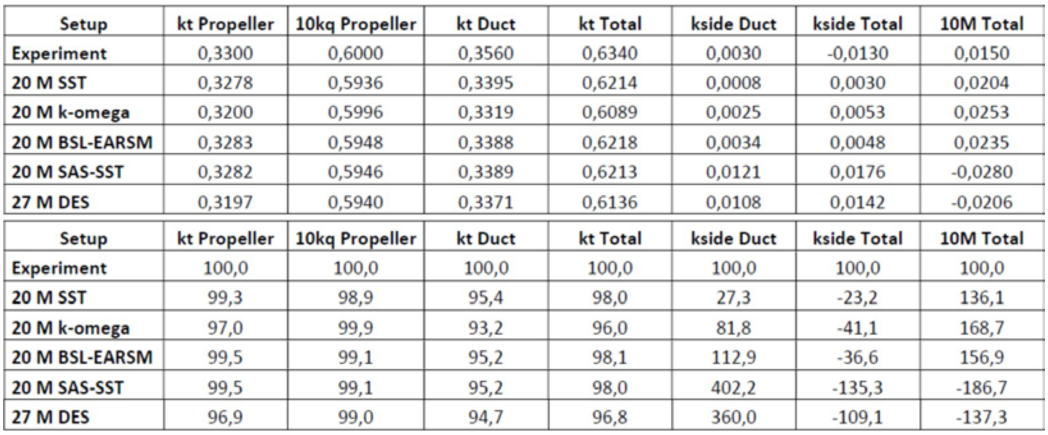

Setup	kt Propeller	10kq Propeller	kt Duct	kt Total	kside Duct	kside Total	10M Total
Experiment	0,3300	0,6000	0,3560	0,6340	0,0030	-0,0130	0,0150
20 M SST	0,3278	0,5936	0,3395	0,6214	0,0008	0,0030	0,0204
20 M k-omega	0,3200	0,5996	0,3319	0,6089	0,0025	0,0053	0,0253
20 M BSL-EARSM	0,3283	0,5948	0,3388	0,6218	0,0034	0,0048	0,0235
20 M SAS-SST	0,3282	0,5946	0,3389	0,6213	0,0121	0,0176	-0,0280
27 M DES	0,3197	0,5940	0,3371	0,6136	0,0108	0,0142	-0,0206

Setup	kt Propeller	10kq Propeller	kt Duct	kt Total	kside Duct	kside Total	10M Total
Experiment	100,0	100,0	100,0	100,0	100,0	100,0	100,0
20 M SST	99,3	98,9	95,4	98,0	27,3	-23,2	136,1
20 M k-omega	97,0	99,9	93,2	96,0	81,8	-41,1	168,7
20 M BSL-EARSM	99,5	99,1	95,2	98,1	112,9	-36,6	156,9
20 M SAS-SST	99,5	99,1	95,2	98,0	402,2	-135,3	-186,7
27 M DES	96,9	99,0	94,7	96,8	360,0	-109,1	-137,3

Table 4.12: Simulation results of turbulence model variation for case 2, coefficient values top and percentage of experimental value bottom

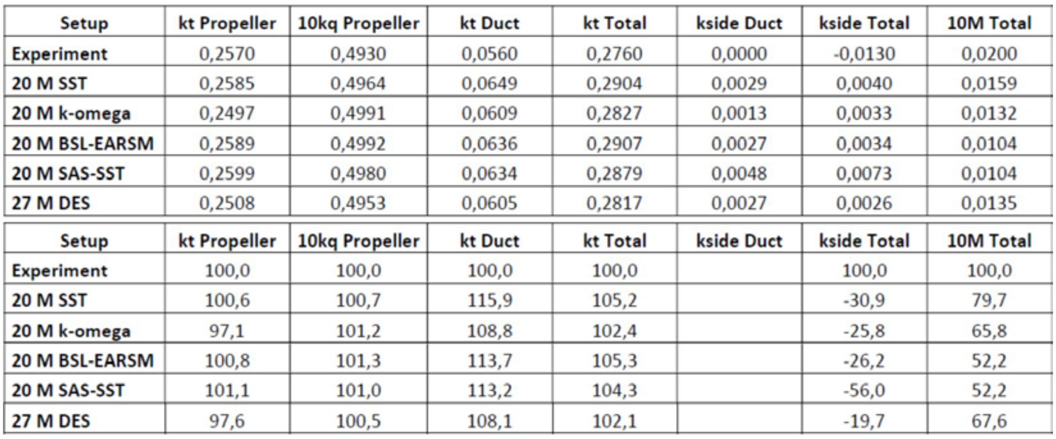

Setup	kt Propeller	10kq Propeller	kt Duct	kt Total	kside Duct	kside Total	10M Total
Experiment	0,2570	0,4930	0,0560	0,2760	0,0000	-0,0130	0,0200
20 M SST	0,2585	0,4964	0,0649	0,2904	0,0029	0,0040	0,0159
20 M k-omega	0,2497	0,4991	0,0609	0,2827	0,0013	0,0033	0,0132
20 M BSL-EARSM	0,2589	0,4992	0,0636	0,2907	0,0027	0,0034	0,0104
20 M SAS-SST	0,2599	0,4980	0,0634	0,2879	0,0048	0,0073	0,0104
27 M DES	0,2508	0,4953	0,0605	0,2817	0,0027	0,0026	0,0135

Setup	kt Propeller	10kq Propeller	kt Duct	kt Total	kside Duct	kside Total	10M Total
Experiment	100,0	100,0	100,0	100,0		100,0	100,0
20 M SST	100,6	100,7	115,9	105,2		-30,9	79,7
20 M k-omega	97,1	101,2	108,8	102,4		-25,8	65,8
20 M BSL-EARSM	100,8	101,3	113,7	105,3		-26,2	52,2
20 M SAS-SST	101,1	101,0	113,2	104,3		-56,0	52,2
27 M DES	97,6	100,5	108,1	102,1		-19,7	67,6

Table 4.13: Simulation results of turbulence model variation for case 3, coefficient values top and percentage of experimental value bottom

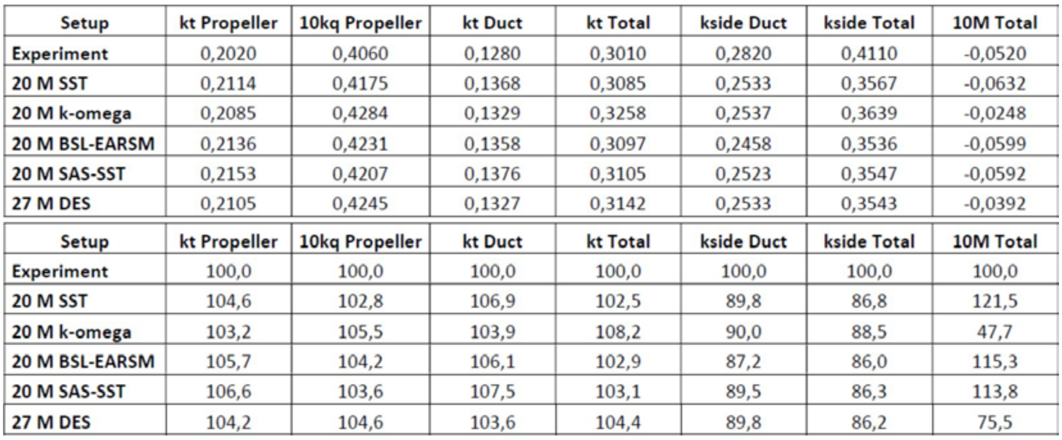

Setup	kt Propeller	10kq Propeller	kt Duct	kt Total	kside Duct	kside Total	10M Total
Experiment	0,2020	0,4060	0,1280	0,3010	0,2820	0,4110	-0,0520
20 M SST	0,2114	0,4175	0,1368	0,3085	0,2533	0,3567	-0,0632
20 M k-omega	0,2085	0,4284	0,1329	0,3258	0,2537	0,3639	-0,0248
20 M BSL-EARSM	0,2136	0,4231	0,1358	0,3097	0,2458	0,3536	-0,0599
20 M SAS-SST	0,2153	0,4207	0,1376	0,3105	0,2523	0,3547	-0,0592
27 M DES	0,2105	0,4245	0,1327	0,3142	0,2533	0,3543	-0,0392

Setup	kt Propeller	10kq Propeller	kt Duct	kt Total	kside Duct	kside Total	10M Total
Experiment	100,0	100,0	100,0	100,0	100,0	100,0	100,0
20 M SST	104,6	102,8	106,9	102,5	89,8	86,8	121,5
20 M k-omega	103,2	105,5	103,9	108,2	90,0	88,5	47,7
20 M BSL-EARSM	105,7	104,2	106,1	102,9	87,2	86,0	115,3
20 M SAS-SST	106,6	103,6	107,5	103,1	89,5	86,3	113,8
27 M DES	104,2	104,6	103,6	104,4	89,8	86,2	75,5

Table 4.14: Simulation results of turbulence model variation for case 4, coefficient values top and percentage of experimental value bottom

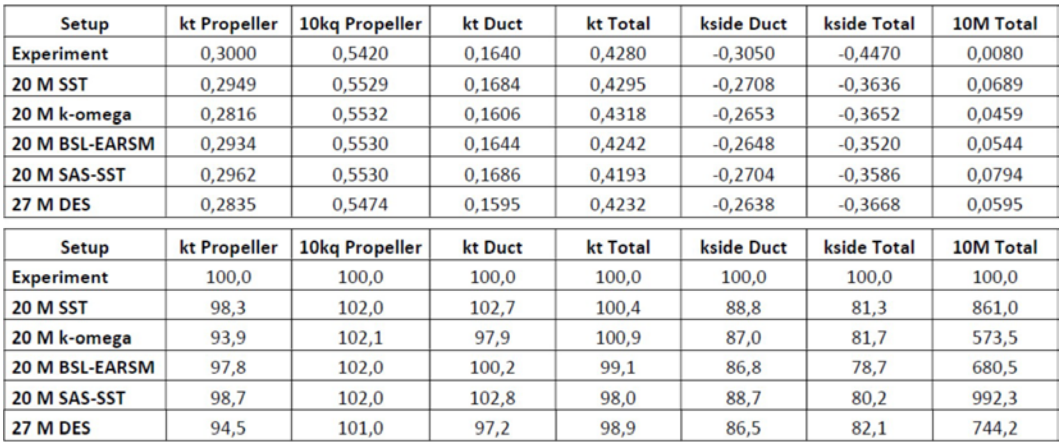

Setup	kt Propeller	10kq Propeller	kt Duct	kt Total	kside Duct	kside Total	10M Total
Experiment	0,3000	0,5420	0,1640	0,4280	-0,3050	-0,4470	0,0080
20 M SST	0,2949	0,5529	0,1684	0,4295	-0,2708	-0,3636	0,0689
20 M k-omega	0,2816	0,5532	0,1606	0,4318	-0,2653	-0,3652	0,0459
20 M BSL-EARSM	0,2934	0,5530	0,1644	0,4242	-0,2648	-0,3520	0,0544
20 M SAS-SST	0,2962	0,5530	0,1686	0,4193	-0,2704	-0,3586	0,0794
27 M DES	0,2835	0,5474	0,1595	0,4232	-0,2638	-0,3668	0,0595

Setup	kt Propeller	10kq Propeller	kt Duct	kt Total	kside Duct	kside Total	10M Total
Experiment	100,0	100,0	100,0	100,0	100,0	100,0	100,0
20 M SST	98,3	102,0	102,7	100,4	88,8	81,3	861,0
20 M k-omega	93,9	102,1	97,9	100,9	87,0	81,7	573,5
20 M BSL-EARSM	97,8	102,0	100,2	99,1	86,8	78,7	680,5
20 M SAS-SST	98,7	102,0	102,8	98,0	88,7	80,2	992,3
27 M DES	94,5	101,0	97,2	98,9	86,5	82,1	744,2

For case 1 and 2 the propeller thrust is well predicted by all used turbulence models within a deviation of only 1% except the $k - \omega$ and DES where the deviation is up to 3%. The deviation of propeller torque is in a range of 1%.

Regarding the thrust of duct, all turbulence models under-predict (max. 5%) in case 1 and over-predict (max. 14%) in case 2 due to the existence of the duct mounting as mentioned before. The accuracy of $k - \omega$ and DES are slightly lower than the other ones in both cases. The deviation of total thrust is mainly composed of propeller and duct and ranges from 2 to 5%.

For the azimuth angles of $\psi = \pm 35^\circ$ the propeller thrust is over-predicted about $3 \sim 6\%$ for case 3 and under-predicted about $2 \sim 6\%$ for case 4. The $k - \omega$ and DES show smaller thrust coefficients than the others. The propeller torque predicted by all turbulence models fits quite well for cases 3 and 4.

The deviation of duct thrust is $3 \sim 7\%$ above the experimental values in case 3 and $2 \sim 3\%$ in case 4, in which the $k - \omega$ and DES models give lower duct thrust coefficients than the others.

Over-predicted propeller and duct thrust in case 3 result in an over-predicted total thrust by $3 \sim 8\%$. In case 4, the deviation is below 2% due to the under-predicted propeller thrust.

It is difficult to make a clear statement in the lack of the accuracy from the measured results regarding the transverse force and steering moment.

The variation of the turbulence model shows, that no turbulence model results in a distinct improvement within the cases. All of them show a sufficient data match with the experimental results. DES should provide more accurate results in cases where a huge quantity of separated flow occurs. Overall, using SST turbulence model is still the first choice for industrial application.

4.1.3. T2.1.4 - Numerical investigation of cavitating flow on azimuth thrusters at various inflow angles

Occurring high heading angle of a ship can lead to a huge dynamic change of working conditions of the MP. If the pressure on the blades drops below the vapour pressure, cavitation will take place. In addition to the loss of thrust, cavitation can also produce undesirable noise derived from bubble implosion due to sudden pressure change.

The selected condition of ψ = 120◦ (J = 1.0) is referred to the maximal propeller load. Furthermore different azimuth angles from ψ = 0◦ to 180◦ (J = 0.6) are also conducted to show the development of cavitating flow. An overview of the calculation matrix is given in Tab. 4.15.

Table 4.15: Selected cases for the simulation of cavitation

azimuth angle ψ [deg]	propeller diameter D [m]	propeller speed n_P [Hz]	advance coefficients J [-]
120	4.2	2.1	1.0
0 - 180 every 30	4.2	2.1	0.6

As mentioned, a new propeller geometry based on the Kaplan propeller Ka 4-70 is applied. The modified skew distribution is shown in Fig. 4.4. The negative skew near the root has the purpose of balancing the extra spindle moment caused by the upper part with positive skew. The illustration is found in Fig. 4.5.

Fig. 4.4: New skew distribution over radius

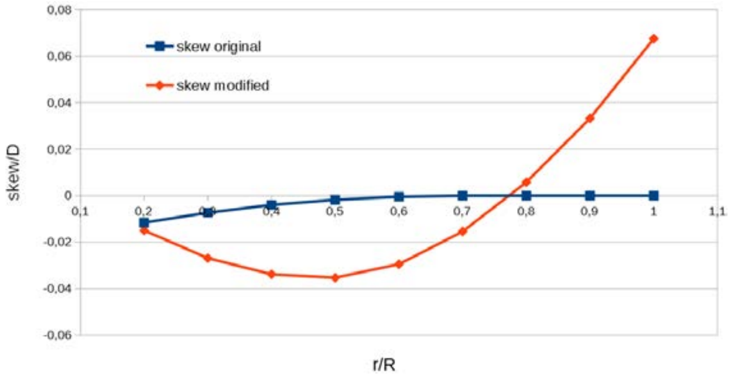

Fig. 4.5: Modified propeller and thruster configuration

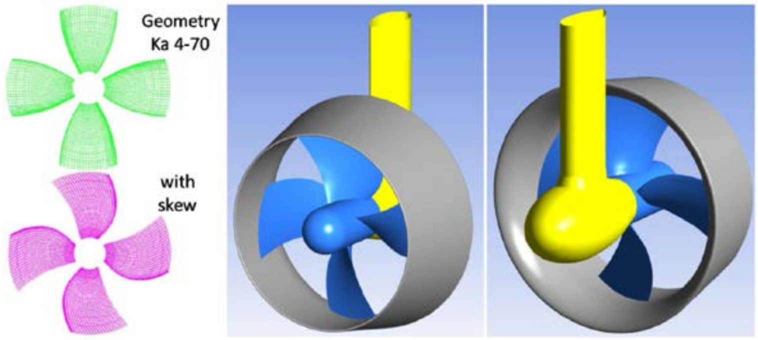

Zwart model is available which is based on simplified Rayleigh-Plesset equation (CFX modelling guide, Cavitation Model [6]) and describes the mass transfer between liquid and vapour. When cavitation occurs, both phases are assumed to share the same cell but with individual volume fraction and travel with the same velocity. If the liquid velocity differs from that of the vapour, the cavitation model is called an inhomogeneous model. At this investigation only homogeneous model is activated. SST model is applied for turbulence modelling.

The propeller axis locates 6 m under the top boundary. The saturation pressure of water is assumed to be p_{sat} = 2350 Pa. The atmospheric pressure as well as hydrostatic pressure is taken into account. As initial guess, a converged solution without cavitation is used.

4.1.3.1. Cavitating flow at operating point of $\psi = 120^\circ$ and $J = 1.0$

Different cavity types are introduced by John [7] e.g. tip vortex cavitation, sheet cavitation, bubble cavitation and cloud cavitation. Each type of the cavitation has its own position where it frequently occurs. Fig. 4.6 illustrates exemplary the vortex visualized by Q- criterion. Plenty of cavities can be found on the right side of the figure. Considering its shape and appearing location, it does not belong to any types mentioned before. It is more in line with the type as reported by Huse [11] called Propulsion-Hull Vortex (PHV) which depicts the backflow effect due to water deficiency in the case of high loading and low tip clearance, as a result, the propeller attempt to draw water from downstream. Fig. 4.7 demonstrates this effect clearly. The red backflow (positive in body-fixed coordinate system) appears on the luv side near the nose of duct.

Fig. 4.6: Occurring cavitation pattern characterized with the water volume fraction

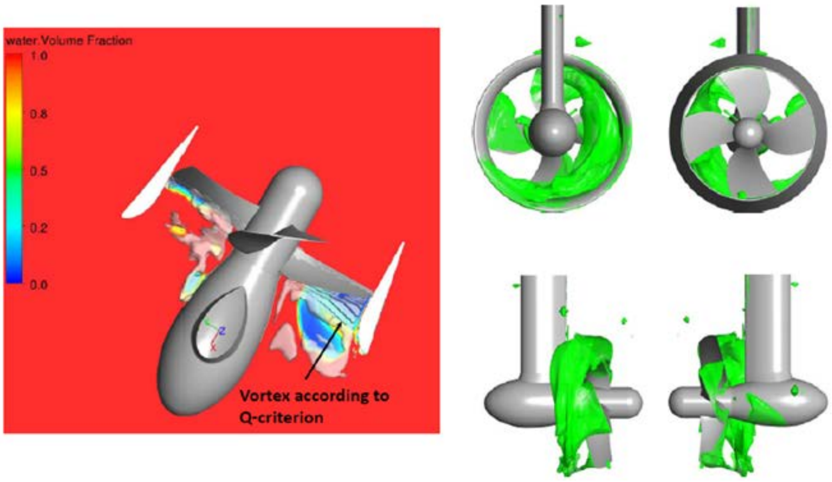

Fig. 4.7: Velocity field with streamlines at $\psi = 120^\circ$

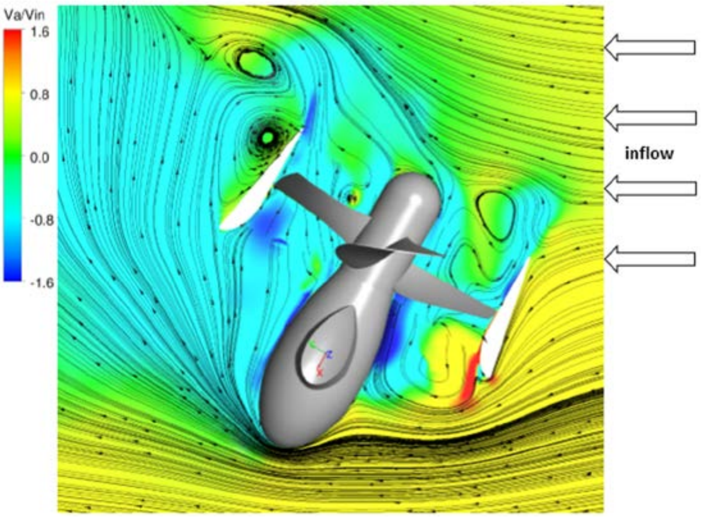

A comparison of time history of one blade longitudinal force with- and without cavitation model during one period of revolution is shown in Fig. 4.8. The amplitude of the oscillation from cavitation is even smaller than that without cavitation. It can be explained that the massive cavities can homogenize the pressure distribution not only for the suction side but also partly for the pressure side as shown in Fig. 4.9.

Fig. 4.8: Time history of blade thrust during one blade revolution with- and without cavitation model

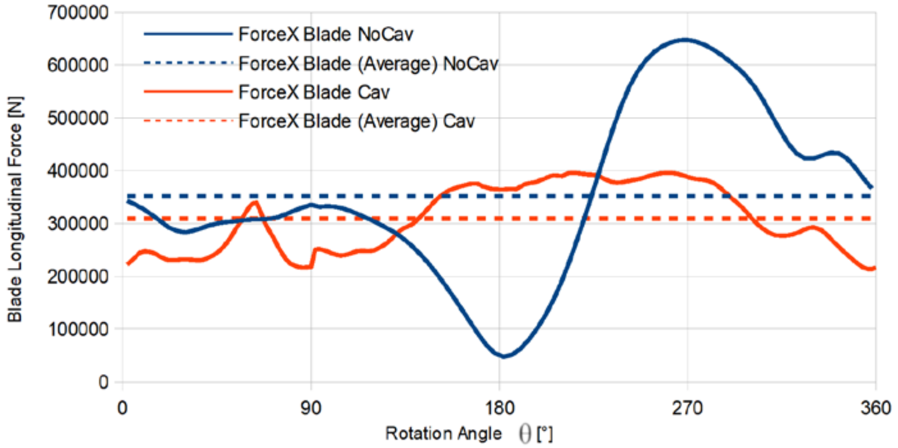

Fig. 4.9: Pressure distribution for the calculation with- and without cavitation model

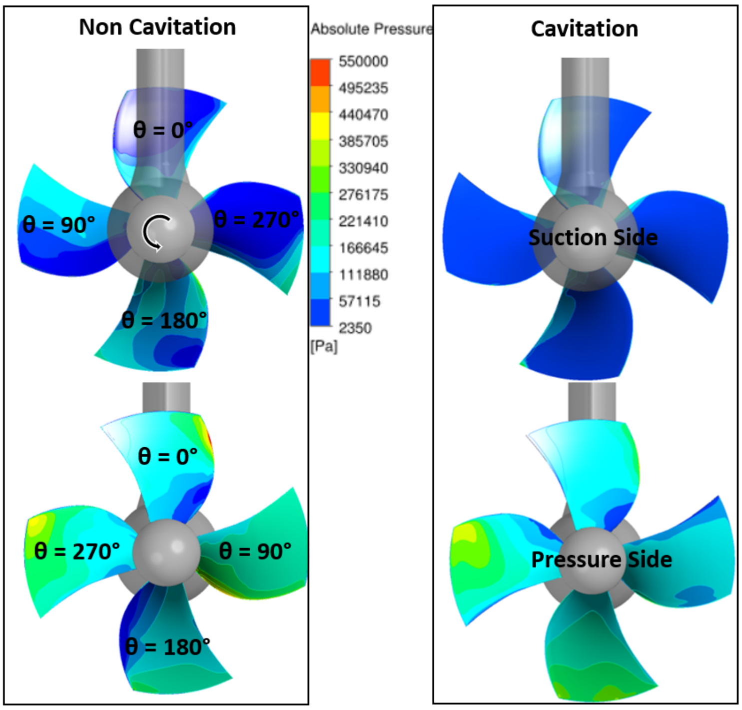

Tab. 4.16 shows some values of the result. The first part presents the coefficients for the cavitating and non-cavitating cases. The second part gives the percentage of the total value from each component (duct, propeller and housing). The last part stands for the percentage change of the cavitating case relative to non-cavitating one. Generally, cavitation causes a reduction of the total thrust and moment (kF X+Y and kQ X+Y) of about 25%.

The fist table in Tab. 4.17 gives an overview of the standard deviation of the different coefficients for the cavitating and non-cavitating condition and the second shows the percentage ratio of the cavitating case with respect to non-cavitating one. Generally, the fluctuation range of cavitation is higher for duct and housing and lower for the propeller in comparison to the cases without cavitation.

Table 4.16: Calculated coefficients for cavitating and non-cavitating case (top), percentage of total value (middle) and comparison of cavitating and non-cavitating (bottom)

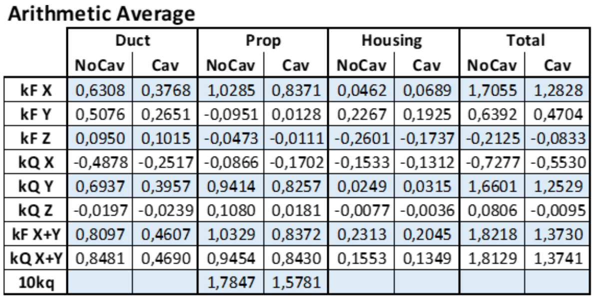

Arithmetic Average

	Duct		Prop		Housing		Total	
	NoCav	Cav	NoCav	Cav	NoCav	Cav	NoCav	Cav
kF X	0,6308	0,3768	1,0285	0,8371	0,0462	0,0689	1,7055	1,2828
kF Y	0,5076	0,2651	-0,0951	0,0128	0,2267	0,1925	0,6392	0,4704
kF Z	0,0950	0,1015	-0,0473	-0,0111	-0,2601	-0,1737	-0,2125	-0,0833
kQ X	-0,4878	-0,2517	-0,0866	-0,1702	-0,1533	-0,1312	-0,7277	-0,5530
kQ Y	0,6937	0,3957	0,9414	0,8257	0,0249	0,0315	1,6601	1,2529
kQ Z	-0,0197	-0,0239	0,1080	0,0181	-0,0077	-0,0036	0,0806	-0,0095
kF X+Y	0,8097	0,4607	1,0329	0,8372	0,2313	0,2045	1,8218	1,3730
kQ X+Y	0,8481	0,4690	0,9454	0,8430	0,1553	0,1349	1,8129	1,3741
10kq			1,7847	1,5781				

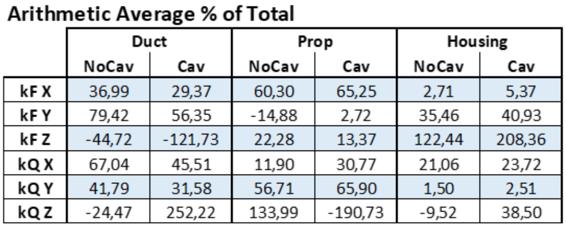

Arithmetic Average % of Total

	Duct		Prop		Housing	
	NoCav	Cav	NoCav	Cav	NoCav	Cav
kF X	36,99	29,37	60,30	65,25	2,71	5,37
kF Y	79,42	56,35	-14,88	2,72	35,46	40,93
kF Z	-44,72	-121,73	22,28	13,37	122,44	208,36
kQ X	67,04	45,51	11,90	30,77	21,06	23,72
kQ Y	41,79	31,58	56,71	65,90	1,50	2,51
kQ Z	-24,47	252,22	133,99	-190,73	-9,52	38,50

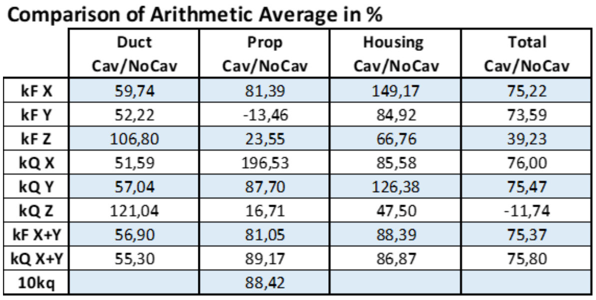

Comparison of Arithmetic Average in %

	Duct	Prop	Housing	Total
	Cav/NoCav	Cav/NoCav	Cav/NoCav	Cav/NoCav
kF X	59,74	81,39	149,17	75,22
kF Y	52,22	-13,46	84,92	73,59
kF Z	106,80	23,55	66,76	39,23
kQ X	51,59	196,53	85,58	76,00
kQ Y	57,04	87,70	126,38	75,47
kQ Z	121,04	16,71	47,50	-11,74
kF X+Y	56,90	81,05	88,39	75,37
kQ X+Y	55,30	89,17	86,87	75,80
10kq		88,42		

Table 4.17: Calculated standard deviation in coefficient values for cavitating and non-cavitating case (top) and comparison of cavitating and non-cavitating (bottom)

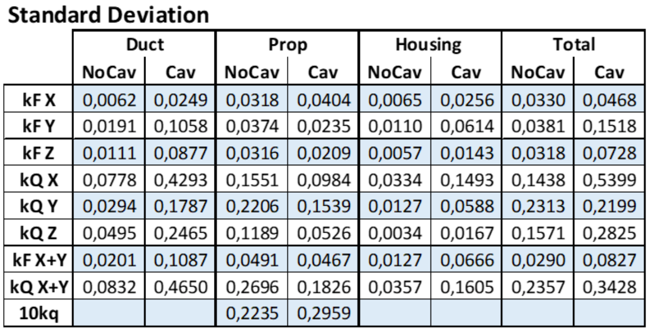

Standard Deviation

	Duct		Prop		Housing		Total	
	NoCav	Cav	NoCav	Cav	NoCav	Cav	NoCav	Cav
kF X	0,0062	0,0249	0,0318	0,0404	0,0065	0,0256	0,0330	0,0468
kF Y	0,0191	0,1058	0,0374	0,0235	0,0110	0,0614	0,0381	0,1518
kF Z	0,0111	0,0877	0,0316	0,0209	0,0057	0,0143	0,0318	0,0728
kQ X	0,0778	0,4293	0,1551	0,0984	0,0334	0,1493	0,1438	0,5399
kQ Y	0,0294	0,1787	0,2206	0,1539	0,0127	0,0588	0,2313	0,2199
kQ Z	0,0495	0,2465	0,1189	0,0526	0,0034	0,0167	0,1571	0,2825
kF X+Y	0,0201	0,1087	0,0491	0,0467	0,0127	0,0666	0,0290	0,0827
kQ X+Y	0,0832	0,4650	0,2696	0,1826	0,0357	0,1605	0,2357	0,3428
10kq			0,2235	0,2959				

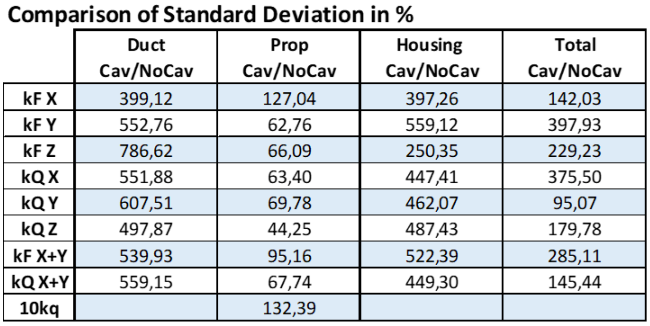

Comparison of Standard Deviation in %

	Duct	Prop	Housing	Total
	Cav/NoCav	Cav/NoCav	Cav/NoCav	Cav/NoCav
kF X	399,12	127,04	397,26	142,03
kF Y	552,76	62,76	559,12	397,93
kF Z	786,62	66,09	250,35	229,23
kQ X	551,88	63,40	447,41	375,50
kQ Y	607,51	69,78	462,07	95,07
kQ Z	497,87	44,25	487,43	179,78
kF X+Y	539,93	95,16	522,39	285,11
kQ X+Y	559,15	67,74	449,30	145,44
10kq		132,39		

4.1.3.2. Variation of ψ at J=0.6

The investigation of cavitating flow at different azimuth angles will be discussed here. Fig. 4.10 shows the pressure distribution, limiting streamlines and cavitation pattern (orange) represented by a vapour volume fraction of $\alpha = 0.5$. At $\psi = 0°$, the cavitating flow can be found rarely at the blade tip where the blade passes the wake of the shaft in the 12 o'clock position. At $\psi = 30°$ the quantity of cavitation increases slightly on the leading edge from 3 to 6 o'clock due to the additional circumferential velocity from the oblique flow. From azimuth angle of $\psi = 60°$ to $\psi = 120°$, large areas of cavitation cover the region of the duct extending to the blade. The reason of appearing cavitating flow near the duct has been explained according to Fig. 4.7. After $\psi = 120°$, the amount decrease (see $\psi = 150°$ and 180°).

A detailed comparison of the different coefficients with- and without cavitation over the azimuth angles is given from Fig. 4.11 to Fig. 4.16.

Fig. 4.11 presents the propeller thrust. The difference occurs after $\psi = 30°$. At $\psi = 60°$ as well as 90° the propeller thrust is higher in the cavitating case of about 12 − 15%. Between $\psi = 120°$ and 150° the thrusts are more or less on the same level. Less thrust is generated by the propeller in case of cavitating case at $\psi = 180°$. The development of the propeller torque (see Fig. 4.12) shows the same tendency such as the propeller thrust, as it is expected. Fig. 4.13 depicts the duct thrust in dependency of azimuth angles. Because the cavitation does not appears within small azimuth angles, the coefficients match very well up to $\psi = 30°$. Due to massive cavitation, then the difference increases continuously with increasing azimuth angle up to $\psi = 120°$. The thrust drops dramatically up to $\psi = 150°$ in both cases.

The steering moment is shown in Fig. 4.14. The both curves are quite different after $\psi = 30°$. At cavitating condition, the maximal steering moment occurs at $\psi = 150°$, which is even higher than the maximal value in the case without cavitation. The massive cavitation suppresses the growing steering moment especially from $\psi = 30°$ to $\psi = 90°$.

Fig. 4.15 and Fig. 4.16 show the development of the total force and bending moment. Both curves show the same tendency because the bending moment is derived from the force multiplied by a lever arm. The difference begins from $\psi = 60°$ and ends at $\psi = 150°$. Basically, the total loads are reduced in the presence of cavitation. The cavitating flow may enlarge the oscillation of loads on duct and housing and reduce them to the propeller. The study regarding various azimuth angles has shown that the maximal difference appears between $\psi = 90°$ and $\psi = 120°$. The duct dominates essentially the difference by cause of massive cavitating flow in that range.

Fig. 4.10: Pressure distribution and limiting streamlines on the propeller blades and cavitation pattern ($\alpha = 0.5$) for different azimuth angles at $J = 0.6$ and $t = 6$m

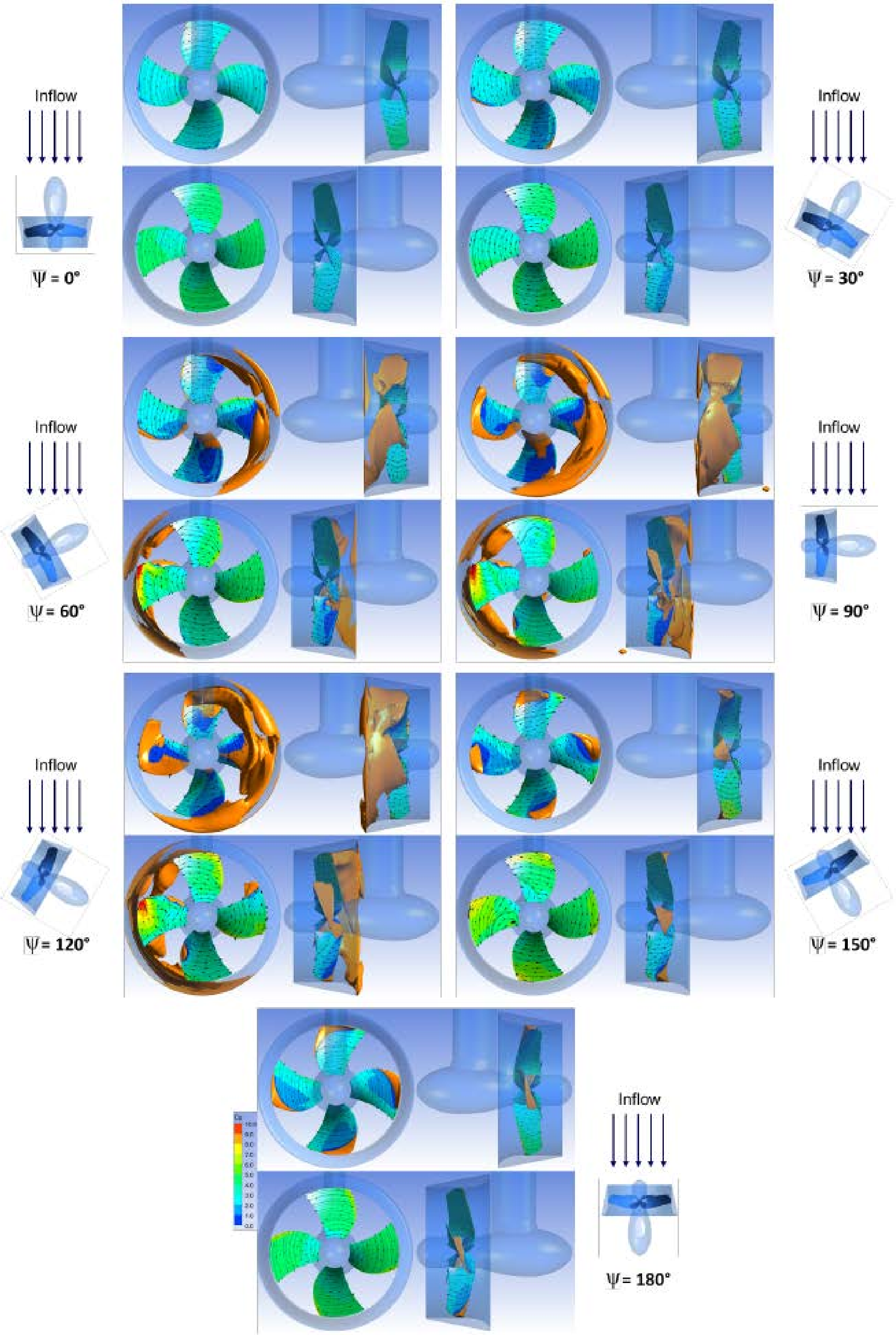

Fig. 4.11: Comparison of development of propeller thrust over different azimuth angles for cavitating and non-cavitating conditions

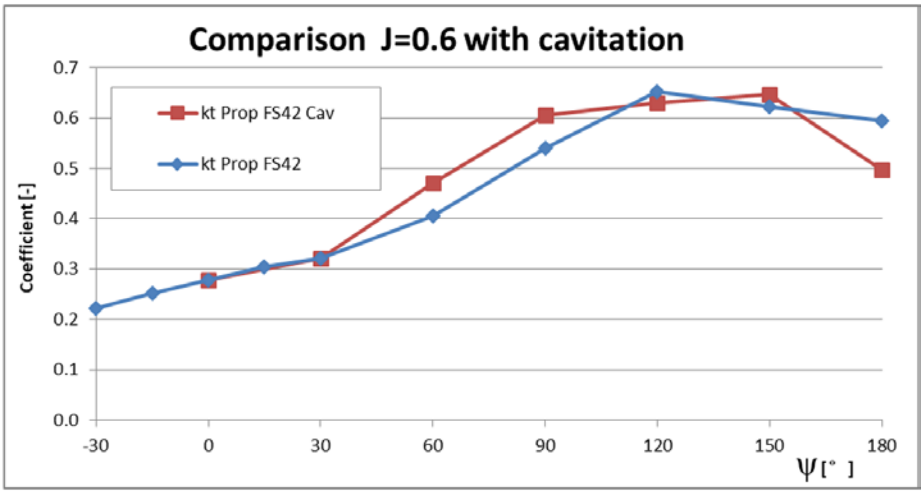

Fig. 4.12: Comparison of development of propeller torque over different azimuth angles for cavitating and non-cavitating conditions

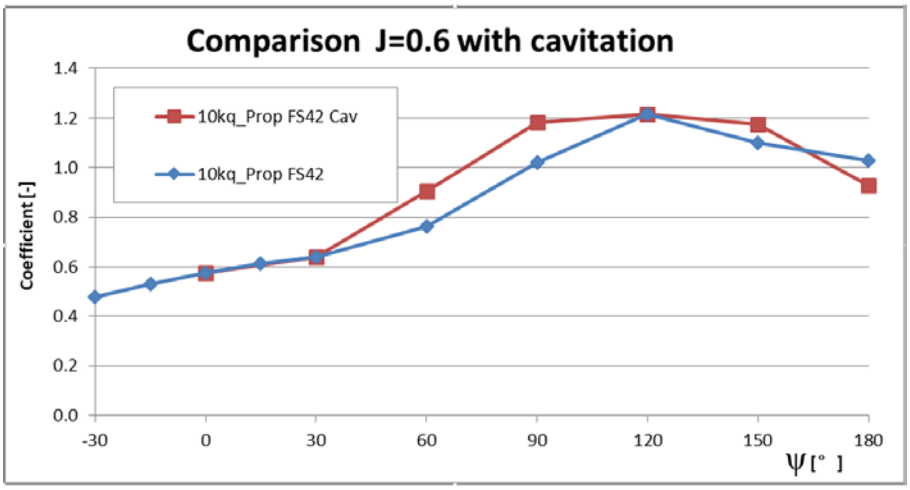

Fig. 4.13: Comparison of development duct thrust over different azimuth angles for cavitating and non-cavitating conditions

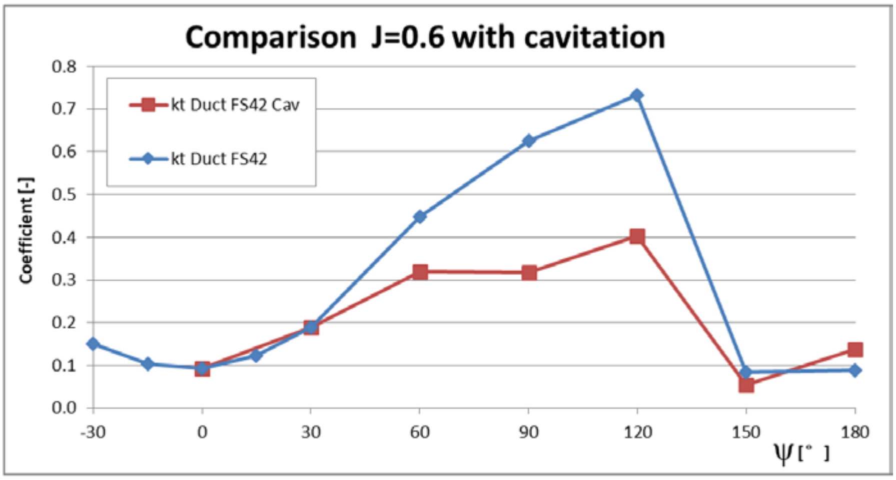

Fig. 4.14: Comparison of development of steering moment over different azimuth angles for cavitating and non-cavitating conditions

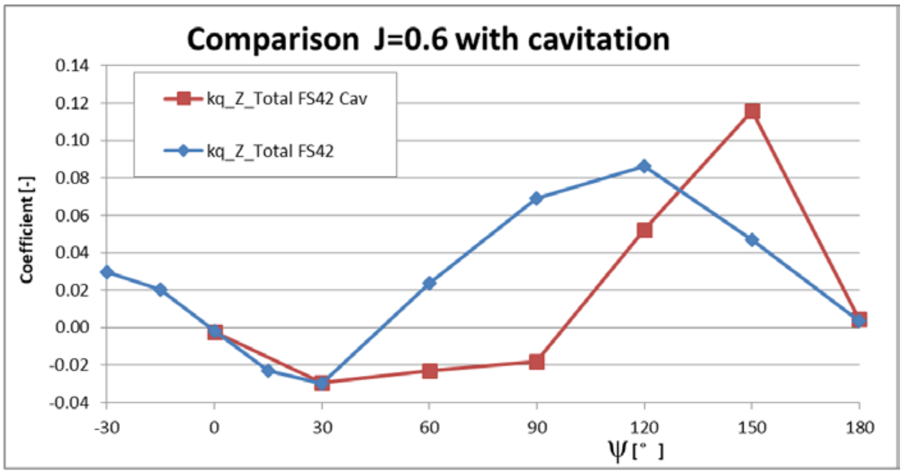

Fig. 4.15: Comparison of development of total force over different azimuth angles for cavitating and non-cavitating conditions

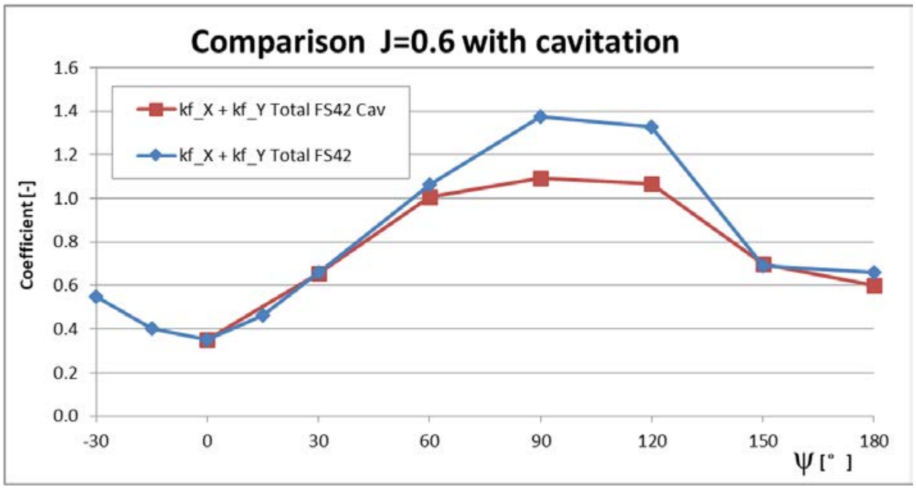

Fig. 4.16: Comparison of development of total bending moment over different Azimuth angles for cavitating and non-cavitating conditions

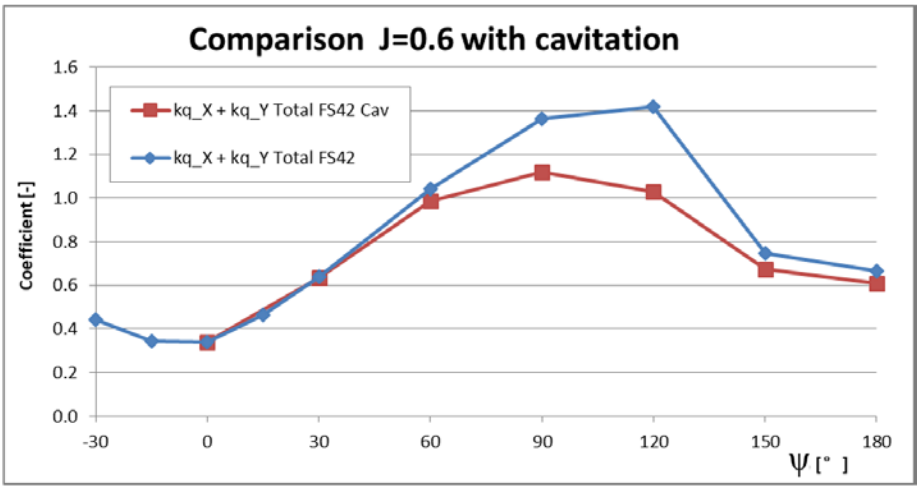

4.1.4. T2.1.5 - Numerical investigation of the flow around azimuth thruster at different operating points

The target of this working task is to identify off-design cases where the azimuth thruster is exposed to high loads. A calculation matrix is built by combination of the following parameters, suggested by project partner VOITH.

- azimuth angle (ψ),
- advance coefficient (J) and
- propeller diameter (D).

As discussed in section of mesh studies (see Sec. 4.1.1) a mesh with 6 to 10 million cells is sufficient for the accuracy of the simulation. Additionally, a mesh of about 20 million nodes is generated for DES simulation at selected cases of interest.

Three sizes of propeller are conducted in order to capture the scale effects. With combination of operating conditions, 243 simulations are taken place totally.

Table 4.18: Parameter selected for simulations with fixed azimuth angles

Size	**Power [kW]**	***D* [m]**	***n* [1/s]**	**ψ [°]**	***J* [-]**
Model Scale (MS)	–	0.25	11	-30, -15 0, 15 30, 60 90, 120 150, 180	0, 0.2, 0.4, 0.6, 0.8, 1.0, 2,5, infinity
Full Scale (FS 24)	1500	2.4	3.45		
Full Scale (FS 42)	5500	4.2	2.1		

The SST model is used as discussed in section 4.1.2. The time step is set to 4° propeller rotation, except the simulation for DES, where a time step is set to 1°. Several propeller revolutions are conducted until a periodic solution (quasi-steady) behaviour is achieved. A mean value is calculated from several propeller revolutions while the standard deviation accounts for the evaluation of loads fluctuation.

The following quantities are evaluated:

- propeller thrust and torque,
- duct thrust,
- forces and moments in each spatial dimension (x, y or z) for housing, duct, propeller and total,
- combined total force (K X+Y) and bending moment (Q X+Y) calculated by $\sqrt{F_x^2 + F_y^2}$ and $\sqrt{Q_x^2 + Q_y^2}$, where F and Q stand for the force and moment.

Since the calculation matrix is quite large, only a few representative examples are discussed.

Fig. 4.17 shows vortex structures and flow field at model scale for different azimuth angles exemplary for two *J*-values. As expected, the propeller suction effect at *J*=0.2 is stronger than at *J*=0.8. The flow separation is massive at high azimuth angles. As shown in Fig. 4.18, the maximal load occurs nearly by ψ = 120°. The load collapse after ψ = 120° due to a sudden reduction of duct thrust.

The existing differences in Fig. 4.19 are caused mainly through the scale effects due to different sizes of flow separation areas. More interesting, at 35° and −35° provide different loads as shown in Fig. 4.18. The difference is not derived from the duct (blue curve), but from the propeller (red curve). The reason is due to the combination of rotating direction between propeller and thruster and will be explained in T2.2 sec. 4.2.1.6.

Fig. 4.17: Vortex structures and flow field at model scale for different azimuth angles

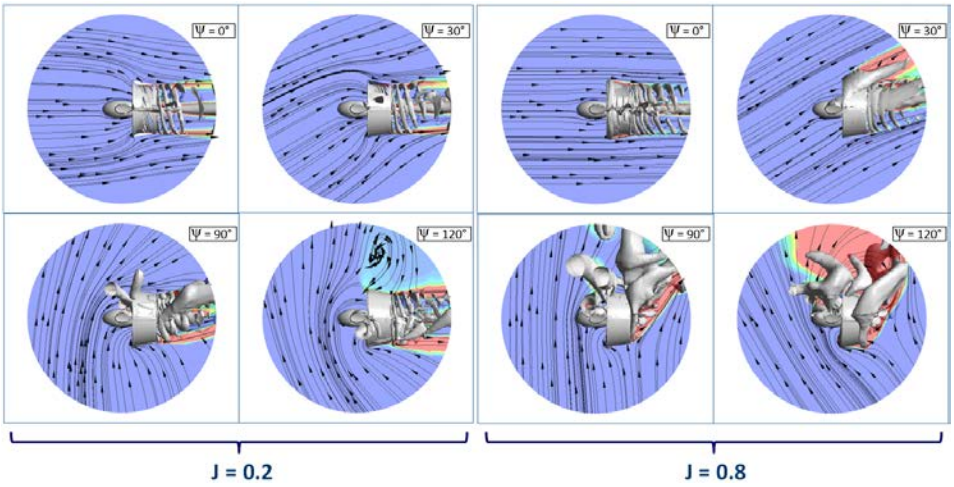

Fig. 4.18: Total force and moment development over ψ, example from FS 42 at *J* = 0.8

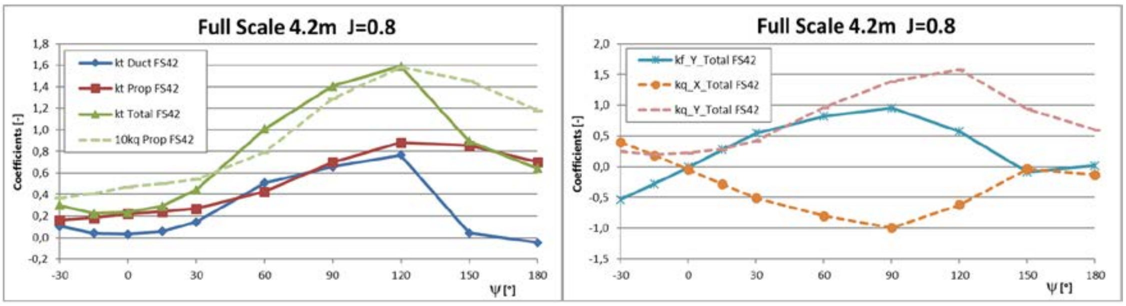

Fig. 4.19: Development of duct thrust over ψ for three different scales at *J*=0.8

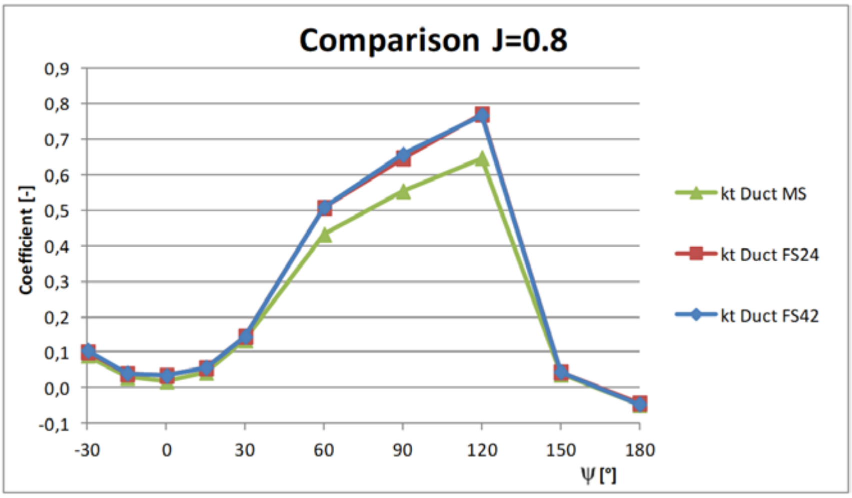

Cases with the largest values of forces and moments and their standard deviations (SD) are referred to the full-scale propeller with diameter of D=4.2m. It should be noted that at high J-values such as J=2 and 5, the propeller speed cannot be selected as high as in the reality. It has to be reduced to a more reasonable value, namely n = 1.05 Hz for J = 2 and 0.42 Hz for J = 5 (50% and 20% of n = 2.1 Hz), respectively. The evaluation criterion has to be followed by the absolute value of the forces and moments. After this, three cases occur frequently (see Tab. 4.19). Most of the critical cases are between $\psi = 90° \sim 120°$ and $J = 0.6 \sim 1$.

Table 4.19: Determining the highest loads and most frequently occurring cases

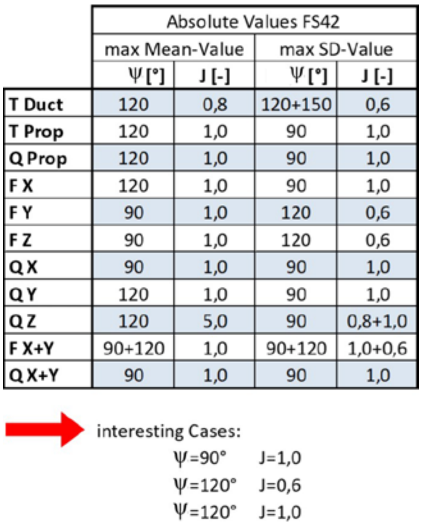

	Absolute Values FS42			
	max Mean-Value		max SD-Value	
	Ψ [°]	J [-]	Ψ [°]	J [-]
T Duct	120	0,8	120+150	0,6
T Prop	120	1,0	90	1,0
Q Prop	120	1,0	90	1,0
F X	120	1,0	90	1,0
F Y	90	1,0	120	0,6
F Z	90	1,0	120	0,6
Q X	90	1,0	90	1,0
Q Y	120	1,0	90	1,0
Q Z	120	5,0	90	0,8+1,0
F X+Y	90+120	1,0	90+120	1,0+0,6
Q X+Y	90	1,0	90	1,0

➡ interesting Cases:

Ψ	J
Ψ=90°	J=1,0
Ψ=120°	J=0,6
Ψ=120°	J=1,0

4.1.4.1. Detailed analysis of selected cases

4.1.4.1.1. Case: $\psi = 90^{\circ}$ and $J = 1.0$

Because of previous analysis, the case with azimuth angle of ψ = 90° and an advance ratio of J = 1.0 is exemplary discussed. The total coefficient splits into three components (duct, propeller and housing) as seen in Tab. 4.20. The values in red present the highest forces or moments among all the investigated cases, whereas the values in blue denote parts with the biggest fraction of the total load.

Table 4.20: Apportionment of total force and moment coefficient into different structural components.

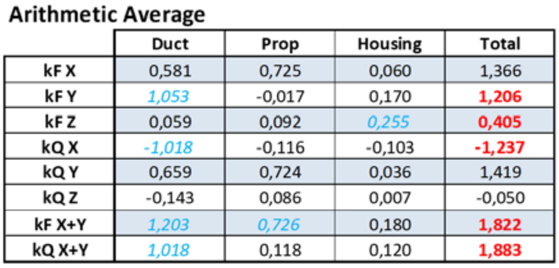

Arithmetic Average

	Duct	**Prop**	**Housing**	**Total**
kF X	0,581	0,725	0,060	1,366
kF Y	*1,053*	-0,017	0,170	**1,206**
kF Z	0,059	0,092	*0,255*	**0,405**
kQ X	*-1,018*	-0,116	-0,103	**-1,237**
kQ Y	0,659	0,724	0,036	1,419
kQ Z	-0,143	0,086	0,007	-0,050
kF X+Y	*1,203*	*0,726*	0,180	**1,822**
kQ X+Y	*1,018*	0,118	0,120	**1,883**

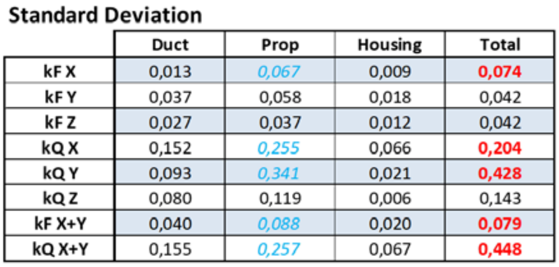

Standard Deviation

	Duct	**Prop**	**Housing**	**Total**
kF X	0,013	*0,067*	0,009	**0,074**
kF Y	0,037	0,058	0,018	0,042
kF Z	0,027	0,037	0,012	0,042
kQ X	0,152	*0,255*	0,066	**0,204**
kQ Y	0,093	*0,341*	0,021	**0,428**
kQ Z	0,080	0,119	0,006	0,143
kF X+Y	0,040	*0,088*	0,020	**0,079**
kQ X+Y	0,155	*0,257*	0,067	**0,448**

The duct possesses a large fraction of transverse force and, at the same time, it can provide thrust comparably to the propeller. For the vertical force (kF Z), the housing component is the most important one. According to the standard deviation, propeller is the component providing the greatest part of the fluctuation.

Fig. 4.20 shows the pressure distribution and streamlines on the duct. A high and low-pressure area are visible on the left and right side of the figure, respectively. The pressure difference accounts for the high value of total force (kF X+Y), total bending moment (kQ X+Y) and the moment around die x-axis (kQ X).

Fig. 4.20: Development of duct thrust over *ψ* for three different scales at *J*=0.8

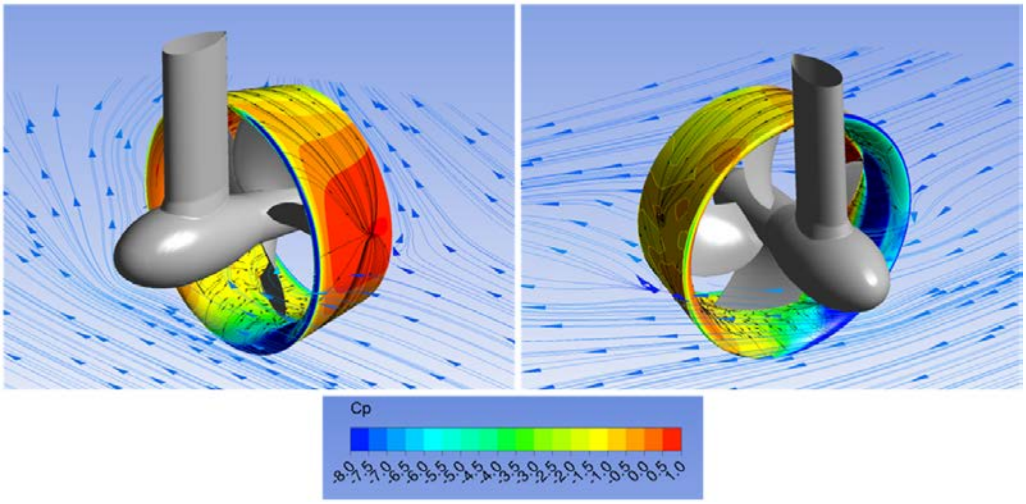

Fig. 4.21 shows the pressure distribution and streamlines at the housing. The equilibrium of the pressure on the housing causes the low pressure region on the bottom as shown on the right side. Then the vertical force (kF Z) is positive.

Fig. 4.21: Development of duct thrust over *ψ* for three different scales at *J*=0.8

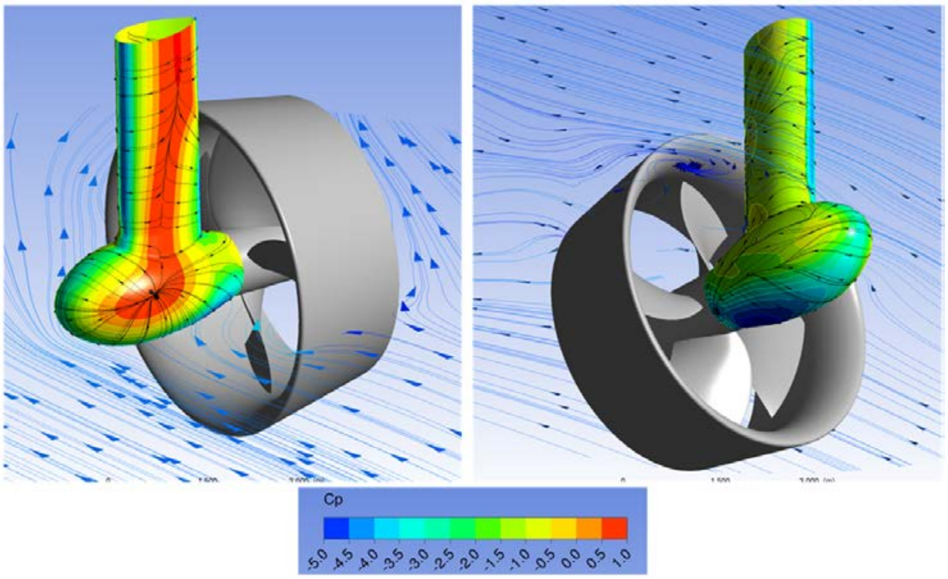

Looking over all the components, the steering moment (kQ Z) in this case is quite small. There are two moments acting against each other, namely a positive moment from propeller and a negative one from duct. The pressure distribution (see Fig. 4.22) indicates, that the force on blade 2 is lower than that on blade 4. The explanation of low pressure on the duct inside is referred again to the mentioned PHV effect.

Fig. 4.22: Development of duct thrust over *ψ* for three different scales at *J*=0.8

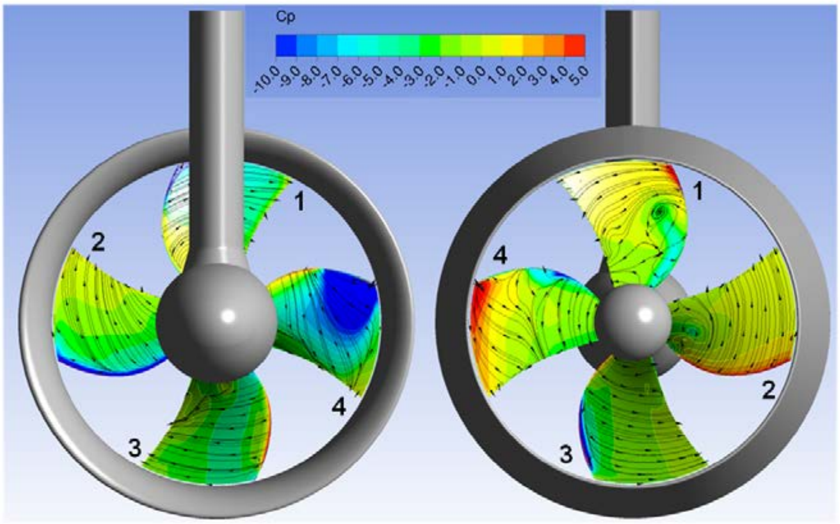

4.1.4.1.2. Case: Validation of turbulence models at *ψ* = 120° and *J* = 1.0

Due to the small azimuth angles (±35°), the difference between using anisotropic and isotropic turbulence models has not been identified in chapter 4.1.2. The opportunity to check the simulation result of using an anisotropic turbulence model for the selected high load case is applied. The comparison between SST and DES is found in Fig. 4.23.

Generally, the loads predicted by DES are about (5% ~ 10%) smaller than those by SST whereas the deviation is higher because of the growing quantities of eddies. The time history of the blade forces over last 4 revolutions are demonstrated in Fig. 4.24. Remarkable, there is no periodicity found for DES within the development of the forces. The explanation should be referred to the definition of the anisotropic turbulence model, that the eddy viscosity is unequal in each spatial direction.

Fig. 4.23: Comparison between SST and DES

Fig. 4.24: Comparison of force development of one propeller blade over the last 4 revolutions for SST and DES simulation

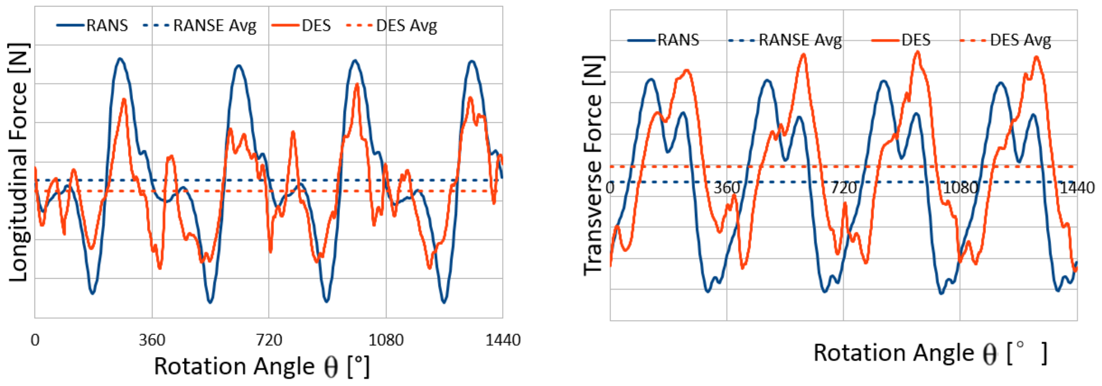

It is summarized, that most of the critical cases with high dynamic loads appear between the azimuth angle of ψ = 90° ~ 120° and advance ratio of J = 0.6 ~ 1.0. The total coefficients predicted by DES are 5 ~ 15% lower than those by SST, depending on the considered force or moment. So far, SST will be further used for the following tasks.

4.1.5. T2.1.6 - Influence of gap size on the loads of propulsor at different operating points

The gap clearance has influence on the formation and development of propeller tip vortices. Thus, the study of this parameter is carried out under various working conditions. The full-scale propeller with diameter of D = 4.2m (FS 42) is used. The simulation domain and mesh setups are the same as presented in the previous section Sec. 4.1.4.

The original gap size is h_G = 23.4mm (named as 25mm). The desired size can be obtained by extending or cutting the blades. Four propeller grids were generated, two with smaller and two with larger gap size (see Tab. 4.21), assuming that the smallest one of h_G = 5mm can be technically realized. As operation points, three different advance ratios J combined with zero azimuth angle are considered.

Table 4.21: Overview of investigated cases in the gap size study

Investigated cases				
Gap clearance h_G [mm]	h_G /D [%]	J=0	J=0.6	J=1.1
5	0.119	x	x	x
15	0.357	x	x	x
23.4	0.557	x	x	x
35	0.833	x	x	x
45	1.071	x	x	x

4.1.5.1. J = 0

The results can be seen in Tab. 4.22 and Fig. 4.25. A straight line can cover the relationship between the loads and gap sizes. The maximal difference related to the thrust of duct are up to 9%, whereas the propeller torque is less affected by the changing clearance. Fig. 4.26 shows the pressure distribution, the limiting streamlines and the tip vortex structure for the smallest, the original and the largest gap size. The development of tip vortex system is visible from top to bottom on the right side. The limiting streamlines are directed more outwards due to elongated low-pressure region on the propeller suction side around the tip.

Table 4.22: Results of gap size investigation at *J* = 0, coefficients (top) and deviation referred to h_G = 23.4mm (bottom)

Gap Size h_G [mm]	kT_Duct [-]	kT_Prop [-]	kF_X_Housing [-]	kT_Total [-]	10kQ_Prop [-]	kN/kW
5	0,4226	0,3467	-0,0350	0,7343	0,6947	0,1907
15	0,4141	0,3432	-0,0345	0,7228	0,6884	0,1895
23,4	0,4074	0,3399	-0,0341	0,7132	0,6826	0,1885
35	0,3971	0,3365	-0,0335	0,7002	0,6759	0,1869
45	0,3881	0,3339	-0,0329	0,6891	0,6708	0,1854

% of h_G=23.4mm

Gap Size h_G [mm]	kT_Duct	kT_Prop	kF_X_ Housing	kT_Total	10kQ_Prop
5	103,74	102,00	102,67	102,96	101,78
15	101,65	100,97	101,17	101,35	100,86
23,4	100,00	100,00	100,00	100,00	100,00
35	97,49	98,99	98,18	98,18	99,03
45	95,28	98,23	96,53	96,63	98,28

Fig. 4.25: Development of thrusts and torque for various gap sizes referred to h_G = 23.4mm at *J* = 0

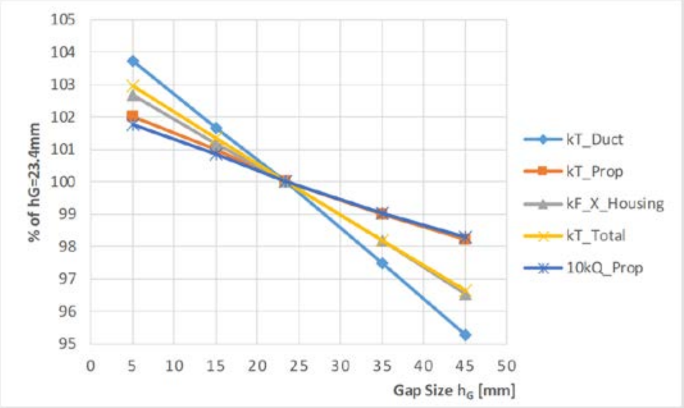

Fig. 4.26: Comparison of the pressure distribution and limiting streamlines on the propeller blades and tip vortex structure for various gap sizes at *J*=0

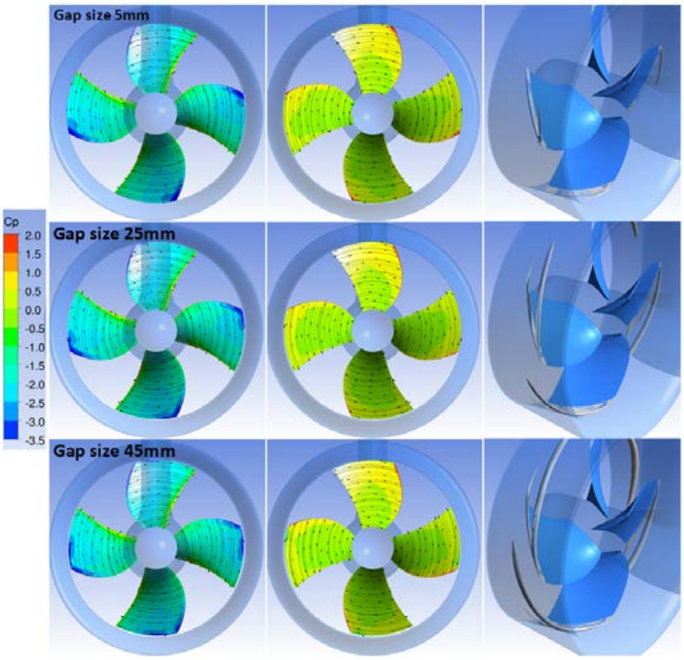

4.1.5.2. *J* = 0.6

The results for *J* = 0.6 are found in Tab. 4.23 and Fig. 4.27. The same statements can be summarized as *J* = 0. The maximal difference is observed from duct thrust about 18% between the smallest and largest gap size. The improvement of efficiency from the smallest gap size against the biggest one is about 2%.

Fig. 4.28 shows the pressure distribution, the limiting streamlines on the propeller blades and the tip vortex structure. The elongated low-pressure region is less pronounced in comparison to *J* = 0 due to the reduction of propeller load.

Table 4.23: Results of gap size investigation at *J* = 0.6, coefficients (top) and deviation referred to h_G = 23.4mm (bottom)

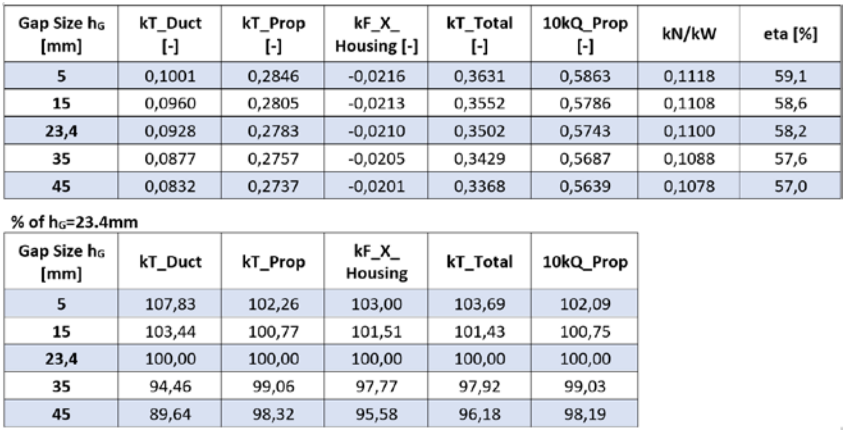

Gap Size h_G [mm]	kT_Duct [-]	kT_Prop [-]	kF_X_ Housing [-]	kT_Total [-]	10kQ_Prop [-]	kN/kW	eta [%]
5	0,1001	0,2846	-0,0216	0,3631	0,5863	0,1118	59,1
15	0,0960	0,2805	-0,0213	0,3552	0,5786	0,1108	58,6
23,4	0,0928	0,2783	-0,0210	0,3502	0,5743	0,1100	58,2
35	0,0877	0,2757	-0,0205	0,3429	0,5687	0,1088	57,6
45	0,0832	0,2737	-0,0201	0,3368	0,5639	0,1078	57,0

% of h_G=23.4mm

Gap Size h_G [mm]	kT_Duct	kT_Prop	kF_X_ Housing	kT_Total	10kQ_Prop
5	107,83	102,26	103,00	103,69	102,09
15	103,44	100,77	101,51	101,43	100,75
23,4	100,00	100,00	100,00	100,00	100,00
35	94,46	99,06	97,77	97,92	99,03
45	89,64	98,32	95,58	96,18	98,19

Fig. 4.27: Development of thrusts and torque for various gap sizes referred to h_G = 23.4mm at *J* = 0.6

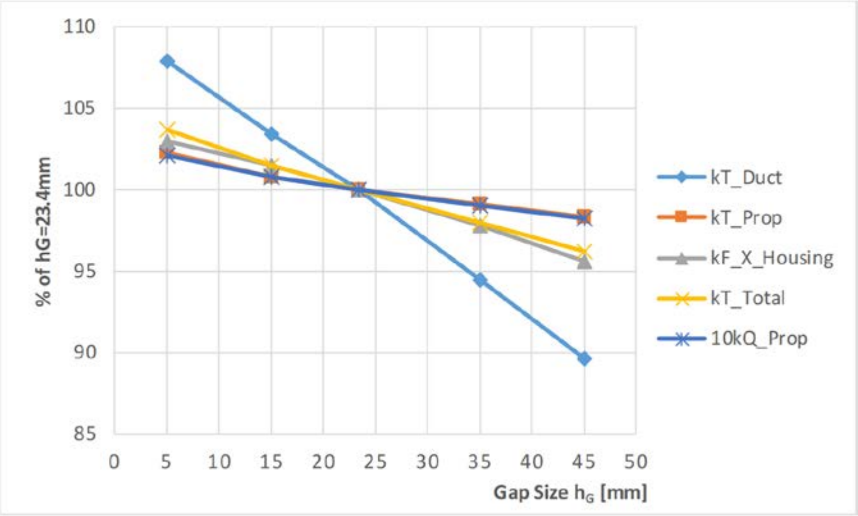

Fig. 4.28: Comparison of the pressure distribution and limiting streamlines on the propeller blades and tip vortex structure for different gap sizes at *J* = 0.6

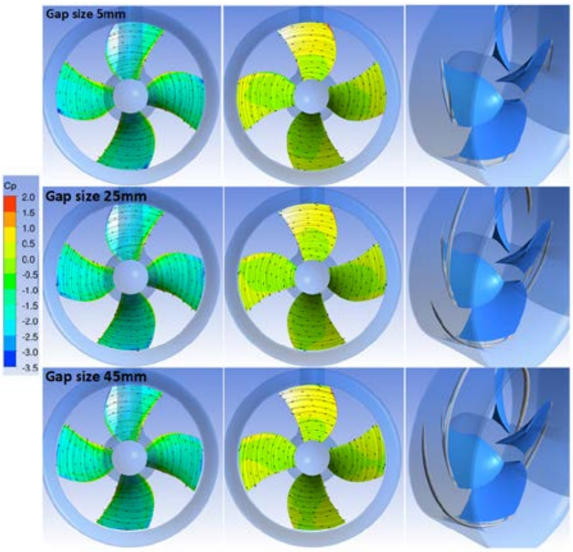

4.1.5.3. *J* = 1.1

The operating point of the azimuth thruster at *J* = 1.1 is close to the point where the total thrust of the unit is close to zero (see Tab. 4.24). All values considered show a non-linear dependency (see Fig. 4.29). The effect of the gap size decreases with growing gap size. Due to the flow separation, the duct thrust is negative. The deviation of the total thrust is up to 220% because of their small values. From this reason, it is not drawn in Fig. 4.29. The efficiency at this operation point is not of interest.

Significant change is hardly found regarding the limiting streamlines and the pressure distribution (see Fig. 4.30). The tip vortex travels more or less in the chordal direction of the blade tip section.

Table 4.24: Results of gap size investigation at *J* = 1.1, coefficients (top) and deviation referred to h_G = 23.4mm (bottom)

Gap Size h_G [mm]	**kT_Duct [-]**	**kT_Prop [-]**	**kF_X_ Housing [-]**	**kT_Total [-]**	**10kQ_Prop [-]**	**kN/kW**	**eta [%]**
5	-0,0517	0,0871	-0,0181	0,0174	0,2341	0,0134	7,1
15	-0,0535	0,0830	-0,0179	0,0115	0,2253	0,0092	4,9
23,4	-0,0553	0,0810	-0,0179	0,0079	0,2205	0,0064	3,4
35	-0,0569	0,0795	-0,0178	0,0048	0,2157	0,0040	2,1
45	-0,0570	0,0780	-0,0177	0,0032	0,2122	0,0027	1,5

% of h_G=23.4mm

Gap Size h_G [mm]	**kT_Duct**	**kT_Prop**	**kF_X_ Housing**	**kT_Total**	**10kQ_Prop**
5	93,54	107,60	101,10	220,86	106,20
15	96,85	102,46	100,47	146,30	102,18
23,4	100,00	100,00	100,00	100,00	100,00
35	103,02	98,16	99,47	61,14	97,83
45	103,24	96,30	99,25	40,91	96,25

Fig. 4.29: Development of thrusts and torque for various gap sizes referred to h_G = 23.4mm at *J* = 1.1

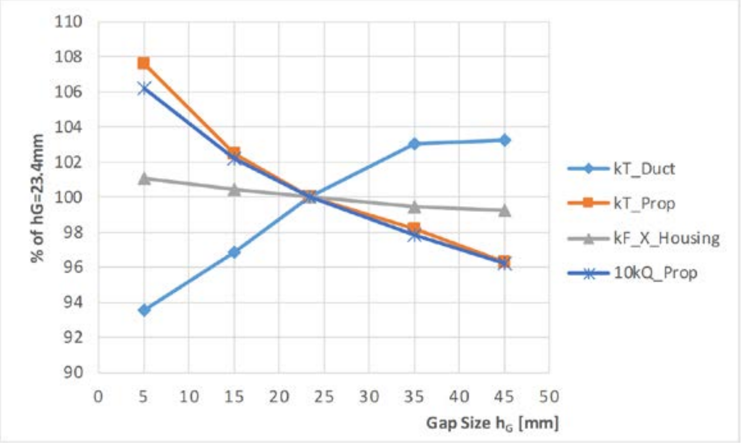

Fig. 4.30: Comparison of the pressure distribution and limiting streamlines on the propeller blades and tip vortex structure for different gap sizes at *J*=1.1

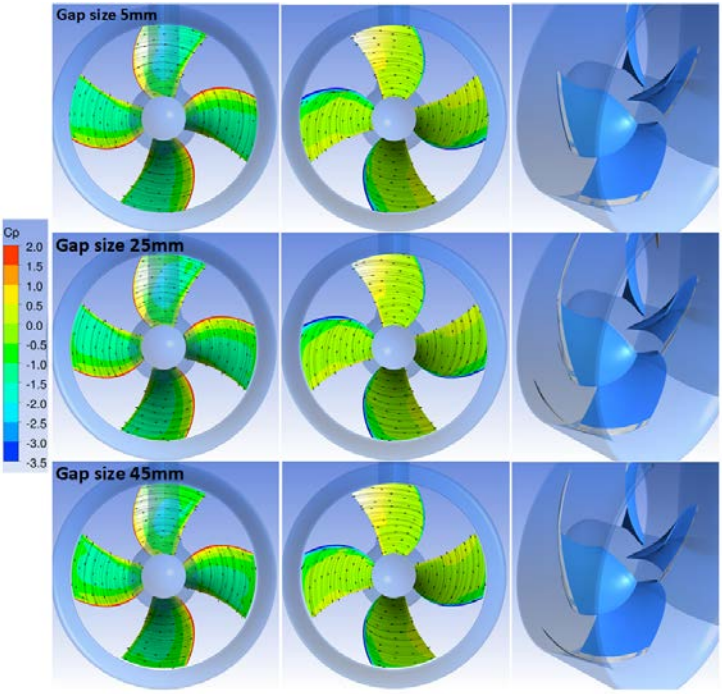

Generally, decreasing gap clearance can get better performance. The gap clearance affects mostly on the thrust of duct and minimally on the propeller torque. On the conditions of *J*=0 and *J*=0.6, a linear relationship can be observed between the loads and clearance whereas the change of the loads at *J*=1.1 is moderate with increasing gap size. These statements are in agreement with the findings by Yongle [23].

4.2 T2.2 - Loads due to unsteady operation conditions

The azimuth angle changes continuously with the time, the hydrodynamic loads can be gathered through either the experimental tests ([4], [3], [13] and [12]) or numerical approaches ([5] and [18]). Within these publications, it seems that the predictions after ψ = 50° azimuth angles are still rely on the model tests and there are rare published works have been found recently for the detailed investigation on the azimuth thruster working on the dynamic conditions.

In the working task T2.2, the same ducted propeller (FS42: full-scale propeller with diameter of 4.2 m) is used. As usual, the prediction of forces and moments is followed by using RANS approach, the critical operating conditions are determined. Finally, the corresponding physical phenomena are analysed.

The crash-stop manoeuvre can be achieved by reversing the azimuth thruster from ψ = 0° to 180° or −180° as shown in Fig. 4.31. The cylindrical thruster domain including the rotating propeller rotates continuously with different azimuthing speeds *f*. For this reason, the mesh motion is involved. In this method, the explicit displacement of the nodes of the domains (propeller and thruster) have to be given to a fixed coordinate system. For the thruster domain, only the rotation around the steering axis is considered, whereas for the propeller domain the rotation around the propeller axis has to be taken into account additionally. The numerical domains and the mesh size as well as the boundary conditions are the same as described in Sec. 4.1.4 (T2.1.5). In all simulations, five inner iterations per time step (4° of propeller rotation) are applied. As initial solutions the results from the fixed azimuth angle of ψ = 0° are used. The effect of free surface and wake from the hull on the ducted azimuth thruster are neglected.

Fig. 4.31: Domain set for dynamic conditions

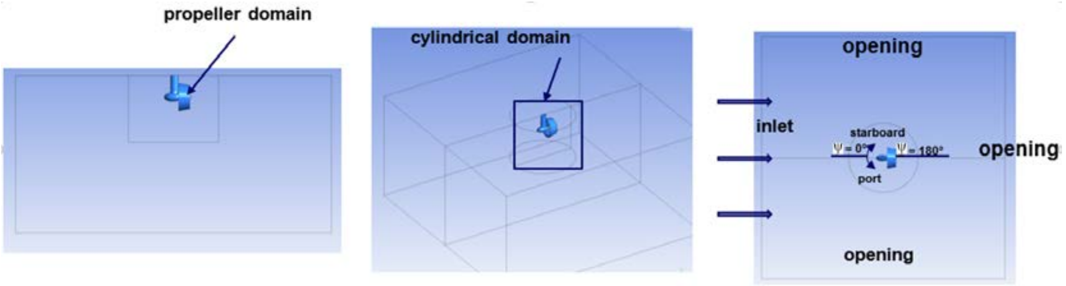

Three major tasks from T2.2.1 to 2.2.3 are considered on the dynamic conditions at constant propeller speed with varied advance ratios *J* and azimuthing speeds *f* in rpm. Beyond that, some comparative simulations are also carried out to provide sufficient information about the dynamic loads on the thruster. The calculation matrix is listed in Tab. 4.25. Some results of the calculations are selected for the comparison with fixed azimuth angle. It should be noted, that high azimuth speeds are not allowed according to the requirements from SOLAS. Normally, it is 2.5°/s at ship design speed. A rate of 5°/s is allowed when the steering moment is accepted during manoeuvring at slow speed. A rate of 12°/s (*f* = 2) is treated as special case. In this task, *f* = 2 und 3 are chosen concerning the suggestion from VOITH. Azimuthing speeds *f*=6 and 1 are also carried out in order to find some tendencies. Turning to starboard is the situation of interest. For some selected cases, turning to port side is also conducted.

Table 4.25: Parameter selection for simulations with rotating thruster

J [-]	Azimuth Speed *f* [rpm]
0.0	1, 2, 3, 6
0.6	2, 3, 6
0.6	2, 3, 6
0.6	2, 3, 6

4.2.1 T2.2.1-2.2.3 - Simulation of the flow around the propulsor during reversing operation

Before varying the working conditions, a study is performed for the influences of different initial propeller blade angular positions and time steps based on the case of *J*=0.6 and *f*=3.

4.2.1.1 Initial blade position

Three simulations with varied initial blade angular positions are taken into account. Fig. 4.32 shows the time history of total thrust over the azimuth angles. The blade positions are coincident with the positions of 0, 1 and 2 o'clock. They differ only from the phase shift with respect to the mean values. Thus, the parameter of initial blade position seems to be not significant for the performance of azimuth thruster.

Fig. 4.32: Comparison of different initial propeller positions

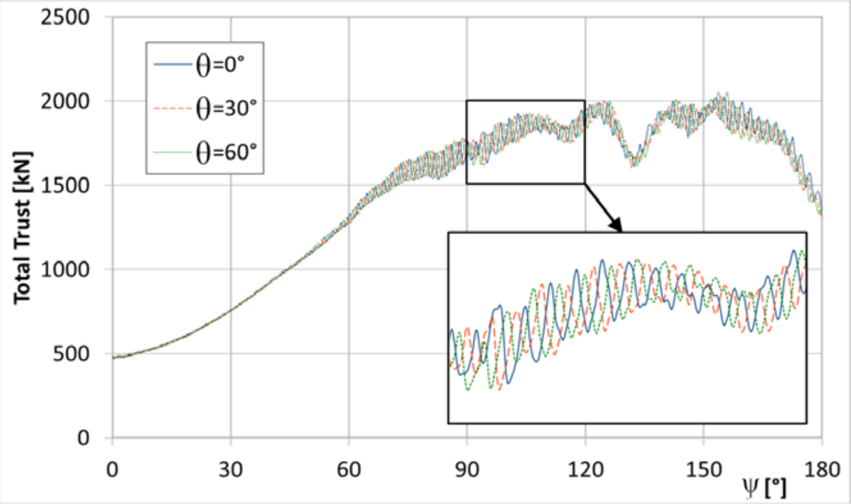

4.2.1.2 Time steps

Two time steps of 1° and 4° of propeller rotations are investigated. Fig. 4.33 depicts the results for the total thrust. The deviations appear mostly after reaching the maximal load where the region is of less importance. Thus, 4° of propeller rotation will take precedence over small time steps in order to reduce the computational effort.

Fig. 4.33: Comparison of different time steps

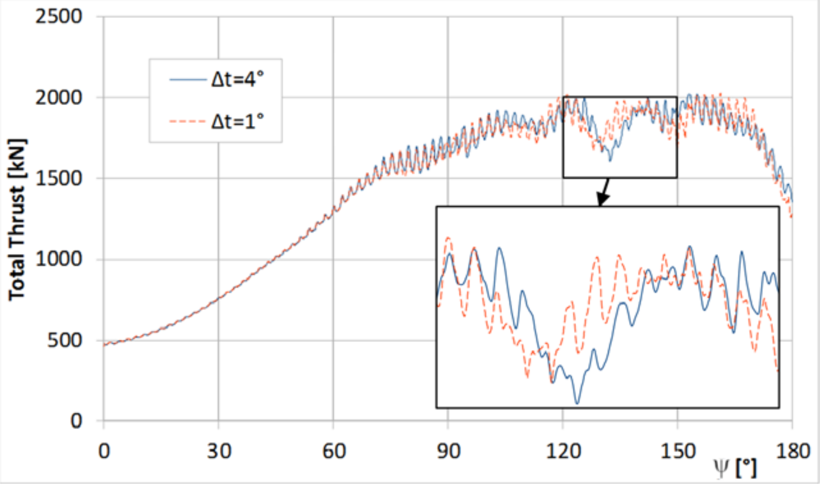

4.2.1.3 Variation of azimuth speed at constant inflow velocity

Fig. 4.34 and Fig. 4.35 illustrate the time history of the total thrust and transverse force about the azimuth angles at *J* = 0. Both forces show an increment with increasing azimuth angles. The transverse force is more sensitive to the azimuth speed f than the longitudinal thrust. The relation between transverse force and azimuth speed is nearly linear. The maximal increment of the thrust within all considered azimuth speeds is only about 13%.

Fig. 4.34: Time history of total trust at *J* = 0 for different azimuth speeds *f*=1, 2, 3 and 6

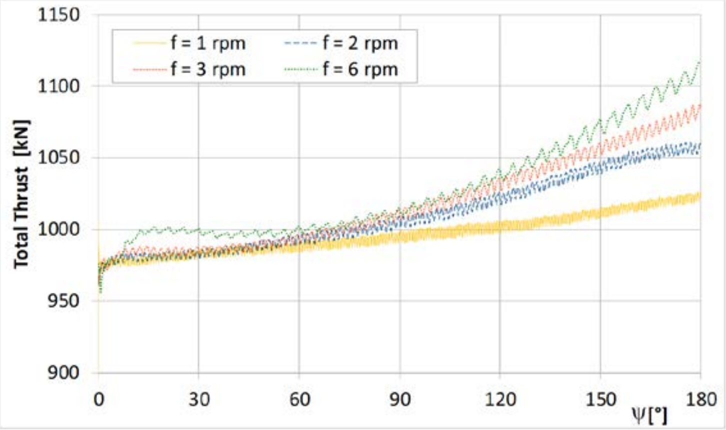

Fig. 4.35: Time history of total side force at *J*=0 for different azimuth speeds *f*=1, 2, 3 and 6

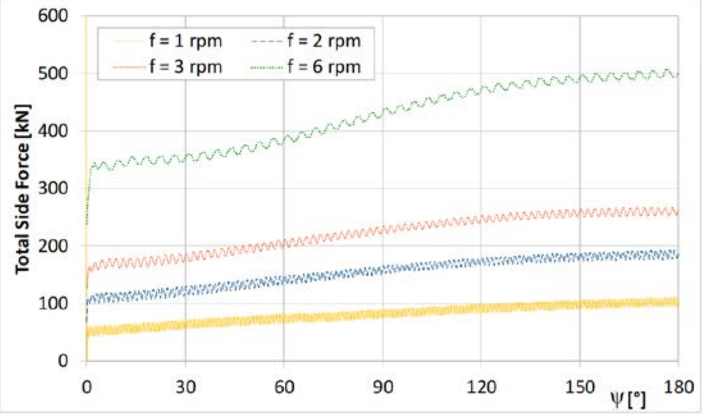

4.2.1.4 Variation of inflow velocity at constant azimuth speed

The time history of longitudinal and transverse force over azimuth angles in dependency of advance ration *J* are shown in Fig. 4.36 and Fig. 4.37.

In this case, the azimuth speed is kept constant (*f*=3). At zero azimuth angle, the total thrust decreases with increasing *J* as expected. Then the difference is getting closer up to 45°, after that, the three curves are going separately from each other. Between 90° and 120°, the longitudinal and transverse forces reach their maximal values given by *J*=0.6 which are almost two and five times higher respectively than the values on the bollard pull condition (*J*=0). These two forces are responsible for the bending moment. A high value should be avoided in order to reduce the possibility of the failure of the structure.

Fig. 4.36: Time history of total trust at azimuth speeds of *f*=3 for different advance ratios *J*=0, 0.1, and 0.6

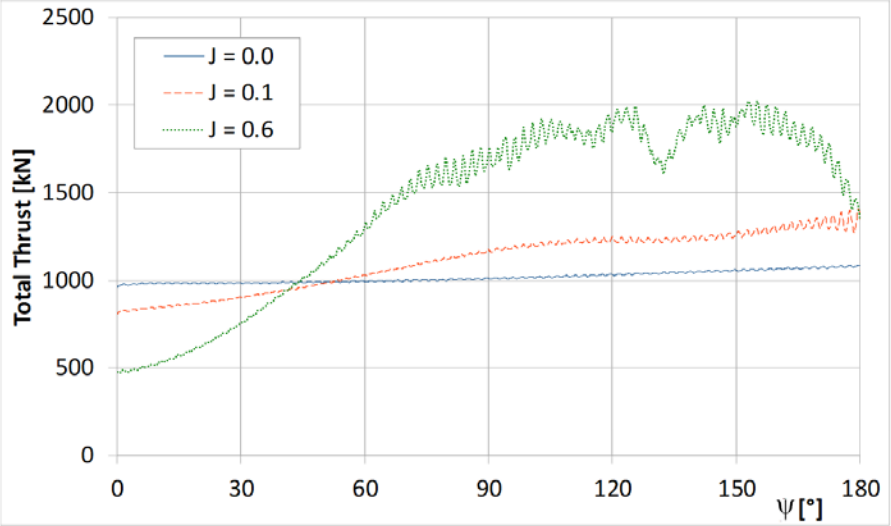

Fig. 4.37: Time history of total side force at an azimuth speeds of *f*=3 for different advance ratios *J*=0, 0.1, and 0.6

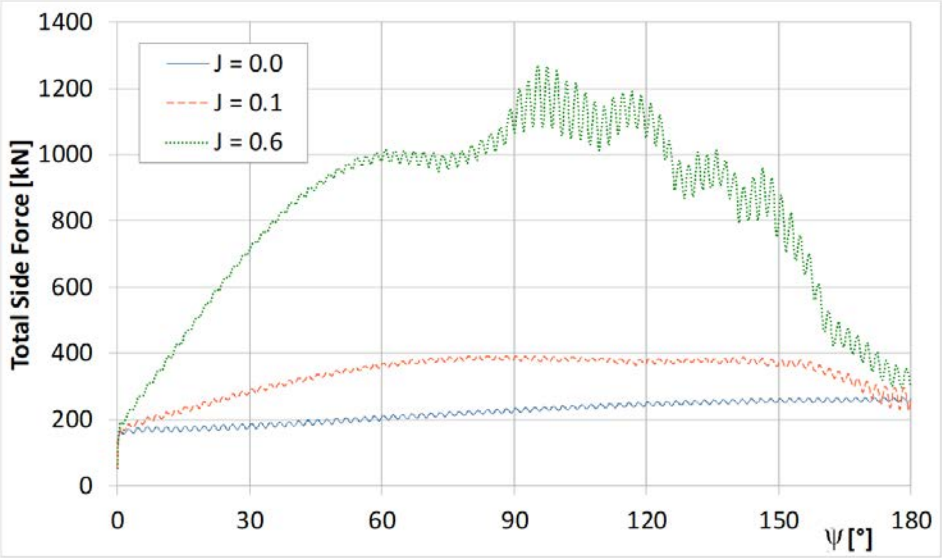

4.2.1.5 Comparison of the results with fixed azimuth angles

A step forward, the results between fixed and dynamic conditions as well as the rotating directions of the thruster should be compared. Fig.(4.38) shows the pressure distribution on the thruster and velocity field on a section plane located in the height of the propeller rotating axis for the operating point of ψ = 120° and *J*=0.6. Obvious differences can be found especially in the region of propeller downstream.

Fig. 4.38: Pressure distribution and velocity field for ψ = 120° and *J*=0.6. Left: fixed azimuth angle; right: snap-shot during azimuth rotation

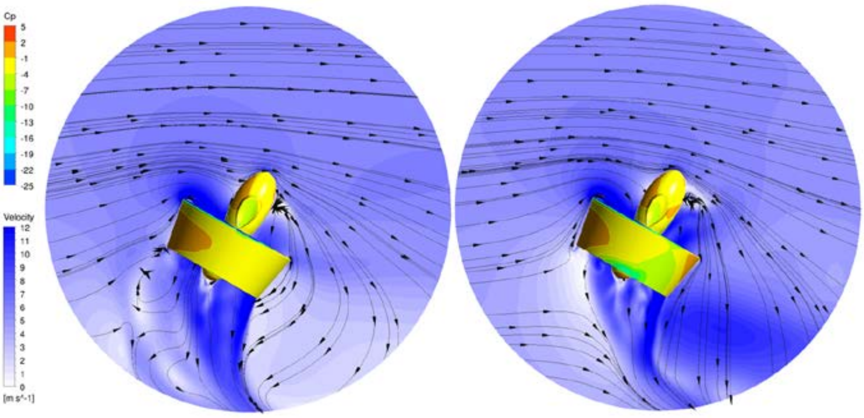

The time history of total thrust and transverse force over the azimuth angles are shown in Fig. 4.39 and Fig. 4.40, respectively. The solid curves present the results obtained from azimuth speed of *f*=3 in two azimuth rotating directions (starboard and portside), and the symbols denote the results obtained from the fixed azimuth angles. The thrust values from both conditions match well up to ψ = 120°.

On the contrary, the transverse force from both turning directions are more or less symmetrical as shown in Fig. 4.39. However, they are lower than those from the dynamic condition are. The deviation is almost constant up to ψ = 90°. Beyond that angle, the deviation is getting larger because of interacted flow from propeller slipstream and inflow.

It should be noted, that the azimuth angles should be negative while turning to the port side, but for the sake of comparison, the negative angles are changed into positive ones.

Fig. 4.39: Influence on total thrust for different azimuth rotation directions in comparison with fixed azimuth angles at *J*=0.6

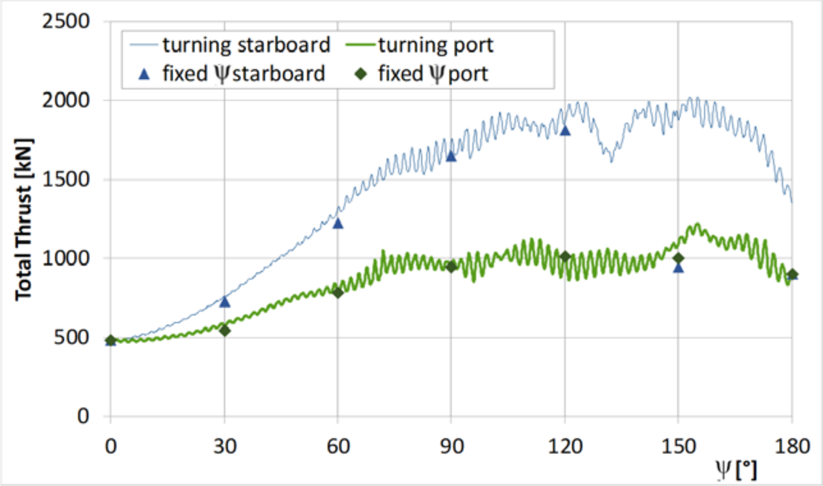

Fig. 40: Influence on total side force for different azimuth rotation directions in comparison with fixed azimuth angles at *J*=0.6

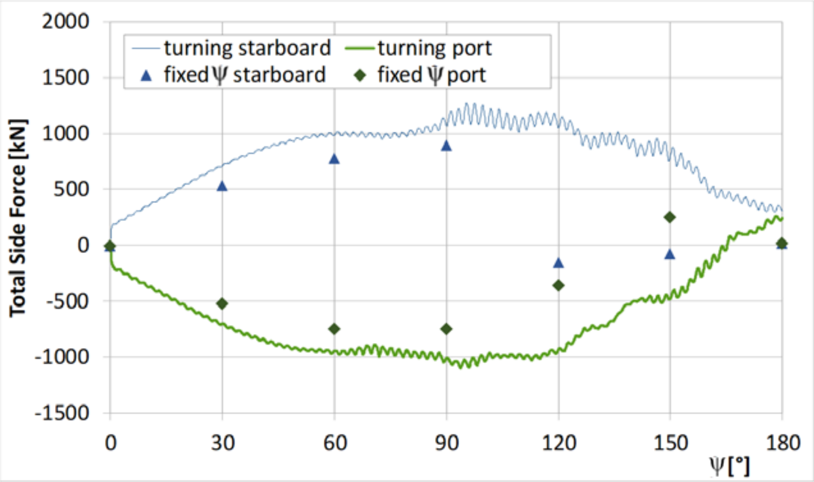

4.2.1.6 Detailed analysis of selected cases

The explanation of the results illustrated above is further discussed to understand the physical phenomenon. The cases selected are according to the distinctive feature of the curves.

4.2.1.6.1 Case 1: $\psi = 132°$, $f = 3$ and $J = 0.6$

Two fully propeller revolutions are taken place from azimuth angle 124° to 141° as shown in Fig. 4.41. $\psi = 132°$ locates in the middle and corresponds one propeller revolution counting from 124°. Within these two revolutions, eight peak values (4 blades at 2 revolutions) can be found. The total force consists of the force from duct (nozzle), housing (strut) and propeller. The fitting curves are modelled by using "smoothing spline method". The aim in this task is, to find out the reason for the drop in total thrust at $\psi = 132°$.

Obviously, the force of propeller and duct are still the major components of the total force. They drop from $\psi = 124°$ to 132° during the first revolution and rise from $\psi = 132°$ to 141° during the second revolution. Since the rate of increase of the propeller force from $\psi = 132°$ is greater than the rate of duct force. This conspicuous phenomenon is certainly caused by the propeller.

Fig. 41: The history of longitudinal force about the azimuth angle of different parts for the operation point *J* = 0.6 and *f* = 3 rpm

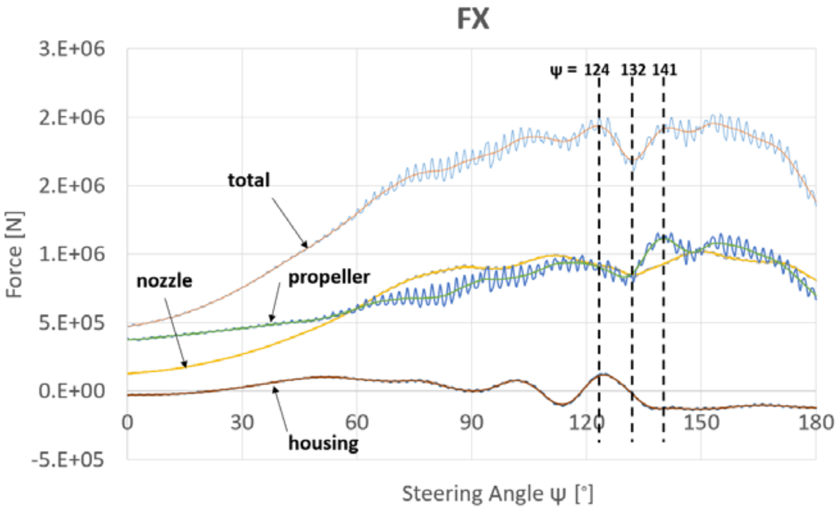

Table 4.26: Longitudinal force of each part at the three azimuth angles

Loads on Parts [kN]	*ψ* = 124°	*ψ* = 132°	*ψ* = 141°
Propeller	898	871	1110
Duct	919	851	938
Housing	115	-33	-127
Total	1932	1689	1921

Each blade is separately considered and numbered as shown in Fig. 4.42. The blade thrust is listed individually in Tab. 4.27 at the three different angles. Blade 1 has only 5% reduction at *ψ* = 132° and 3% at *ψ* = 141° respectively in compare to *ψ* = 124°. Blades 2 and 4 increase with the increasing *ψ* which have no contribution to the decrement. However, blade 3 has 51% reduction. Possibly, this is the reason for changing the curve tendency between *ψ* = 124° and *ψ* = 141°.

As mentioned, the three angles differ only from the number of whole revolution. The blade position relative to the housing do not change and the blade number denotes the same blade even at different azimuth angles *ψ*. Besides *ψ* = 132°, a region with low pressure is circled near the root on the suction side. The reason tends to the influence of the wake from the housing. Fig. 4.43 illustrates the distribution of wall stress (c_f). Dark blue coloured regions points out the place where the shear stress is equal to zero. At *ψ* = 132°, due to zero shear stress on the gondola, the propeller can draw the flow easily. Fig. 4.43 below shows the progress of the vortex coloured according to the pressure. As shown in Fig. 4.44 at *ψ* = 132°, the difference of pressure is getting closer between suction and pressure side of blade 3.

Fig. 42: Pressure distribution on the suction side of different azimuth angles

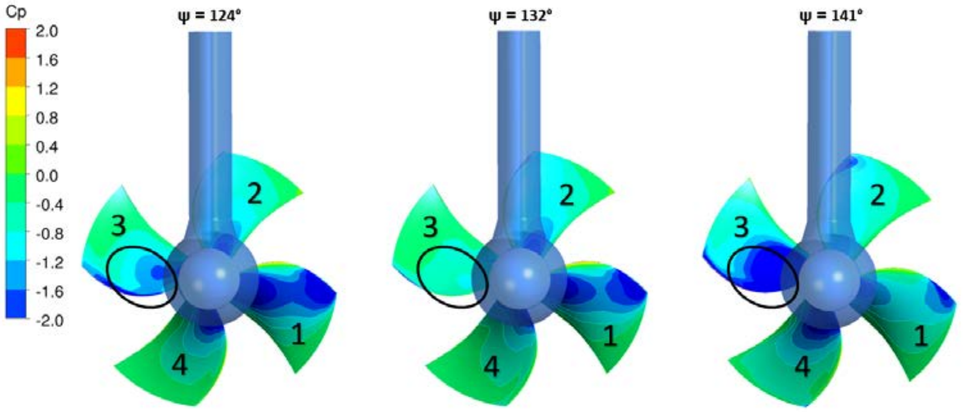

Table 4.27: Detained comparison of longitudinal forces between different blades at different azimuth angles

Loads on Blade FX [kN]	*ψ* = 124°	*ψ* = 132°	*ψ* = 141°
1	411	390	399
to 124°	100%	95%	97%
2	171	266	368
to 124°	100%	156%	215%
3	260	127	222
to 124°	100%	49%	85%
4	56	88	122
to 124°	100%	158%	219%

Fig. 43: Above: wall shear distribution on the housing, below: pressure distribution on the vortex drawn by blade 3

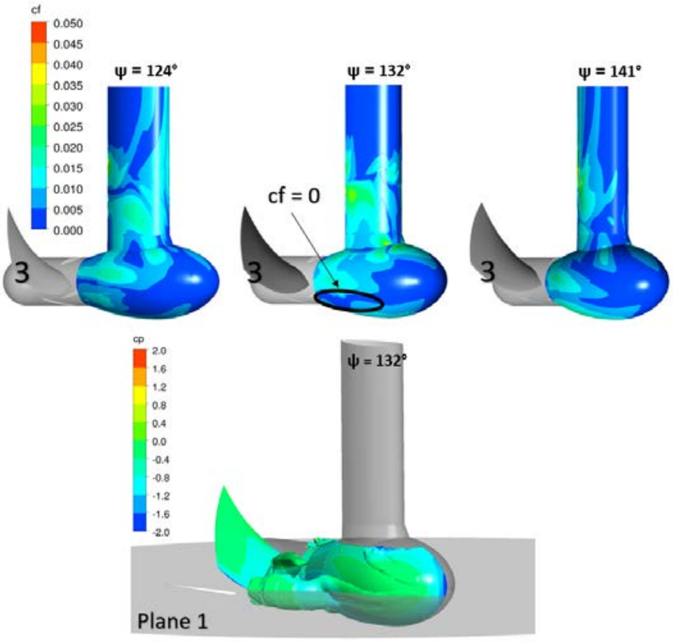

Fig. 44: Pressure distribution on “Plane 1” and the local vortex caused by the separated flow on the gondola

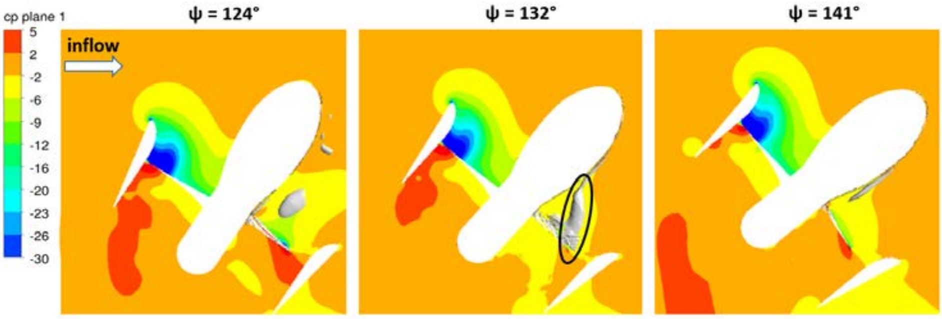

4.2.1.6.2 Case 2: *ψ* = 180°, *f* = 3 and *J* = 0

Without considering propeller influence, the force acting on the duct as well as on the housing should be the same whether the thruster turns to starboard or portside. However, in the presence of the working propeller, the force is actually different. Fig. 4.45 shows the time history of the total thrust at *J* = 0. Like the other case of *J*=0.6 (see Fig. 4.39), the thrust from turning to starboard is bigger than the values from turning to the opposite side (portside). The maximal difference occurs at *ψ* = 180°. 10% and −5% denote the production and reduction of thrust in comparison with the thrust at zero azimuth angle. As usual, the individual thrust at *ψ* = 180° is listed in Tab. 4.28. Propeller has the highest growth of 17% in terms of rotating direction. Tab. 4.29 shows the blade forces associated with the blade number as illustrated in Fig. 4.47.

Two additional velocities are induced during the rotating, namely Vt and Vx (see Fig. 4.46), which are the two components of the rotation velocity according to the thruster rotation axis. The directions of the velocities are different owing to the different azimuth rotating directions.

Fig. 45: Influence on total trust for different azimuth rotation directions at *J*=0

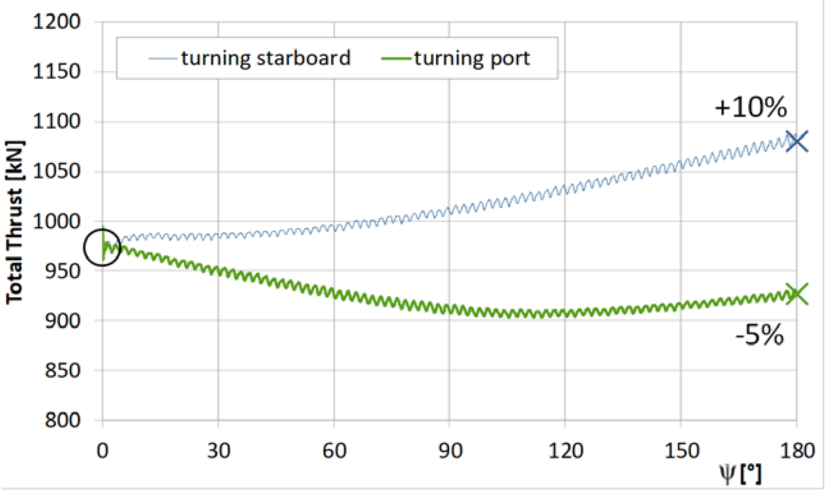

Fig. 46: Different velocity field due to different direction of rotation

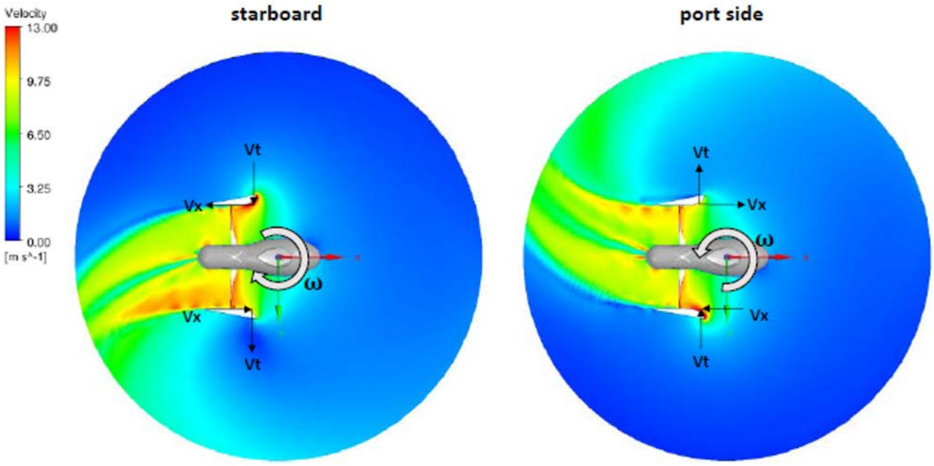

Blade 2 from starboard provides 50% more thrust than Blade 2 from port as calculated in Tab. 4.29.

The difference of force in terms of blade 4 is very small; the pressure distribution on blade 4 is also similar. It could be supposed that the existing wake from the housing causes loss of effectivity from Vt.

Blade 1 from starboard and blade 3 from port side face the same situation related to the velocities (Vx and Vt). Tab. 4.29 shows that the improvement from Blade 1 is about 28%. The reason can be retraced from Fig. 4.48, which shows two section planes located separately on starboard and port side for blade 1 and blade 3, respectively. The negative vertical velocity towards the blade 1 on starboard plane (+ω) causes the difference.

The last comparison between blade 3 from starboard and blade 1 from portside is also caused by the different strength of the induced vertical velocity as show in the same figure. The deviation is about 10%.

The difference consists mainly of two factors, the first factor is according to the tangential velocity Vt affecting on the blade in the 6 o’clock position and the second one is related to the vertical velocity induced by propeller slipstream.

Table 4.28: Detailed comparison of longitudinal force of different parts at ψ = 180°

Loads on Part FX [kN]	starboard	port	difference	difference [%]
Duct	635	570	-65	-10
Housing	171	266	5	-12
Propeller	260	127	-85	-17

Table 4.29: Longitudinal force on each blade

Number of Blade	1	2	3	4
long. force (starboard) [kN]	143	136	113	120
related to total propeller force	28%	27%	22%	23%
long. force (port) [kN]	103	90	112	121
related to total propeller force	24%	21%	26%	28%

Fig. 47: Pressure distribution on the suction side of the propeller at the operation point of J = 0, left: starboard, right: port side

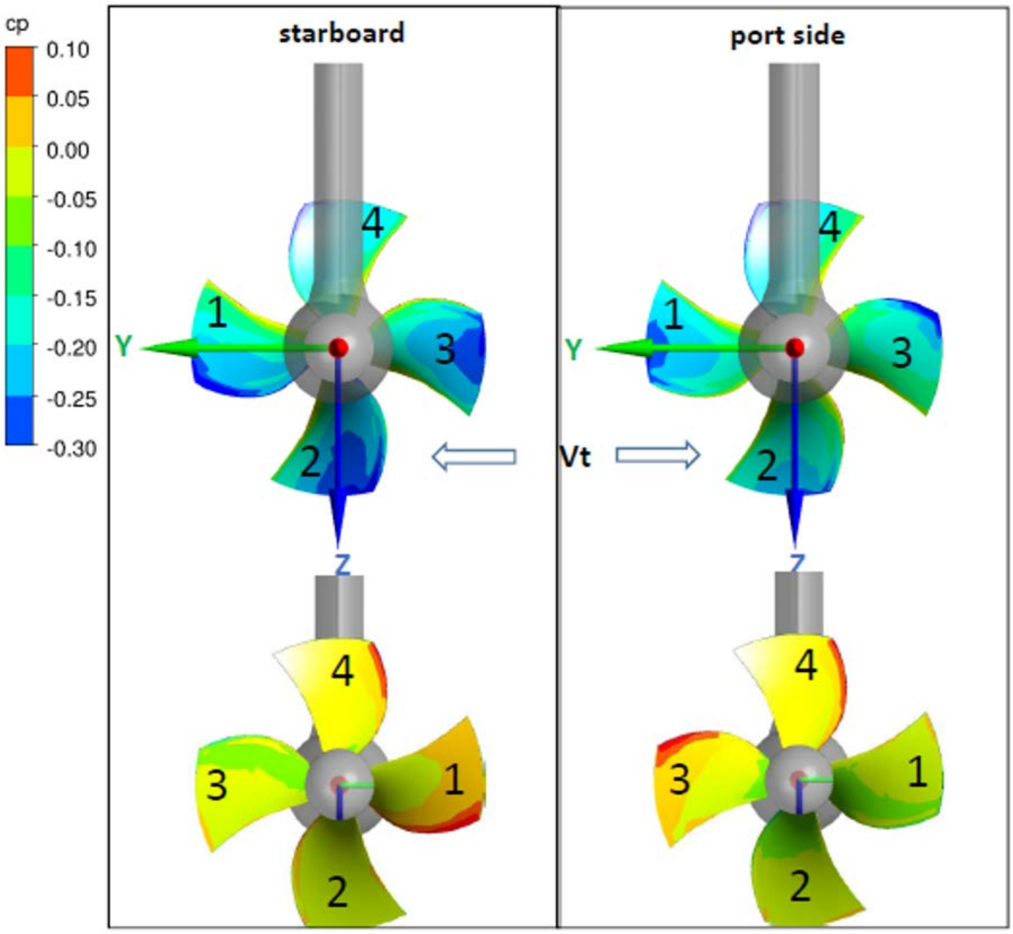

Fig. 48: Vertical velocity on the XZ-Plane

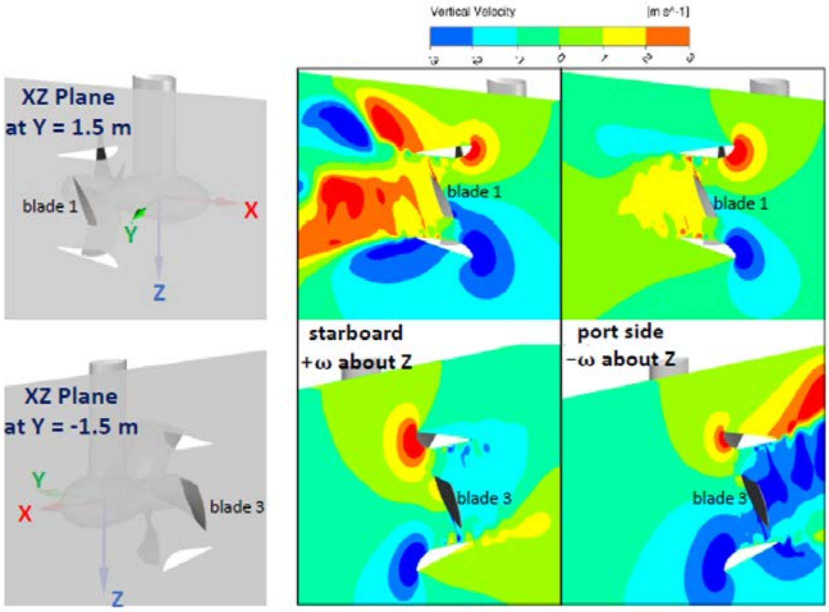

4.2.1.6.3 Case 3: Varied advance ratios of *J*=0/0.01/0.6 at *ψ* = 90° with azimuth speed *f* = 3

The object is to investigate the thrust differences at different *J*. *ψ* = 90° is selected as denoted with the vertical dashed line (see Fig. 4.49).

Fig. 49: Development of the total longitudinal force about the azimuth angle on dynamic condition at operation point of *f* =3 rpm

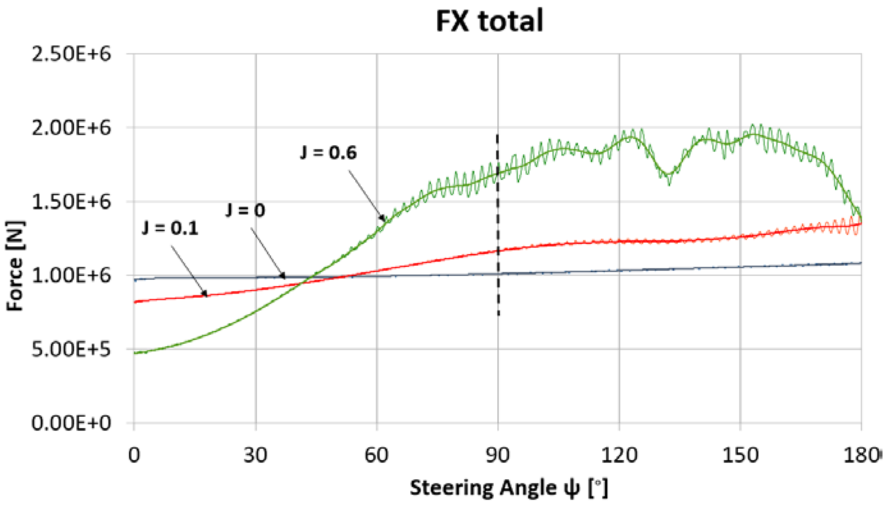

The thrust for each component (duct, housing and propeller) is given in Tab. 4.30. The maximal increment is 74% with respect to the propeller thrust. As mentioned that the duct is a passive part, the propeller should account for the differences.

Table 4.30: Longitudinal force for the components (propeller, duct and housing) and the percentage of changing thrust referred to *J* = 0 (in the bracket)

FX [kN]	**Propeller**	**Duct**	**Housing**
J=0	472	583	-45
J=0.1	529(+12%)	660(+13%)	-14
J=0.6	823(+74%)	916(+57%)	-4

The time history of one blade thrust during one revolution beginning from $\vartheta = 270°$ is shown in Fig. 4.51. The loads of other blades can be represented by corresponding values on the curve at the rotating angles of 0°, 90° and 180°, respectively.

The blades in the 12 o’clock position ($\vartheta = 0°$) produce similar forces due to the presence of the housing. At $\vartheta = 180°$, the blade rotates against the inflow (see Fig. 4.51 below), the thrust has to be increased by increasing J.

In the 3 and 9 o’clock positions ($\vartheta = 90°$ and $\vartheta = 270°$), the pressure on the suction side at J=0.6 is significantly higher than that on other advance ratios. The explanation can be drawn from Fig. 4.52, which shows the streamlines and the vertical velocities. On the third row of the figure, two sets of free vortices can be found (except for J=0). They differ from each other regarding the distance to the propeller plane due to different inflow velocities. The closer distance of J=0.6 leads to a higher induced velocity on the propeller blade compared with the condition of J=0.1.

As seen on the second row, the blade on the port side (3 o’clock position) is mainly affected by the lower vortices whereas the blade on the starboard (9 o’clock position) is affected by the upper vortices.

Fig. 50: Time history of the force of one revolution of one rotating blade since rotating angle of 270° from azimuth angle of 90°

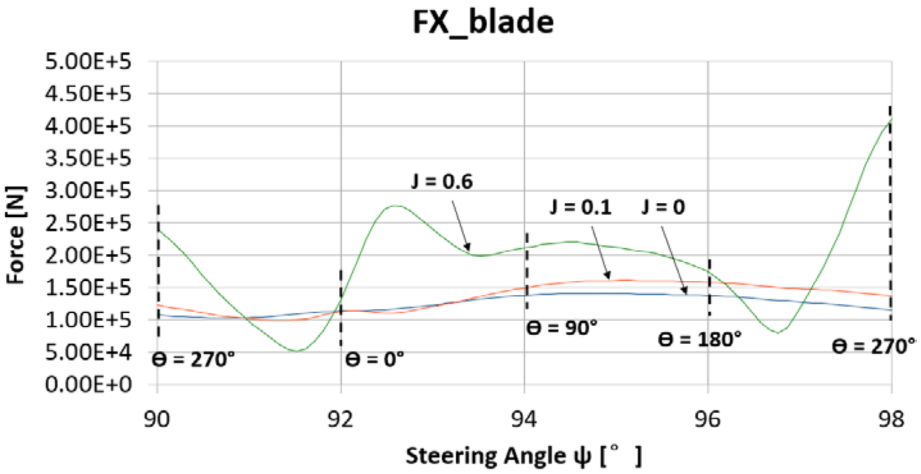

Fig.51: Pressure distributions of three inflow velocities at azimuth angle of 90°

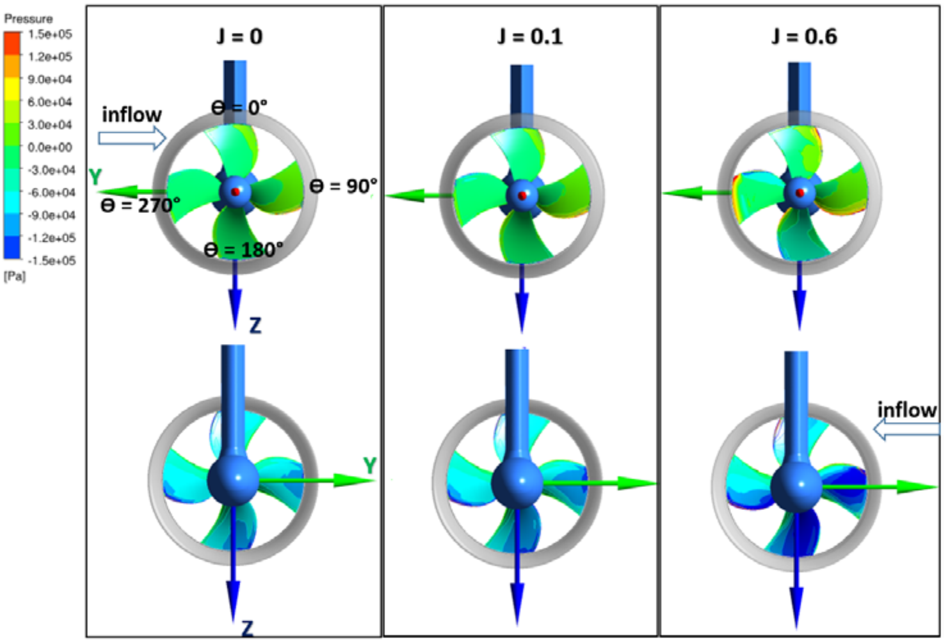

Fig. 52: Demonstrated vertical velocities on the xy-plane at *z* = 0 and the streamlines around the entire unit

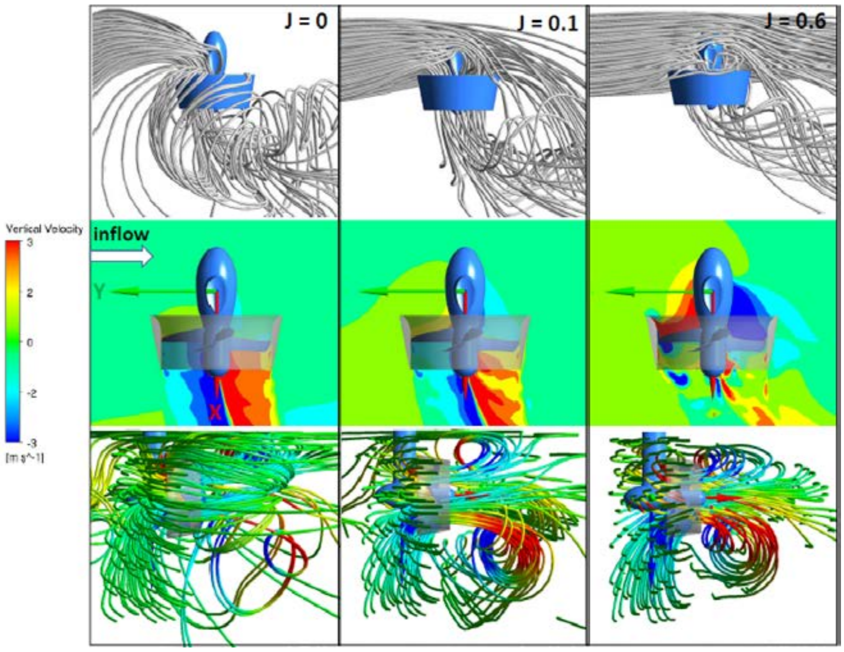

4.2.1.6.4 Case 4: Comparison between fixed and dynamic azimuth angle of ψ = 30° at J = 0.6

Previous investigations intend to explain the physical phenomena within the pure dynamic conditions. However, the more interesting part is the comparison with the steady results. The working condition of ψ = 30° und J=0.6 is chosen for this part of investigation.

Tab. 4.31 summaries the coefficients for the different components. ”δ” denotes the difference between dynamic and static one. Obviously, δkF Y and δkQ X from duct should be taken into account regarding the high deviations. Since kQ X is the moment obtained by transverse force kF Y. Thus, only δkF Y is of interest.

Table 4.31: The difference of longitudinal force between steady and unsteady condition for ψ = 30° and J = 0.6

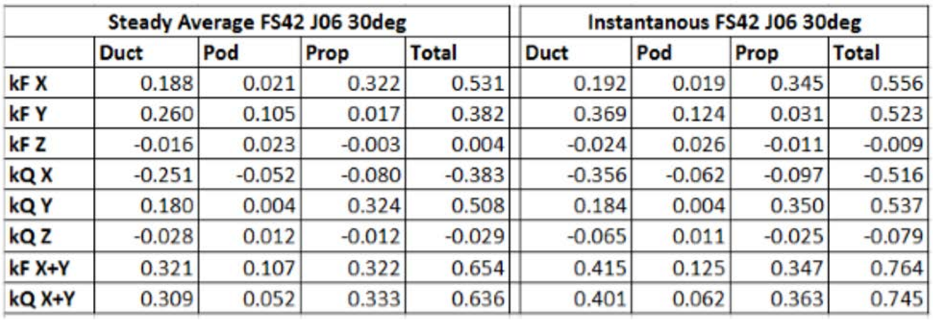

	Steady Average FS42 J06 30deg				Instantanous FS42 J06 30deg			
	Duct	**Pod**	**Prop**	**Total**	**Duct**	**Pod**	**Prop**	**Total**
kF X	0.188	0.021	0.322	0.531	0.192	0.019	0.345	0.556
kF Y	0.260	0.105	0.017	0.382	0.369	0.124	0.031	0.523
kF Z	-0.016	0.023	-0.003	0.004	-0.024	0.026	-0.011	-0.009
kQ X	-0.251	-0.052	-0.080	-0.383	-0.356	-0.062	-0.097	-0.516
kQ Y	0.180	0.004	0.324	0.508	0.184	0.004	0.350	0.537
kQ Z	-0.028	0.012	-0.012	-0.029	-0.065	0.011	-0.025	-0.079
kF X+Y	0.321	0.107	0.322	0.654	0.415	0.125	0.347	0.764
kQ X+Y	0.309	0.052	0.333	0.636	0.401	0.062	0.363	0.745

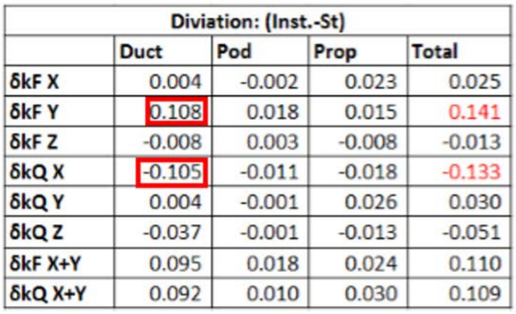

	Diviation: (Inst.-St)			
	Duct	**Pod**	**Prop**	**Total**
δkF X	0.004	-0.002	0.023	0.025
δkF Y	0.108	0.018	0.015	0.141
δkF Z	-0.008	0.003	-0.008	-0.013
δkQ X	-0.105	-0.011	-0.018	-0.133
δkQ Y	0.004	-0.001	0.026	0.030
δkQ Z	-0.037	-0.001	-0.013	-0.051
δkF X+Y	0.095	0.018	0.024	0.110
δkQ X+Y	0.092	0.010	0.030	0.109

The entire duct is divided into four parts as shown in Fig. 4.53. For each part the transverse force as well as its difference between the two conditions is given. Obviously, part 3 and 4 provide the highest transverse force in comparison with part 1 and 2 due to the different intensity of the pressure distribution as shown in the same figure.

The explanation is based on the induced velocity derived from the azimuth speed. The accelerating nozzle can lead to an accelerating flow passing though the duct. Fig. 4.54 shows the velocity field of difference obtained by subtracting the longitudinal velocity at steady condition. The framed area shows clearly that the increasing difference of velocity is associated directly with growing azimuth speed f. The increased velocity for parts 3 and 4 and the decreased velocity for part 1 and 2 cause the difference of the pressure distribution on the duct.

Fig. 53: Difference of side force and pressure distribution between steady- and unsteady condition

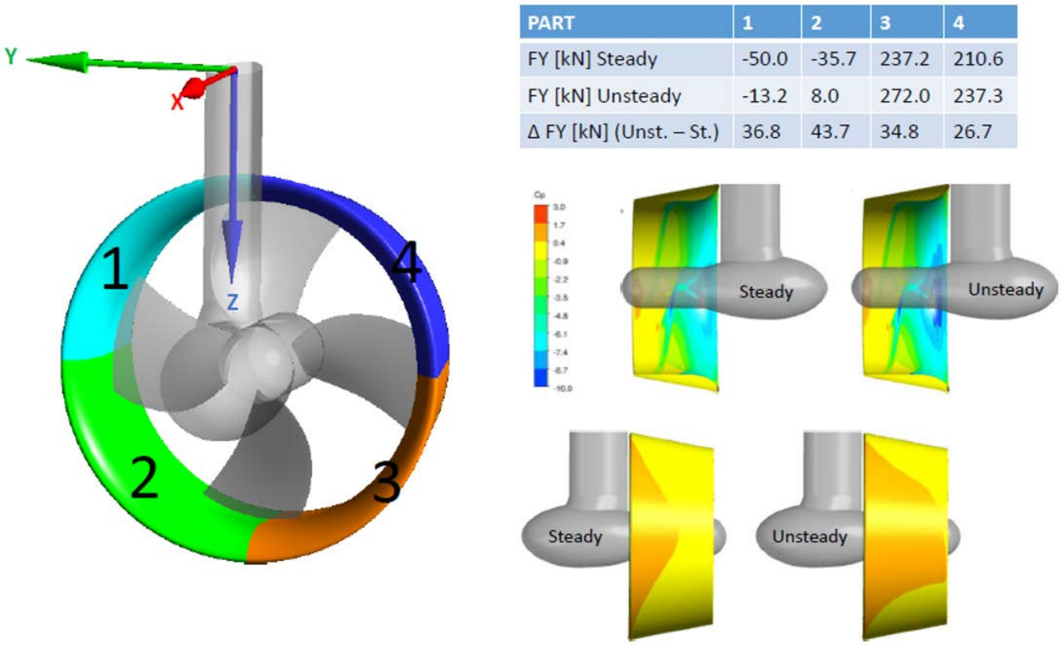

PART	1	2	3	4
FY [kN] Steady	-50.0	-35.7	237.2	210.6
FY [kN] Unsteady	-13.2	8.0	272.0	237.3
Δ FY [kN] (Unst. – St.)	36.8	43.7	34.8	26.7

Fig. 54: Velocity field of difference at two azimuth speeds in the case of ψ = 30°

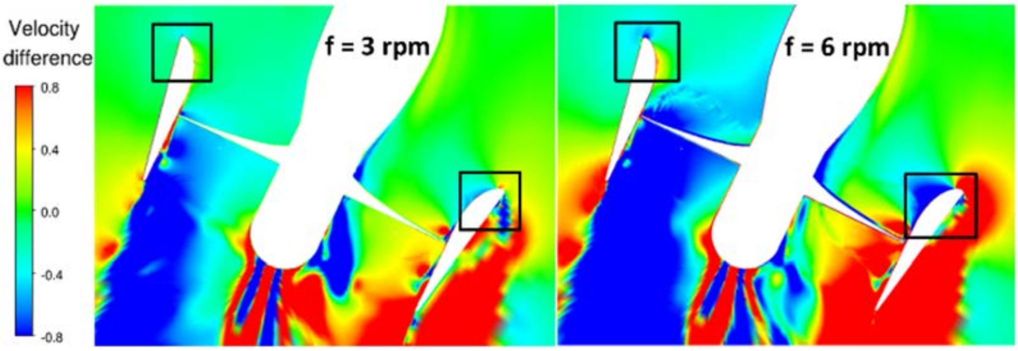

4.2.1.6.5 Case 5: Comparison of the longitudinal forces between the two the conditions at $\psi = 150°$ and $J = 0.6$

The deviation at this operation point is very huge as shown in Fig. 4.55. The reason will be discussed in details.

Tab. 4.32 shows the longitudinal forces for the different parts. δ describes the growth of the thrust related to the steady result. Because of the highest increment (814%) like the difference of the pressure distribution as shown in Fig. 4.56, the duct need to be concerned specially.

A x-y section plane named ”Plane 1” is placed as shown in Fig. 4.57. In order to compare the velocity, the figure on the second row shows the velocity field of difference like the previous treatment in case 4. A backflow takes place on both conditions, but the quantity of the backflow is different. It is not only originated by balancing the pressure between the suction and pressure side of the blade, but also by the interaction between inflow and propeller slipstream. At steady situation, it is difficult for the inflow to interfere the flow upstream in presence of a fully developed propeller slipstream. However, it can interfere the flow upstream easily in turn, if the slipstream has no blockage effect on the inflow.

Fig. 55: Compared history of longitudinal force about the azimuth angle between unsteady and steady condition for the operation point $J = 0.6$ and $f = 3$ rpm

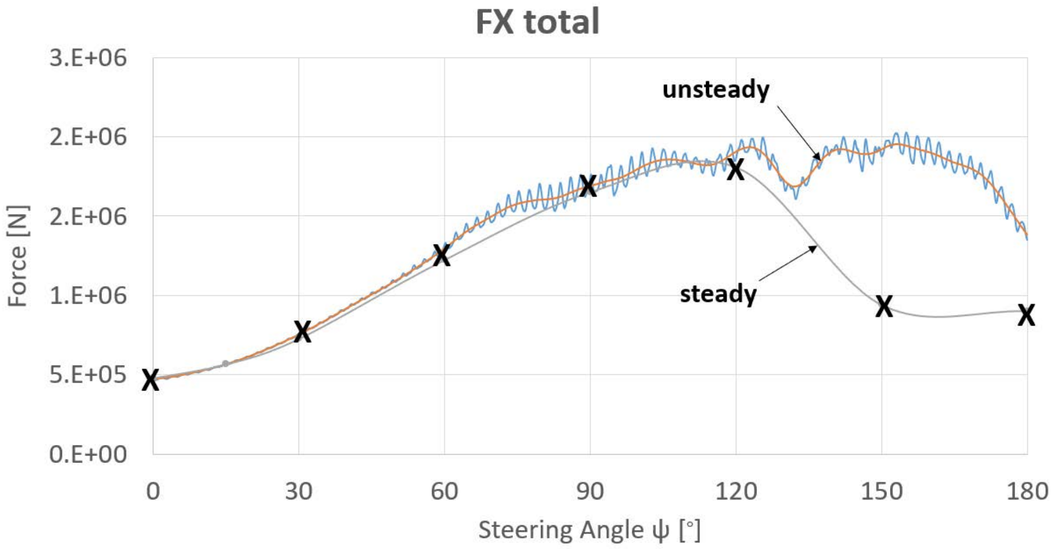

Table 4.32: Detained comparison of longitudinal force for different parts

Loads on Parts FX [kN]	Steady	Unsteady	δ[%]
Duct	112	1019	814
Housing	-25	-131	435
Propeller	852	1035	21

Fig. 56: Pressure distribution on the duct at ψ = 150° and J = 0.6

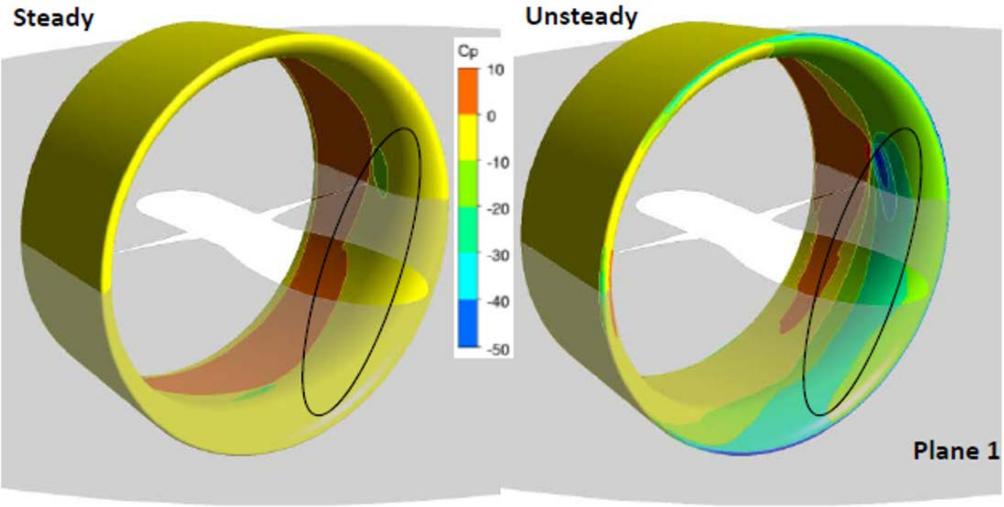

Fig. 57: The axial velocity distribution (above) and the velocity of difference between unsteady and steady condition (below) on Plane 1

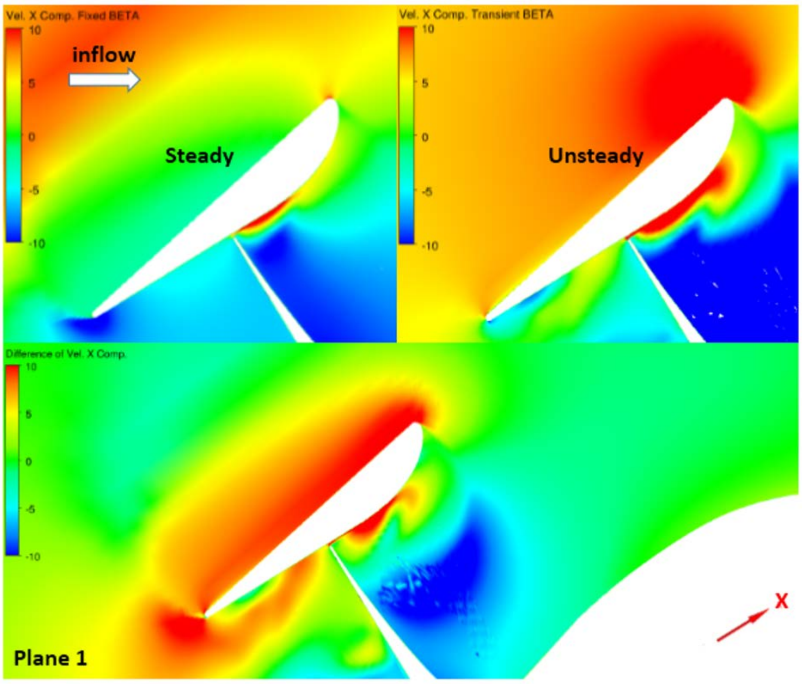

The same statement holds like it from the fixed azimuth angles that most of the critical situations are taken place between ψ = 90° and 120°. The induced velocity causes the increment of transverse and longitudinal force from azimuth speed on the duct and propeller slipstream on the blades, respectively.

The dynamic effect is represented by the transverse force, which depends on the azimuth speed. The relation between them can be treated as linear function.

The turning direction of the entire thruster has a considerable influence on the forces and moments. The difference of the thrust regarding the turning directions is due to the combination of propeller and thruster rotating direction.

5 Working Package WP3

The object of WP3 focuses on improving the performance of tunnel thrusters, aimed at reducing the noise, based on systematic numerical studies. Another focusing point is to evaluate the performance of tunnel thrusters in ship’s turning manoeuvre.

At the task in T3.1 - Influence of design parameters on tunnel thruster performance – a parametric model for the description of the propeller geometry has been developed, which allows varying the propeller geometry by parameters. Furthermore, a propeller model is developed to reduce the computational effort for selecting design parameters.

At the tasks in T3.3 - Influence of operation conditions on tunnel thruster performance - especially the performance of tunnel thruster is considered on turning circle condition. In this task a forced motion followed by model tests of Planar Motion Mechanism (PMM) are carried out by using RANSE method. The simulations in drift motion required from T3.3.1 and T3.3.2 are replaced by the dynamic sway motions, which can be further evaluated for T3.3.3 and T3.3.4, respectively.

An overview of task WP3 is found in Tab. 5.1.

Table 5.1.: Sub working tasks of task T3.1 and T3.2

WP3: Design and performance of tunnel thrusters	
Working task	Description
T3.1	**Influence of design parameters on tunnel thruster performance**
T3.1.1	Development of a parametric model for description of the propeller geometry
T3.1.2	Development of a propeller model for simulation of the propeller influence on the flow of bow thrusters
T3.3	**Influence of operation conditions on tunnel thruster performance**
T3.3.1	Simulation of the flow around the tunnel thruster in drift motion of the ship, including the ship hull (first operating point)
T3.3.2	Simulation of the flow around the tunnel thruster in drift motion of the ship, including the ship hull (second operating point)
T3.3.3	Simulation of the flow around the thruster at turning circle condition involving the hull (first operating point)
T3.3.4	Simulation of the flow around the thruster at turning circle condition involving the hull (second operating point)

5.1 T3.1 - Influence of design parameters on tunnel thruster performance

The parametric model for propeller geometry is based on a data in PFF-format which is developed by Potsdam Ship Model Basin (SVA Potsdam). A description is introduced in subsect 5.1.1.2. The modification of characteristic curves like pitch distribution is controlled by the third order splines. The propeller geometry provided by Jastram is also applied for the development of propeller model in T3.1.2.

5.1.1 T3.1.1 - Development of a parametric model for description of the propeller geometry

The focus of working task 3.1.1 is to modify the shape of the propeller blade geometry by changing a set of specific parameters. As mentioned, the modification will be realized based on an existing PFF-file (Propeller Free Format) by changing characteristic curves. After that, a new PFF-file is generated, which can be converted into other software, e.g. in-house developed code panMARE or commercial software ANSYS TurboGrid.

5.1.1.1 Main definition

The definition of propeller geometry is according to ITTC – Recommended Procedures and Guidelines (7.5-01 02-01) [14]. There are three major lines (see Fig. 5.1) appearing frequently in this documentation.

- Propeller reference line: The propeller blade is defined about a line normal to the shaft axis called the propeller reference line, which contains the reference point of the root section.
- Generator line: Generator line is displaced from propeller reference line in direction of shaft with distance of generator rake.
- Blade reference line: It is defined as a line through the reference points, which are the mid-chord points of the blade sections.

Fig. 5.1: ITTC Recommended Reference Lines from [14]

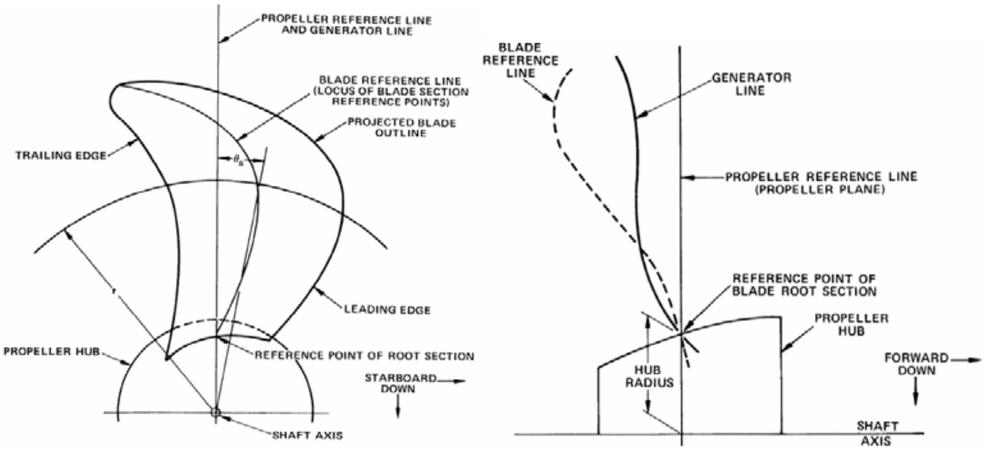

Total rake (iT) consists of two components, generator rake (iG) and skew induced rake (iS) as shown in Fig.(5.2). Generator rake (iG) is the displacement from the propeller plane to generator line. Aft displacement is considered as positive rake. The skew considered pertains to mid-chord skew recommended by ITTC. It is also proposed by other literature to use the point of maximum thickness. A positive skew means that the skew attempts to create a positive rake (iS: skew induced rake).

Fig. 5.2: View of unrolled cylindrical sections at blade root and any radius *r* from [14]

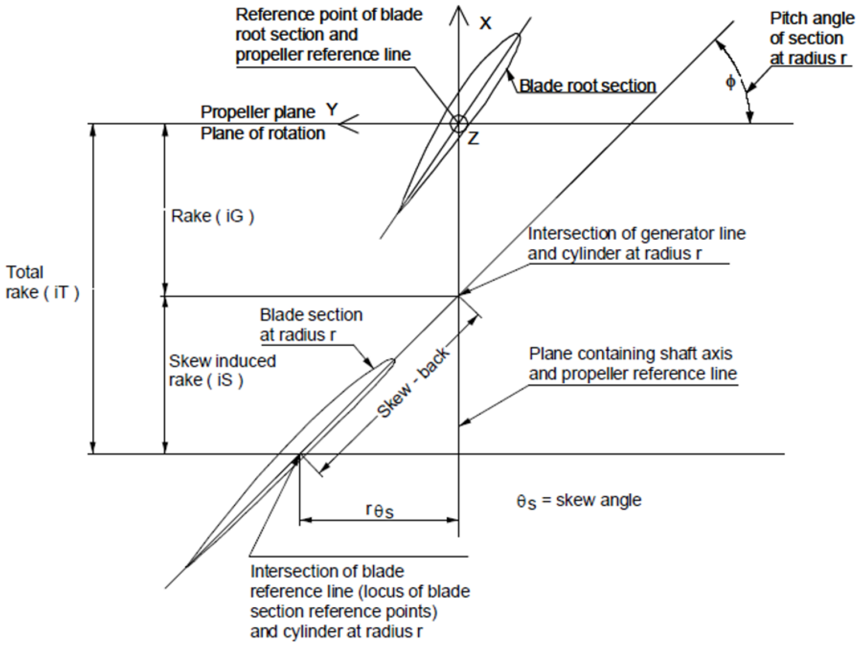

5.1.1.2 PFF overview

The first couple of lines of a PFF-format data contain the main specification of the propeller including propeller diameter, hub diameter, number of the blades, direction of rotation etc. If ”Orientation” equals 1 the propeller is right-handed otherwise it is left- handed. ”N.Radii” is the number of annular sections counted in radial direction whereas ”No.CordPart” is the number of characteristic points in chordal direction. “Station“ indicates the location of those points measured from leading edge (LE) normalized by chord length (”ChordLength”). ”Dist.SucS” and ”Dist.PressS” denote distance between the station point and its perpendicular projected point to the upper side (suction side) and lower side (pressure side) of the profile, respectively. The ”DistLeaEdge” defines the distance between leading edge point and propeller reference point. Rake is displacement from propeller plane to the generator line in the direction of the shaft axis.

Fig. 5.3 shows the general definitions of one arbitrary blade section according to the PFF-format. The name specified in other PFF-file may be different, for example instead of using ”Orientation” the name of ”Dir.of.Rot” is applied. The unit in PFF-format is usually millimetre set as default. “Scale” is intended to upscale or downscale blade dimensions.

Fig. 5.3: General definition of blade section in PFF-file before transformation

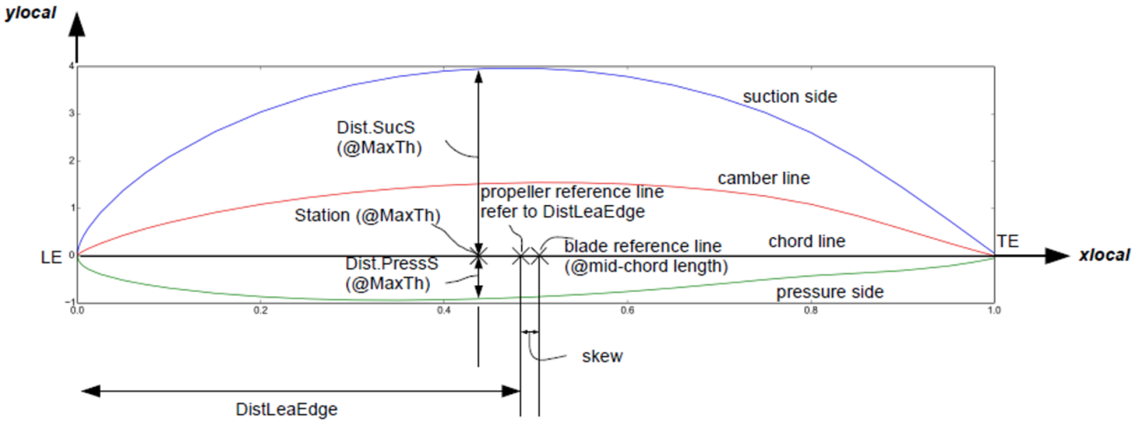

5.1.1.3 Definition of spline

Some of the characteristic curves of the propeller cannot be depicted simply by using third order polynomial. Subsequently, polynomials of the higher order need to be applied, but it can lead to a bad robustness if the distribution is going to be modified. The advantage of using spline is to avoid the instability of higher order polynomials. Fig. 5.4 shows a spline described piecewise by several cubic polynomials.

Fig. 5.4: Definition of cubic spline

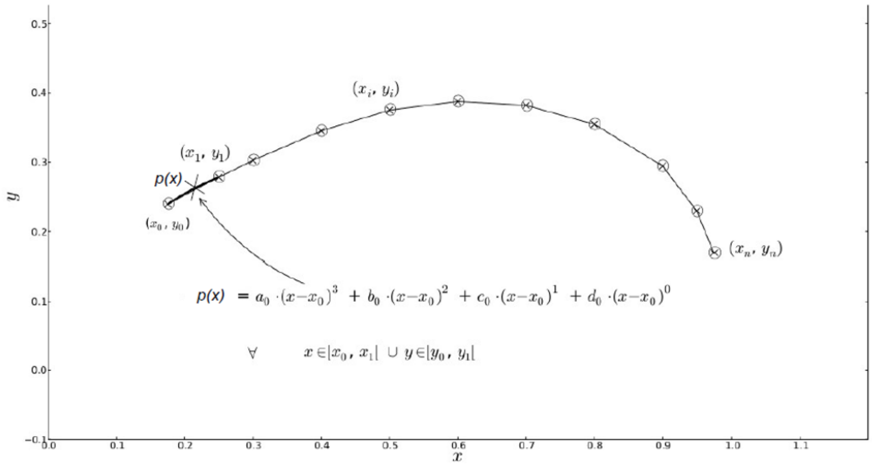

Here (x_i, y_i) are the location of the junction point between two segments. $p(x)$ describes the cubic polynomial of one segment. a_i, b_i, c_i and d_i are the coefficients. The solution of the coefficients is followed by the matrix built in eq. 5.1 under the condition of two segments at their connection point sharing the same value and the value of slope.

$$\underline{\underline{A}} \cdot \underline{B} = \underline{C} \tag{5.1}$$

$$\underline{\underline{A}} = \begin{pmatrix} 2(x_2 - x_0) & (x_2 - x_1) & . & . & . \\ (x_2 - x_1) & 2(x_3 - x_1) & (x_3 - x_2) & . & . \\ . & (x_3 - x_2) & 2(x_4 - x_2) & (x_4 - x_3) & . \\ . & . & . & . & . \\ . & . & . & . & . \\ . & . & . & (x_{n-1} - x_{n-2}) & 2(x_n - x_{n-2}) \end{pmatrix},$$

$$\underline{B} = \begin{pmatrix} B_1 \\ B_2 \\ B_3 \\ . \\ . \\ B_{n-1} \end{pmatrix}, \qquad \underline{C} = 6 \cdot \begin{pmatrix} \frac{y_2 - y_1}{x_2 - x_1} - \frac{y_1 - y_0}{x_1 - x_0} \\ \frac{y_3 - y_2}{x_3 - x_2} - \frac{y_2 - y_1}{x_2 - x_1} \\ \frac{y_4 - y_3}{x_4 - x_3} - \frac{y_3 - y_2}{x_3 - x_2} \\ . \\ . \\ . \\ \frac{y_n - y_{n-1}}{x_n - x_{n-1}} - \frac{y_{n-1} - y_{n-2}}{x_{n-1} - x_{n-2}} \end{pmatrix}.$$

$$\begin{aligned} a_i &= \frac{B_{i+1} - B_i}{6 \cdot (x_{i+1} - x_i)}, \\ b_i &= \frac{B_i}{2}, \\ c_i &= \frac{y_{i+1} - y_i}{(x_{i+1} - x_i)} - \frac{2 \cdot (x_{i+1} - x_i) \cdot B_i + (x_{i+1} - x_i) \cdot B_{i+1}}{6}, \\ d_i &= y_i. \end{aligned}$$

5.1.1.4 Parameterization of propeller geometry

The modification is based on the original curve named $f_1(x)$ as shown in Fig. 5.5. The second one called $f_2(x)$ consists of two cubic polynomials. The modified one $f_3(x)$ is obtained by adding $f_1(x)$ and $f_2(x)$. Through shifting the green arrows on $f_2(x)$ in horizontal (xhub, xMid and xTip) as well as in vertical (xhub, xMid and xTip) direction, $f_3(x)$ will be changed automatically.

Fig. 5.5: Superposition of splines

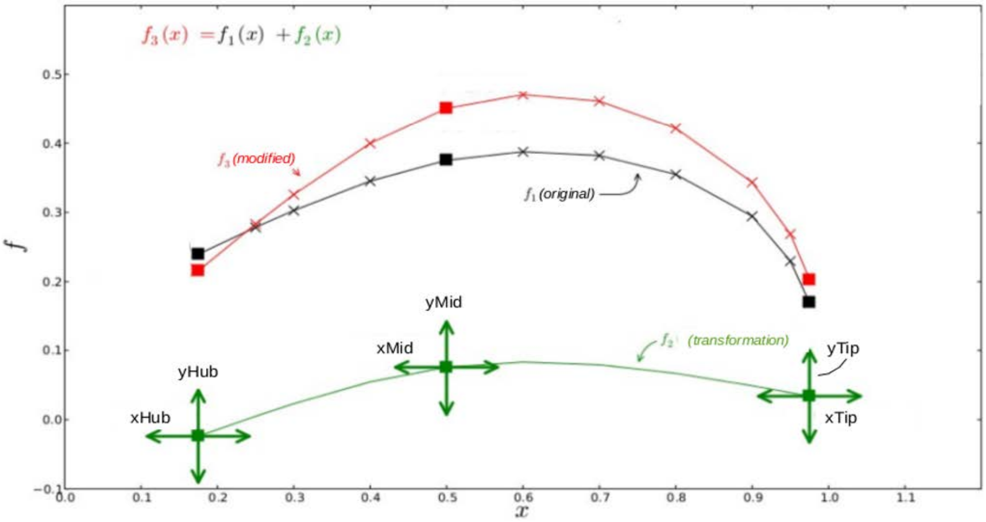

X-axis and y-axis can be the radius and propeller characteristic curves, respectively. Following distributions are taken into account:

- pitch,
- chord length
- rake,
- skew,
- maximum thickness and
- maximum camber

It is assumed, that the distribution of thickness and camber in chordal direction is followed by the change of maximum thickness and camber.

To keep the number of parameters as less as possible, two assumptions are made:

- the relation between maximal radius as well as minimal radius and the propeller radius is constant, xTip and xHub are discarded.
- xMid is equal to 0.5 (positioned on the middle section of propeller)

Remaining parameters are yHub, yMid and yTip. The range of parameter can be set by considering the requirement of the optimization.

5.1.1.5 Coordinate transformation

In PFF-format data, the location of points refer to the local coordinate system, i.e. x-axis starts at leading edge and leads to the trailing edge. The transformation from (x_l, y_l) to (x_g, y_g), as shown in Fig. 5.6, is carried out by the following five steps.

5.1.1.5.1 Step 1 - Consideration of distance to leading edge (DistLeaEdge)

First, the origin of local coordinate defined as (x_1, y_1) as shown in Fig. 5.6 is moved to the propeller reference line which is oriented normal to the shaft axis. Every point of *i*–th section is displaced with the distance of ”DistLeaEdge(*i*)” given in PFF.

$$x_2 = x_1 - \mathrm{DistLeaEdge}(i) \tag{5.2}$$

$$y_2 = y_1 \tag{5.3}$$

Fig. 5.6: Transformation by ”DistLeaEdge”

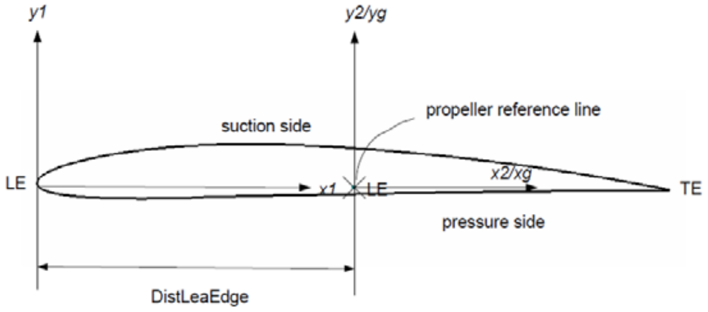

Skew is given implicitly related to the ”DistLeaEdge(*i*)”. From Fig. 5.3 it is easy to get the value of skew in Eq. 5.4.

$$\mathrm{skew}(i) = 0.5 \cdot \mathrm{Chordlength}(i) - \mathrm{DistLeaEdge}(i) \tag{5.4}$$

5.1.1.5.2 Step 2 - Consideration of pitch

The values of pitch is given directly by PFF. The rotation of *i*–th section is related to the pitch angle, which can be written as follows:

$$\mathrm{PitchAngle}(i) = \arctan(\frac{\mathrm{pitch}(i)}{2 \cdot \pi \cdot \mathrm{r}(i)}) \tag{5.5}$$

The expressions for the pitch transformation from (x_2, y_2) to (x_3, y_3) are different according to the direction of propeller rotation (see Fig. 5.7).

For right-handed propeller, we get the eq. 5.6 ~ Eq. 5.7

$$x_3 = -x_2 \cdot \sin(\mathrm{PitchAngle}(i)) + y_2 \cdot \cos(\mathrm{PitchAngle}(i)) \tag{5.6}$$

$$y_3 = x_2 \cdot \cos(\mathrm{PitchAngle}(i)) + y_2 \cdot \sin(\mathrm{PitchAngle}(i)) \tag{5.7}$$

For left-handed propeller, we get the Eq. 5.8 ~ Eq. 5.9

$$x_3 = -x_2 \cdot \sin(\mathrm{PitchAngle}(i)) + y_2 \cdot \cos(\mathrm{PitchAngle}(i)) \tag{5.8}$$

$$y_3 = -x_2 \cdot \cos(\mathrm{PitchAngle}(i)) - y_2 \cdot \sin(\mathrm{PitchAngle}(i)) \tag{5.9}$$

Fig. 5.7: Transformation by pitch angle for right handed propeller (left) and left handed propeller (right)

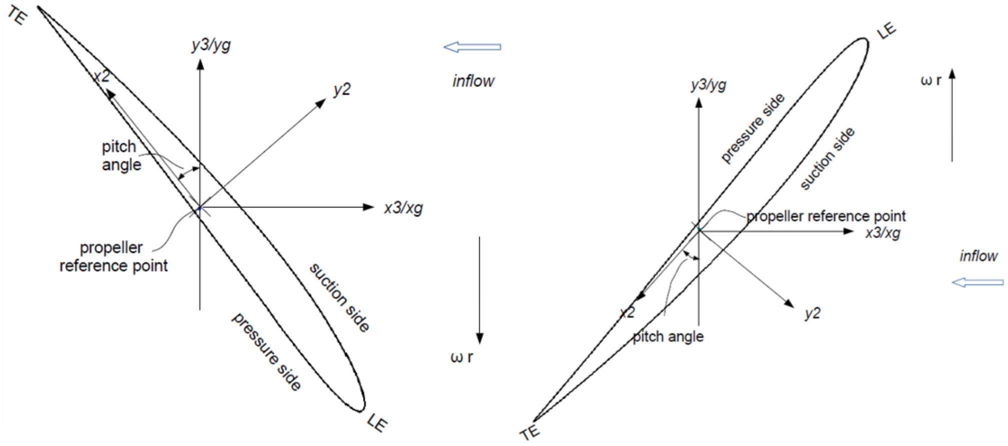

5.1.1.5.3 Step 3 - Consideration of rake (iG)

Rake mentioned here means generator line rake. The coordinate transformation now is from propeller reference line to generator line.

$$x_g = x_3 - \mathrm{Rake}(i) \tag{5.10}$$

Fig. 5.8: Transformation by rake for left handed propeller

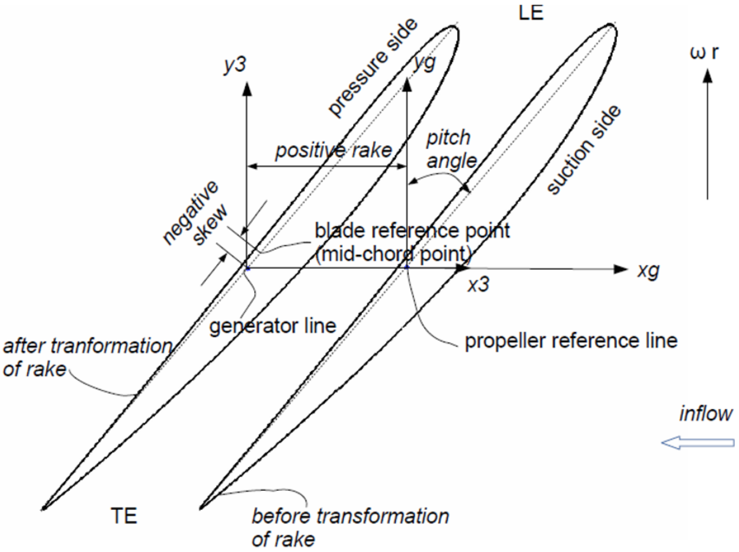

The total rake (iT) is obtained from Fig. 5.8:

$$\mathrm{rakeTotal}(i) = \mathrm{rake}(i) + \mathrm{skew}(i) \cdot \sin(\mathrm{PitchAngle}(i)) \tag{5.11}$$

5.1.1.5.4 Step 4 - Wrapping on the cylinder

A point with its location (p_1, p_2, p_3) in section of radius r will be rotated to cylindrical blade section with the new location (p_4, p_5, p_6). The condition is that the arc length $\hat{L}$ and p_2 must have the same length. The arc length is equals to the radius r times γ as shown in Fig. 5.9. γ can be estimated from Eq. 5.12

$$\gamma = \frac{\hat{L}}{r} \tag{5.12}$$

Eq. 5.13 and Eq. 5.14 can obtain the location of p4 and p5, respectively.

$$p_5 = p_3 \cdot \cos(\gamma) \tag{5.13}$$

$$p_6 = p_3 \cdot \sin(\gamma) \tag{5.14}$$

The basic formulations are:

$$\begin{aligned} x_g &= x_3 \\ y_g &= z_3 \cdot \cos(\gamma) \\ z_g &= z_3 \cdot \sin(\gamma) \end{aligned}$$

with

$$\gamma = \frac{y_3}{r}$$

Fig. 5.9: Wrapping of point (p_1, p_2, p_3) on the cylinder with radius r for left handed propeller

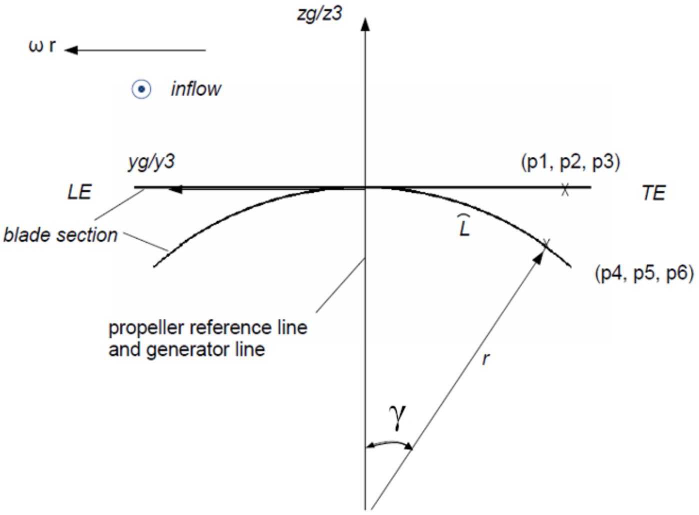

5.1.1.5.5 Step 5 - Adjustment of root section

The ITTC recommends that a point called *preference point of root section* should be taken place in the root section. The point is a cross point of *blade reference line* and *propeller reference line* or *generator line* as shown in Fig. 5.10. The target of this step is to adjust the root section till getting a zero rake and skew without changing the blade shape (see Fig. 5.10 right). After that, the new skew and rake distribution about radius need to be updated again though the step 1 to 4.

Fig. 5.10: Adjusting blade shape as recommended by ITTC

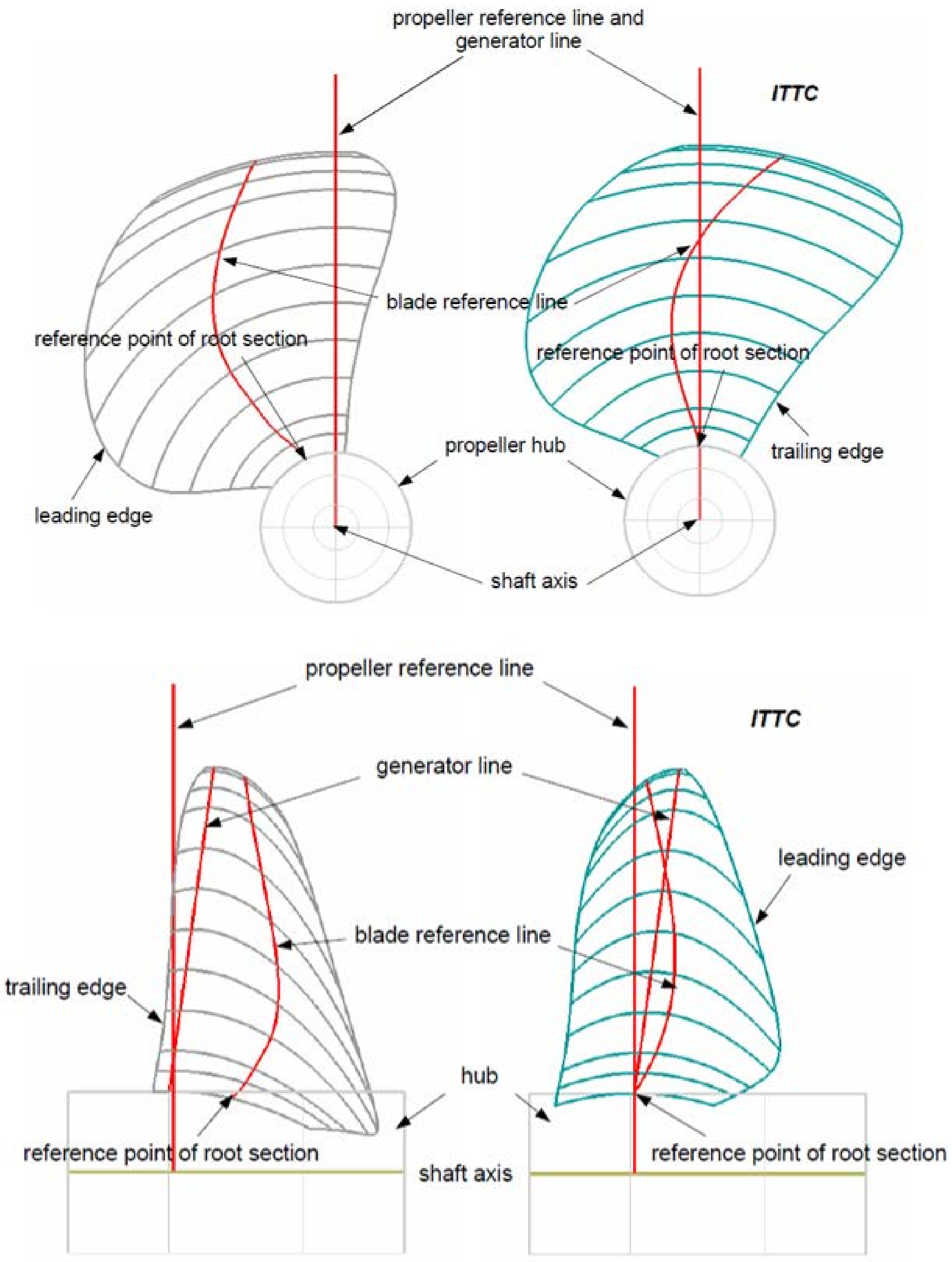

Adjustment of rake (iG): Rake is referred only to the displacement in shaft axis; each section has to be moved with the same rake (iG) as the root section (see Fig. 5.11).

Fig. 5.11: Displacement with respect to the rake of root section

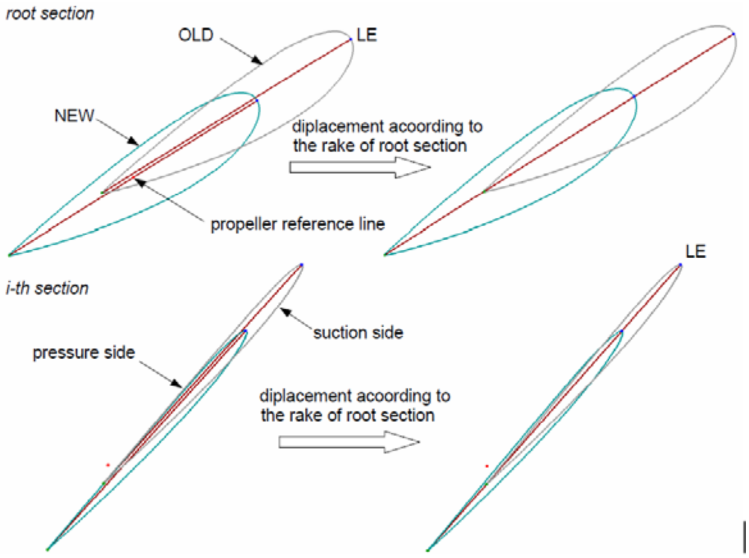

Adjustment of skew: The skew of the root section has two components, one is the skew induced rake in x-axis and another is the skew induced distance in y-axis. The displacement in *y*-direction for each section is not same because of the varied radius. The displacement in *y*-direction is obtained from the skew induced *y*-component of the root section (see Eq. 5.15).

$$y(i) = \text{skew}(\text{root}) \cdot \cos(\text{PitchAngle}(\text{root})) \cdot \frac{r(i)}{r(\text{root})} \quad (5.15)$$

The displacement in x direction has the same value as skew induced rake in the root section:

$$x(i) = \text{skew}(\text{root}) \cdot \sin(\text{PitchAngle}(\text{root})) \quad (5.16)$$

We obtain the length L_i (see Fig. 5.12)

$$L(i) = \sqrt{x(i)^2 + y(i)^2} \quad (5.17)$$

The "DisLeaEdge(i)" is then corrected with the length of *L*(*i*) respectively for each blade section.

Fig. 5.12: Displacement considered about the skew of root section

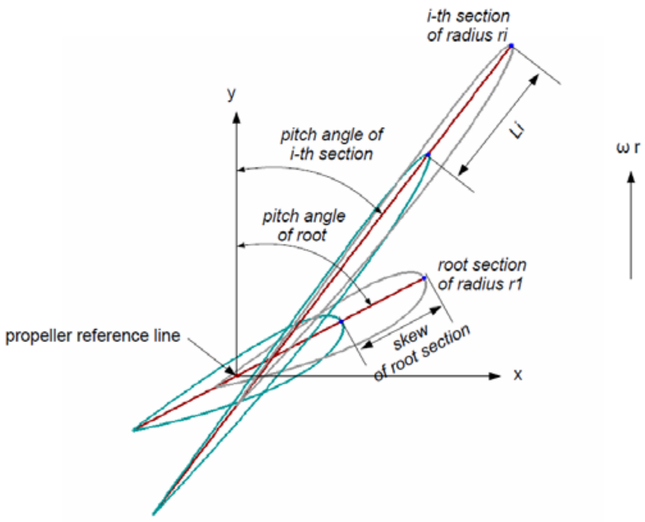

Finally, the geometry of propeller is adjusted from Fig. 5.10 left to right. If the propeller geometry is received from the manufacturer, the origin point defined may differ from the ITTC recommendation, and then the last step is unnecessary.

In order to modify the geometry, an input-file is provided, but it has to be noted that the change of the parameters such as yHub, yMitt and yTip for individual characteristic curves must be given in percentage of the original ones.

5.1.2 T3.1.2 - Development of a propeller model for simulation of propeller influence on the flow of bow thrusters

In this documentation, an actuator disc model is employed and based on volume forces being distributed over a disc domain by a distribution function. The method is implemented in the solver CFX by using internal CFX Expression Language (CEL) (which is used here) or by user coding. Both applications are available from the institute *Fluid Dynamics and Ship Theory*.

5.1.2.1 Pre-Calculation

Before using the propeller model, a reasonable function of force distribution over a disc need to be find out. The volume force can be applied as source terms in the governing Navier-Stokes equation. An example of using actuator disc is the study by Neitzel [20]; in his paper a function introduced by Stern [21] is used. The result shows a good correlation with the experimental data, but the function cannot be applied for ducted propeller due to different working environments. Therefore, a fully modelled propeller is applied for providing the force distribution. The blade mesh is generated from ANSYS TurboGrid.

A simplified tunnel geometry is applied for this investigation (see Fig. 5.13). The domain boundary has a length of 10D , width of 5D and height of 6D where D stand for the propeller diameter of 1.93m. The propeller plane is located with 0.294 m offset from the centre of the tunnel.

The variant C in Tab. 5.2 is selected for the validation test. The propeller has a rotation rate of 317.5rpm (5.3 1/s) with the torque coefficient of 0.0607.

Fig. 5.13: Simplified computational domain and boundary condition

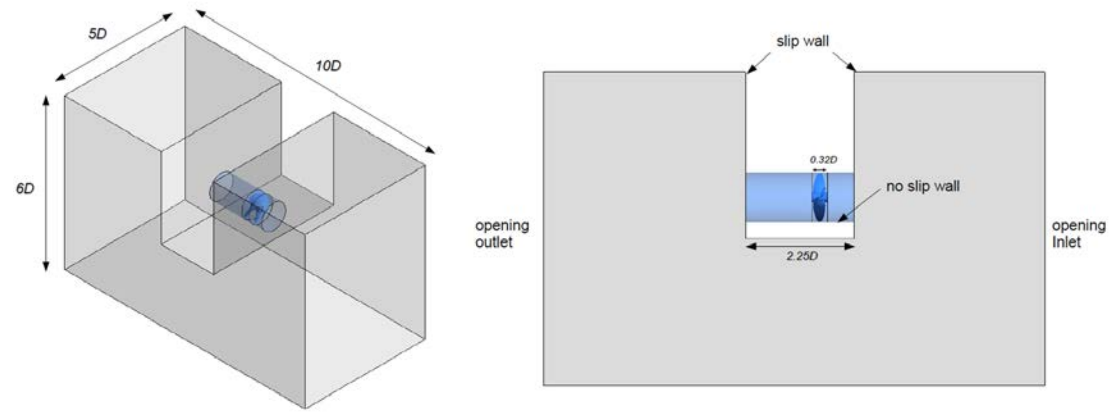

Blades and tunnel surface are treated as ”no slip wall”. Inlet and outlet are defined as ”opening”. ”slip wall” condition is used for other surfaces. Finite-volume mesh is generated with totally 4 million number of cells.

Fig. 5.14: Computational mesh for tunnel and propeller

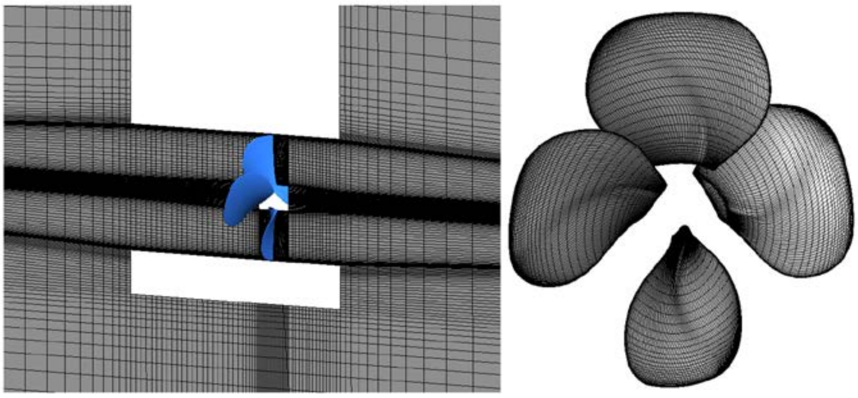

Table 5.2.: Thruster data provided by Jastram

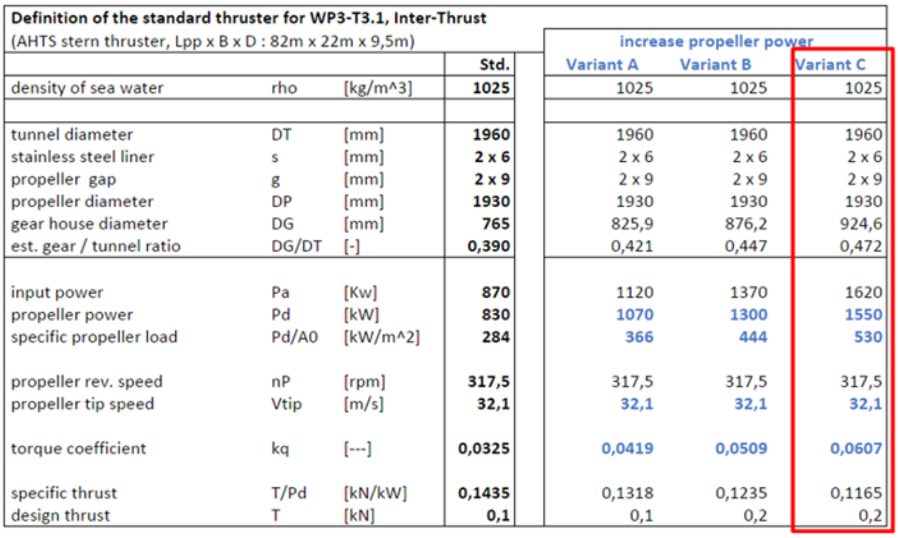

Definition of the standard thruster for WP3-T3.1, Inter-Thrust
(AHTS stern thruster, Lpp x B x D : 82m x 22m x 9,5m)

				increase propeller power		
			Std.	Variant A	Variant B	Variant C
density of sea water	rho	[kg/m^3]	**1025**	1025	1025	1025
tunnel diameter	DT	[mm]	**1960**	1960	1960	1960
stainless steel liner	s	[mm]	**2 x 6**	2 x 6	2 x 6	2 x 6
propeller gap	g	[mm]	**2 x 9**	2 x 9	2 x 9	2 x 9
propeller diameter	DP	[mm]	**1930**	1930	1930	1930
gear house diameter	DG	[mm]	**765**	825,9	876,2	924,6
est. gear / tunnel ratio	DG/DT	[-]	**0,390**	0,421	0,447	0,472
input power	Pa	[Kw]	**870**	1120	1370	1620
propeller power	Pd	[kW]	**830**	**1070**	**1300**	**1550**
specific propeller load	Pd/A0	[kW/m^2]	**284**	**366**	**444**	**530**
propeller rev. speed	nP	[rpm]	**317,5**	317,5	317,5	317,5
propeller tip speed	Vtip	[m/s]	**32,1**	**32,1**	**32,1**	**32,1**
torque coefficient	kq	[---]	**0,0325**	**0,0419**	**0,0509**	**0,0607**
specific thrust	T/Pd	[kN/kW]	**0,1435**	0,1318	0,1235	0,1165
design thrust	T	[kN]	**0,1**	0,1	0,2	0,2

In order to get a smooth function of distribution, the propeller surface is split into 28 segments named *”Iso Clips”* along the annular direction with the same height (δR) (see Fig. 5.15).

Fig. 5.15: *”IsoClip”* between each two adjacent solid lines over the radius

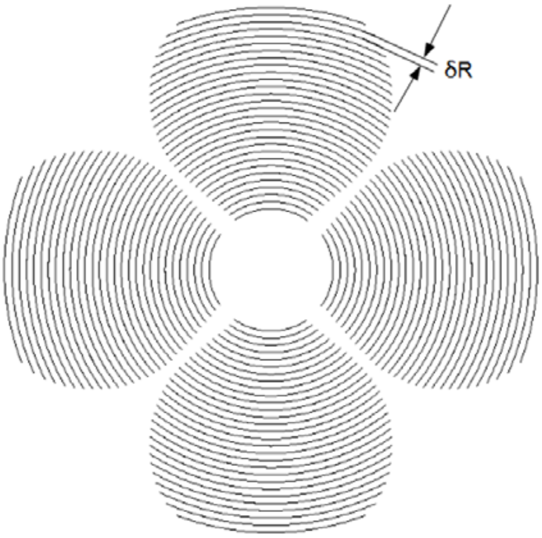

The expressions of normalized force distribution $V F_X$ and $V F_T$ are related to Eq. 5.18 and Eq. 5.19. Here i stand for the i–th *"Iso Clips"*, F_X (i) and Q_X (i) denote the axial force and moment on the i–th *"Iso Clips"*. V (i) stand for the volume of i–th section in propeller domain.

The distribution of $V F_X$ and $V F_T$ are shown in Fig. 5.16. The maximal value of $V F_X$ appears near the propeller tip; however, the development of $V F_T$ is almost uniform except the regions of root and tip due to equalization of pressure taking place.

The deviation of calculated torque coefficient is 4.4% comparing with the value given in Tab. 5.2. It might be caused by the simplification of the computational domain. Furthermore, two additional rotation rates (n=2.0 Hz and 8.48 Hz) are carried out and the results can be found in Tab. 5.3.

$$V F_X = \frac{\frac{F_X(i)}{V(i)}}{\sum_{i=1}^{n} \frac{F_X(i)}{V(i)}} \tag{5.18}$$

$$V F_T = \frac{\frac{\frac{Q(i)}{r(i)}}{V(i)}}{\sum_{i=1}^{n} \frac{\frac{Q(i)}{r(i)}}{V(i)}} \tag{5.19}$$

Fig. 5.16: Normalized volume force distribution over radius for axial (top) and tangential forces (bottom)

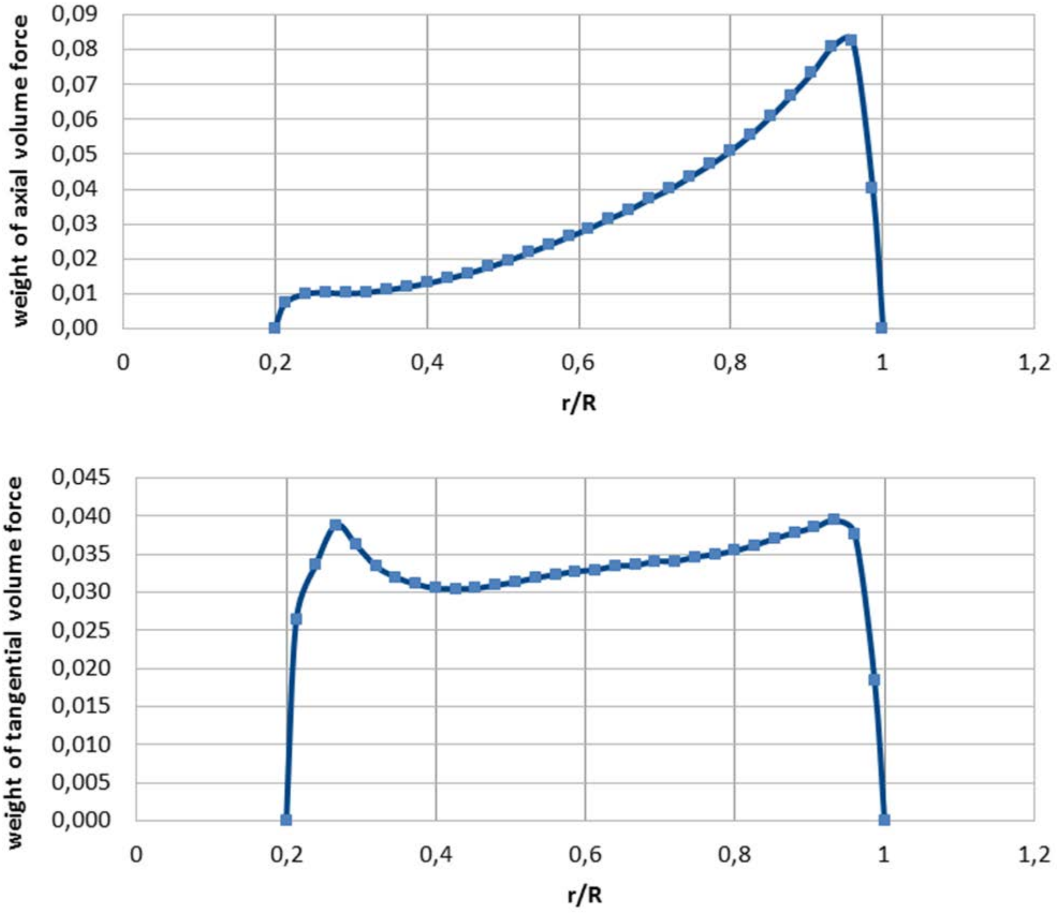

Table 5.3.: Propeller coefficients for different rotation rates.

n [1/s]	U_a	**J [-] evaluated**	k_t **[-]**	k_q **[-]**
2.0	2.34	0.6	0.371	0.064
5.3	6.22	0.6	0.373	0.063
8.48	9.98	0.6	0.374	0.063

Here U_a is the average axial velocity taken from the ”reading plane” which is placed 0.25D in front of the propeller plane (see Fig. 5.17). J is the local advance coefficient related to ”reading plane” and equal to:

$$J = \frac{U_a}{nD} \tag{5.20}$$

It seems that J, k_t and k_q remain almost unchanged (see Tab. 5.3). From the formulation of eq. 5.21 and eq. 5.22, the statement can be easily made that on one hand thrust T and torque Q have the dependency of n^2 and on the other hand the normalized volume force distribution does not change during the variation of n.

$$k_t = \frac{T}{\rho \cdot n^2 \cdot D^4} \tag{5.21}$$

$$k_q = \frac{T}{\rho \cdot n^2 \cdot D^5} \tag{5.22}$$

5.1.2.1.1 Actuator disc method

The target of actuator disc method is to replace the fully modelled propeller by a volume force to get a similar velocity field in a cylindrical disk domain. The distribution of thrust and velocity are uniform over the annular stream tube. The computational meshes for both cases outside of propeller domain are the same. The mesh contains about 2 million elements in the flow domain. A boundary called *”reading plane”* has to be defined during the mesh generation, so it can be associated later for the utilization of CEL.

Fig. 5.17: Actuator disc domain comparison with propeller domain

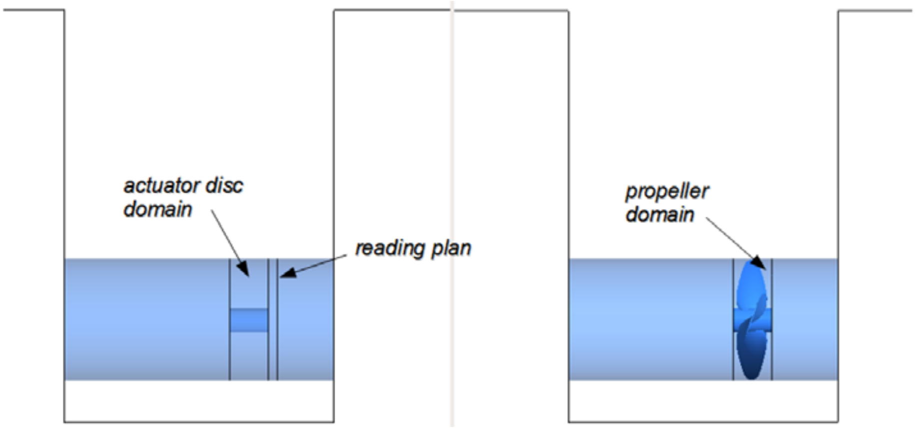

The propeller forces are placed in the domain via multiplication of *”step”* functions. The *”step”* function has the value of 1 if a predefined condition is true, otherwise its value is equal to 0. *”StepRotor”* is aimed to restrict the size of the actuator disc domain. Two parts of “step” functions are applied. ”StepX” (see Eq. 5.25) and ”StepR” (see Eq. 5.25) are responsible for the boundaries in the axial and radial directions of the disc domain, respectively.

$$\mathrm{StepRotor} = \mathrm{StepX} \cdot \mathrm{StepR} \tag{5.23}$$

where

$$\mathrm{StepX} = \mathrm{Step(x\text{-}xDiscOut)} \cdot \mathrm{Step(xDiscIn\text{-}x)} \tag{5.24}$$

$$\mathrm{StepR} = \mathrm{Step(R\text{-}R_{hub})} \cdot \mathrm{Step(R_{prop}\text{-}R)} \tag{5.25}$$

"xDiscIn" and *"xDiscOut"* are the locations of disc domain inlet and outlet, if *x* is greater than *"xDiscOut"* and less than *"xDiscIn"*, *"StepX"* will be 1, otherwise it will be 0. Like "StepX", "StepR" will be 1, if the radius is located between hub and tip.

Besides the two "step" functions, two corrections are considered during the calculation:

- The first correction is a volume correction called "ratioVol" which is the ratio between two values of volume as introduced by Keck [16], because the volume of computational grid takes place does not perfectly match the geometrical volume of the disc domain.
- The second correction is the ratio between the velocities called "ratioVel", which describes the difference between the velocity averaged on the "reading plane" and the required velocity of $U_{req} = J \cdot n \cdot D$ (here J=0.6).

The calculating process is shown in Fig. 5.18. The two corrections are multiplied by the Force (*F*) and their values are listed in Tab. 5.4.

Fig. 5.18: Calculating progress to actuator disc model

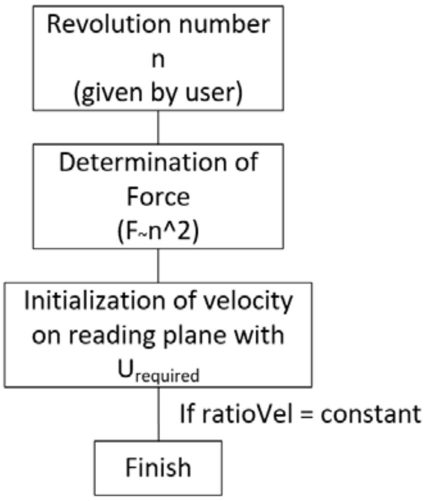

Table 5.4.: Corrections for the rotation rate of 5.3 Hz used in actuator disc model

n [1/s]	**ratioVol [-]**	**ratioVel [-]**
5.3	1.0324	0.997

The distribution of axial velocity on *"reading plane"* of actuator disc model in comparison to fully modelled propeller can be found in Fig. 5.19. The axial force distribution within the disc domain is shown in Fig. 5.20. The negative force means the appearance of back flow near the hub and tip. The only condition is the consistence of the propeller thrust *T* and moment *Q* given in the disc. The size of the disc domain seems not to be important.

Fig. 5.19: Distribution of the axial velocity on the ”reading plane”, the actuator disc model (left) and fully modelled propeller (right)

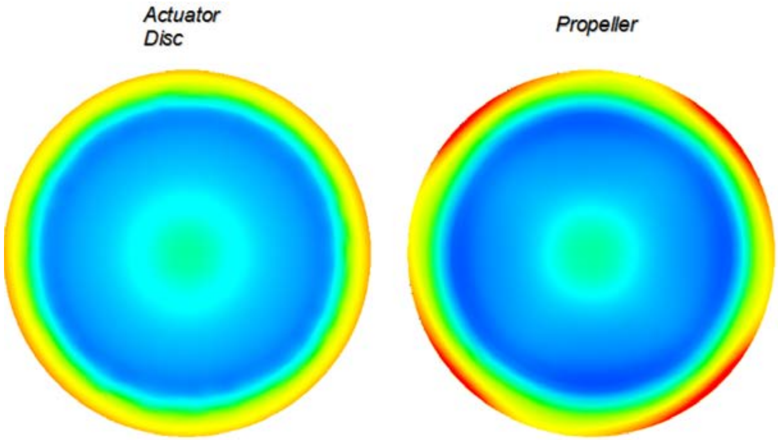

Fig. 5.20: Axial force distribution in actuator disc domain

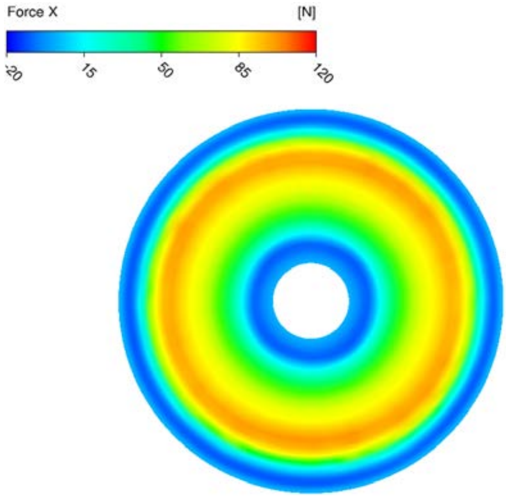

5.1.2.1.2 Presentation of the results

In order to test the method, other propeller rotation rates are applied. The results are presented in Tab. 5.5. The small deviation of the force is caused by the small change of k_t, which is assumed to be constant in the disc model, but it changes slightly in the case of fully rotating propeller (see Tab. 5.3).

Table 5.5.: Verification of actuator disc method

n [1/s]	ratioVel [-]	force actuator disc [kN]	force propeller [kN]	deviation [%]
0.53	1.014	1.512	1.470	2.86
2	0.997	21.168	21.073	0.45
5.3	0.992	147.873	148.904	-0.69
8.48	0.989	377.491	382.328	-1.27

The comparison of the flow downwards is very important to investigate the interaction between propeller slipstream and ship hull. Three planes place in the tunnel domain as shown in Fig. 5.21. Plane 3 is located near the exit. The distance between the planes nearby is 1 m. The averaged velocities on the planes for actuator disc model and fully modelled propeller (in bracket) are listed in Tab. 5.6. The differences of axial velocities might be caused by application of the actuator disc. Because the propeller solid body possesses some space, the mass flow has to be moving faster than that in the actuator disc model according to the Continuity Equation.

The relation between force and velocity on the reading plane has to be varied from one condition to another condition. In this case only the bollard pull condition is taken place. A function of force about the velocity is expected in the further work.

Table 5.6.: Average velocities on plane 1, 2, and 3. Value in brackets are the results of fully modelled propeller

Case n=5.3 Hz	**Plane 1**	**Plane 2**	**Plane 3**
Averaged axial velocity [m/s]	-3.99 (-4.58)	-5.31 (-5.74)	-5.84 (-6.24)
Averaged total velocity [m/s]	5.81 (5.49)	6.02 (6.38)	6.35 (6.73)

Fig. 5.21: Distribution of velocities on the cut planes being in the downstream of this left-handed propeller with rotation rate of 5.3 1/s. From up to down are axial flow velocity, velocity in y direction and the magnitude velocity

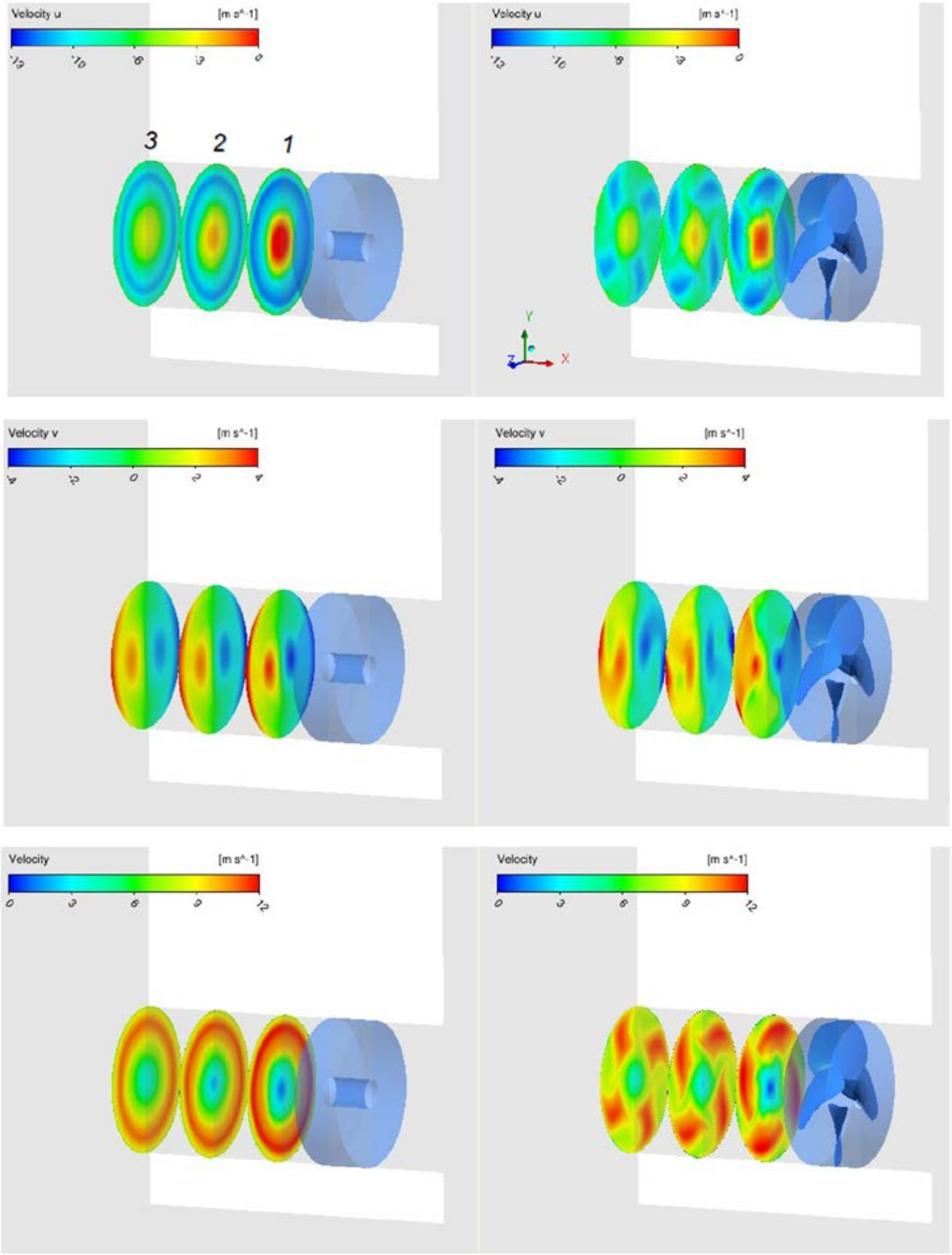

5.2 T3.3 - Influence of operation conditions on tunnel thruster performance

Following subjects will be discussed in working package WP3:

Table 5.7.: Sub working tasks of T3.3

T3.3	**Influence of operation conditions on tunnel thruster performance, optimization**
T3.3.1	Simulation of the flow around the tunnel thruster in drift motion of the ship, including the ship hull (first operating point)
T3.3.2	Simulation of the flow around the tunnel thruster in drift motion of the ship, including the ship hull (second operating point)
T3.3.3	Simulation of the flow around the thruster at turning circle condition involving the hull (first operation point)
T3.3.4	Simulation of the flow around the thruster at turning circle condition involving the hull (first operation point)

The ship manoeuvring can be predicted by using present empirical database, experimental results or CFD simulation. The prediction consists of two parts, first one is the direct manoeuvring simulation which leads to high requirements on the used code, second one is a simulation based on the hydrodynamic derivatives (simply ”HD”).

The main task of working task (T3.3.1) and (T3.3.2) is to get the hydrodynamic derivatives through the CFD simulations carried out by forced motion of the ship. In order to follow the model tests of Planar Motion Mechanism (PMM) the mesh motion is set in ANSYS CFX. The simulation deals with the fully modelled TT. The hydrodynamic derivatives obtained from the tasks (T3.3.1) and (T3.3.2) will be taken into account for the further working tasks (T3.3.3) and (T3.3.4) of simulating turning circle manoeuvres. In the following sections, a detailed description will be presented how the applied methods works.

5.2.1 Main definition

The definition has been clarified according to ITTC – International Towing Tank Conference Recommended Procedures and Guidelines (2014).

5.2.1.1 Coordinate system

The body-fixed coordinate system is a right-handed Cartesian system with axes *x*, *y* and *z.* It moves relative to the earth-fixed system (x_0, y_0 and z_0 in Fig. 5.24). *X*-axis is positive in ship's heading direction, *y*-axis is positive towards the starboard and *z*-axis is positive downwards as shown in Fig. 5.22.

Fig. 5.22: Definition of body-fixed coordinate system

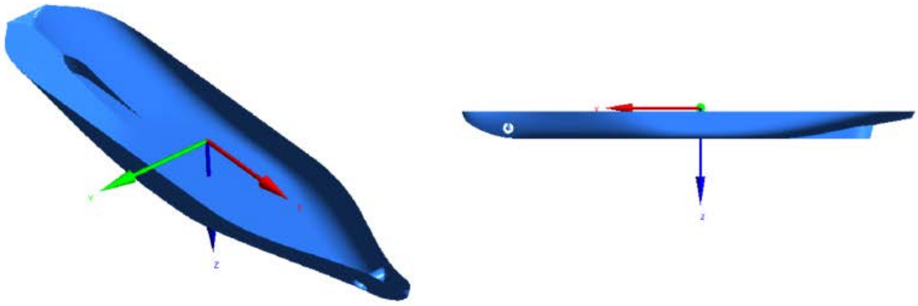

5.2.1.2 Dimensionless numbers

The forces and moment are normally non-dimensionalized by using the characteristic scales such as L_{pp}, U and ρ, where L_{pp} is the ship length between perpendiculars, U is ship's speed and ρ is the water density. The dimensionless numbers v', u', r' and ω' are shown in Tab. 5.8 and 5.9. Further non-dimensionalized forces and moments are listed in appendix H.

Table 5.8.: Non-dimensional forces and moments

$X' = \frac{X}{0.5\rho U^2 L_{pp}^2}$	$Y' = \frac{Y}{0.5\rho U^2 L_{pp}^2}$	$N' = \frac{N}{0.5\rho U^2 L_{pp}^3}$

Table 5.9.: Non-dimensional velocities and frequencies

$\omega' = \frac{\omega L_{pp}}{U}$	$v' = \frac{v}{U}$	$r' = \frac{r L_{pp}}{U}$	$u' = \frac{u}{U}$

5.2.2 Mathematical model

Since the TT has its effect only at ship's low velocity, the moving of heave, pitch and roll can be neglected. Only the dynamic tests of surge, sway and yaw are considered. If the origin point of body-fixed coordinate system is located in the point of centre of gravity as shown in Fig. 5.22. The equations of rigid body can be simplified to

$$X = m(\dot{u} - vr) \tag{5.26}$$

$$Y = m(\dot{v} + ur) \tag{5.27}$$

$$N = I_{zz}\dot{r} \tag{5.28}$$

The external forces X and Y can be subdivided into different components. The main parts are ship's hull, main propulsor and auxiliary components such like tunnel thruster (simply "TT"). The purpose of this task is to investigate the performance of TT on ship's turning circle condition. The main propulsor (simply "MP") are not included in the computation with the ship's hull. Its effect on the ship are described by the deduction factor and wake fraction taken over from the ship's design speed.

In order to extract the interaction between ship's hull and TT, two set of calculations are carried out, namely, ship with and without rotating propeller. It is assumed that the forces and moment are functions of ship motion parameters u, v, r, $\dot{u}$, $\dot{v}$ and $\dot{r}$. The vector $\vec{T}$ including the forces X, Y and moment N can be expressed by using Taylor-series expansions under three assumptions:

- acceleration terms of first order,
- velocity terms up to third order and
- no cross-coupling between acceleration and velocity like $\dot{r}v$

$$
\begin{aligned}
\vec{T} &= \begin{pmatrix} X \\ Y \\ N \end{pmatrix} \\
&\cong \vec{T}_0 \\
&+ \vec{T}_u \Delta u + \vec{T}_{uu} \Delta u^2 + \vec{T}_{uuu} \Delta u^3 + \vec{T}_{\dot{u}} \dot{u} + \vec{T}_{\dot{u}u} \dot{u} \Delta u + \vec{T}_{\dot{u}uu} \dot{u} \Delta u^2 \\
&+ \vec{T}_v v + \vec{T}_{vv} v^2 + \vec{T}_{vvv} v^3 + \vec{T}_{\dot{v}} \dot{v} + \vec{T}_{\dot{v}v} \dot{v} v + \vec{T}_{\dot{v}vv} \dot{v} v^2 \\
&+ \vec{T}_r r + \vec{T}_{rr} r^2 + \vec{T}_{rrr} r^3 + \vec{T}_{\dot{r}} \dot{r} + \vec{T}_{\dot{r}r} \dot{r} r + \vec{T}_{\dot{r}rr} \dot{r} r^2 \\
&+ \vec{T}_{vu} v \Delta u + \vec{T}_{ru} r \Delta u \\
&+ \vec{T}_{(vv)u} v^2 \Delta u + \vec{T}_{(rr)u} r^2 \Delta u + \vec{T}_{vru} v r \Delta u \\
&+ \vec{T}_{v(uu)} v \Delta u^2 + \vec{T}_{r(uu)} r \Delta u^2 \\
&+ \vec{T}_{vr} v r + \vec{T}_{rrv} r^2 v + \vec{T}_{vvr} v^2 r
\end{aligned}
\tag{5.29}
$$

This approach differs from the mathematical model proposed by Abkowitz 1964 [2] for a symmetric ship. Due to the consideration of interaction between TT and ship's hull according to the propeller slipstream this phenomena can break the symmetric condition of the ship. It should be noted, that the equation shown above is not the final mathematical model, a model reduction will be introduced in subsec. 7.2.0.1. Although the combined terms from acceleration and velocity such as $\overrightarrow{T_{\dot{v}v}}\dot{v}v$ have no physical meaning, but they will be very useful for the contribution aimed at curve fitting. This approach is general formulation and can suit widely to the ship with asymmetric appendages.

The connection of Eq. 5.26 ~ 5.28 and Eq. 5.29 is the equality of the forces *X*, *Y* and the moment *N*. The acceleration-related terms can be moved to one side of the equation system and the remaining terms to the other side. The velocities *u*, *v* and *r* are determined through Euler's method. The track of the ship has to be given in the earth-fixed frame; a coordinate transformation is additionally required. An example has been done, based on the research by Wolff 1981 [22] (Appendix G).

In the report of Wolff 1981 [22], five ship models are involved in the investigation of manoeuvrability, a tanker, a bulker of Serie 60, a mariner, a container vessel and a ferry. The HD of all ship's types are available and validated by comparison with the freely manoeuvring model. As an example, the Serie 60 bulker is selected. The HD and corresponding manoeuvring model can be found in Appendix G.

The series of hydrodynamic derivatives contain two parts, the first part is the acceleration-related terms (added mass). The remaining parts are the velocity-related terms (damping). Both sets of terms can be chosen from the table given in the Appendix G.

The body-fixed coordinate system of the ship investigated by Wolff is not located in the centre of gravity. The equations of rigid body are shown in the Eq. 5.26 ~ 5.28.

$$X = m(\dot{u} - vr - r^2 x_G) \tag{5.30}$$

$$Y = m(\dot{v} + ur + \dot{r} x_G) \tag{5.31}$$

$$N = I_{zz} \dot{r} + m(ur + \dot{v}) x_G \tag{5.32}$$

Here x_G is defined as the distance between the fixed body-axis of the ship and the centre of gravity.

With the utilization of the hydrodynamic derivatives given in eq. 5.29, the forces *X*, *Y* and moment *N* can be written in the following way of using Taylor-series expansions.

$$X = X_{\dot{u}}\dot{u} + X_{\dot{u}uu}\dot{u}uu + X(\mathrm{d}) \tag{5.33}$$

$$Y = Y_{\dot{v}}\dot{v} + Y_{\dot{v}vv}\dot{v}vv + Y_{\dot{r}}\dot{r} + Y_{\dot{r}rr}\dot{r}rr + Y(\mathrm{d}) \tag{5.34}$$

$$N = N_{\dot{v}}\dot{v} + N_{\dot{v}vv}\dot{v}vv + N_{\dot{r}}\dot{r} + N_{\dot{r}rr}\dot{r}rr + N(\mathrm{d}) \tag{5.35}$$

Here X(d), Y(d) and N(d) stand for the damping-related terms without accelerations. By substituting Eq. 5.30 ∼ 5.32 into Eq. 5.33 ∼ 5.35 and after doing some calculus, one obtains

$$m\dot{u} - X_{\dot{u}}\dot{u} - X_{\dot{u}uu}\dot{u}uu = mvr + mr^2x_G + X(\mathrm{d}) \tag{5.36}$$

$$m\dot{v} - Y_{\dot{v}}\dot{v} - Y_{\dot{v}vv}\dot{v}vv - Y_{\dot{r}}\dot{r} - Y_{\dot{r}rr}\dot{r}rr + m\dot{r}x_G = -mur + Y(\mathrm{d}) \tag{5.37}$$

$$-N_{\dot{v}}\dot{v} - N_{\dot{v}vv}\dot{v}vv + m\dot{v}x_G + I_{zz}\dot{r} - N_{\dot{r}}\dot{r} - N_{\dot{r}rr}\dot{r}rr = -murx_G + N(\mathrm{d}) \tag{5.38}$$

The matrix form of Eq.(5.36)~(5.38) is

$$\begin{pmatrix} m - X_{\dot{u}} - X_{\dot{u}uu}uu & 0 & 0 \\ 0 & m - Y_{\dot{v}} - Y_{\dot{v}vv}vv & -Y_{\dot{r}} - Y_{\dot{r}rr}rr + mx_G \\ 0 & -N_{\dot{v}} - N_{\dot{v}vv}vv + mx_G & I_{zz} - N_{\dot{r}} - N_{\dot{r}rr}rr \end{pmatrix} \begin{pmatrix} \dot{u} \\ \dot{v} \\ \dot{r} \end{pmatrix} = \begin{pmatrix} mvr + mr^2x_G + X(\mathrm{d}) \\ -mur + Y(\mathrm{d}) \\ -murx_G + N(\mathrm{d}) \end{pmatrix} \tag{5.39}$$

The solution of *u*, *v* and *r* is based on the Euler's method. The information of subsequent time is transferred from the previous time. The initial values are set to zero, except for *u* due to ship's velocity u_0 before ship's turn. The expressions of the velocities can be written as

$$u_{[i+1]} = u_{[i]} + \Delta u_{[i+1]} + u_0 \tag{5.40}$$

$$v_{[i+1]} = v_{[i]} + \Delta v_{[i+1]} \tag{5.41}$$

$$r_{[i+1]} = r_{[i]} + \Delta r_{[i+1]} \tag{5.42}$$

With

$$\Delta u_{[i+1]} = \dot{u}_{[i+1]}\Delta t \tag{5.43}$$

$$\Delta v_{[i+1]} = \dot{v}_{[i+1]}\Delta t \tag{5.44}$$

$$\Delta r_{[i+1]} = \dot{r}_{[i+1]}\Delta t \tag{5.45}$$

Here Δt stands for the time step and $\dot{u}$, $\dot{v}$ and $\dot{r}$ are obtained from matrix (5.39).

The velocity in earth-fixed coordinate system at *i*–th time step is obtained according to Fig. 5.24. The velocities *u*, *v* and *r* are the velocities in ship-axis.

$$u_{0[i]} = u_{[i]}\cos(\chi_{[i]}) - v_{[i]}\sin(\chi_{[i]}) \tag{5.46}$$

$$v_{0[i]} = u_{[i]}\sin(\chi_{[i]}) + v_{[i]}\cos(\chi_{[i]}) \tag{5.47}$$

The trajectory of the ship can be obtained through the numerical integration of eq. 5.46 ∼ 5.47 about time.

$$x_{0[i+1]} = x_{0[i]} + \Delta t(u_{[i]}\cos(\chi_{[i]}) - v_{[i]}\sin(\chi_{[i]})) \tag{5.48}$$

$$y_{0[i+1]} = y_{0[i]} + \Delta t(u_{[i]}\sin(\chi_{[i]}) + v_{[i]}\cos(\chi_{[i]})) \tag{5.49}$$

Here $\chi_{[i]}$ is the course angle of the ship at *i*–th time step.

$$\chi_i = \chi_{[i-1]} + \frac{1}{2}(r_{[i]} + r_{[i-1]})\Delta t \tag{5.50}$$

The simulating results with these manoeuvring variables are in good agreement with the freely manoeuvring model carried out by Wolff [22] as shown in fig. 5.23. For this example a script, written in python, is attached to this report (file *CircleTest.py*).

Fig. 5.23: Simulation of turning manoeuvre with rudder angle $\delta = -35^\circ$ for the bulker of Series 60. Top: trajectory of the ship. Bottom: time history of parameters

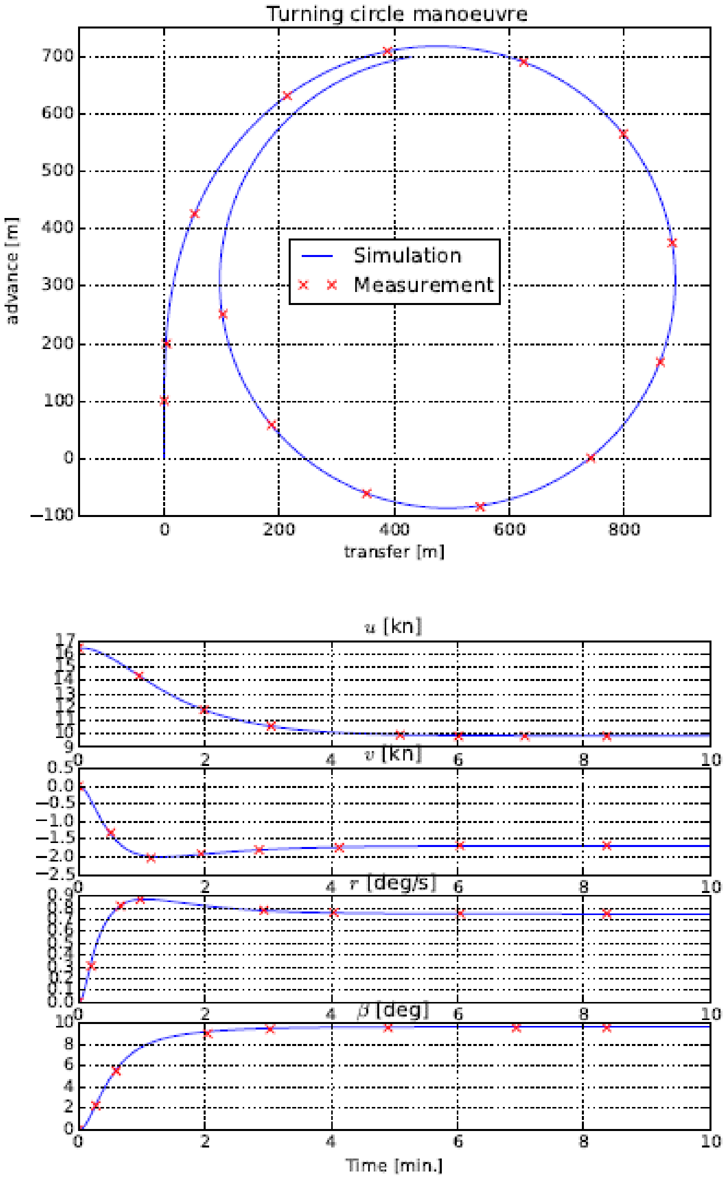

5.2.3 Virtual PMM tests

The hydrodynamic derivatives (simply ’HD’) of vector $\vec{T}$ including *X*, *Y* and *N* are determined through CFD simulation, which consists of static and dynamic tests. In the static tests, the ship is fixed. The results can only provide the terms without accelerations. In order to get the acceleration terms, the dynamic tests (surge, pure sway, pure yaw and combined sway-yaw) are conducted. The ship has a forced harmonic motion. The time history of the forces (*X*, *Y*) and moment (*N*) are analysed by using Fourier series.

5.2.3.1 Description of ship motion

The model set up for planar motion tests is described in Crane [8]. Motions at two points (one located near the bow and the another one near the stern with the same distance to midship) need to be set separately. Furthermore, the phasing of oscillation can be adjusted by the relative motion between these two points. Here a coordinate transformation is used. In terms of a sinusoidal function the body-fixed coordinates (*x*, *y, z*) are moving relative to the earth-fixed ones (x_0, y_0, z_0) as shown in fig. 5.24. The velocities (*u*, *v*, *r*) are the oscillating velocities of the ship, set for the dynamic tests. It is convenient for the RANS-computation that u_0 is set as inlet boundary condition of velocity instead of forward moving ship.

Fig. 5.24: Coordinate systems and motion parameters

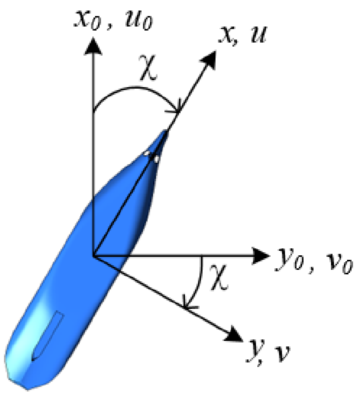

5.2.3.1.1 Pure surge

The ship performs pure longitudinal oscillations along the x-axis. Movements at the other degrees of freedom will not occur.

$$\begin{aligned} u &= \hat{u}\cos(\omega t) \\ v &= 0 \\ r &= 0 \end{aligned} \tag{5.51}$$

Here the symbol ˆ denotes the amplitude of the velocity. Displacements and course angle in ship axis system are calculated by integration of the velocities.

$$\begin{aligned} x &= \hat{x}\sin(\omega t) + \text{constant} \\ y &= \text{constant} \\ \chi &= \text{constant} \end{aligned} \tag{5.52}$$

In the earth-axis system the displacements are

$$\begin{aligned} x_0 &= x\cos(\chi) - y\sin(\chi) \\ y_0 &= x\sin(\chi) + y\cos(\chi) \\ \chi &= \text{constant} \end{aligned} \tag{5.53}$$

5.2.3.1.2 Pure sway

The ship performs pure lateral oscillations along the y-axis. Movements at the other degrees of freedom will not occur. In body-fixed coordinate system the velocities are

$$\begin{aligned} u &= 0 \\ v &= \hat{v}\cos(\omega t) \\ r &= 0 \end{aligned} \tag{5.54}$$

and displacements and course angle are

$$\begin{aligned} x &= \text{constant} \\ y &= \hat{y}\sin(\omega t) + \text{constant} \\ \chi &= \text{constant} \end{aligned} \tag{5.55}$$

In earth-axis system, the displacements and course angle have the same formulation as eq. 5.53.

5.2.3.1.3 Pure yaw

The ship performs pure rotational oscillations about the z-axis. Movements at the other degrees of freedom will not occur. The velocities *u* and *v* are zero.

$$\begin{aligned} u &= 0 \\ v &= 0 \\ r &= \hat{r}\cos(\omega t) \end{aligned} \tag{5.56}$$

By integration of v_0

$$y_0 = \int v_0 dt = \int u_0 \frac{v_0}{u_0} dt \tag{5.57}$$

the displacement y_0 is determined. From fig. 5.24 the relations between *v*, u_0 and v_0 is determined

$$\begin{aligned} u_0 \sin\psi - v_0 \cos(\psi) &= v = 0 \\ \Rightarrow & \frac{v_0}{u_0} = \tan(\chi) \end{aligned} \tag{5.58}$$

By using eq. 5.58, eq. 5.57 becomes

$$y_0 = \int u_0 \tan(\chi) dt \tag{5.59}$$

and the course angle χ is

$$\chi = \hat{\chi}\sin(\omega t) + \text{constant} \tag{5.60}$$

The oscillating velocity *u* is not exactly equal to zero. To full-fill the condition of *u* = 0 in eq. 5.56, two assumptions are made:

- the amplitude of χ is small and
- non-linear terms are negligible.

Then, using the relation from fig. 5.24, the longitudinal velocity of the ship u_s

$$\begin{aligned} u_s &= u_0 \cos\chi + v_0 \sin\chi \\ &= u_0 \end{aligned}$$

which denotes implicitly that the oscillating u can be assumed to be zero.

5.2.3.1.4 Combined sway-yaw

The ship performs a combined lateral and rotational oscillation

$$\begin{aligned} v &= \hat{v}\cos(\omega t) \\ r &= \hat{r}\cos(\omega t) \end{aligned} \tag{5.61}$$

and the set of planar motions is

$$\begin{aligned} u &= 0 \\ v &= \hat{v}\cos(\omega t) \\ r &= \hat{r}\cos(\omega t) \end{aligned} \tag{5.62}$$

From fig. 5.24 also the relation between v, u_0 and v_0 is obtained.

$$u_0 \sin\chi + v\cos\omega t = v_0 \cos\chi \tag{5.63}$$

It follows that

$$y_0 = \int \frac{\hat{v}\cos(\omega t) + u_0 \sin(\chi)}{\cos(\chi)} dt \tag{5.64}$$

with

$$\chi = \hat{\chi}\sin(\omega t) + \text{constant} \tag{5.65}$$

All constants are set to be zero. The constant in χ (see eq. 5.52, 5.55, 5.60 and 5.65) indicates the static drift angle β. A variation test for β has not been carried out.

An overview of the motions considered is presented in Tab. 5.10. The calculation of the integrals can be made numerically by using Runge-Kutta integration scheme.

Table 5.10.: Displacements in the earth-fixed coordinate system

		Surge	Sway	Yaw	Sway + Yaw
PMM motion	u	$\hat{u}\cos(\omega t)$	0	0	0
	v	0	$\hat{v}\cos(\omega t)$	0	$\hat{v}\cos(\omega t)$
	r	0	0	$\hat{r}\cos(\omega t)$	$\hat{r}\cos(\omega t)$
Displacement	x_0	$\hat{x}_0\sin(\omega t)$	0	0	0
	y_0	0	$\hat{y}_0\sin(\omega t)$	$\int u_0 \tan(\chi) dt$	$\int \frac{\hat{v}\cos(\omega t)+u_0\sin(\chi)}{\cos(\chi)} dt$
	χ	0	0	$\hat{\chi}\sin(\omega t)$	$\hat{\chi}\sin(\omega t)$

5.2.3.2 Determination of Hydrodynamic Derivatives

Four dynamic forced tests are performed (surge, pure sway, pure yaw and combined sway-yaw). Following the determination of hydrodynamic derivatives in surge, sway and yaw is described.

In case of sway test, the vector $\vec{T}$ is only a function of *v*-related terms and is described using a third order Taylor-series expansion.

$$\vec{T}(v,\dot{v}) \cong \vec{T_0} + \vec{T_v}v + \vec{T_{vv}}v^2 + \vec{T_{\dot{v}v}}\dot{v}v + \vec{T_{vvv}}v^3 + \vec{T_{\dot{v}vv}}\dot{v}vv \tag{5.66}$$

$$\begin{aligned}\vec{T}(v,\dot{v}) \quad &\cong \quad \vec{T_0} + \vec{T_v}\hat{v}\cos(\omega t) + \vec{T_{\dot{v}}}(-\hat{v}\omega\sin(\omega t)) \\ &+ \quad \vec{T_{vv}}\hat{v}^2\cos^2(\omega t) + \vec{T_{\dot{v}v}}(\hat{v}^2\omega\sin(\omega t)\cos(\omega t)) \\ &+ \quad \vec{T_{vvv}}\hat{v}^3\cos^3(\omega t) + \vec{T_{\dot{v}vv}}(-\hat{v}^3\omega\sin(\omega t)\cos^2(\omega t))\end{aligned} \tag{5.67}$$

Using trigonometric relations (see tab. 5.11)

Table 5.11.: Trigonometric relations

$\sin^2(\omega t) = \frac{1}{2} - \frac{1}{2}\cos(2\omega t)$
$\sin^3(\omega t) = \frac{3}{4}\sin(\omega t) - \frac{1}{4}\sin(3\omega t)$
$\cos^2(\omega t) = \frac{1}{2} + \frac{1}{2}\cos(2\omega t)$
$\cos^3(\omega t) = \frac{3}{4}\cos(\omega t) + \frac{1}{4}\cos(3\omega t)$

eq. 5.67 is transformed to

$$\begin{aligned}\vec{T} \quad &\cong \quad (\vec{T_0} + \frac{1}{2}\vec{T_{vv}}\hat{v}^2) \\ &+ \quad (\vec{T_v}\hat{v}^3 + \frac{3}{4}\vec{T_{vvv}}\hat{v}^3)\cos(\omega t) + (-\vec{T_{\dot{v}}}\hat{v}\omega - \frac{1}{4}\vec{T_{\dot{v}vv}}\omega\hat{v}^3)\sin(\omega t) \\ &+ \quad (\frac{1}{2}\vec{T_{vv}}\hat{v}^2)\cos(2\omega t) + (-\frac{1}{2}\vec{T_{\dot{v}v}}\hat{v}^2\omega\sin(2\omega t)) \\ &+ \quad (\frac{1}{4}\vec{T_{vvv}}\hat{v}^3)\cos(3\omega t) + (-\frac{1}{4}\vec{T_{\dot{v}vv}}\hat{v}^3\omega)\sin(3\omega t)\end{aligned} \tag{5.68}$$

or in matrix notation

$$\begin{pmatrix} 1 & 0 & 0 & \frac{1}{2}\hat{v}^2 & 0 & 0 & 0 \\ 0 & \hat{v} & 0 & 0 & 0 & \frac{3}{4}\hat{v}^3 & 0 \\ 0 & 0 & -\hat{v}\omega & 0 & 0 & 0 & -\frac{1}{4}\omega\hat{v}^3 \\ 0 & 0 & 0 & \frac{1}{2}\hat{v}^2 & 0 & 0 & 0 \\ 0 & 0 & 0 & 0 & -\frac{1}{2}\omega\hat{v}^2 & 0 & 0 \\ 0 & 0 & 0 & 0 & 0 & \frac{1}{4}\hat{v}^3 & 0 \\ 0 & 0 & 0 & 0 & 0 & 0 & -\frac{1}{4}\omega\hat{v}^3 \end{pmatrix} \begin{pmatrix} \vec{T_0} \\ \vec{T_v} \\ \vec{T_{\dot{v}}} \\ \vec{T_{vv}} \\ \vec{T_{\dot{v}v}} \\ \vec{T_{vvv}} \\ \vec{T_{\dot{v}vv}} \end{pmatrix} = \begin{pmatrix} \vec{A_0} \\ \vec{A_1} \\ \vec{B_1} \\ \vec{A_2} \\ \vec{B_2} \\ \vec{A_3} \\ \vec{B_3} \end{pmatrix} \tag{5.69}$$

The coefficients on r.h.s of eq. 5.69 are the Fourier coefficients obtained from the CFD-results for simulation the time history of forces and moment during one period. The unknown variables ($\overrightarrow{T_0}, \overrightarrow{T_v}, \overrightarrow{T_{\dot{v}}}, \overrightarrow{T_{vv}}, \overrightarrow{T_{\dot{v}v}}, \overrightarrow{T_{vvv}}$ and $\overrightarrow{T_{\dot{v}vv0}}$) can be estimated from eq. 5.68 resp. 5.69.

At the pure surge and yaw tests $\vec{T}$ is only a function of *u*- or *r*-related terms. The unknown variables $(\overrightarrow{T_0}, \overrightarrow{T_u}, \overrightarrow{T_{\dot{u}}}, \overrightarrow{T_{uu}}, \overrightarrow{T_{\dot{u}u}}, \overrightarrow{T_{uuu}}$ and $\overrightarrow{T_{\dot{u}uu}})$ or $(\overrightarrow{T_0}, \overrightarrow{T_r}, \overrightarrow{T_{\dot{r}}}, \overrightarrow{T_{rr}}, \overrightarrow{T_{\dot{r}r}}, \overrightarrow{T_{rrr}}$ and $\overrightarrow{T_{\dot{r}rr}})$ at these cases can be estimated similar.

The coupled terms $(\overrightarrow{T_{rv}}, \overrightarrow{T_{rrv}}$ and $\overrightarrow{T_{rvv}})$ are determined from combined sway-yaw test (see Maksoud [1]). Here the third-order Taylor expansion for the force vector $\vec{T}$ is

$$\begin{aligned} \vec{T}(v, r, \dot{v}, \dot{r}) &\cong \vec{T_0} \\ &+ \vec{T_r} r + \vec{T_{\dot{r}}} \dot{r} + \vec{T_{rr}} r^2 + \vec{T_{rrr}} r^3 + \vec{T_{\dot{r}r}} \dot{r} r + \vec{T_{\dot{r}rr}} \dot{r} r r \\ &+ \vec{T_v} v + \vec{T_{\dot{v}}} \dot{v} + \vec{T_{vv}} v^2 + \vec{T_{vvv}} v^3 + \vec{T_{\dot{v}v}} \dot{v} v + \vec{T_{\dot{v}vv}} \dot{v} v v \\ &+ \vec{T_{rv}} r v + \vec{T_{rrv}} r r v + \vec{T_{vvr}} v v r \end{aligned} \tag{5.70}$$

The terms relating to pure sway or pure yaw in eq. 5.70 are known from these tests and is defined as $\overrightarrow{T_k}$. This part of HD remains and will brought to l.h.s of eq. 5.70.

$$\begin{aligned} \vec{T} - \vec{T_k} &\cong \vec{T_0} \\ &+ \vec{T_{rv}} r v + \vec{T_{rrv}} r r v + \vec{T_{vvr}} v v r \end{aligned} \tag{5.71}$$

$$\begin{aligned} \vec{T} - \vec{T_k} &\cong \vec{T_0} \\ &+ \frac{1}{2} \vec{T_{rv}} \hat{r} \hat{v} \\ &+ \frac{3}{4} \vec{T_{rrv}} \hat{r} \hat{r} \hat{v} \cos(\omega t) + \frac{3}{4} \vec{T_{vvr}} \hat{v} \hat{v} \hat{r} \cos(\omega t) \\ &+ \frac{1}{2} \vec{T_{rv}} \hat{r} \hat{v} \cos(2\omega t) \\ &+ \frac{3}{4} \vec{T_{rrv}} \hat{r} \hat{r} \hat{v} \cos(3\omega t) + \frac{1}{4} \vec{T_{vvr}} \hat{v} \hat{v} \hat{r} \cos(3\omega t) \end{aligned} \tag{5.72}$$

$$\begin{pmatrix} 1 & \frac{1}{2}\hat{r}\hat{v} & 0 & 0 \\ 0 & 0 & \frac{3}{4}\hat{r}\hat{r}\hat{v} & \frac{3}{4}\hat{v}\hat{v}\hat{r} \\ 0 & \frac{1}{2}\hat{r}\hat{v} & 0 & 0 \\ 0 & 0 & \frac{1}{4}\hat{r}\hat{r}\hat{v} & \frac{1}{4}\hat{v}\hat{v}\hat{r} \end{pmatrix} \begin{pmatrix} \vec{T_0} \\ \vec{T_{rv}} \\ \vec{T_{rrv}} \\ \vec{T_{vvr}} \end{pmatrix} = \begin{pmatrix} \vec{A_0} \\ \vec{A_1} \\ \vec{A_2} \\ \vec{A_3} \end{pmatrix} \tag{5.73}$$

Here are the A_n the Fourier coefficients of $\vec{T}$ - $\overrightarrow{T_k}$.

The system 5.73 is an under-estimated system for determining $\overrightarrow{T_{rrv}}$ and $\overrightarrow{T_{rvv}}$. To close the system a second amplitude for the velocities of sway $\hat{v}_{(2)}$ or yaw $\hat{r}_{(2)}$ is introduced.

$$\begin{pmatrix} 1 & \frac{1}{2}\hat{r}_{(1)}\hat{v}_{(1)} & 0 & 0 \\ 0 & \frac{1}{2}\hat{r}_{(1)}\hat{v}_{(1)} & 0 & 0 \\ 0 & 0 & \frac{1}{4}\hat{r}_{(1)}\hat{r}_{(1)}\hat{v}_{(1)} & \frac{1}{4}\hat{v}_{(1)}\hat{v}_{(1)}\hat{r}_{(1)} \\ 0 & 0 & \frac{1}{4}\hat{r}_{(2)}\hat{r}_{(2)}\hat{v}_{(2)} & \frac{1}{4}\hat{v}_{(2)}\hat{v}_{(2)}\hat{r}_{(2)} \end{pmatrix} \begin{pmatrix} \vec{T_0} \\ \vec{T_{rv}} \\ \vec{T_{rrv}} \\ \vec{T_{vvr}} \end{pmatrix} = \begin{pmatrix} \vec{A}_{0(1)} \\ \vec{A}_{1(1)} \\ \vec{A}_{3(1)} \\ \vec{A}_{3(2)} \end{pmatrix} \tag{5.74}$$

The solution of entire HD are listed in tab. 5.12, where the Fourier coefficients $\vec{A}_n$ and $\vec{B}_n$ differ from each other according to the different dynamic tests.

The surge-coupled HD like $(\overrightarrow{T_{vu}}, \overrightarrow{T_{vur}}, \overrightarrow{T_{vuu}}, \overrightarrow{T_{vvu}}, \overrightarrow{T_{ru}}, \overrightarrow{T_{rru}}, \overrightarrow{T_{ruu}}, \overrightarrow{T_{\dot{v}u}}, \overrightarrow{T_{\dot{v}vu}}$ and $\overrightarrow{T_{\dot{r}ru}})$ are determined by repeating the tests (surge, sway, yaw, coupled sway and yaw) over several times with various ship speed *U*. The number of reruns depends on the order of *u* in the specific HD; for example, $\overrightarrow{T_{vuu}}$ is the second derivative of $\overrightarrow{T_v}$ on u, the number of reruns is than three in order to build up a 2nd order polynomial.

$$\begin{aligned} \vec{T}_{v/r/vr/vv/rr}(u) &= au^2 + bu + c \\ \vec{T}_{vu/ru/vru/vvu/rru}(u) &= 2au + b \\ \vec{T}_{vuu/ruu}(u) &= 2a \end{aligned} \tag{5.75}$$

Tab. 5.12.: Determination of hydrodynamic derivatives in relation with Fourier coefficients

	Surge	Sway	Yaw		Sway + Yaw
$\vec{T}_0$	$\vec{A}_0 - \vec{A}_2$	$\vec{A}_0 - \vec{A}_2$	$\vec{A}_0 - \vec{A}_2$	$\vec{T}_0$	$\vec{A}_{0(1)} - \vec{A}_{2(1)}$
$\vec{T}_{u/v/r}$	$\frac{\vec{A}_1 - 3\vec{A}_3}{\hat{u}}$	$\frac{\vec{A}_1 - 3\vec{A}_3}{\hat{v}}$	$\frac{\vec{A}_1 - 3\vec{A}_3}{\hat{r}}$	$\vec{T}_{rv}$	$\frac{2\vec{A}_{2(1)}}{\hat{r}_{(1)}\hat{v}_{(1)}}$
$\vec{T}_{uu/vv/rr}$	$\frac{2\vec{A}_2}{\hat{u}^2}$	$\frac{2\vec{A}_2}{\hat{v}^2}$	$\frac{2\vec{A}_2}{\hat{r}^2}$	$\vec{T}_{vvr}$	$\frac{4\vec{A}_{3(1)}\hat{r}_{(2)}\hat{r}_{(2)}\hat{v}_{(2)} - 4\vec{A}_{3(2)}\hat{r}_{(1)}\hat{r}_{(1)}\hat{v}_{(1)}}{\hat{v}_{(1)}\hat{v}_{(1)}\hat{r}_{(1)}\hat{r}_{(2)}\hat{r}_{(2)}\hat{v}_{(2)} - \hat{v}_{(2)}\hat{v}_{(2)}\hat{r}_{(2)}\hat{r}_{(1)}\hat{r}_{(1)}\hat{v}_{(1)}}$
$\vec{T}_{uuu/vvv/rrr}$	$\frac{4\vec{A}_3}{\hat{u}^3}$	$\frac{4\vec{A}_3}{\hat{v}^3}$	$\frac{4\vec{A}_3}{\hat{r}^3}$	$\vec{T}_{rrv}$	$\frac{4\vec{A}_{3(1)}\hat{v}_{(2)}\hat{v}_{(2)}\hat{r}_{(2)} - 4\vec{A}_{3(2)}\hat{v}_{(1)}\hat{v}_{(1)}\hat{r}_{(1)}}{\hat{r}_{(1)}\hat{r}_{(1)}\hat{v}_{(1)}\hat{v}_{(2)}\hat{v}_{(2)}\hat{r}_{(2)} - \hat{r}_{(2)}\hat{r}_{(2)}\hat{v}_{(2)}\hat{v}_{(1)}\hat{v}_{(1)}\hat{r}_{(1)}}$
$\vec{T}_{\dot{u}/\dot{v}/\dot{r}}$	$-\frac{\vec{B}_1 - \vec{B}_3}{\omega\hat{u}}$	$-\frac{\vec{B}_1 - \vec{B}_3}{\omega\hat{v}}$	$-\frac{\vec{B}_1 - \vec{B}_3}{\omega\hat{r}}$		
$\vec{T}_{\dot{u}u/\dot{v}v/\dot{r}r}$	$-\frac{2\vec{B}_2}{\hat{u}^2\omega}$	$-\frac{2\vec{B}_2}{\hat{v}^2\omega}$	$-\frac{2\vec{B}_2}{\hat{r}^2\omega}$		
$\vec{T}_{\dot{u}uu/\dot{v}vv/\dot{r}rr}$	$-\frac{4\vec{B}_3}{\hat{u}^3\omega}$	$-\frac{4\vec{B}_3}{\hat{v}^3\omega}$	$-\frac{4\vec{B}_3}{\hat{r}^3\omega}$		
Number of Simulations	1	1	1		2

5.2.4 RANSE-based simulations

Two set of simulations have been carried out, namely, ship with bow thruster tunnel and gear housing (without TT) and with working bow thruster (with TT). The results will be compared in order to extract the effect of TT. The manoeuvring model of ship without TT will be extended accounting for the influence of TT.

5.2.4.1 Ship geometry

The ship (three tunnels, no working TT) including its propulsion test at design speed is provided by the project partner SINTEF. Jastram embeds the current tunnel position as well as the geometry of TT.

Tab. 5.13.: Main ship specification

Length between perpendiculars	L_{pp}	74.4	[m]
Draught mean	T	5	[m]
Beam-Draught ratio	B/T	3.52	[-]
Vertical Center of Gravity (from keel)	CG_z	5.60	[m]
Longitudinal Center of Gravity (from AP)	CG_x	35.1	[m]
Moment of inertia	I_{zz}	1.66E9	[kgm^2]
Displacement volume	∇	468	[m^3]
Design speed	v_s	14	[knots]

Fig. 5.25: Side view of the ship including hull, one tunnel and the skeg

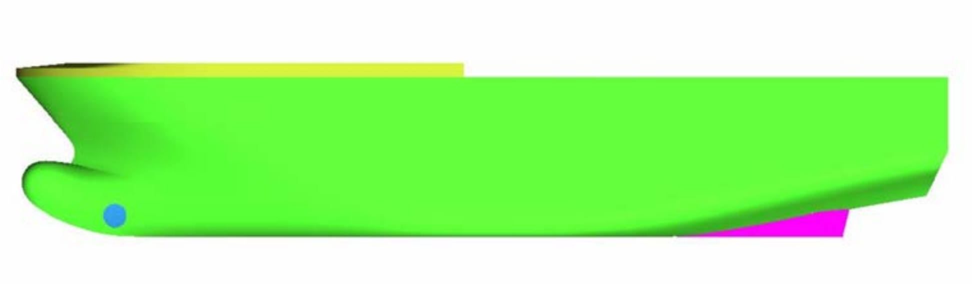

Tab. 5.14.: Specification of tunnel

Number of TT	N	1	[-]
Diameter of thruster	D_p	1.93	[m]
Diameter of tunnel	D_t	1.96	[-]
Longitudinal origin point of Propeller rotating axis (from AP)	CP_x	70.8	[m]
Transverse origin point of Propeller rotating axis (from CL)	CP_y	-0.495	[m]
Vertical origin point of Propeller rotating axis (from keel)	CP_z	1.92	[m]
Tunnel length (averaged)	TL	2.747	[m]
Propeller rpm	n_p	317.5	[rev/min]

Fig. 5.26: Detailed view in the tunnel. Left: ship with bow thruster tunnel and gear housing, right: ship with working bow thruster

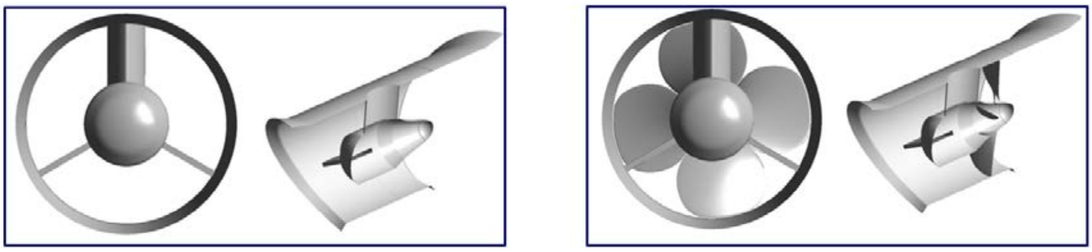

5.2.4.2 Numerical setups

Structured grids are applied and generated with ICEM CFD. The domains are separated into bare hull (including the far field), tunnel and propeller domain. They are treated separately. The information are exchanged through the interface defined between each domain. Near-wall grid resolution depends on y^+ value, which should be smaller than 1. The grids are generated based on the conditions of ship at design speed (14 kn). Fig. 5.27 left shows the y^+ values. The areas with high curvature lead to y^+ values above 1 (max. 5). However, it is sufficient for the operating condition of TT to operate below the design speed. Slip wall conditions are used for the free surface, bottom, port- and starboard sidewalls as seen in fig. 5.27 right. The size of the far field should big enough in order to get unaffected by the initial conditions applied for the port- and starboard sidewalls, which can lead to difficulties to reach numerical convergence.

Fig. 5.27: y^+ value on the hull (left) and domain boundary conditions (right)

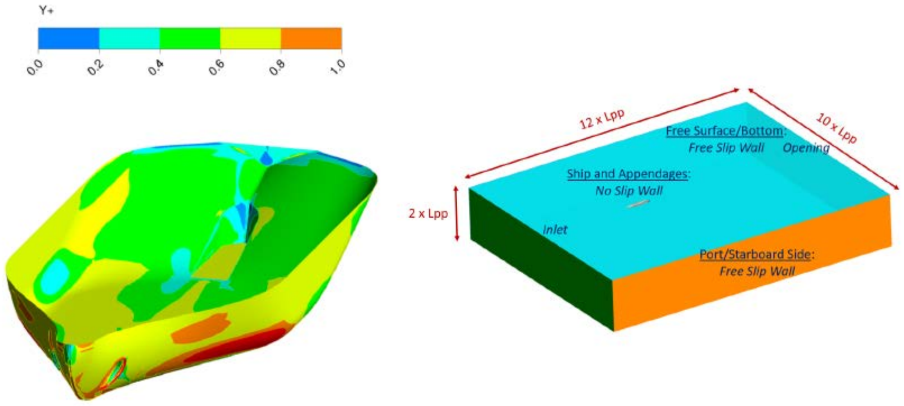

Three sizes of mesh are generated with the same near-wall grid resolution (same y^+) for the full-scale ship. Concerning the flow separation, the refinement mainly focuses on the hull in the longitudinal direction as seen in fig. 5.28. The calculations for the grid validation were carried out without TT. However, the other components such as gear housing in the tunnel and skeg in the hull domain are all included.

The mesh sensitivity study is shown in fig. 5.28. *X*-axis denotes the number of cells and *y*-axis shows the dimensionless value of resistance divided by the resistance from the finest mesh. The slop of the curve is going to be zero while increasing the nodes number. In comparsion with the finest mesh, the coarse mesh has only 1.6 % deviation and thus it is applied for the further simulations. The number of nodes including the propeller domain is totally 6 Mio.

Fig. 5.28: Grid study at ship design speed without tunnel thruster

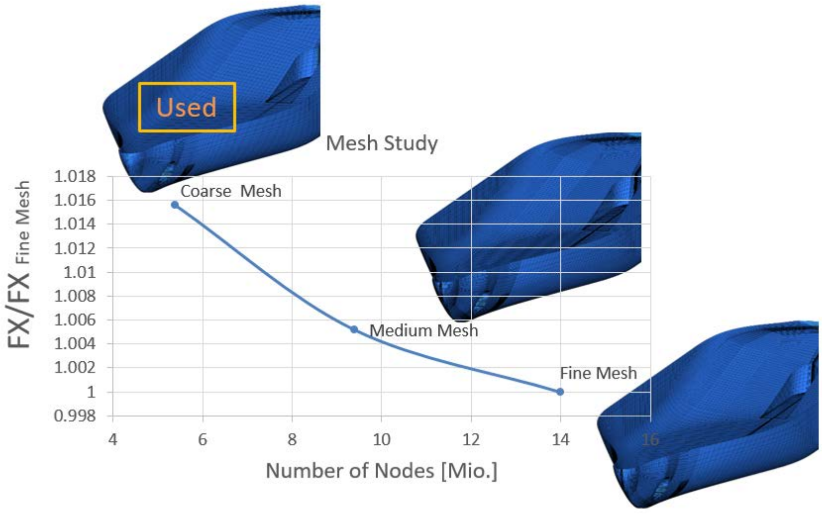

The CFD-result from propulsion test show, that the propulsor need a thrust of T = 215 kN to keep the ship moving with design speed. The resistance of the ship can be roughly estimated by using the thrust deduction factor t = 0.106 taken from the experimental results.

$$\begin{aligned} R_I &= T \cdot (1-t) \\ &= 215\text{kN} \cdot (1-0.106) \qquad (5.76) \\ &= 192.21\text{kN} \end{aligned}$$

The ship has dual-end podded unit with co-rotating propellers and three bow TT. The resistance of each shaft of podded unit has been assumed 8kN and each tunnel possesses 8% of the total thrust. Current ship has only one tunnel and zero podded-unit. By subtracting the resistance mentioned, we yield:

$$\begin{aligned} R_{II} &= R_I - 2 \cdot 8\text{kN} - 0.08 \cdot 2 \cdot T \\ &= 192.21\text{kN} - 16\text{kN} - 34.4\text{kN} \\ &= 142\text{kN} \end{aligned} \tag{5.77}$$

The wind resistance at ship's design speed is assumed 5kN.

$$\begin{aligned} R_{III} &= R_{II} - 5\text{kN} \\ &= 142\text{kN} - 5\text{kN} \\ &= 137\text{kN} \end{aligned} \tag{5.78}$$

The hydrodynamic resistance of the ship predicted at design speed is about 137 kN. Some values can be over- or underestimated. Overall, a reasonable result can be obtained by this set of mesh.

Tab. 5.15.: Hydrodynamic resistance of different mesh resolutions

Mesh	Total Number of Nodes [milo.]	FX Total [kN]
Coarse	5.5	136.7
Medium	9.4	135.3
Fine	14.0	134.6

The reason to merge sub-domains of hull (subdomain I) and far fields (subdomain II and subdomain III) as one domain (see fig. 5.29) is, that on one hand no information is getting lost because of the 1:1 interfaces between the sub-domains and on the other hand the mesh deformation at each subdomain can be treated separately. For example, during the simulation of pure yaw, subdomain I rotated over some of angles from left to right in fig. 5.29. It is required, that no mesh deformation occurred inside the subdomain I. However, the deformation in terms of rotation was contributed by the subdomain II through a user-defined function while subdomain III contributes only the translation. The individual deformation of cell depends on its stiffness; small size cells have bigger stiffness than large size. Therefore, the mesh density in the sub-domains should have the sequence I > II > III, so that the domains far from the ship can provide more space than near the hull.

Fig. 5.29: Mesh deformation during the yaw motion

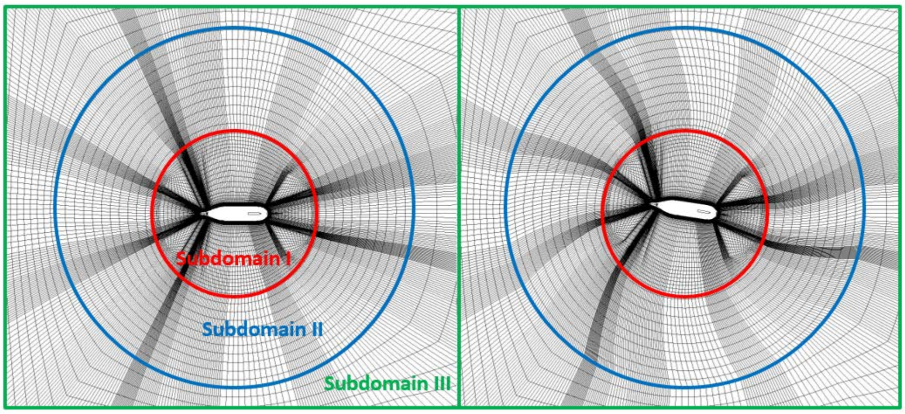

The explicit mesh motion relative to a fixed coordinate system has to be determined in the setup. Ship motion are pure translation (surge, sway) or combined motion of rotation and translation (yaw, coupled sway-yaw), whereas for the TT, the mesh displacement of rotating propeller around the shaft axis inside the tunnel has to be considered additionally. The simulations are modelled by Rigid Body Motion (RBM) approach. The force on the solid body are transformed interactively from the fluid by resolving fluid equations in Arbitrary-Lagrangian-Eulerian (ALE) form during the mesh motion. The initial solution is obtained by Multiple Frame of Reference (MFR) approach. Thus, at the beginning of the simulation a small time scale is required. The calculation can be terminated if periodicity is found. As mentioned, for the determination of u-related coupled derivatives like $\overrightarrow{T_{vuu}}$, three ship speeds are necessary. In the presence of the TT, time scales are selected by the propeller revolution number n_p; the phase step is set to 10°. For ship without TT, time scales are varied in order to reach the same time steps. The sensitivity study of the time scale as well as the non-dimensional motion parameters such as ω', v', r' and u' in tab. 5.10 has not been considered in the project. It should be noticed, that the selection of ω' is related to memory effects. The smallest value of ITTC [15] recommendation is $\omega' = 0.25$ and highest value is $\omega' = 4$. The high-order HD can be determined from the high amplitude of u', v' and r', but the displacement calculated from tab. 5.10 is limited by small amplitude $\hat{\chi}$ at selected ω'. The motion parameters are referred to ITTC [15] and shown in tab. 5.16. The numerical settings are listed in tab. 5.17, where n_p is the propeller revolution number, even there is no rotating bow thruster in case of "Without TT".

Tab. 5.16.: Motion parameter set for the dynamic tests

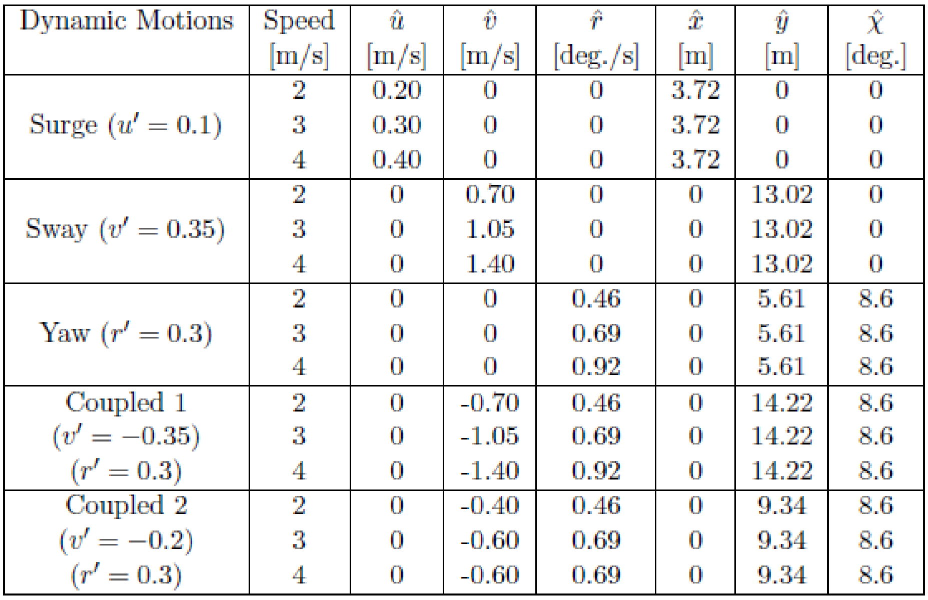

Dynamic Motions	Speed [m/s]	$\hat{u}$ [m/s]	$\hat{v}$ [m/s]	$\hat{r}$ [deg./s]	$\hat{x}$ [m]	$\hat{y}$ [m]	$\hat{\chi}$ [deg.]
Surge ($u' = 0.1$)	2	0.20	0	0	3.72	0	0
	3	0.30	0	0	3.72	0	0
	4	0.40	0	0	3.72	0	0
Sway ($v' = 0.35$)	2	0	0.70	0	0	13.02	0
	3	0	1.05	0	0	13.02	0
	4	0	1.40	0	0	13.02	0
Yaw ($r' = 0.3$)	2	0	0	0.46	0	5.61	8.6
	3	0	0	0.69	0	5.61	8.6
	4	0	0	0.92	0	5.61	8.6
Coupled 1 ($v' = -0.35$) ($r' = 0.3$)	2	0	-0.70	0.46	0	14.22	8.6
	3	0	-1.05	0.69	0	14.22	8.6
	4	0	-1.40	0.92	0	14.22	8.6
Coupled 2 ($v' = -0.2$) ($r' = 0.3$)	2	0	-0.40	0.46	0	9.34	8.6
	3	0	-0.60	0.69	0	9.34	8.6
	4	0	-0.60	0.69	0	9.34	8.6

Tab. 5.17.: Simulation setups

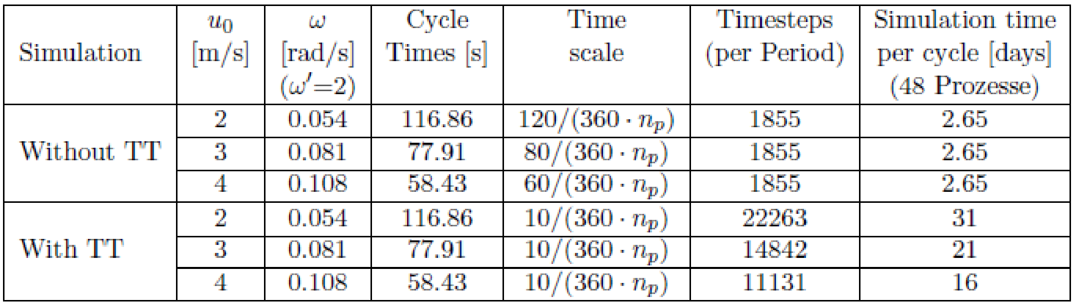

Simulation	u_0 [m/s]	ω [rad/s] (ω'=2)	Cycle Times [s]	Time scale	Timesteps (per Period)	Simulation time per cycle [days] (48 Prozesse)
Without TT	2	0.054	116.86	$120/(360 \cdot n_p)$	1855	2.65
	3	0.081	77.91	$80/(360 \cdot n_p)$	1855	2.65
	4	0.108	58.43	$60/(360 \cdot n_p)$	1855	2.65
With TT	2	0.054	116.86	$10/(360 \cdot n_p)$	22263	31
	3	0.081	77.91	$10/(360 \cdot n_p)$	14842	21
	4	0.108	58.43	$10/(360 \cdot n_p)$	11131	16

5.2.4.3 Manoeuvring tests for ship without working TT

The pre-defined path of ship are sinusoidal oscillations for surge and sway (fig. 5.30 and 5.31 left). As mentioned before, the ship has asymmetric appendages inside the tunnel, which can cause asymmetric flow, so that the non-dimensional values of *Y* and *N* differ from zero in the surge test.

Fig. 5.30: Longitudinal oscillation (left) and non-dimensional forces and moment (right) during one period of surge test

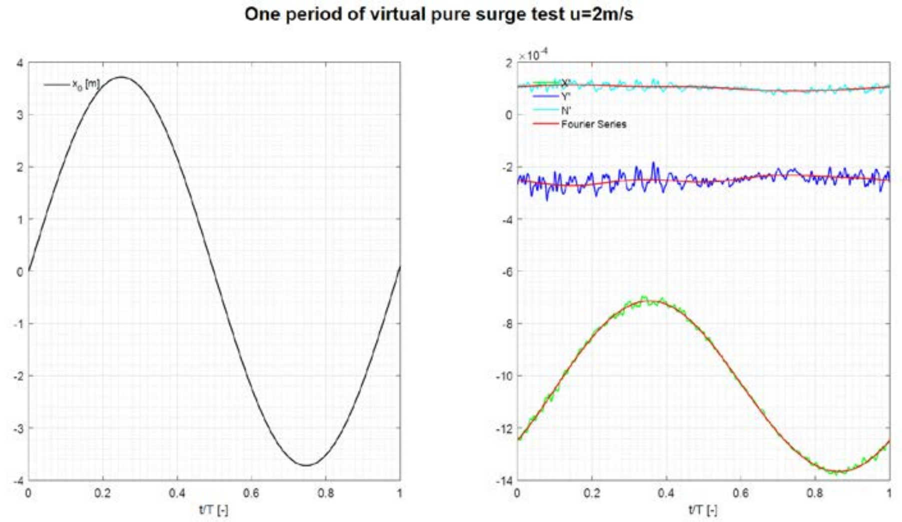

Fig. 5.31: Time history of translation (left) and non-dimensional forces and moment (right) during one period of pure sway test

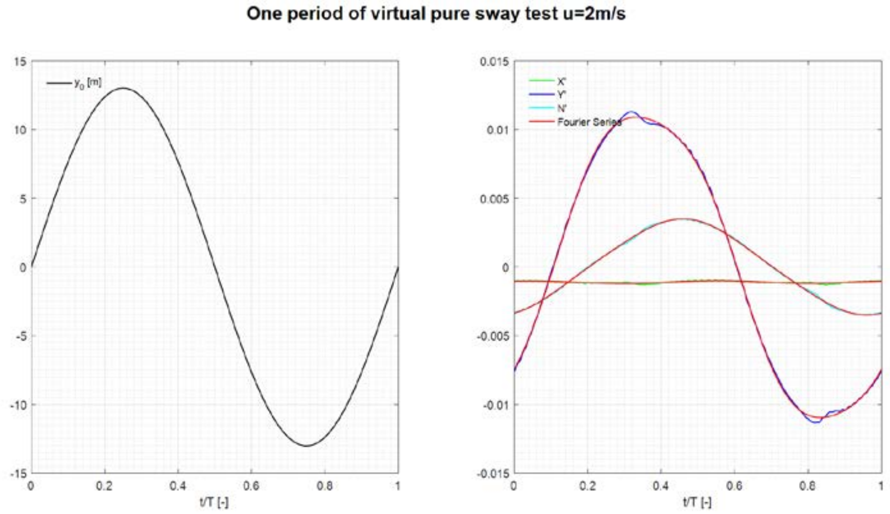

In case of yaw oscillation, the phase shift calculated by eq. 5.57 between yaw angle and sway translation is 90° as shown in fig. 5.32.

Fig. 5.32: Time history of yaw angle and translation (left) and non-dimensional forces and moment (right) during one period of pure yaw test

One period of virtual pure yaw test u=2m/s

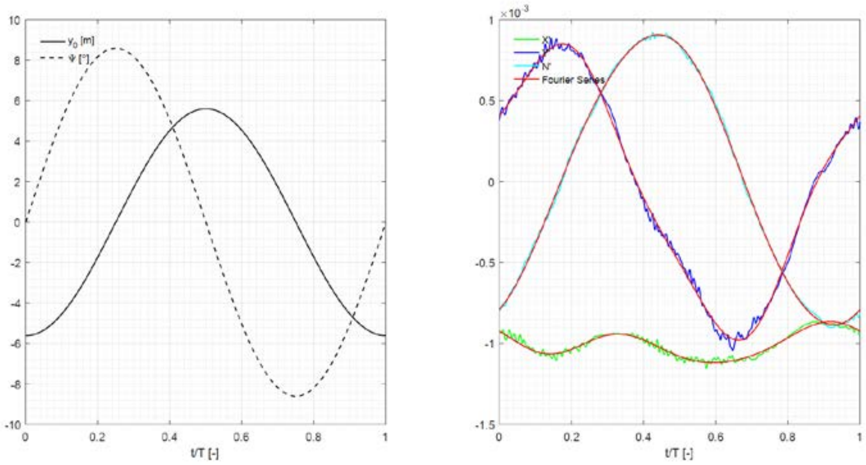

For the both combined sway-yaw tests, we keep the value of $\hat{r}$ and change the value of $\hat{v}$, so the time history of yaw angle are the same whereas the translation solved by eq. 5.64 is different as shown in fig. 5.33.

Fig. 5.33: Time history of yaw angle and translation (left) and non-dimensional forces and moment (right) during one period of combined sway-yaw test

One period of 1st combined virtual sway-yaw test u=2m/s

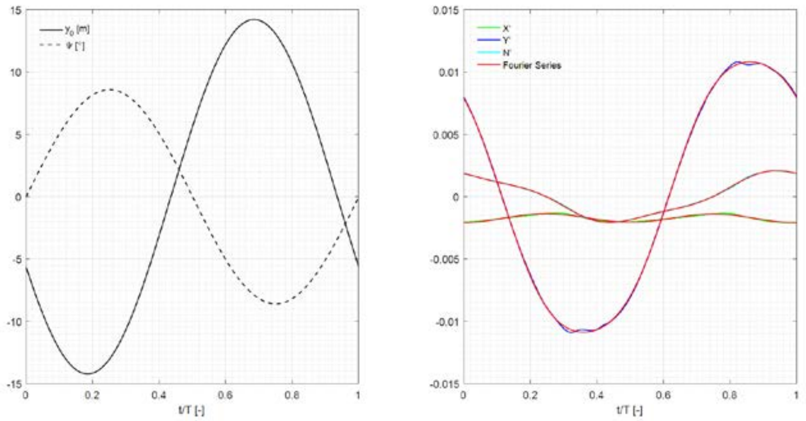

One period of 2nd combined virtual sway and yaw test u=2m/s

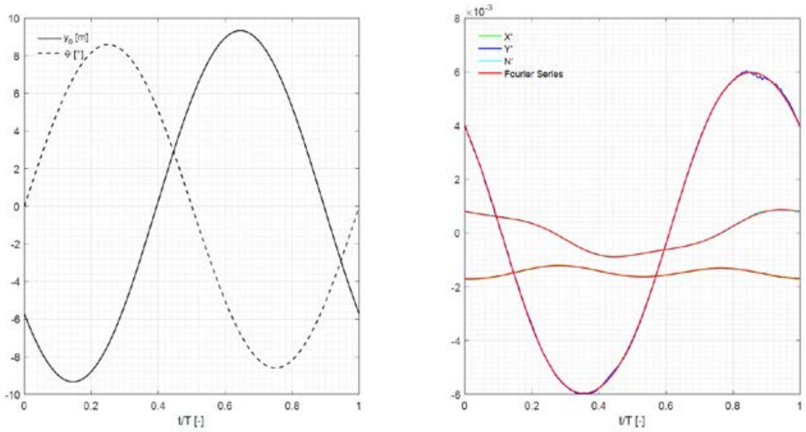

It is unnecessary to evaluate the Fourier coefficients directly from these curves, because according to eq. 5.71, we need first know the curve of difference in terms of $\vec{T}$ - $\overrightarrow{T_k}$ (fig. 5.34). The HD can be estimated by eq. 5.74.

Fig. 5.34: Time history of differences of forces and moment for the first combined sway- yaw test (left) and second one (right) during one period

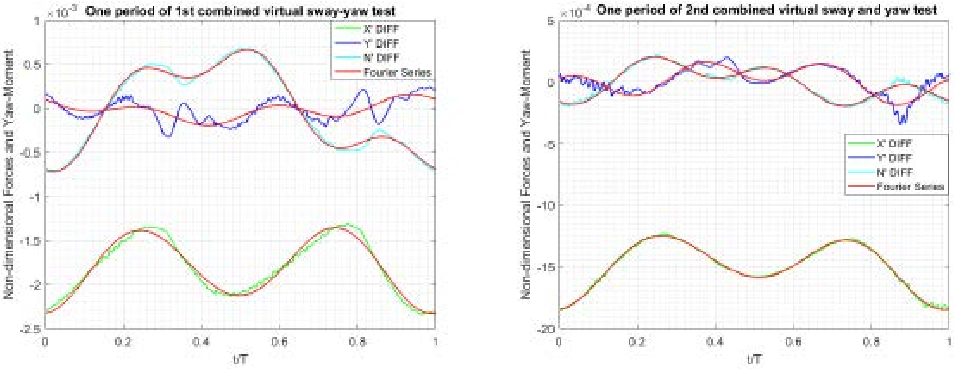

The time history of non-dimensional hydrodynamic forces X', Y' and moment N' at three velocities for different oscillating tests are shown in fig. 5.35. It seems that X' is more sensitive to ship speed than Y' and N'. It can be explained by Reynold's number effects that X' grows with decreasing ship speed. The fluctuation of Y' and N' in surge test seems to be very strong, but the range of the fluctuation is still small in comparison with the values from Y' and N' in sway test. The small HD has small influence on the ship manoeuvre.

Two statements can be obtained from these results.

- The velocity u = 2 m/s is close to the operating condition of TT. This condition is relevant for further investigation.
- Cross-coupled terms with u such as $\overrightarrow{T_{vu}}, \overrightarrow{T_{vru}}, \overrightarrow{T_{vvu}}$, $\overrightarrow{T_{ru}}$, $\overrightarrow{T_{rru}}$ and $\overrightarrow{T_{ruu}}$ have been ignored because of small deviations between the curves.

Fig. 5.35: Comparison of non-dimensional forces and moment for three velocities (2, 3, and 4 m/s) in the five forced dynamic motions without working tunnel thruster (from top to bottom: surge, sway, yaw, 1st and 2nd combined sway- yaw test)

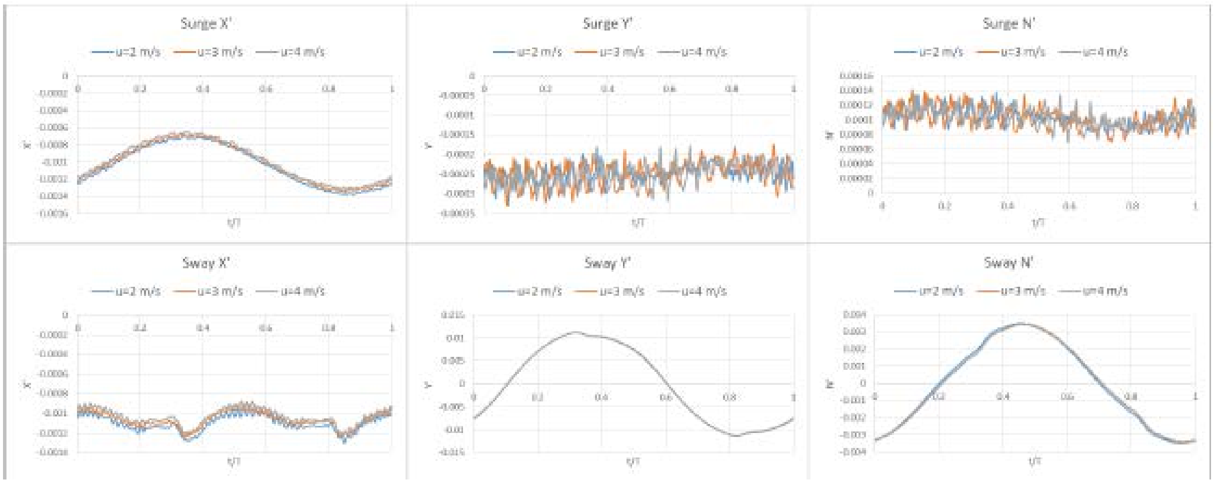

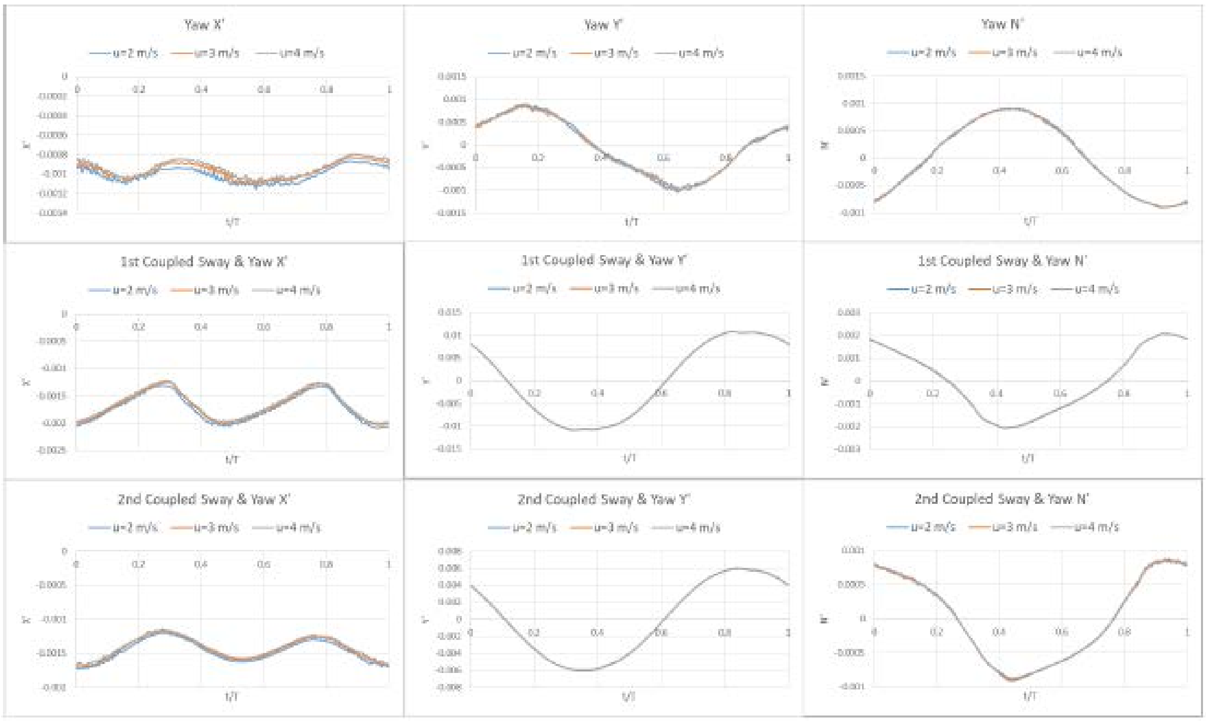

Fig. 5.36: Comparison of time history of forces *X*, *Y* and moment *N* during one period of pure sway test between original (blue), regression (red) and reduction (green) curve

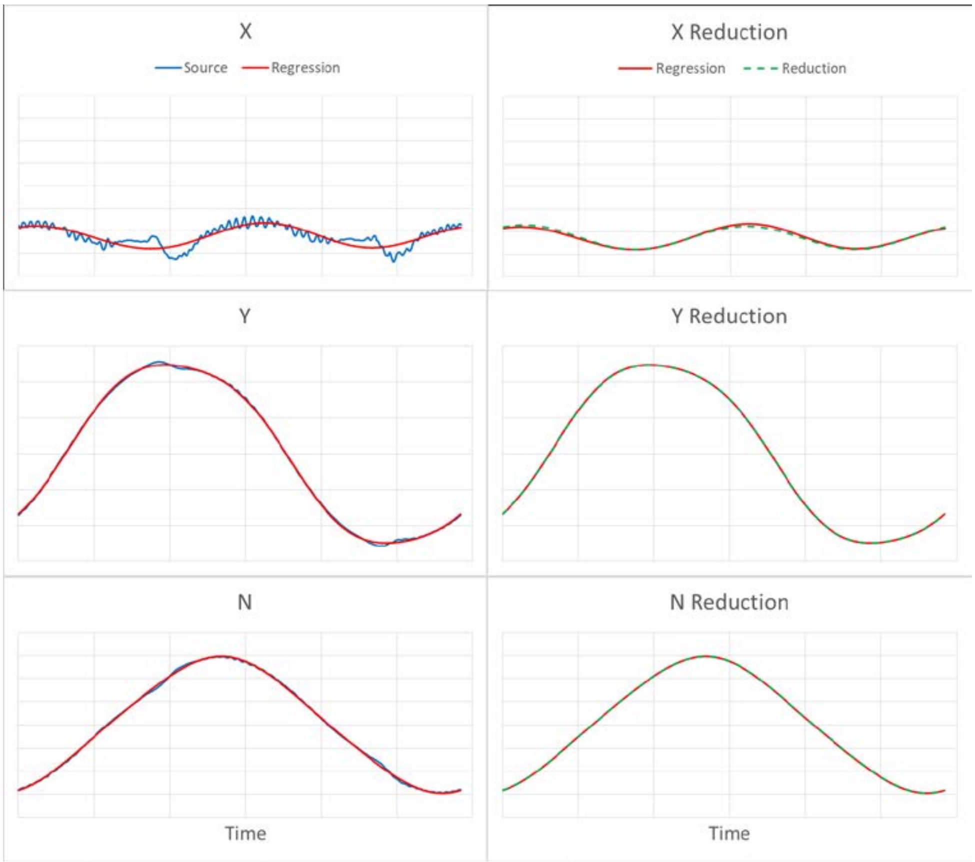

A model reduction is needed to establish the mathematical model for the ship without TT. For example, we examine the pure sway test. There are three coloured curves in fig. 5.36. The blue curves are the results from the basic data calculated from the CFD simulation. The red curves are the regression curves obtained from the HD in eq. 5.66. The “Reduction” curves are established by neglecting all non-significant terms in HD in eq. 5.66. Only terms remain in eq. 5.66 which contribute significantly to $\vec{T}$. Further reductions are in appendix I.

In Tab. 5.18 the significant components of the HD are coloured green. The corresponding modelling for ship without TT is presented in eq. 5.79 ∼ 5.81. The entire non-dimensional HD set is given in tab. 5.19.

Tab. 5.18.: Hydrodynamic derivatives for the ship without TT (significant terms are coloured green)

u			v			r			rv		
X_u	Y_u	N_u	X_v	Y_v	N_v	X_r	Y_r	N_r	X_{rv}	Y_{rv}	N_{rv}
X_{uu}	Y_{uu}	N_{uu}	X_{vv}	Y_{vv}	N_{vv}	X_{rr}	Y_{rr}	N_{rr}	X_{rrv}	Y_{rrv}	N_{rrv}
X_{uuu}	Y_{uuu}	N_{uuu}	X_{vvv}	Y_{vvv}	N_{vvv}	X_{rrr}	Y_{rrr}	N_{rrr}	X_{vvr}	Y_{vvr}	N_{vvr}
$X_{\dot{u}}$	$Y_{\dot{u}}$	$N_{\dot{u}}$	$X_{\dot{v}}$	$Y_{\dot{v}}$	$N_{\dot{v}}$	$X_{\dot{r}}$	$Y_{\dot{r}}$	$N_{\dot{r}}$			
$X_{\dot{u}u}$	$Y_{\dot{u}u}$	$N_{\dot{u}u}$	$X_{\dot{v}v}$	$Y_{\dot{v}v}$	$N_{\dot{v}v}$	$X_{\dot{r}r}$	$Y_{\dot{r}r}$	$N_{\dot{r}r}$			
$X_{\dot{u}uu}$	$Y_{\dot{u}uu}$	$N_{\dot{u}uu}$	$X_{\dot{v}vv}$	$Y_{\dot{v}vv}$	$N_{\dot{v}vv}$	$X_{\dot{r}rr}$	$Y_{\dot{r}rr}$	$N_{\dot{r}rr}$			

$$\begin{aligned} X &\cong X_0 \\ &+ X_u \Delta u + X_{uuu} \Delta u^3 + X_{\dot{u}} \dot{u} \\ &+ X_{vv} v^2 \\ &+ X_{rrr} r^3 \\ &+ X_{rv} rv \end{aligned} \tag{5.79}$$

$$\begin{aligned} Y &\cong Y_0 \\ &+ Y_v v + Y_{vvv} v^3 + Y_{\dot{v}} \dot{v} + Y_{\dot{v}vv} \dot{v} v^2 \\ &+ Y_r r + Y_{rrr} r^3 + Y_{\dot{r}} \dot{r} + Y_{\dot{r}rr} \dot{r} r^2 \\ &+ Y_{rrv} r^2 v + Y_{vvr} v^2 r \end{aligned} \tag{5.80}$$

$$\begin{aligned} N &\cong N_0 \\ &+ N_v v + N_{vvv} v^3 + N_{\dot{v}} \dot{v} + N_{\dot{v}vv} \dot{v} v^2 \\ &+ N_r r + N_{rrr} r^3 + N_{\dot{r}} \dot{r} + N_{\dot{r}rr} \dot{r} r^2 \\ &+ N_{rrv} r^2 + N_{vvr} v^2 r \end{aligned} \tag{5.81}$$

In eq. 5.79 the longitudinal force *X* is an odd function of yaw velocity. The reason is due to the asymmetric gear housing located in the tunnel, which causes different pressure distribution on the tunnel wall between the negative and positive yaw velocity. The flow transferring around ship bottom in the pure sway test causes the low pressure on the area of bilge radius. The low pressure is independent on whether the transverse velocity is positive or negative. Thus *X* is an even function of *v*. The forces and moment distribution is in Appendix J.

Tab. 5.19.: Manoeuvring derivatives multiplied by 1e5 for bare hull at U = 2 m/s

X_0	-137.175	Y_0	-4.162	N_0	0.45
X_u	-197.804	Y_u	-17.605	N_u	5.052
X_{uu}	-84.989	Y_{uu}	-97.501	N_{uu}	53.295
X_{uuu}	-2134.645	Y_{uuu}	2087.980	N_{uuu}	-455.318
$X_{\dot{u}}$	-127.948	$Y_{\dot{u}}$	6.584	$N_{\dot{u}}$	-5.085
$X_{\dot{u}u}$	-14.186	$Y_{\dot{u}u}$	54.864	$N_{\dot{u}u}$	-17.803
$X_{\dot{u}uu}$	-344.769	$Y_{\dot{u}uu}$	25.859	$N_{\dot{u}uu}$	-3.596
X_v	-6.585	Y_v	-1578.367	N_v	-845.845
X_{vv}	124.150	Y_{vv}	-15.289	N_{vv}	-0.055
X_{vvv}	43.355	Y_{vvv}	-4401.338	N_{vvv}	-924.524
$X_{\dot{v}}$	-0.324	$Y_{\dot{v}}$	-1378.843	$N_{\dot{v}}$	-126.357
$X_{\dot{v}v}$	-43.943	$Y_{\dot{v}v}$	-7.762	$N_{\dot{v}v}$	-0.677
$X_{\dot{v}vv}$	26.093	$Y_{\dot{v}vv}$	2273.011	$N_{\dot{v}vv}$	-256.437
X_r	-0.712	Y_r	244.689	N_r	-256.791
X_{rr}	15.592	Y_{rr}	-24.812	N_{rr}	20.249
X_{rrr}	244.095	Y_{rrr}	-1029.989	N_{rrr}	-170.673
$X_{\dot{r}}$	-2.407	$Y_{\dot{r}}$	-119.206	$N_{\dot{r}}$	-67.764
$X_{\dot{r}r}$	93.476	$Y_{\dot{r}r}$	40.242	$N_{\dot{r}r}$	-18.935
$X_{\dot{r}rr}$	46.650	$Y_{\dot{r}rr}$	324.497	$N_{\dot{r}rr}$	50.973
X_{rv}	811.918	Y_rv	-42.946	N_{rv}	13.959
X_{rrv}	363.425	Y_{rrv}	-4512.177	N_{rrv}	301.680
X_{vvr}	86.761	Y_{vvr}	-3739.200	N_{vvr}	-1269.099

5.2.4.4 Manoeuvring Tests for Ship with Working TT

The time history of forces and moment during one period at 2 m/s is shown in fig. 5.37 and 5.38. The fluctuation is clearly to seen which represents the blade frequency. The red curve from Fourier series covers the tendency of them. In case of sway test, a local minimum occurs on Y' at about 1/3 period. The reason can be supposed, that after ship reaching the maximal displacement and moving to the starboard side, the fluid, surrounding the hull, need some time to response and change its direction. Consequently, the slipstream will be attaching on the portside of the hull. This low-pressure area may reduce the transverse force. This takes place only temporally, because the transverse velocity of the ship increases while moving to starboard. Then the slipstream will be pushed to the bottom of the ship. Inversely, there is no effect of the slipstream on the hull, if the ship moves to starboard after reaching minimal y_0.

Three temporary points have been selected (see fig. 5.39 right) during one period of pure yaw. The position of transverse displacement and yaw angle are also indicated in fig. 5.39 left. The fig. 5.40 shows the pressure distribution on the x − y plane from point 1 to 3. Point 1 has the highest Y' value. On contrary, point 3 has the lowest one within these three points. The reason is due to the pressure distribution on the portside, which directly depends on the quantity of the slipstream in contact with the hull. The arrows denote the tendency of the motion. At point 1, yaw motion attempts to position the hull approaching the slipstream, however, the ship is moving away to starboard, and as a result, the slipstream attached partly. At point 2, the ship has zero yaw angle while reaching the maximal y_0, the translation tries to reduce the effect of the slipstream, but the yaw motion benefits the attached area. During the change of yaw angle from point 2 to 3, the area of low pressure grows to the maximal value, as consequence, at point 3, the transverse force is minimal.

Fig. 5.37: Time history of displacement (left) and forces and moment (right) during one period of surge, sway and yaw from top to bottom

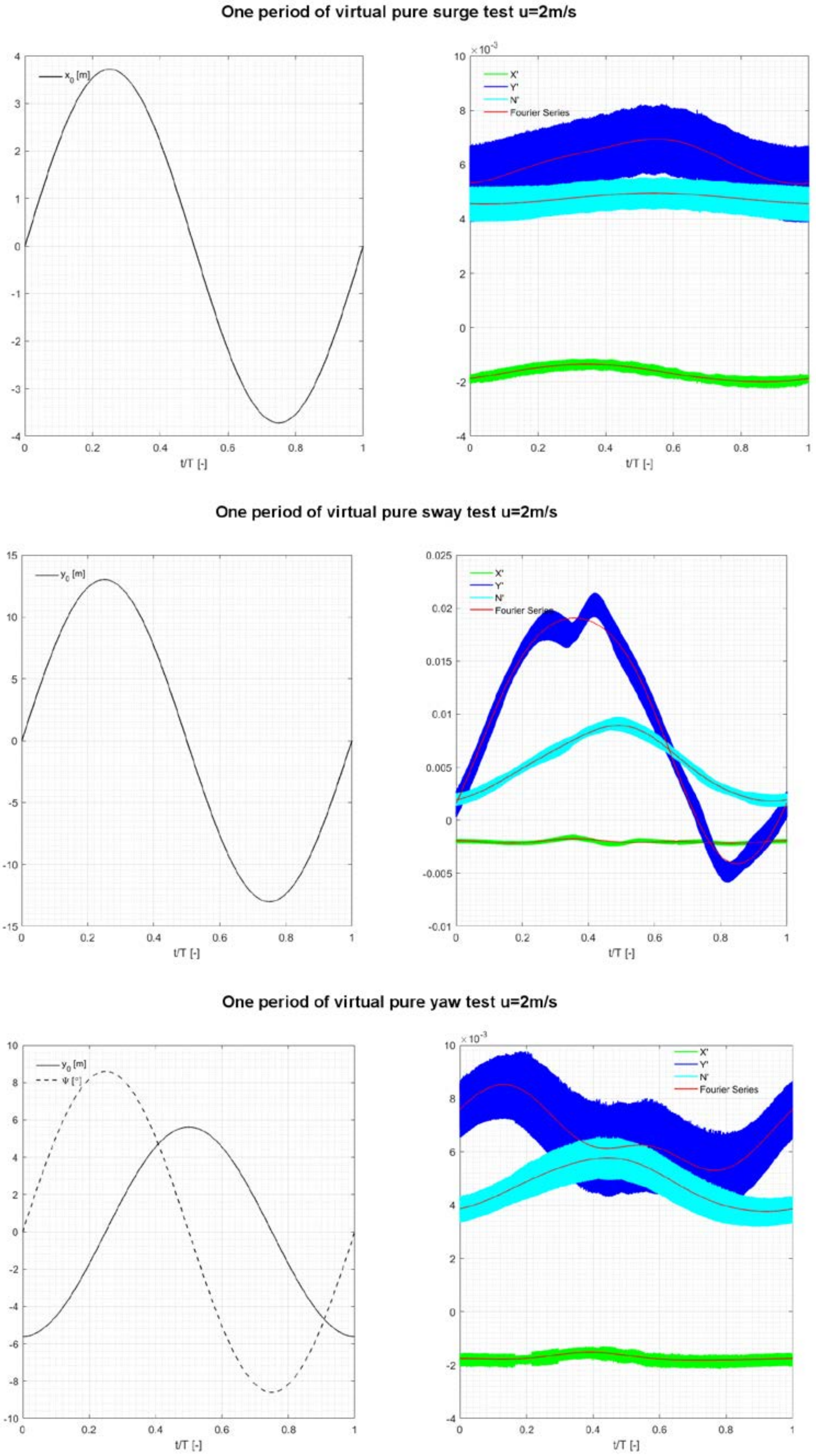

Fig. 5.38: Time history of displacement (left) and forces and moment (right) during one period of first and second combined sway-yaw tests from top to bottom

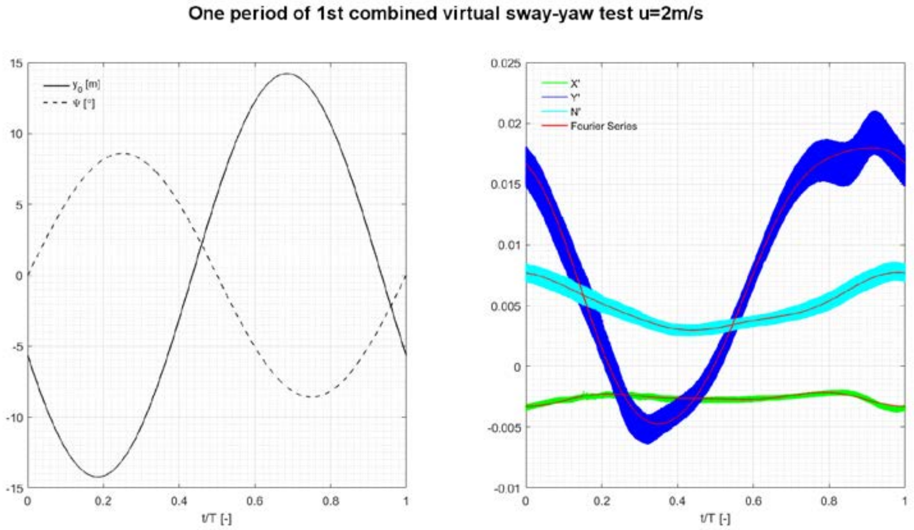
One period of 1st combined virtual sway-yaw test u=2m/s

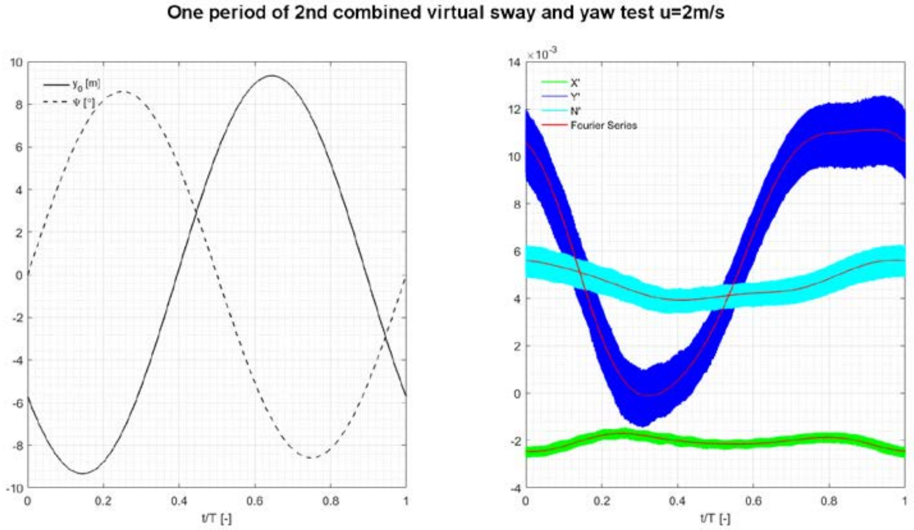
One period of 2nd combined virtual sway and yaw test u=2m/s

Fig. 5.39: Points of consideration during one period of pure yaw

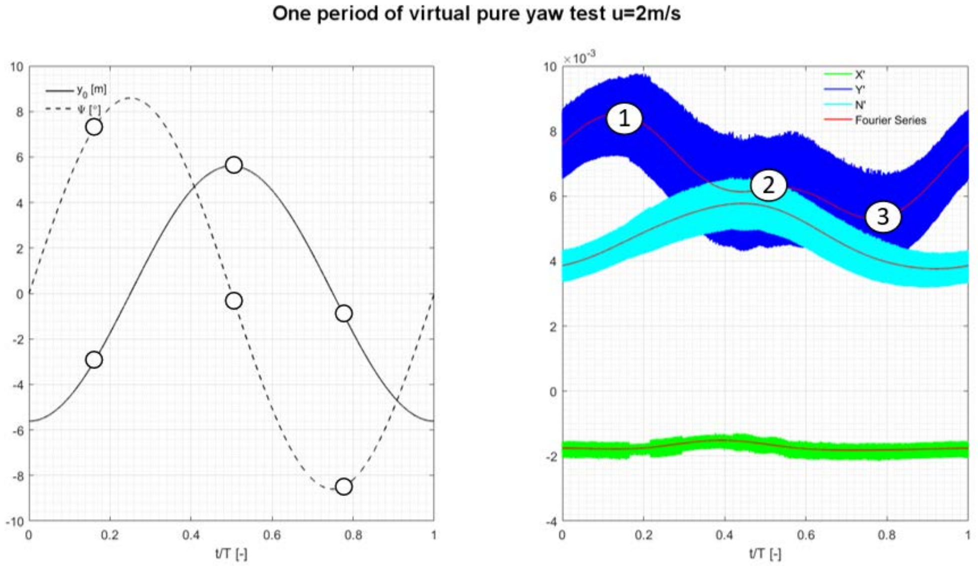
One period of virtual pure yaw test u=2m/s

Fig. 5.40: Distribution of c_p at the points of time relating to fig. 5.39 right on the sectional plane located in the height of propeller rotating axis. Pressure increases from blue (low-pressure) to red (high-pressure)

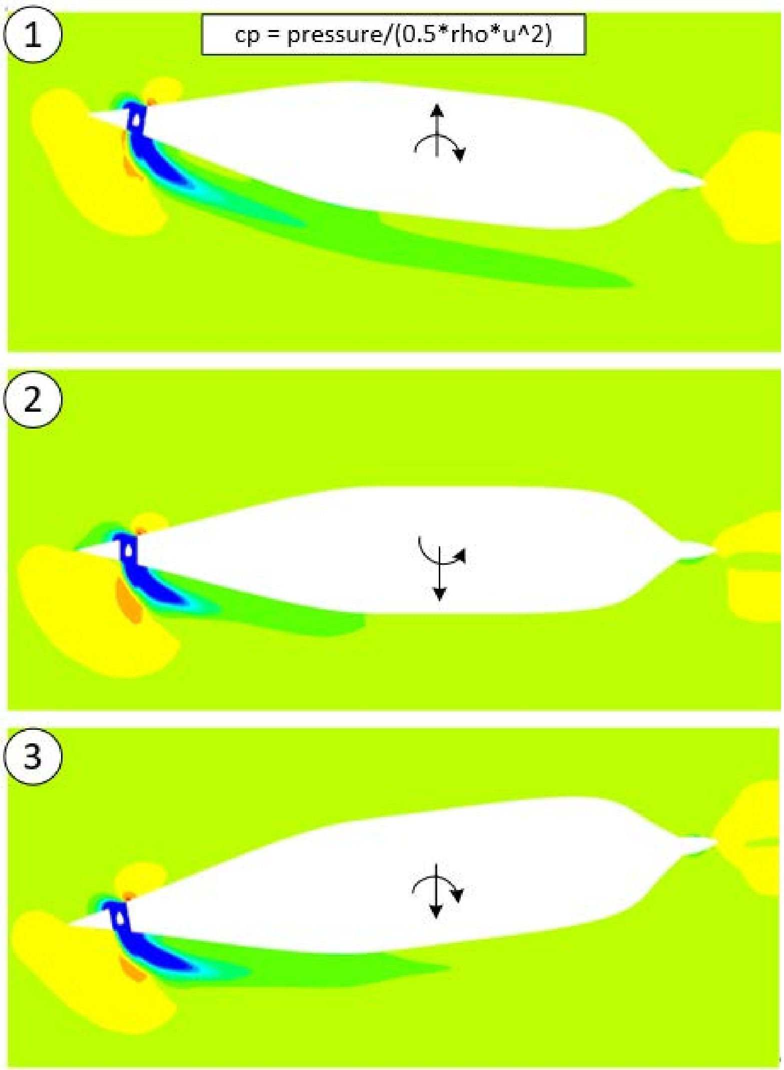

Fig. 5.41: Points of consideration during one period of pure sway

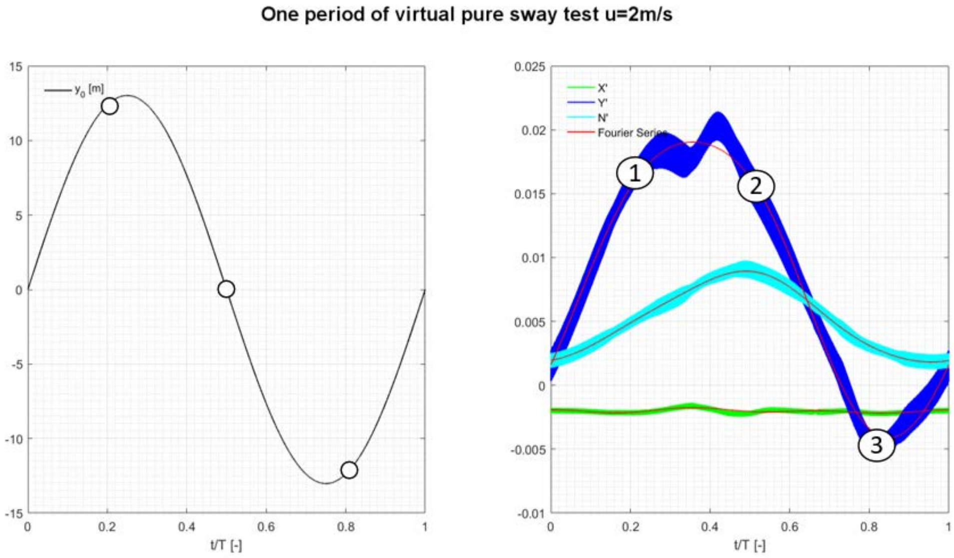

Fig. 5.42: Distribution of c_p at the points of time relating to fig. 5.41 right on the sectional plane located in the height of propeller rotating axis. Pressure increases from blue (low-pressure) to red (high-pressure)

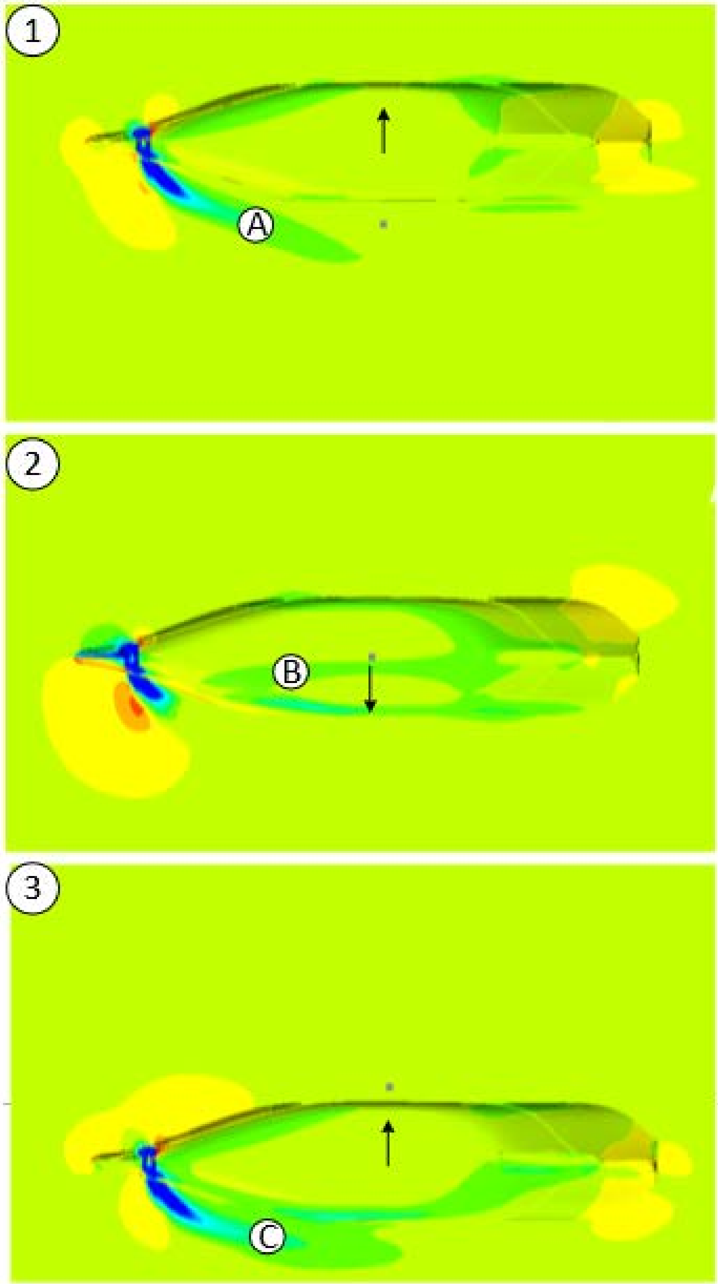

In order to compare the forces and moment, only the dimensionless regression curves are shown in fig. 5.43. It can be seen, that the forces and moment are very close to each other between 3 and 4*m/s* compared with the results at 2*m/s*. This is well founded by the absence of effectiveness of TT working upon a certain ship speed. The second finding is that Y' and N' in sway and combined sway-yaw tests only differ by a constant value. Nevertheless, Y' is very different in yaw test. It becomes smoother with increasing ship speed.

Fig. 5.43: Comparison of non-dimensional forces and moment of three velocities in the forced dynamic motion with working tunnel thruster (from top to bottom: surge, sway, yaw, 1st and 2nd combined sway-yaw test)

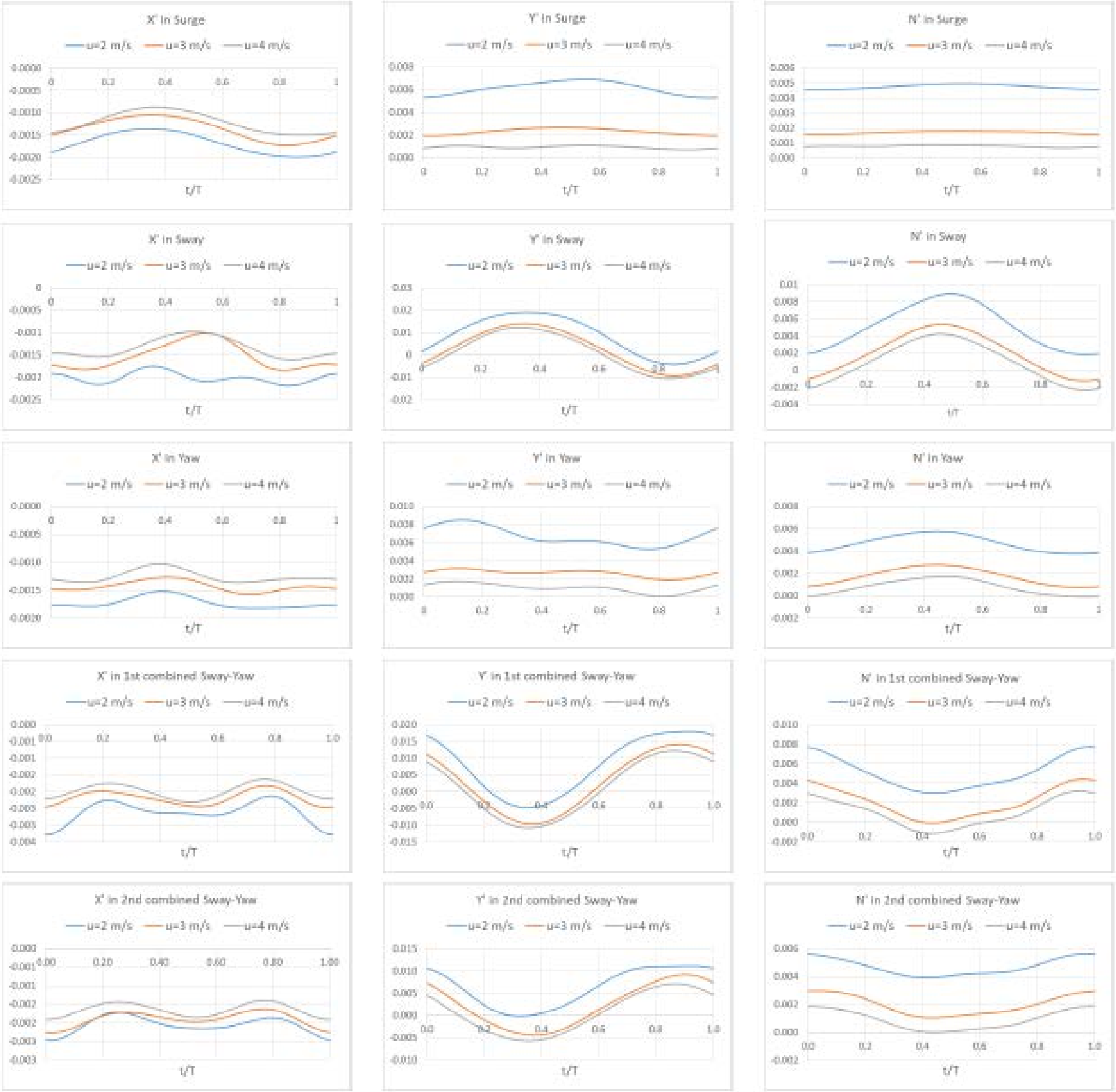

The comparison at 2 m/s will be discussed. The dimensionless HD in tab. 5.20 are calculated with appropriate water density, ship length and ship speed (2 m/s). The values of X_0, Y_0 and N_0 are obtained from the difference between ship with- and without TT in terms of combined sway-yaw test. Fig. 5.44 shows the turning circle on the basis of HD listed in tab. 5.20 and the motion parameters such as *u*, *v*, *r* and β.

Tab. 5.20.: Manoeuvring hydrodynamic derivatives multiplied by 1e5 for working TT

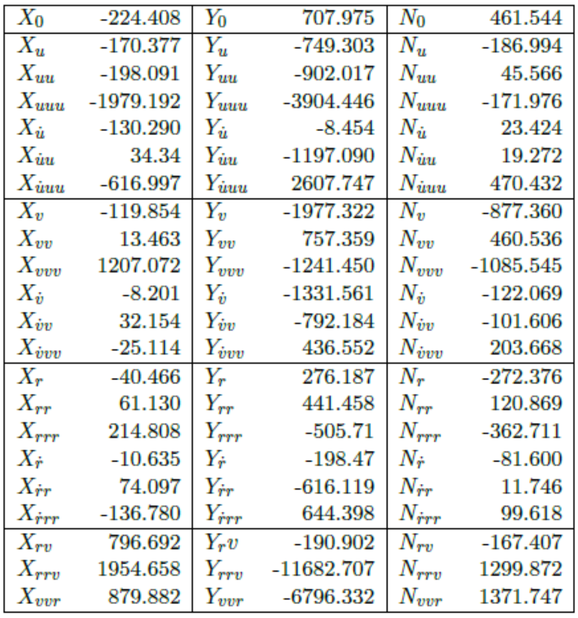

X_0	-224.408	Y_0	707.975	N_0	461.544
X_u	-170.377	Y_u	-749.303	N_u	-186.994
X_{uu}	-198.091	Y_{uu}	-902.017	N_{uu}	45.566
X_{uuu}	-1979.192	Y_{uuu}	-3904.446	N_{uuu}	-171.976
$X_{\dot{u}}$	-130.290	$Y_{\dot{u}}$	-8.454	$N_{\dot{u}}$	23.424
$X_{\dot{u}u}$	34.34	$Y_{\dot{u}u}$	-1197.090	$N_{\dot{u}u}$	19.272
$X_{\dot{u}uu}$	-616.997	$Y_{\dot{u}uu}$	2607.747	$N_{\dot{u}uu}$	470.432
X_v	-119.854	Y_v	-1977.322	N_v	-877.360
X_{vv}	13.463	Y_{vv}	757.359	N_{vv}	460.536
X_{vvv}	1207.072	Y_{vvv}	-1241.450	N_{vvv}	-1085.545
$X_{\dot{v}}$	-8.201	$Y_{\dot{v}}$	-1331.561	$N_{\dot{v}}$	-122.069
$X_{\dot{v}v}$	32.154	$Y_{\dot{v}v}$	-792.184	$N_{\dot{v}v}$	-101.606
$X_{\dot{v}vv}$	-25.114	$Y_{\dot{v}vv}$	436.552	$N_{\dot{v}vv}$	203.668
X_r	-40.466	Y_r	276.187	N_r	-272.376
X_{rr}	61.130	Y_{rr}	441.458	N_{rr}	120.869
X_{rrr}	214.808	Y_{rrr}	-505.71	N_{rrr}	-362.711
$X_{\dot{r}}$	-10.635	$Y_{\dot{r}}$	-198.47	$N_{\dot{r}}$	-81.600
$X_{\dot{r}r}$	74.097	$Y_{\dot{r}r}$	-616.119	$N_{\dot{r}r}$	11.746
$X_{\dot{r}rr}$	-136.780	$Y_{\dot{r}rr}$	644.398	$N_{\dot{r}rr}$	99.618
X_{rv}	796.692	$Y_r v$	-190.902	N_{rv}	-167.407
X_{rrv}	1954.658	Y_{rrv}	-11682.707	N_{rrv}	1299.872
X_{vvr}	879.882	Y_{vvr}	-6796.332	N_{vvr}	1371.747

Fig. 5.44: Turning circle simulation supported by the working TT at 2m/s ship speed

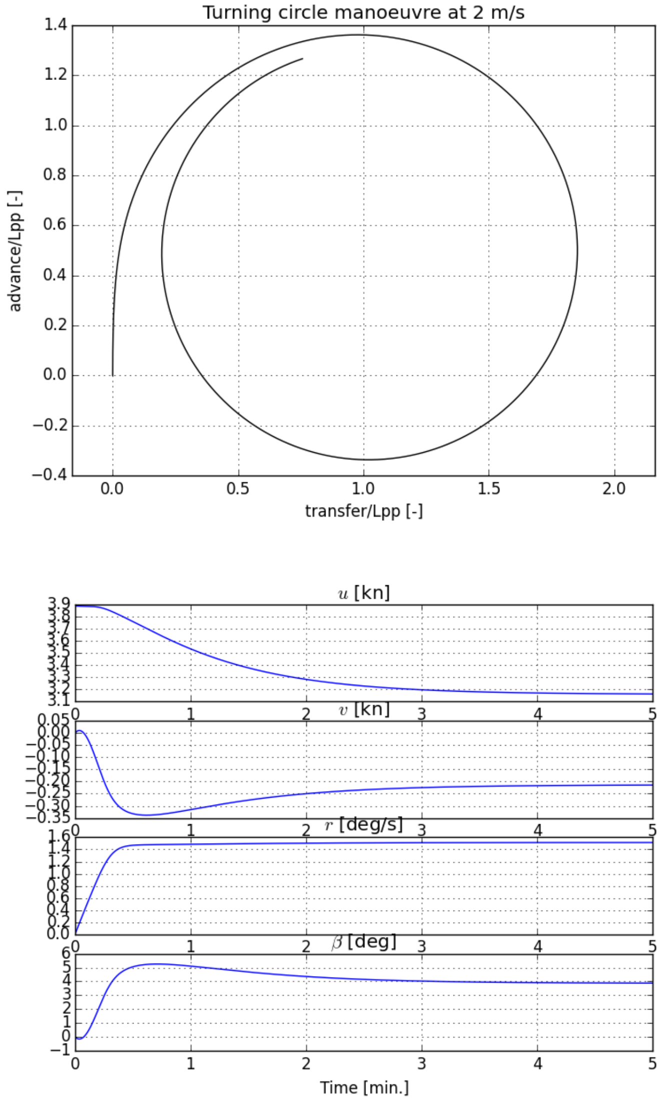

6 Working Package WP4

The purpose in this task is to investigate the performance of bow thruster as well as the main propulsor under off-design conditions, focusing primarily on the low speed operation conditions. A design-oriented model should be developed based on the systematic CFD calculations taken from the previous tasks.

An overview of task WP4 is found in tab. 6.1.

Table 6.1.: Sub working tasks of task T4.2 and T4.3

WP4: Development of design oriented models.	
Work task	Description
T4.2	**Operating behaviour under changing working conditions**
T4.2.1	Development of a mathematical model taking into account the influence of operating conditions on the efficiency of the tunnel thrusters.
T4.3	**Effects of extended models in the manoeuvring model**
T4.3.1	Development of a calculation method for the simulation of ship motions, taking into account the influence of operating conditions on the efficiency of tunnel thrusters and main propulsors.

6.1 T4.2 - Operating behaviour under changing working conditions with working TT

6.1.1 Variation of ship inflow velocity

The most of the efficiency loss of tunnel thruster occurs mainly at high vessel speed. In tab. 6.2, the total longitudinal as well as the transverse force is listed. The calculations are performed by static conditions with varied inflow velocities. The heading angle of the ship is zero.

Table 6.2.: Operating parameter of bow thruster under changing working conditions

U [m/s]	FX Total [kN]	FY Total [kN]	FY Total/FX Total [-]
0	4.89	151.97	31.08
1	-13.29	146.98	-11.06
2	-19.30	63.88	-3.31
3	-27.88	22.89	-0.82
4	-45.77	28.29	-0.62
7.2	-158.74	41.45	-0.26

At the bollard pull condition, both forces are positive and reach their maximal values. Regardless of this condition, resistance occurs and increases with increasing velocities, whereas an increment of the total transverse force is observed after 3 m/s. The ratio between ”FY Total” and ”FX Total” decreases through the entire velocities. The individual longitudinal force as well as transverse force for each component such as thruster, tunnel and hull (see fig. 6.1) is treated separately (see diagrams in fig. 6.2).

Fig. 6.1: Components of the ship

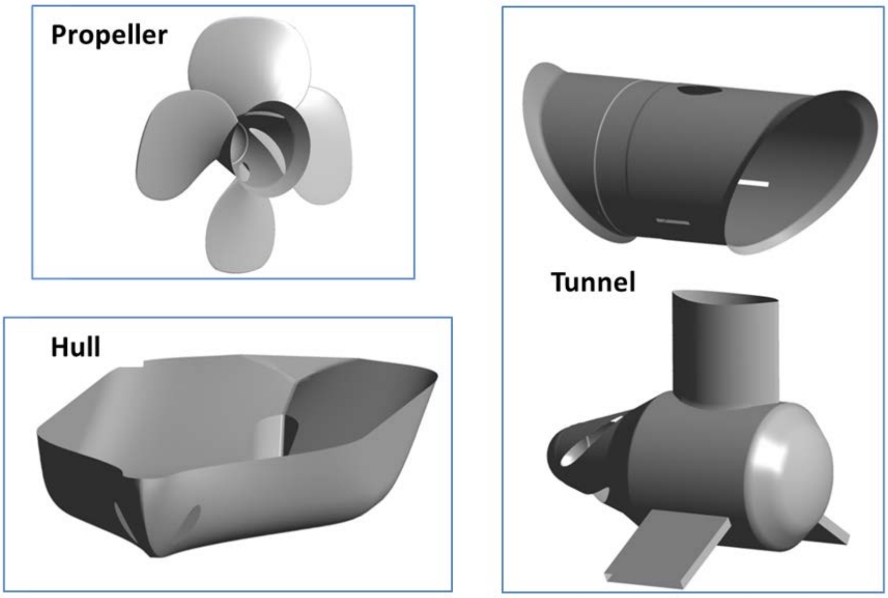

Fig. 6.2: Operating parameter of bow thruster under changing inflow velocity

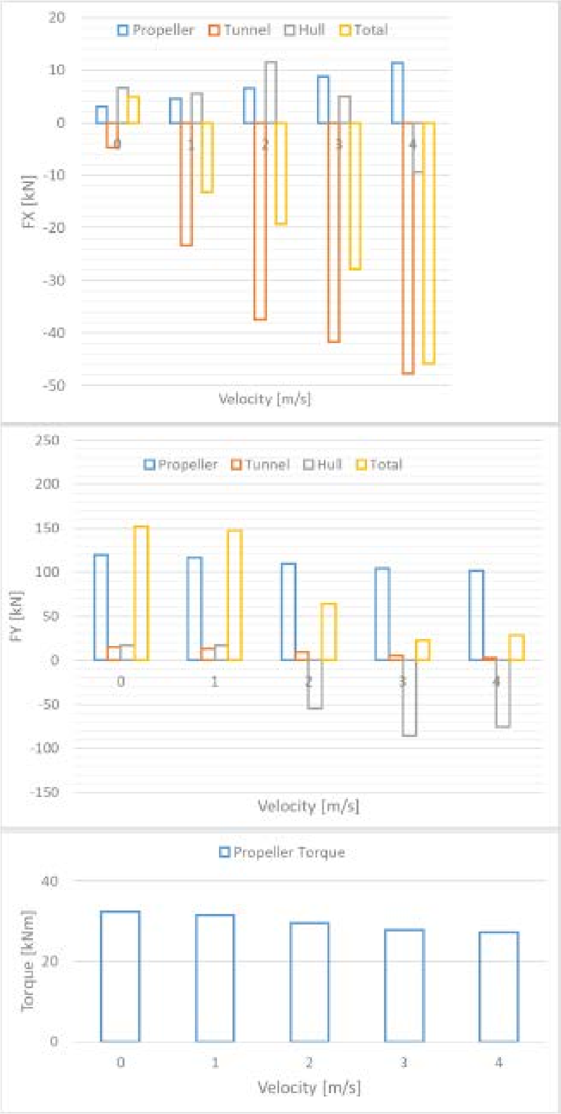

The resistance of tunnel dominates the total longitudinal force; hull and propeller provide positive force.

The propeller thrust and torque has only slightly decrement through the velocities, the reduction of them from 0 to 4 m/s is only about 15%. However, the force acting on the hull is changing dramatically and has the biggest contribution to the change of the total transverse force.

Fig. 6.3 shows the pressure distribution on the hull. In case of 3 m/s (fig. 6.3 left), the slipstream attaches mostly on the side of the hull (circled area), which reduces the effect of the bow thruster. However, at 7m/s, the slipstream is pushed partly towards the ship's bottom due to the strong inflow. The release of the attached slipstream on the hull leads to an increase of the total transverse force after 3 m/s. English [9] also found that an improvement of the transverse force could be observed at a certain ship speed.

Definitely, the waterline angle and longitudinal position of TT have a great effect on the performance of the tunnel thruster.

Fig. 6.3: Distribution of pressure coefficients on the hull and the horizontal plane at height of thruster rotating axis (left: 3m/s, right:7.2 m/s)

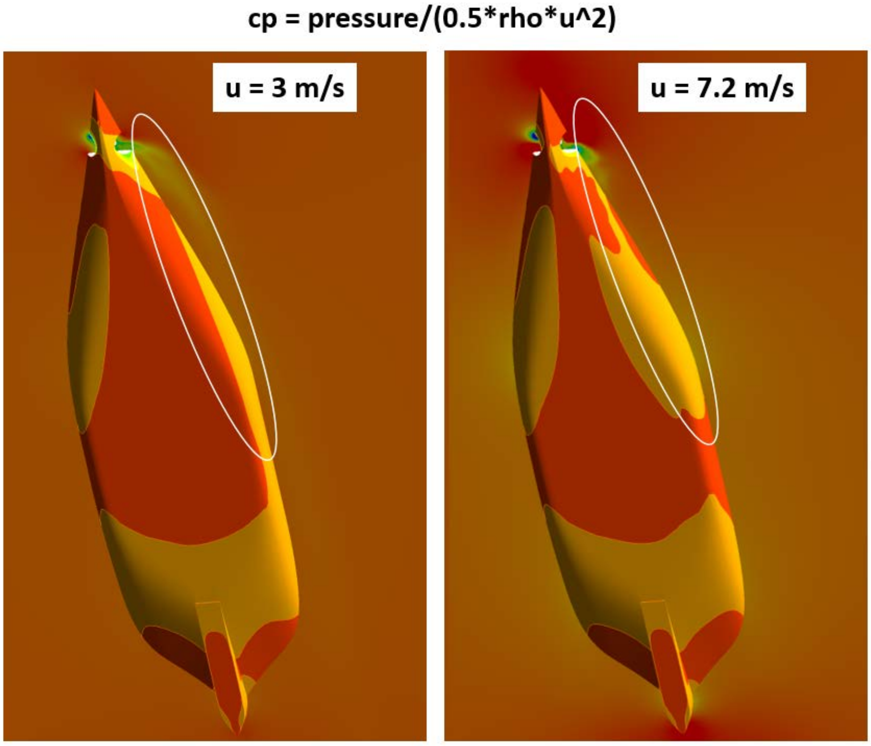

6.1.2 Variation of ship course angle

The behaviour of TT in response to the changing course angles is also of interest. The calculations are performed for the case of 1 m/s with different course angles, namely 0°, ±30°, ±60° and ±90° as illustrated in fig. 6.4.

Fig. 6.4: Variation of course angles at inflow velocity of 1m/s

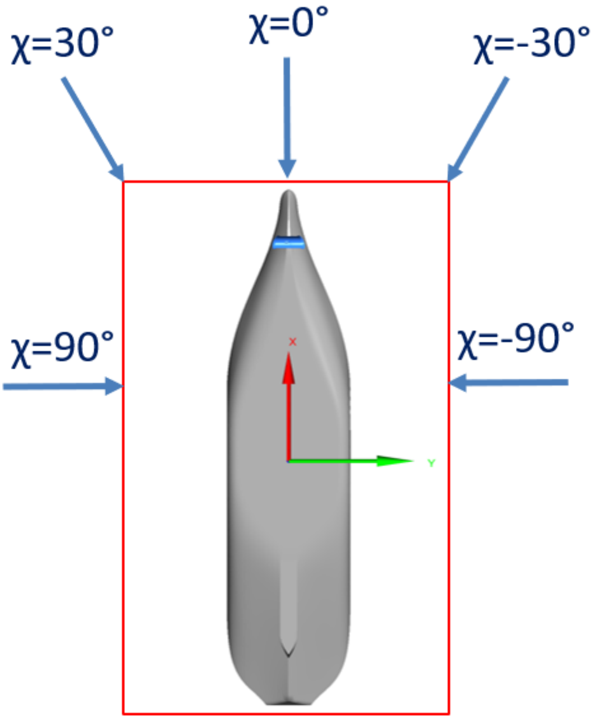

The tunnel produces the highest values for resistance, except at χ = -90°. Hull and propeller provide positive longitudinal force. The maximal total longitudinal force appears at χ = −90° due to suction effect caused by the slipstream (see fig. 6.5).

Fig. 6.5: Pressure- and velocity distribution at χ = -90°

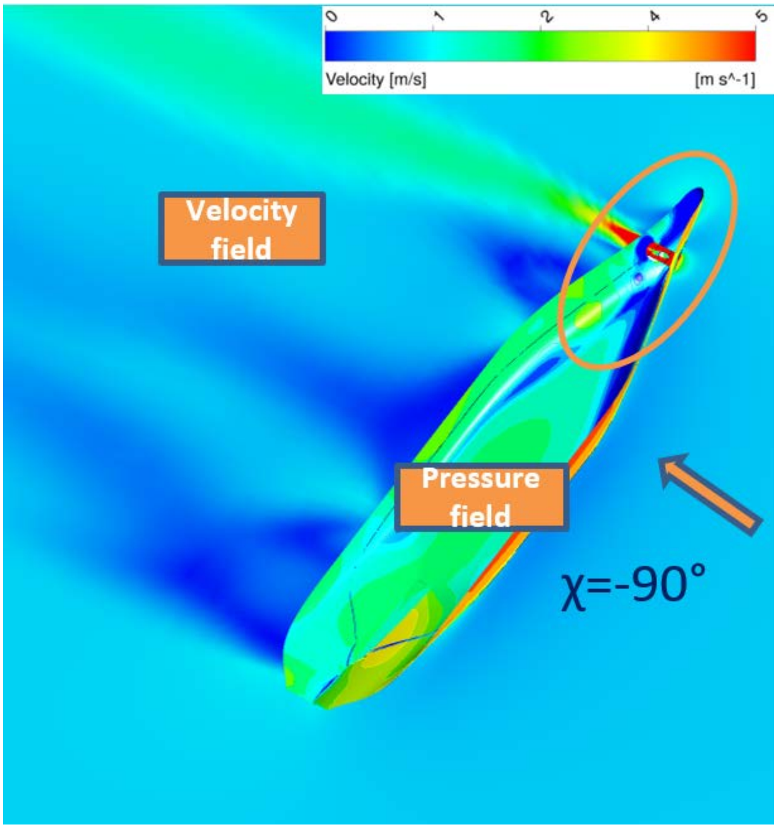

Propeller produces slightly greater transverse force at 90° course angle than at -90° due to the different inflow conditions. At -90°, the total transverse force is almost zero, the balance of the force is found between the propeller and other components. The change of torque from -90° to 90° is very small. Course angle has less effect on the performance of propeller as well as on the tunnel.

Fig. 6.6: Operating behaviour of bow thruster under changing course angles at 1 m/s

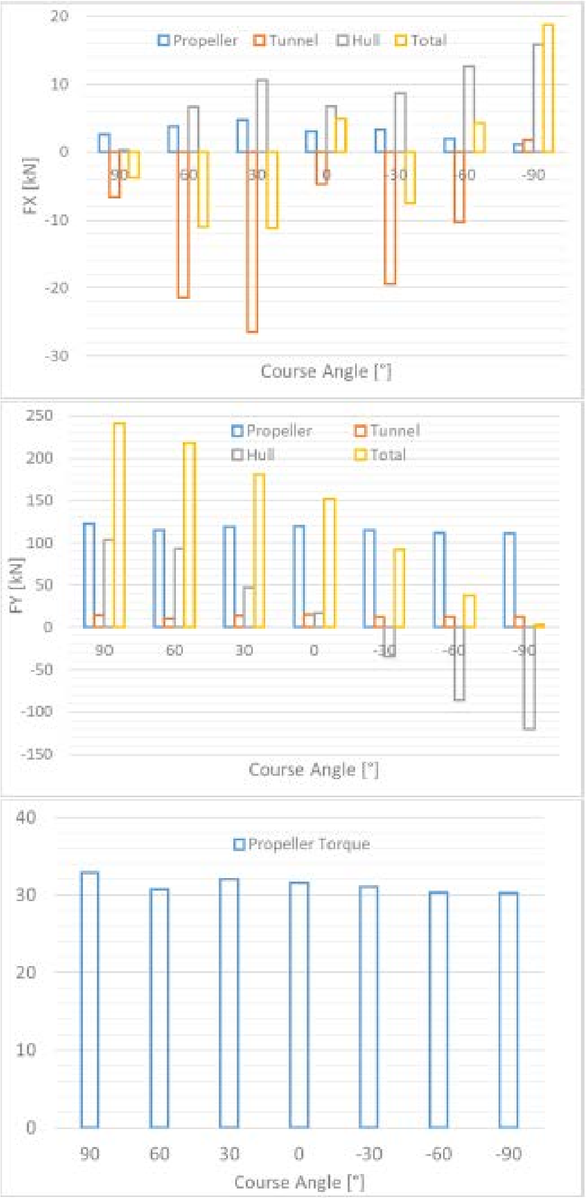

6.1.2.1 T4.2.1 - Development of a mathematical model taking into account the influence of operating conditions on the efficiency of the tunnel thrusters

SINTEF has developed a model for the estimation of efficiency loss of tunnel thrusters. The current mathematical model is based on the momentum theorem and energy conservation theorem on the one hand, on the other hand a systematic tests are required which can be found from the previous studies reported in Krasilnikov, V. [17]. According to these both considerations, two equations can be formulated.

$$K_{TP} = \frac{1}{8} \cdot \pi \cdot (a^2 + \sum \zeta) \cdot J^2 \qquad (6.1)$$

$$K_{TP} = b \cdot J + c \qquad (6.2)$$

Here K_{TP} is the propeller thrust coefficient, a is responsible for the expansion of thruster slipstream, ζ are the hydraulic losses inside the tunnel, J is the advance ratio, b is the slope and c is the bias of K_{TP} -curve derived from experimental result. The only unknown J is obtained from the cross point as shown in fig. 6.7.

Fig. 6.7: Solution of the operation point of tunnel thruster (Krasilnikov, V. [17])

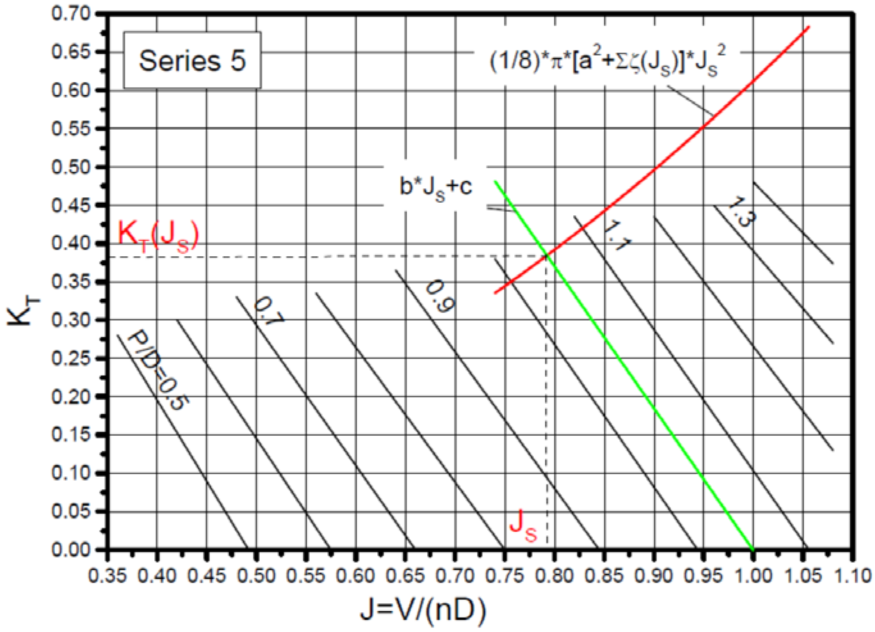

The main purpose is to determinate the corrections of a and ζ possibly being affected by the form of inlet edges, hull shape especially the frame angle and waterline angle, the length of the tunnel and the ship speed. The hydraulic losses ζ contains the losses due to friction in the tunnel, inlet fittings, frame angle, protective grids and the gear housing. The determination of the both corrections a and ζ can be found again in the report from Krasilnikov, V. [17]. Some parts of corrections have not been fully implemented in the released version on Dec. 2017.

Currently, the released version is only valid if the tunnel thruster is working at the bollard pull condition. For other conditions e.g., ship speeds and course angles, the predictions need to be developed appropriately. The big challenge is, if the shape of ship differs from the original version, the development of the slipstream, which can be very different to follow even under the same operation condition.

6.2 T4.3 - Effects of extended models in the manoeuvring model

This task is focusing on the extension of manoeuvring model for TT, developed in T5.2.1, combined with the main propulsor.

6.2.1 T4.3.1 - Development of a calculation method for the simulation of ship motions taking into account the influence of operating conditions on the efficiency of TT and MP

In task T3.3 the interaction between ship and ship propulsion (MP with working TT) is considered through the deduction factor and wake fraction taken from the ship design speed. The operation point of the self-propelled ship is defined as the intersection of two K_t-curves. One is the curve of necessary thrust which originates from ship resistance, deduction factor and wake fraction. The other one is the curve of thrust deliverable from the bare propulsion system obtained from open water test of the ducted propeller (see section T2.2) with a diameter of 4.2 m. The following steps can obtain the K_t-curve of the ship.

The thrust coefficient K_t is equal to

$$K_t = \frac{T}{\rho n^2 D^4} \tag{6.3}$$

The additional wake force on the ship through the working propeller is considered by the deduction factor *t* and then the necessary dimensionless thrust from eq. 6.3 is

$$\begin{aligned} K_t &= \frac{T}{\rho n^2 D^4} && (6.4) \\ &= \frac{R_T}{(\rho n^2 D^4)(1-t)} && (6.5) \end{aligned}$$

K_t should be a function of the advance ratio *J*. Replacing n^2 in eq. 6.5 with eq. 6.6

$$n^2 = \frac{u_a^2}{J^2 D^2} \tag{6.6}$$

we get

$$K_t = \frac{R_T J^2}{(\rho u_a^2 D^2)(1-t)} \tag{6.7}$$

Here u_a is the averaged inflow velocity at the propeller plane. The wake fraction *w* denotes the relation between u_a and the ship speed u_s.

$$\begin{aligned} K_t &= \frac{R_t J^2}{(\rho u_a^2 D^2)(1-t)} && (6.8) \\ &= \frac{R_t}{\rho u_s^2 (1-w)^2 D^2 (1-t)} J^2 && (6.9) \end{aligned}$$

Eq. 6.9 describes the thrust coefficient K_t with respect to J for the ship (see fig. 6.8). The values of *t* and *w* are assumed to be at ship design speed. The resistance R_t with no working TT is given in tab. 6.3. The curve for the propulsor in fig. 6.8 is obtained from the open water test. The example shows that at ship speed of 2 m/s and azimuth angle of 0° the two curves intersect at a point of about J = 0.89. The propeller revolution number is then $u_a/(JD)$ = 0.48 rps. The slight decrease of R_t/u_s^2 (see tab. 6.3) denotes the reduced friction effect while increasing ship speed.

Tab. 6.3: Ship resistance about velocity without working TT

$\mathbf{u}_s$ [m/s]	1	2	3	4
$\mathbf{R}_t$ [kN]	-3.1	-11.5	-25.2	-43.8
$\mathbf{R}_t / u_s^2$	-3.1	-2.9	-2.8	-2.7

Fig. 6.8: Defining the operation point at ship velocity of 2 m/s

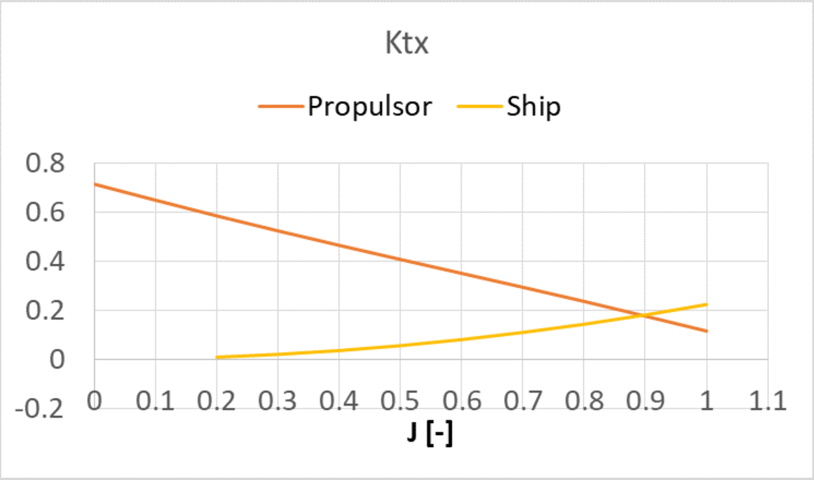

6.2.1.1 Manoeuvring model for the MP without working TT

In order to establish the model for the main propulsor, further operation points from other azimuth angles are necessary. The propeller coefficients given in section T2.1.5 are with respect to the thruster-fixed coordinate system, which need to be given in the ship-fixed coordinate system (see tab. 6.4). Regarding the tasks in T2.1.5, the azimuth angles have been only calculated till −30°. As the same treatment to $\psi = 0^\circ$, the further interacted points for azimuth angles −15° and −30° can be found in fig. 6.9. The corresponding advance ration *J*, the longitudinal force coefficient *Ktx* and the revolution number *n* are listed in tab. 6.5.

Tab. 6.4: The coefficients of the ducted propeller taken from WP2 with respect to thruster- (left) and ship-fixed (right) coordinate systems

	thruster-fixed coordinate			**ship-fixed coordinate**		
$\psi = 0^\circ$						
J	**Kfx**	**Kfy**	**Kqz**	**Ktx**	**Kty**	**Kqn**
0	0.713	0	0	0.713	0	0
0.2	0.584	0	0	0.584	0	0
0.4	0.464	0	0	0.464	0	0
0.6	0.350	0	0	0.350	0	0
0.8	0.236	0	0	0.236	0	0
1	0.115	0	0	0.115	0	0
$\psi = -15^\circ$						
0	0.713	0	0	0.689	-0.185	1.516
0.2	0.578	-0.048	-0.006	0.546	-0.196	1.604
0.4	0.455	-0.121	0.003	0.408	-0.234	1.928
0.6	0.346	-0.206	0.020	0.281	-0.289	2.390
0.8	0.222	-0.276	0.034	0.143	-0.324	2.696
1	0.071	-0.350	0.044	-0.022	-0.356	2.972
$\psi = -30^\circ$						
0	0.713	0	0	0.617	-0.357	2.928
0.2	0.583	-0.090	-0.010	0.460	-0.369	3.025
0.4	0.481	-0.229	0.003	0.302	-0.439	3.608
0.6	0.397	-0.381	0.030	0.153	-0.528	4.371
0.8	0.300	-0.530	0.061	-0.005	-0.609	5.063
1	0.194	-0.700	0.097	-0.182	-0.703	5.873

Fig. 6.9: Defining the operation points at ship velocity of 2m/s for different azimuth angles (0°, −15° and −30°)

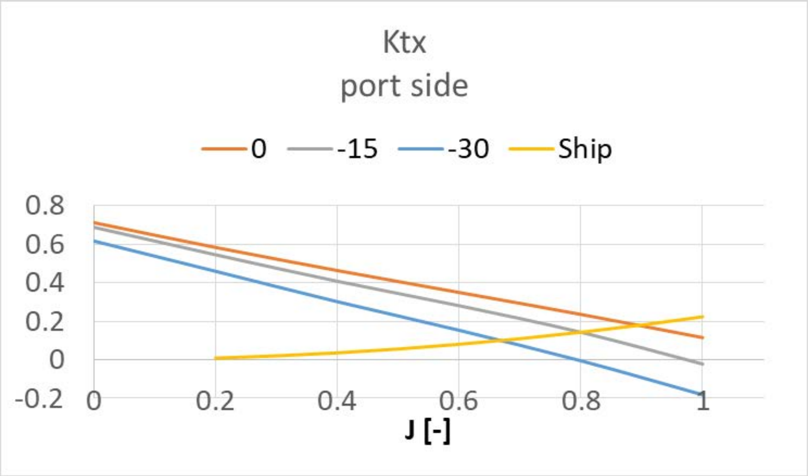

The relations between R_t and u_s^2 are assumed to be constant (see tab. 6.3), thus the intersection point at certain azimuth angle ψ does not change according to eq. 6.9. So the values of *Ktx* as well as *J* are not dependent on ship speed (see tab. 6.5).

Tab. 6.5: Characteristic parameters for the different velocities and azimuth angles

ψ [°]	**Ktx** [-] **(u_s=1,2,3,4m/s)**	**J** [-] **(u_s=1,2,3,4m/s)**	**n** [rps] **(u_s=1 m/s)**	**n** [rps] **(u_s=2 m/s)**	**n** [rps] **(u_s=3 m/s)**	**n** [rps] **(u_s=4 m/s)**
0	0.17	0.89	0.24	0.48	0.71	0.95
-15	0.14	0.80	0.27	0.53	0.80	1.06
-30	0.10	0.67	0.32	0.64	0.97	1.29

The coefficients of a ducted propeller (tab. 6.4) are presented in fig. 6.10. Here Ktx, Kty and Kqn are non-dimensionalized by propeller revolution number, but in the manoeuvring model, the dimensionless values are referred to ship speed and length between perpendiculars. Ship-fixed forces and moment are required and can be obtained from eq. 6.10 ~ 6.12.

Fig. 6.10: Coefficients for longitudinal force, transverse force and steering moment in ship-fixed coordinate system at 2 m/s for the three azimuth angles (0°, −15° and −30°)

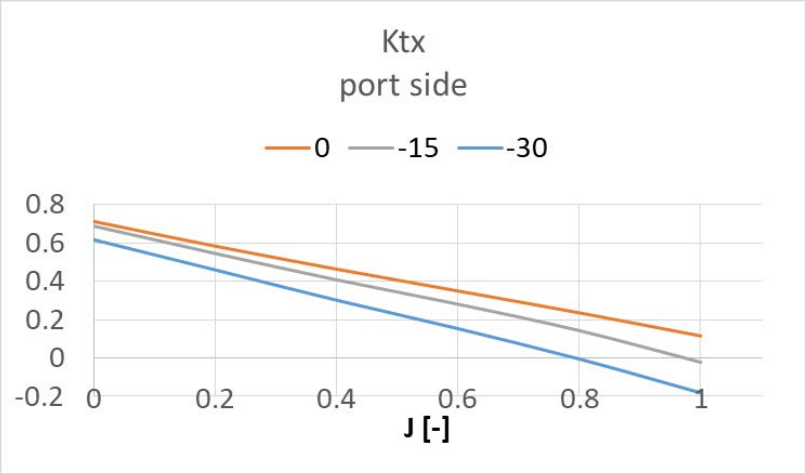

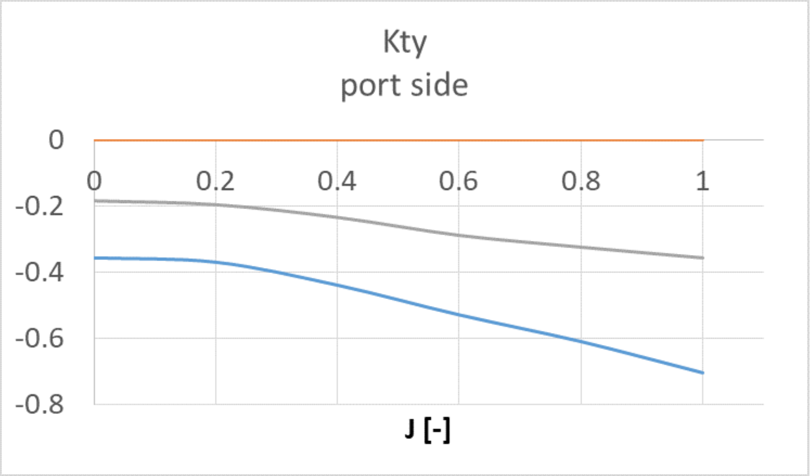

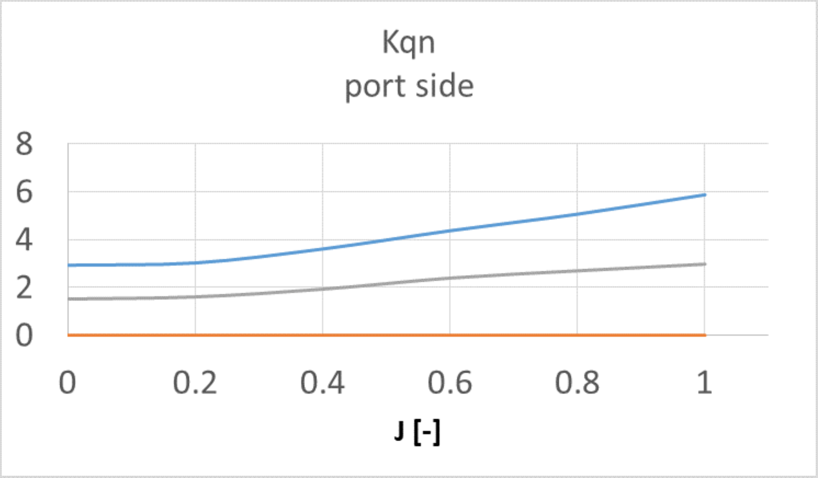

$$X = \mathrm{Ktx} \cdot \rho n^2 \cdot D^4 \tag{6.10}$$

$$Y = \mathrm{Kty} \cdot \rho n^2 \cdot D^4 \tag{6.11}$$

$$N = \mathrm{Kqn} \cdot \rho n^2 \cdot D^5 \tag{6.12}$$

Besides that, two positive azimuth angles are still necessary. Fig. 6.11 shows the forces and moment in dependency of the Azimuth angles on two turning directions (starboard and port) in solid lines. The longitudinal propeller thrust X_{prop} is constant because of the same ship's velocity (here 2 m/s). The idea is that, in order to obtain a pure relation to the Azimuth angle, the inflow velocity must be fixed to a certain value, so that the revolution number of the propeller is variable. From the same figure, the ship-fixed transverse force Y_{prop} and yaw moment N_{prop} can be simply treated as an odd function (dashed lines). The manoeuvring model for the main propulsor up to the third order can be written as Eq.(6.13) ∼ (6.15).

$$X_{prop}(\Delta u) \approx X_0^P + X_u^P \Delta u \tag{6.13}$$

$$Y_{prop}(\psi) \approx Y_0^P + Y_\psi^P \psi + Y_{\psi\psi\psi}^P \psi^3 \tag{6.14}$$

$$N_{prop}(\psi) \approx N_0^P + N_\psi^P \psi + N_{\psi\psi\psi}^P \psi^3 \tag{6.15}$$

Here are X_0^P, Y_0^P and N_0^P are the propeller loads at $\psi = 0°$.

Fig. 6.11: Forces and moment evaluated at ship-fixed coordinate system for the two turning directions of main propulsor at 2 m/s. From top to bottom: total force *X*, total force *Y* and total yaw-moment *N*

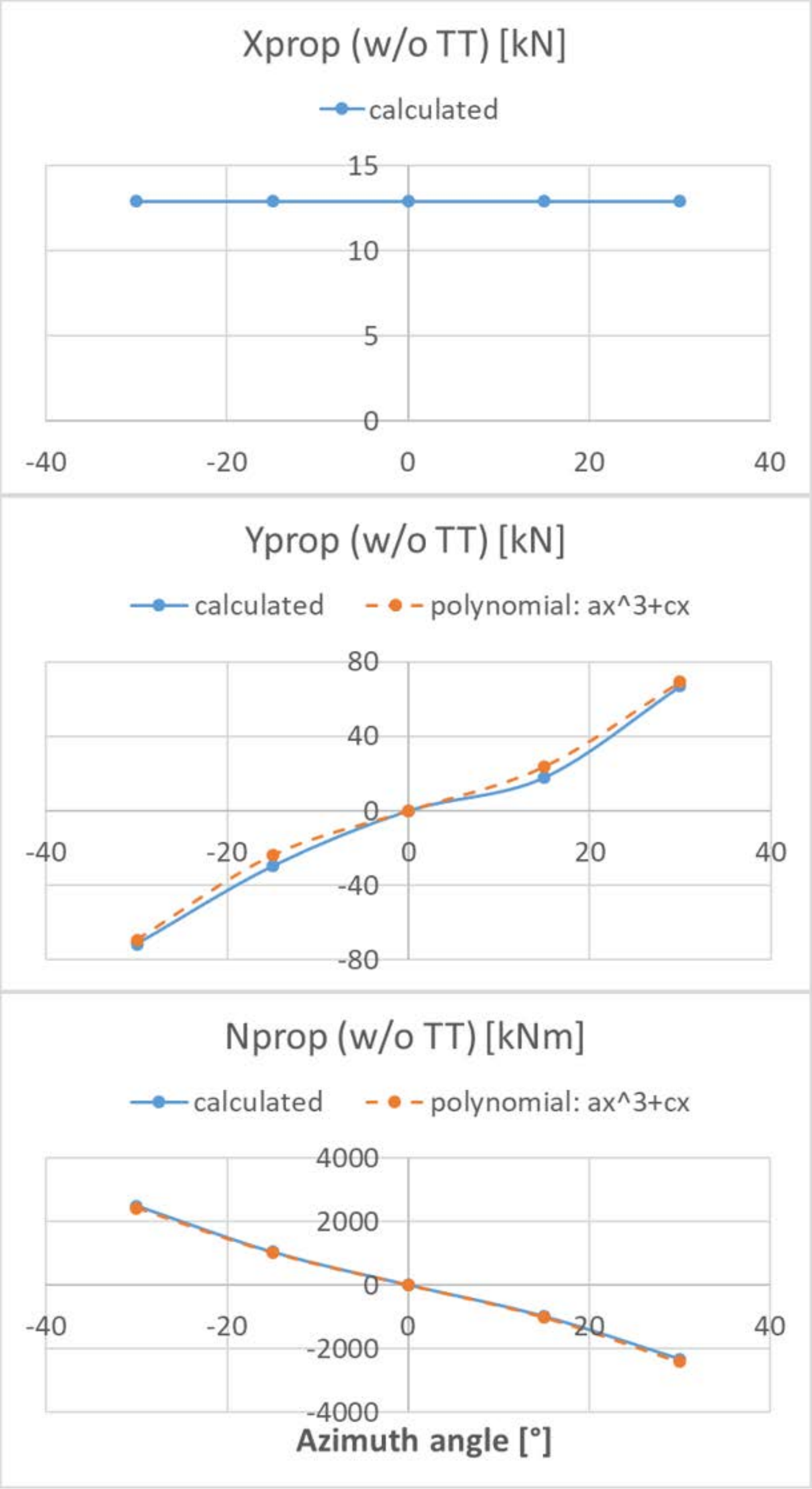

Then the HD are calculated from the polynomials in fig. 6.11.

$$\vec{T}^P_{\psi} = c \tag{6.16}$$

$$\vec{T}^P_{\psi\psi\psi} = a \tag{6.17}$$

The vector $\vec{T}^P$ contains the components Y_{prop} and N_{prop}. The HD for the main propulsor without consideration of a working TT are given at tab. 6.6. Most of the hydrodynamic derivatives not sensitive to the ship speeds except for X_0^P; their derivation according to the velocity in terms of $X_u^P \Delta u$ has to be added at eq. 6.13.

Tab. 6.6: Non-dimensionalized manoeuvring derivatives multiplied by 1e5 for main propulsor

X		Y		N	
us = 1 m/s					
X_0^P	121.06	Y_0^P	0	N_0^P	0
		Y_ψ^P	685.75	N_ψ^P	-435.87
		$Y_{\psi\psi\psi}^P$	1812.07	$N_{\psi\psi\psi}^P$	-428.83
us = 2 m/s					
X_0^P	113.79	Y_0^P	0	N_0^P	0
		Y_ψ^P	680.40	N_ψ^P	-428.44
		$Y_{\psi\psi\psi}^P$	1776.66	$N_{\psi\psi\psi}^P$	-430.54
us = 3 m/s					
X_0^P	110.42	Y_0^P	0	N_0^P	0
		Y_ψ^P	677.89	N_ψ^P	-424.94
		$Y_{\psi\psi\psi}^P$	1760.07	$N_{\psi\psi\psi}^P$	-431.37
us = 4 m/s					
X_0^P	108.16	Y_0^P	0	N_0^P	0
		Y_ψ^P	676.16	N_ψ^P	-422.59
		$Y_{\psi\psi\psi}^P$	1749.01	$N_{\psi\psi\psi}^P$	-431.96

Combining the equations for the ship w/o TT introduced in section T3.3, we get the manoeuvring model for the main propulsor w/o working TT (see eq. 6.18 ~ 6.20).

$$\begin{aligned}
X &\cong X_0 + X_0^P \\
&+ X_u \Delta u + X_{uuu} \Delta u^3 + X_{\dot u} \dot u \\
&+ X_{vv} v^2 \\
&+ X_{rrr} r^3 \\
&+ X_{rv} r v \\
&+ X_u^P \Delta u
\end{aligned} \tag{6.18}$$

$$\begin{aligned}
Y &\cong Y_0 + Y_0^P \\
&+ Y_u \Delta u \\
&+ Y_v v + Y_{vvv} v^3 + Y_{\dot v} \dot v + Y_{\dot v vv} \dot v v^2 \\
&+ Y_r r + Y_{rrr} r^3 + Y_{\dot r} \dot r + Y_{\dot r rr} \dot r r^2 \\
&+ Y_{rrv} r^2 + Y_{vvr} v^2 r \\
&+ Y_\psi^P \psi + Y_{\psi\psi\psi}^P \psi^3
\end{aligned} \tag{6.19}$$

$$\begin{aligned}
N &\cong N_0 + N_0^P \\
&+ N_u \Delta u \\
&+ N_v v + N_{vvv} v^3 + N_{\dot v} \dot v + N_{\dot v vv} \dot v v^2 \\
&+ N_r r + N_{rrr} r^3 + N_{\dot r} \dot r + N_{\dot r rr} \dot r r^2 \\
&+ N_{rrv} r^2 + N_{vvr} v^2 r \\
&+ N_\psi^P \psi + N_{\psi\psi\psi}^P \psi^3
\end{aligned} \tag{6.20}$$

6.2.1.2 Manoeuvring model for the MP with working TT

In presence of TT, the ratio between R_t and u_s^2 can not be assumed to be constant according to the change of ship speed. A comparison of the resistance is made between static and dynamic tests in tab. 6.7. The dynamic resistance denotes the mean value of the total longitudinal force during one period of the sway-yaw test. The ratio of static and dynamic resistance (see tab. 6.7) shows that the working TT produces double resistance in case of static simulation. The increase of resistance addressed to the dynamic tests is about 50%. The change of R_t requires new operation points. The new set of HD can be found in tab. 6.8. The development of the forces and moment over the azimuth angles for the case of working TT is shown in fig. 6.12.

Tab. 6.7: Comparison of ship resistance in kN between static and dynamic simulation with and without working tunnel thruster

	ship w/o TT		ship w/ TT			
u_s (m/s)	R_t **(static) A**	R_t **(dynamic) B**	R_t **(static) C**	R_t **(dynamic) D**	**D/A**	**D/B**
2	-11.5	-15.6	-19.3	-25.4	2.2	1.6
3	-25.2	-34.0	-27.9	-49.2	2.0	1.4
4	-43.8	-59.1	-45.8	-76.9	1.8	1.3

Tab. 6.8: Comparison of non-dimensionalized hydrodynamic derivatives multiplied by 1e5 for the main propulsor between with- (in brackets) and without working TT

X			**Y**			**N**		
u_s **= 2 m/s**								
		ratio			ratio			ratio
X_0^P	113.79 (246.67)	2.17	Y_0^P	0 (0)	-	N_0^P	0 (0)	-
			Y_ψ^P	680.40 (753.87)	1.11	N_ψ^P	-428.44 (-552.38)	1.29
			$Y_{\psi\psi\psi}^P$	1776.66 (2453.86)	1.27	$N_{\psi\psi\psi}^P$	-430.54 (-415.00)	0.96
u_s **= 3 m/s**								
X_0^P	110.42 (214.88)	1.95	Y_0^P	0 (0)	-	N_0^P	0 (0)	-
			Y_ψ^P	677.89 (740.03)	1.09	N_ψ^P	-424.94 (-524.67)	1.23
			$Y_{\psi\psi\psi}^P$	1760.07 (2288.28)	1.30	$N_{\psi\psi\psi}^P$	-431.37 (-416.26)	0.96
u_s **= 4 m/s**								
X_0^P	108.16 (189.94)	1.76	Y_0^P	0 (0)	-	N_0^P	0 (0)	-
			Y_ψ^P	676.16 (727.77)	1.08	N_ψ^P	-422.59 (-502.21)	1.19
			$Y_{\psi\psi\psi}^P$	1749.01 (2159.65)	1.23	$N_{\psi\psi\psi}^P$	-431.96 (-418.17)	0.97

Fig. 6.12: Forces and moment evaluated at ship-fixed coordinate system for the two turning directions of main propulsor at 2 m/s in the presence of working TT. From top to bottom: total force *X*, total force *Y* and total moment *N*

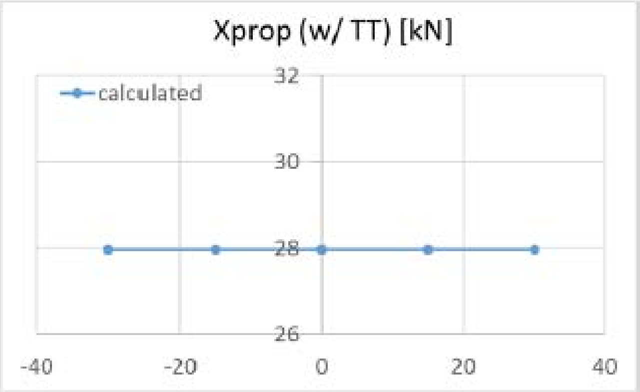

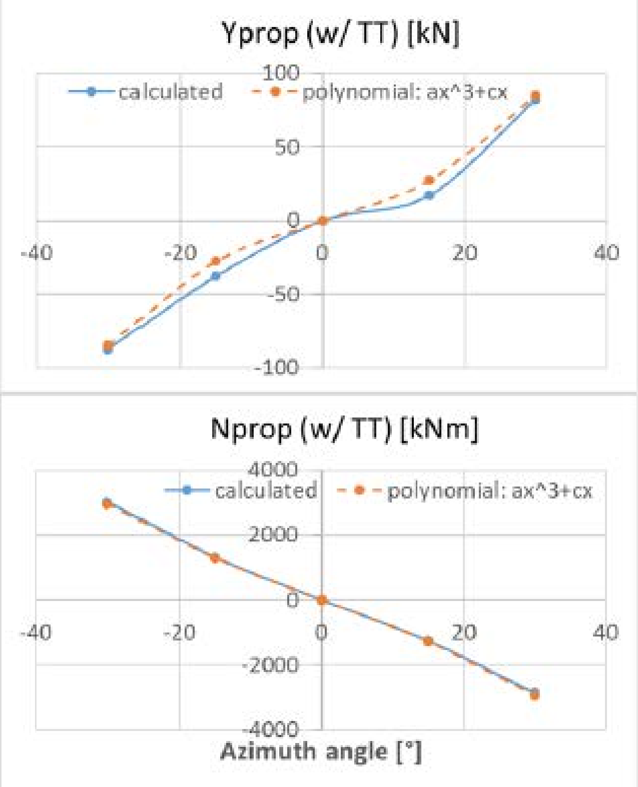

The manoeuvring model described in eq. 6.18 ~ 6.20 could be further applied. Although Y_ψ^P and N_ψ^P are changing with the velocity, but these changes are small. So it is assumed, that the derivations of Y_ψ^P and N_ψ^P will not be taken into account. The non-dimensionalized values are summarized in tab. 6.9. Noted that, the term of X_{uu}^P accounts for the dependency of X_u^P on ship speed. The same values of X_{uu}^P means that the polynomial of *X* is only a second order polynomial about *u*. The Taylor expansions till to the third order are expressed in eq. 6.21 ~ 6.23.

$$\begin{aligned} X_{prop}(\psi) &\approx X_0^P + X_u^P \Delta u + X_{uu}^P \Delta u^2 && (6.21)\\ Y_{prop}(\psi) &\approx Y_0^P + Y_\psi^P \psi + Y_{\psi\psi\psi}^P \psi^3 && (6.22)\\ N_{prop}(\psi) &\approx N_0^P + N_\psi^P \psi + N_{\psi\psi\psi}^P \psi^3 && (6.23) \end{aligned}$$

Tab. 6.9: The additional non-dimensionalized HD related to *u* multiplied by 1e5 for the working TT

u_s [m/s]	X_u^P	X_{uu}^P
2	434.14	157.90
3	342.06	157.90
4	296.02	157.90

A simplification is related to the model reduction of hydrodynamic derivatives as discussed in T5.2.1, the terms of $Y_{\dot{v}vv}\dot{v}v^2$, $Y_{\dot{r}rr}\dot{r}r^2$, $N_{\dot{v}vv}\dot{v}v^2$ and $N_{\dot{r}rr}\dot{r}r^2$ can be discarded. Before ship turns, the ship has a constant heading velocity, the longitudinal force *X* is zero, which means, the sum of X_0, X_0^P and X_0^{TT} has to be zero. Y_0 and N_0 are the transverse force and yaw moment for the ship w/o TT. Their values are negligible compared with the values when the bow thruster is in operation. At zero azimuth angle, the values of Y_0^P and N_0^P are also zero. Combining the manoeuvring model for TT (see eq. 7.14~ 7.16) with the equations for the propulsor (see eq. 6.21 ~ 6.23), we get the equations 6.24 ~ 6.26 for the combined model of main propulsor and tunnel thruster.

$$\begin{aligned} X &\cong X_u \Delta u + X_{\dot{u}} \dot{u} \\ &+ X_{vv} v^2 \\ &+ X_{rrr} r^3 \\ &+ X_{rv} r v \\ &+ X^{TT}_{uuu} \Delta u^3 \\ &+ X^P_u \Delta u + X^P_{uu} \Delta u^2 \end{aligned} \tag{6.24}$$

$$\begin{aligned} Y &\cong Y^{TT}_0 \\ &+ Y_v v + Y_{vvv} v^3 + Y_{\dot{v}} \dot{v} \\ &+ Y_r r + Y_{vvr} v^2 r + Y_{\dot{r}} \dot{r} \\ &+ Y^{TT}_{rrr} r^3 + Y^{TT}_{rrv} r^2 v \\ &+ Y^P_\psi \psi + Y^P_{\psi\psi\psi} \psi^3 \end{aligned} \tag{6.25}$$

$$\begin{aligned} N &\cong N^{TT}_0 \\ &+ N_v v + N_{vvv} v^3 + N_{\dot{v}} \dot{v} \\ &+ N_r r + N_{rrr} r^3 + N_{\dot{r}} \dot{r} \\ &+ N_{rrv} r^2 v + N_{vvr} v^2 r \\ &+ N^P_\psi \psi + N^P_{\psi\psi\psi} \psi^3 \end{aligned} \tag{6.26}$$

7 Working Package WP5

An overview of task WP5 is found in tab. 7.1.

Table 7.1.: Sub working tasks of T5.1 to T5.3

WP5: Guidelines for design and performance prediction.	
Work task	Description
T5.1	**Guidelines for main propulsors**
T5.1.1	Determination of hazard classes and definition of representative load cases.
T5.2	**Guidelines for tunnel thrusters**
T5.2.1	Development of a prediction method for the determination of the impact of ship manoeuvres on the thrust of tunnel thrusters.
T5.3	**Guidelines for vessel manoeuvrability**
T5.3.1	Development of a calculation method for determining the influence of operating conditions of tunnel thrusters and main propulsors on the manoeuvrability of the vessel.

7.1 T5.1.1 - Determination of hazard classes and definition of representative load cases

As discussed in T2.2, the critical cases with maximal loading caused by the main propulsor appear at azimuth angles between 90° ~ 120°. The thruster-fixed transverse force *Y* depends strongly on the azimuth speed *f* whereas the axial thrust *X* is insensitive to it. The propeller is a right-handed propeller, turning to starboard provides more forces and moment than to port side. Thus, the following predictions focuses on the results from starboard to the maximal loads.

7.1.1 Mathematical estimation for thruster-fixed side force coefficient Kfy

The development of transverse force coefficient *Kfy* with different *J* at different azimuth speed *f* is shown in fig. 7.1. The distance between two curves is almost constant up to 90°. 30° will be selected for the evaluation as shown in tab. 7.2.

Fig. 7.1.: Coefficients *Kty* dependency on azimuth speed *f* and advance ratio *J*

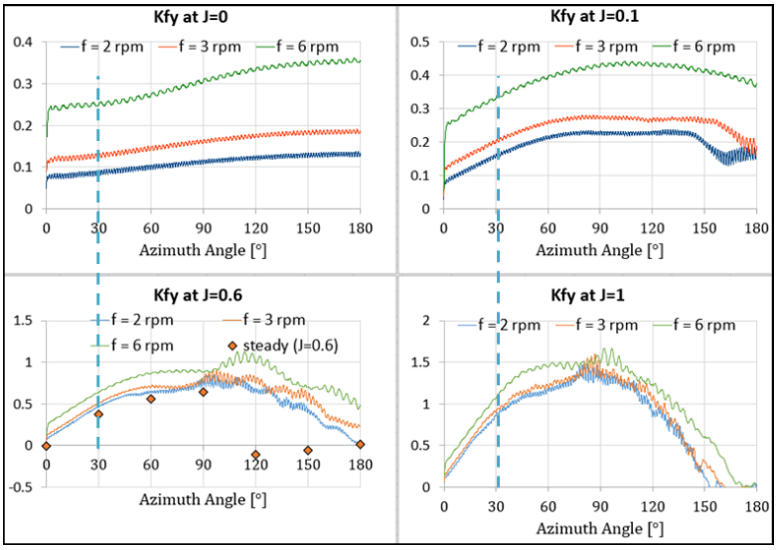

Table 7.2.: Changes of *Kty* due to the advance ratio *J* at azimuth angle of 30°

Kty for Azimuth angle of 30°				
J [-]	**f=0 rps**	**f=0.033 rps (2 rpm)**	**f=0.05 rps (3 rpm)**	**f=0.1 rps (6 rpm)**
0.0	0	0.08726	0.12958	0.25012
0.1	-	0.15796	0.20248	0.33005
0.6	0.37814	0.46241	0.50521	0.63404
1.0	-	0.84961	0.90440	1.06639

In table 7.2 only two static results are available from T2.1 ($f = 0$). Their coefficients are defined as Kty_s. The dynamic *Kfy* should consist of a static part Kty_s and a frequency-dependent part as written in eq. 7.1.

$$\mathrm{Kfy(f)} \quad = \quad \mathrm{Kfy}_s + \mathrm{Kfy}_c \tag{7.1}$$

After exploring tab. 7.2, eq. 7.1 can be rewritten as

$$\mathrm{Kfy(f)} \quad = \quad \mathrm{Kfy}_s + 2.5f \tag{7.2}$$

Fig. 7.2.: Regression curves in comparison with the source data from the CFD-calculation until azimuth angle of 90° at azimuth speed of 2 rpm (0.033 rps)

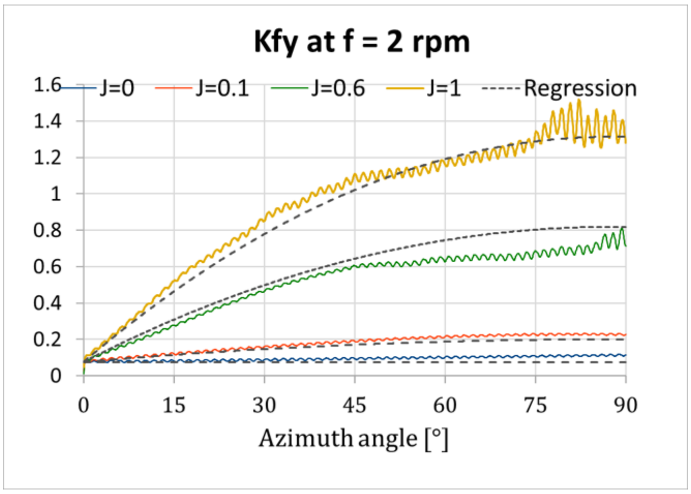

Kfy is also a function of azimuth angle *ψ*. Regarding to fig. 7.2, each curve can be written as a 2nd order polynomial such like

$$\mathrm{Kfy}(\psi) \quad = \quad a\psi^2 + b\psi + c \tag{7.3}$$

The polynomial coefficients are *a*, *b* and *c*. They should dependent on *J*, *c* is the value for $\psi = 0^\circ$ (Kfy_s). Using eq. 7.2, we get

$$\mathrm{Kfy}(\psi, J, f) \quad = \quad a(J)\psi^2 + b(J)\psi + \mathrm{Kfy}_s + 2.5f \tag{7.4}$$

The static transverse coefficient Kfy_s at $\psi = 0^\circ$ is zero, the coefficients *a* and *b*, determined from fig. 7.2, are linear dependent on *J*. The eq. 7.4 can be further developed to

$$\mathrm{Kfy}(\psi, J, f) \quad = \quad \underbrace{-0.53J\psi^2 + 1.62J\psi}_{\text{static}} + \underbrace{2.5f}_{\text{corrector}} \quad \forall\ 0^\circ < \psi < 90^\circ \tag{7.5}$$

The curves derived from eq. 7.5 are also presented in fig. 7.2. The dimensions for the input parameters are [rad], [-] and [rps] for *ψ*, *J* and *f*, respectively.

7.1.2 Mathematical estimation for thruster-fixed longitudinal force coefficient *Kfx*

The excess of body-fixed axial thrust has been explained in T2.2 due to the induced velocity caused by the propeller slipstream. Glauert introduced a mathematical equation accounting for this effect.

$$T = 2\varrho A u_i \sqrt{u_a^2 + u_i^2 - 2u_a u_i cos(\psi)} \tag{7.6}$$

Here ψ is the azimuth angle, A is the propeller disc area, u_i is the propeller-induced velocity perpendicular to the propeller plane and u_a stands for the advance velocity. The purpose of using eq. 7.6 is to find out the solution of u_i by given thrust T that is known from the CFD-calculation. At ψ = 90° T has the maximal value

$$T = 2\rho A u_i \sqrt{u_a^2 + u_i^2} \tag{7.7}$$

T can be non-dimensionalized by propeller revolution number n and diameter D to give

$$\begin{aligned} \mathrm{Kfx_{max}} &= \frac{2\rho A u_i \sqrt{u_a^2 + u_i^2}}{\rho n^2 D^4} \\ &= \frac{\pi}{2n^2 D^2} u_i \sqrt{u_a^2 + u_i^2} \end{aligned} \tag{7.8}$$

The maximal thrust of the investigated azimuth thruster in WP2 occurs at azimuth angle of 120°. To apply eq. 7.6 it is necessary to reduce the azimuth angle from 120° to 90°.

The Ktx_{max} in tab. 7.3 is known from fig. 7.3. The induced velocities are obtained from eq. 7.7. The induced advance ratio is $J_i = u_i/(nD)$ which can be described by 2nd order polynomial written as function of J (see eq. 7.9).

$$J_i = -0.4J^2 + 0.5J + 0.7 \tag{7.9}$$

The induced advance ratio at bollard pull condition is 0.7. The maximal Kfx can be obtained from eq. 7.8.

Fig. 7.3.: Development of *Kfx* about the azimuth angle for different advance ratio *J*

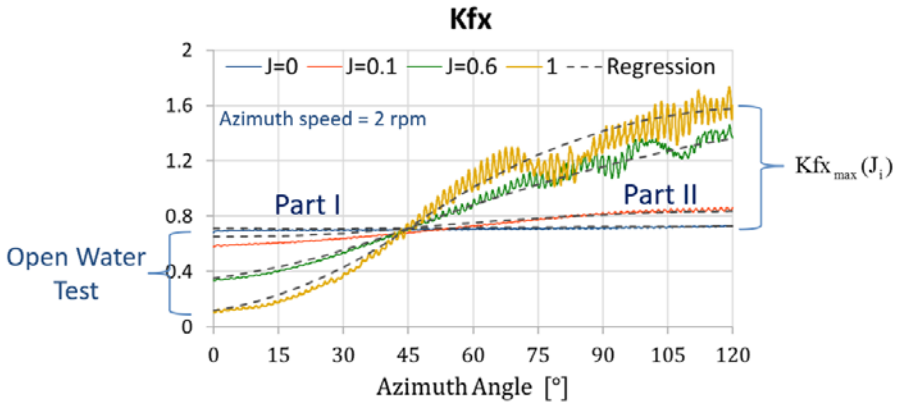

Table 7.3.: Determination of the induced velocity after eq. 7.8 (n = 2.1 Hz and D = 4.2 m)

J [-]	Kfx(120°) [-]	u_a [m/s]	u_i [m/s]	J_i [-]
0.0	0.727	0.000	5.999	0.68
0.1	0.859	0.882	6.491	0.74
0.6	1.370	5.292	7.435	0.84
1.0	1.595	8.820	7.011	0.79

Fig. 7.4.: Determination of the induced velocity after eq. 7.8 (tab. 7.3)

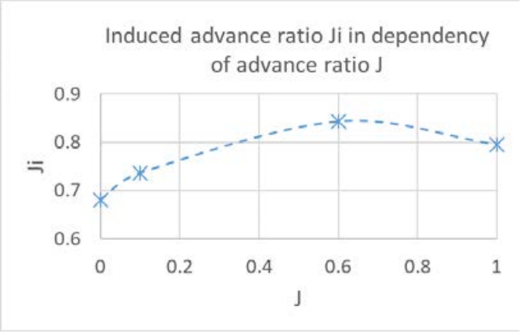

The development of Kfx(*ψ*) is considered into two parts separated at 45° (0.79 rad). The first polynomial covers the range from 0° to 45° and the second one covers 45° to 120°. If 2nd order polynomial is applied, three conditions must be full-filled. The first and second conditions are the value and its first derivation at the point of 45° (see fig. 7.3). The constant value is assumed to be Ktx (*J* = 0) at bollard pull condition and the slope of the curve is well known from fig. 7.3. The third condition is the values at 0° according to the open water test for the first polynomial. For the second polynomial, this third condition is the maximal value predicted after eq. 7.8. Then the regression curves are generated by fulfilling these three conditions as shown in fig. 7.3.

The bending moment (simply "BM") contains two components, one is caused by the longitudinal force *X* and the other part is from the transverse force *Y*. The BM is obtained by multiplying the forces with the distance *h* between propeller rotating axis and the top of the housing mounted in the ship (see Fig. 7.5). BM can be determined by given *Kfx*, *Kfy*, *n* and *D*.

$$BM \quad = \quad \sqrt{(\mathrm{Kfx} \cdot \rho n^2 D^4 \cdot h)^2 + (\mathrm{Kfy} \cdot \rho n^2 D^4 \cdot h)^2} \tag{7.10}$$

Fig. 7.5.: Geometric relation according to eq. 7.10

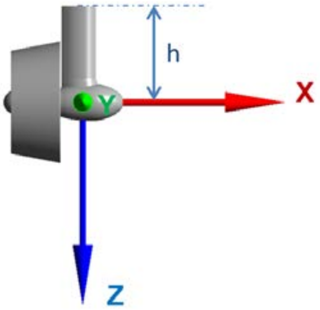

The prediction method presented above is based on the results from the open water tests and might be only valid for the pushing configuration concerning the separated flow from the housing. Nevertheless, it includes the effect of oblique flow on the exceeding loads at bollard pull condition.

7.2 T5.2.1 - Development of a prediction method for the determination of the impact of ship manoeuvers on the thrust of TT

The assessment of the efficiency of TT at ship manoeuvre can be estimated. At a first step, the manoeuvring model for TT need to be established which is based on the manoeuvring model for ship w/o TT. The purpose is to identify the significant HD, which mostly affect the turning parameters such as advance and tactical diameter. These coefficients can be extrapolated for the ship at low velocities (< 2 m/s), so that a prediction can be made instead of time-consuming RANSE-calculations.

There are two curves seen in fig. 7.6. One is obtained from turning circle simulation supported by the working TT at 2m/s ship speed (see fig. 5.44) and other presents the path derived from the HD of ship w/o TT with additional external force and moment Y_0^{TT} and N_0^{TT}. Obviously, the difference is very huge, and some HD with respect to the interaction between propeller slipstream and ship hull are still missing.

Fig. 7.6.: Difference between the turning circle simulation with- and without consideration of the interaction at 2 m/s

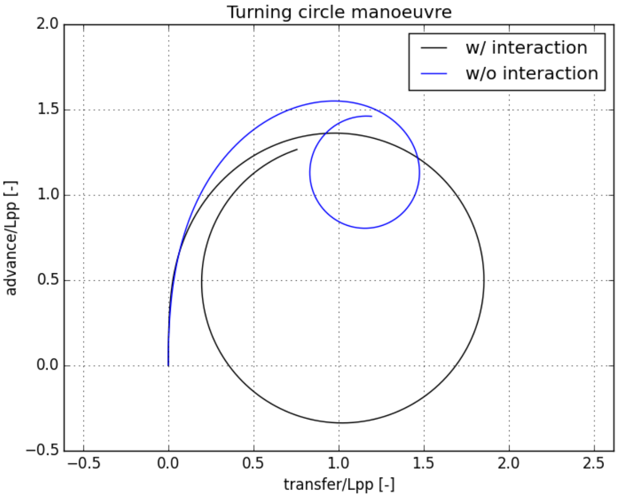

7.2.1 Reduction of Hydrodynamic Derivatives

The non-dimensional forces and moment during one period regardless of their mean values X_0, Y_0 and N_0 are shown at fig. 7.7. Most of the differences between the results for the ship w/o TT and for the ship with working TT appear at surge, pure sway and pure yaw. At surge test, the deviation of *Y*’ and *N*’ are huge, but they are not the dominant ones because of their small values in comparison to the values at sway test (see subfigure 1 ~ 2). At sway- and yaw oscillation the major part of *X*’ is the resistance of the ship, local oscillations cannot change *X*’ evidently (see subfigure 3 ~ 4). Y’ at sway test (see subfigure 5) seems to be the most possible parameter for the difference of the turning circles. Here Y’ has an amplitude of 0.003 (distance between the maximal positive and negative value). The mean value at a yaw test is about 0.007 (see Fig. 5.43). The ratio between dynamic oscillation (0.003) and the mean value (0.007) is very high (above 40%), so these deviations cannot be ignored.

Fig. 7.7.: Comparison of non-dimensional forces and moment between ship w/o TT at the five forced dynamic tests (from top to bottom: surge, sway, yaw, 1st and 2nd combined sway-yaw)

The easy way is to replace the involved *Y* HD as functions of *r* and $\dot{r}$ from ship w/o TT such as $Y_r, Y_{rrr}, Y_{\dot{r}}, Y_{\dot{r}rr}, Y_{rrv}$ and Y_{vvr} (denoted as ’$Y\,(r,\dot{r})$’) through $Y^{TT}(r,\dot{r})$ from ship with TT. The result is shown in fig. 7.8. The deviation of advance and tactical diameter are summarized in tab. 7.4.

Fig. 7.8.: Comparison of the turning circles based on the replaced model

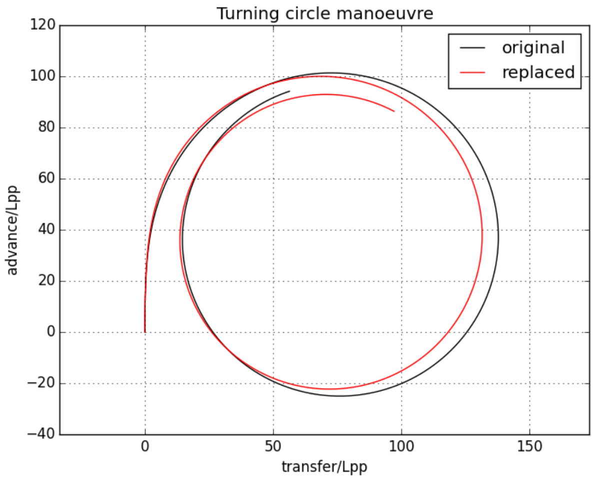

Tab. 7.4.: The deviation of turning circle parameters

	Advance [m]	Tactical Diameter [m]	Turning Diameter [m]
Original	101	138	122
Simplified	99	130	112
Deviation [%]	-2	-6	-8

Further reduction is necessary, to increase the robustness of the model. Although each item in $Y^{TT}(r,\dot{r})$ influences the turning path, but only the most significant ones within $Y^{TT}(r,\dot{r})$ need to be taken into account. They will be revealed by a sensitivity study introduced by Mucha 2015 [19]. The idea is, that we increase one derivative in $Y^{TT}(r,\dot{r})$ at once about a certain percent and keep the others unchanged. An example is shown in tab. (7.5). The deviation is defined as the change in percent in comparison with the original curve. A weighted sum each deviation (20% for advance, 60% for tactical diameter and 20% for turning diameter) is called an error. The deviation after increase of Y_{rrr} as well as Y_{rrv} is over 5%. These are the dominant hydrodynamic derivatives.

Tab. 7.5.: Change of turning parameters after increasing individual hydrodynamic derivatives up to 100%

	Deviation [%]			
	Advance	**Tactical Diameter**	**Turning Diameter**	**Error [%]**
Y_r	-1	4	11	5
Y_{rrr}	0	-6	-23	8
$Y_{\dot{r}}$	-3	-3	0	2
$Y_{\dot{r}rr}$	0	4	1	3
Y_{rrv}	-2	9	34	13
Y_{vvr}	-1	-1	-2	1

The velocity coupled acceleration terms like $Y_{\dot{v}vv}, Y_{\dot{r}rr}, N_{\dot{v}vv}$, and $N_{\dot{r}rr}$ are normally small and can also be discarded from the manoeuvring model as the path of "simplified" shown in Fig.(7.9). The simplified manoeuvring model for ship with TT can be written as eq. 7.11 ~ eq. 7.13.

$$\begin{aligned} X \cong\ & X_0 + X_0^{TT} \\ +\ & X_{\dot{u}}\dot{u} + X_u \Delta u + X_{uuu}\Delta u^3 \\ +\ & X_{vv}v^2 \\ +\ & X_{rrr}r^3 \\ +\ & X_{rv}rv \end{aligned} \tag{7.11}$$

$$\begin{aligned} Y \cong\ & Y_0 + Y_0^{TT} \\ +\ & Y_v v + Y_{vvv}v^3 + Y_{\dot{v}}\dot{v} \\ +\ & Y_r r + Y_{vvr}v^2 r + Y_{\dot{r}}\dot{r} \\ +\ & Y_{rrr}^{TT}r^3 + Y_{rrv}^{TT}r^2 v \end{aligned} \tag{7.12}$$

$$\begin{aligned} N \cong\ & N_0 + N_0^{TT} \\ +\ & N_v v + N_{vvv}v^3 + N_{\dot{v}}\dot{v} \\ +\ & N_r r + N_{rrr}r^3 + N_{\dot{r}}\dot{r} \\ +\ & N_{rrv}r^2 v + N_{vvr}v^2 r \end{aligned} \tag{7.13}$$

Fig. 7.9.: Comparison of the turning circles based on the replaced model

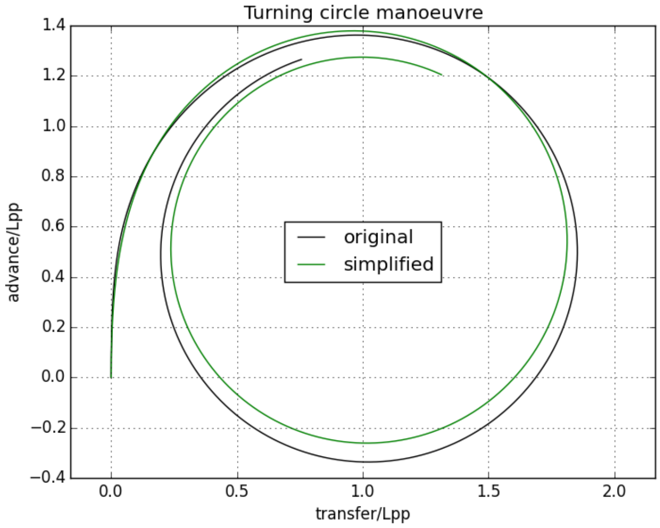

7.2.2 Prediction of hydrodynamic derivatives at ship low velocities

For two reasons a linear extrapolation has been made to find the relations between the two significant HD.

- Within small range of velocities, the linear extrapolation should be sufficient for the prediction.
- The linear dependency of Y_{rrr}^{TT} and Y_{rrv}^{TT} on the velocity has been established (see tab. 7.6).

The extrapolation is not only applied for Y_{rrr}^{TT} and Y_{rrv}^{TT} but also for the mean values $Y_0{}^{TT}$ and $N_0{}^{TT}$. The development of the dimensional and dimensionless values over the ship speed is shown in fig. 7.10. These dimensionless values can be expressed as an exponential function. Two velocities, 1 and 0.5 m/s, are involved in the extrapolation. The extrapolated coefficients are found in tab. 7.6.

Fig. 7.10.: Extrapolation of mean values Y_0 and N_0 from ship w/ TT

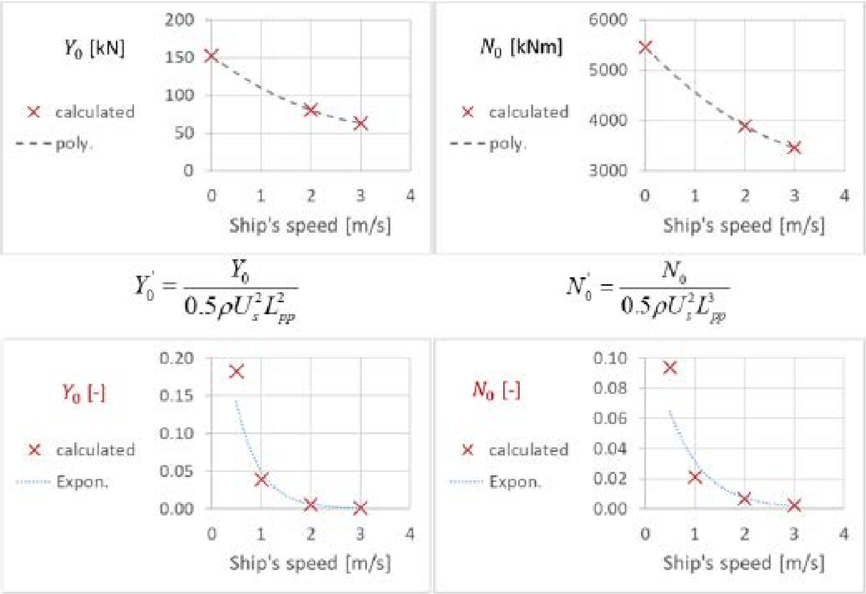

Tab. 7.6.: Dimensionless coefficients of linear extrapolation multiplied by 1e5

	predicted		**calculated**	
u_s **[m/s]**	**0.5**	**1**	**2**	**3**
Y_{rrr}^{TT}	-1319	-1048	-506	36
Y_{rrv}^{TT}	-26601	-21628	-11683	-1738
Y_{0}^{TT}	18259	3020	712	250
N_{0}^{TT}	9393	2242	461	182
X_{uuu}^{TT}	-4665	-3770	-1984	1314

The turning manoeuver of using the predicted HD can be found in fig. 7.11. The tactical diameter are smaller than the turning diameter because of the increase of longitudinal velocity *u*. Even through, the velocity *u* cannot increase continuously. Some of the damping parts are missing, especially in the longitudinal direction.

Fig. 7.11.: Predicted turning circle manoeuver at low velocities caused by the TT. (From top to bottom: 1 and 0.5m/s)

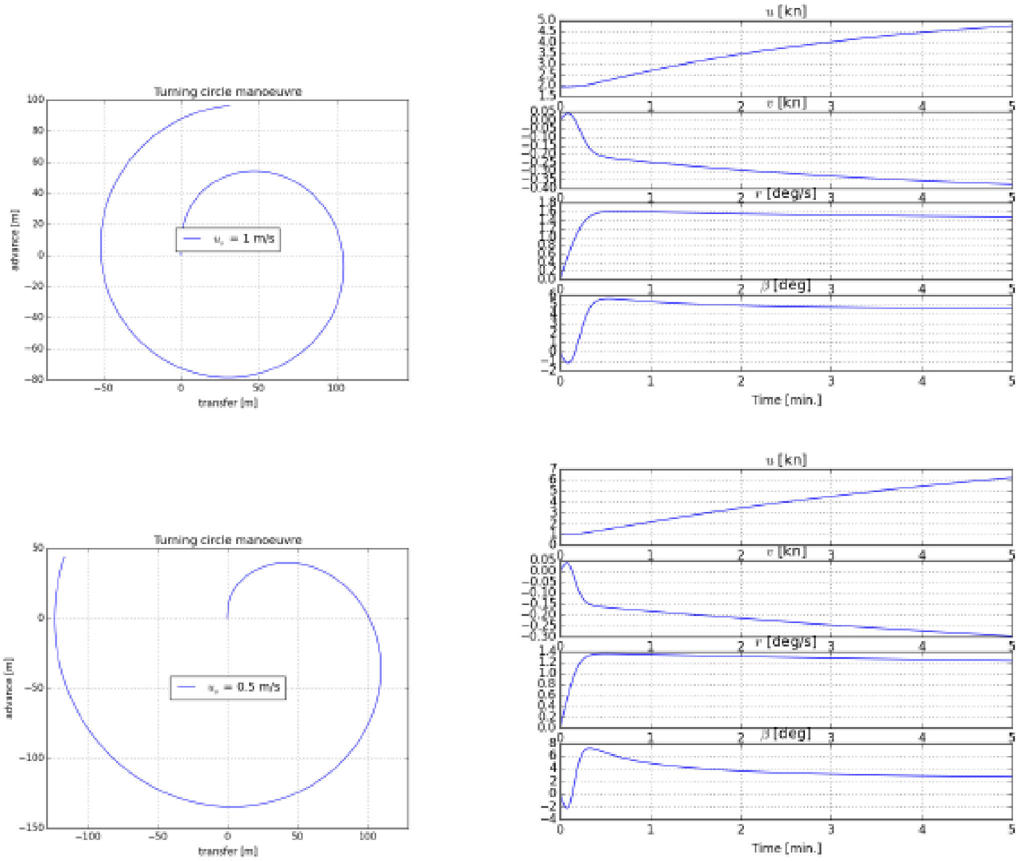

The sensitivity study has to repeat for the terms *X* in relation with *u*. The results are shown in fig. 7.12. Compared with the original curve (all *X* related HD considered which depends on *u*) are the results obtained with an additional coefficient X_{uuu}^{TT} and without X_{uuu}^{TT}.

Obviously, X_{uuu}^{TT} has to be reused for the conditions at slow velocities, but it is not remarkable at 2 m/s (see fig. 5.44). As derived from fig. 7.13 X_{u}^{TT} is sufficient to describe the function *X* of *u* in the negative range of *Δu'*. By comparison, linear approach cannot cover the tendency of the curve with increasing velocities in the positive range of *Δu'*. The predicted values of X_{uuu}^{TT} can also be found in tab. 7.6 obtained by linear interpolation.

Finally, the following equations eq. 7.14 ~ eq. 7.16 are received to present the manoeuvring model for TT.

$$
\begin{aligned}
X \cong\ & X_0 + X_0^{TT} \\
+\ & X_{\dot{u}}\dot{u} + X_u \Delta u + X_{uuu}^{TT} \Delta u^3 \\
+\ & X_{vv} v^2 \\
+\ & X_{rrr} r^3 \\
+\ & X_{rv} r v
\end{aligned} \tag{7.14}
$$

$$
\begin{aligned}
Y \cong\ & Y_0 + Y_0^{TT} \\
+\ & Y_v v + Y_{vvv} v^3 + Y_{\dot{v}}\dot{v} \\
+\ & Y_r r + Y_{vvr} v^2 r + Y_{\dot{r}}\dot{r} \\
+\ & Y_{rrr}^{TT} r^3 + Y_{rrv}^{TT} r^2 v
\end{aligned} \tag{7.15}
$$

$$
\begin{aligned}
N \cong\ & N_0 + N_0^{TT} \\
+\ & N_v v + N_{vvv} v^3 + N_{\dot{v}}\dot{v} \\
+\ & N_r r + N_{rrr} r^3 + N_{\dot{r}}\dot{r} \\
+\ & N_{rrv} r^2 v + N_{vvr} v^2 r
\end{aligned} \tag{7.16}
$$

Fig. 7.12.: Different paths according to X_{uuu}^{TT}

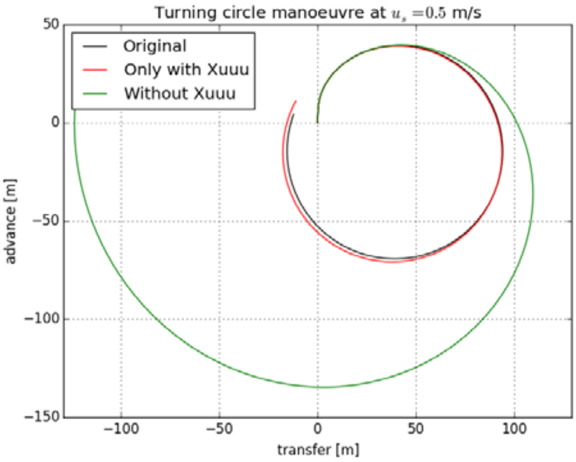

Fig. 7.13.: Dimensionless longitudinal force *X* about dimensionless Δ*u'*

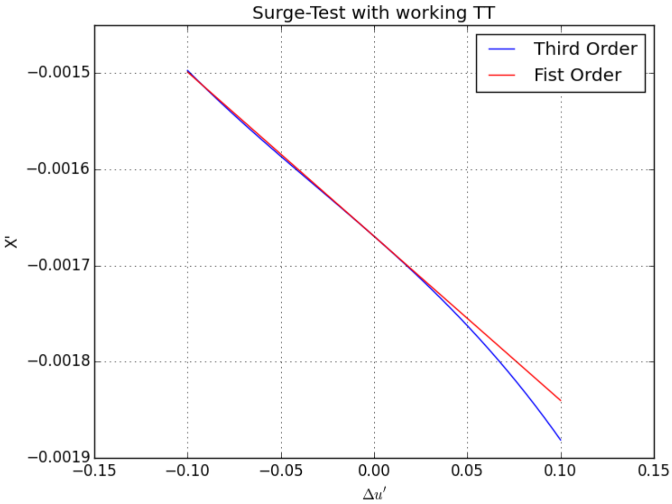

The turning manoeuvre for 3 and 4 m/s can use the same treatment just like at 2 m/s. The results based on the model developed in eq. 7.14 ∼ eq. 7.16 and are shown in fig. 7.14. The path stops in both cases if the longitudinal velocity *u* is zero.

Fig. 7.14.: Turning circle manoeuver at varied velocities

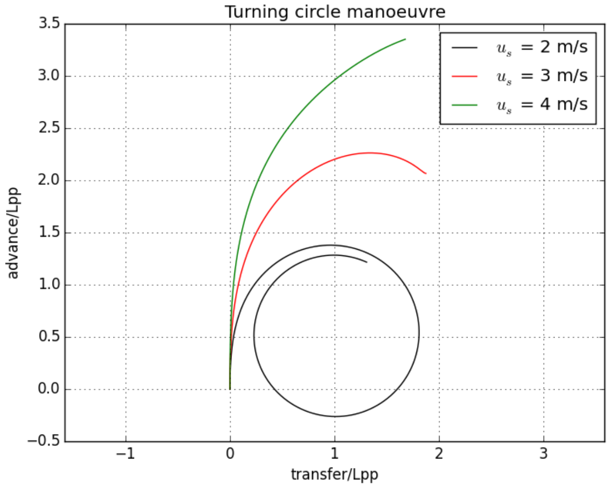

Through the sensitivity study, the terms $Y^{TT}_{rrr}, Y^{TT}_{rrv}$ and Y^{TT}_{uuu} dominate mainly the performance of the TT. The prediction for these HD at small velocities less than 2 m/s is based on the linear extrapolation whereas the HD of mean values of forces and moment have the exponential dependency of the velocity. Some variation tests with respect to revolution number of TT, ship velocity and the number of working TT will be discussed in the next section.

7.3 T5.3.1 - Development of a calculation method for determining the influence of operating conditions of TT and MP on the manoeuvrability of the vessel

The influence of dynamic loads caused by the combination of working MP and TT on the manoeuvrability is currently of interest. The results from T5.2.1 are derived under the assumption, that the MP has no response to the change of ship course angle and speed. In this section, the cooperation of MP and TT at different azimuth angles will be discussed. The simulation is based on the manoeuvring model developed in eq. 6.24 ~ 6.26. According to the operation condition of TT, the velocities at/below 2 m/s will be considered.

Actually, MP is fixed at the position of $\psi = 0°$, a positive inflow angle towards the MP can be still occurred due to ship heading angle β. In order to reduce the turning circle, the azimuth angle ψ has to be negative and overshoot the angle of β as shown in fig. 7.15.

Fig. 7.15.: Definition of the parameters during a turning circle manoeuvre

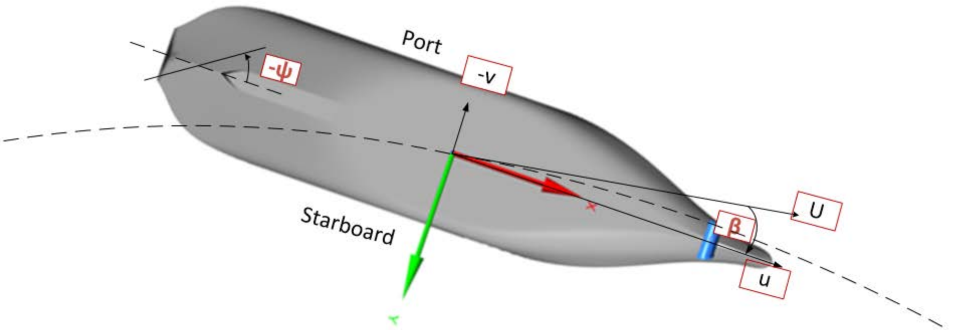

The propeller revolution number during the ship turn is constant and obtained from cross point of K_t-curves as discussed previously. The reduction of longitudinal velocity *u* is taken place in case of ship w/o TT. For this reason, the circle is not completely drawn as shown in fig. 7.16. The asymmetry is due of asymmetric equipped gear housing in the tunnel (no propeller).

Fig. 7.16.: The path of the ship till to the longitudinal velocity u_s being zero at different azimuth angles ψ at u_s = 2 m/s

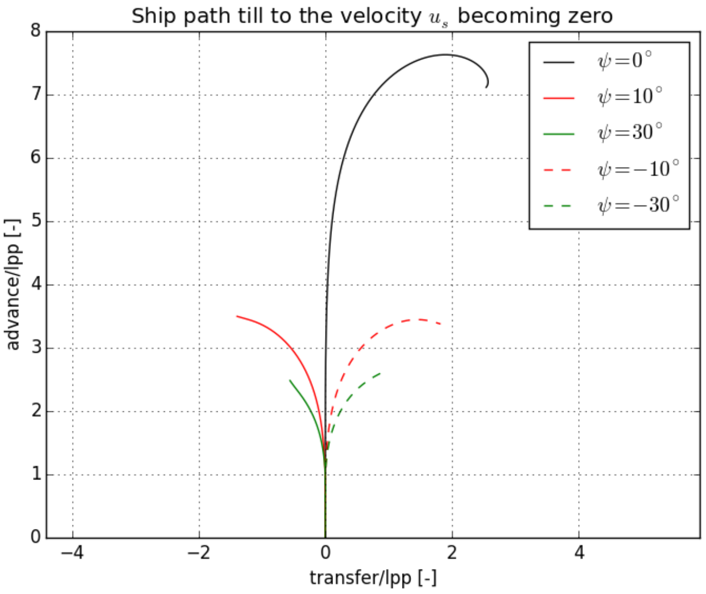

In order to generate a circle, a certain higher revolution number of MP is required, but oppositely, the parameters such as advance and tactical diameter increase because of increasing thrust from MP. It is proper to use the TT as devices supporting the ship in the turning manoeuvre at ship low velocities. The bow thruster can not only provide transverse force and yaw moment but also the longitudinal velocity.

7.3.1 Variation of azimuth angles

The simulation concerning different azimuth angles is shown in fig. 7.17 which is considered only to $\psi = -20°$ otherwise, the maximal β can exceed the defined ”small angles” set in the dynamic tests. The azimuth speed is chosen to be 2°/s, in addition with the yaw velocity of the ship of r < 2°/s (obtained from time history of *r*). The dynamic part of transverse force *Y* is still small (*f* = 0.011 rpm) and can be ignored.

The difference of advance and tactical diameter increases from $\psi = -20° \sim 20°$. The reason is, that at positive ψ the transverse force of TT and MP has the same direction (points to starboard) which leads to an additional shift contributed to the circle whereas it is not the case at negative ψ. The maximal difference of the tactical diameter is about 40% taken from tab. 7.7.

Fig. 7.17.: Variation of azimuth angles ψ in the turning circle simulation of one TT at 2 m/s

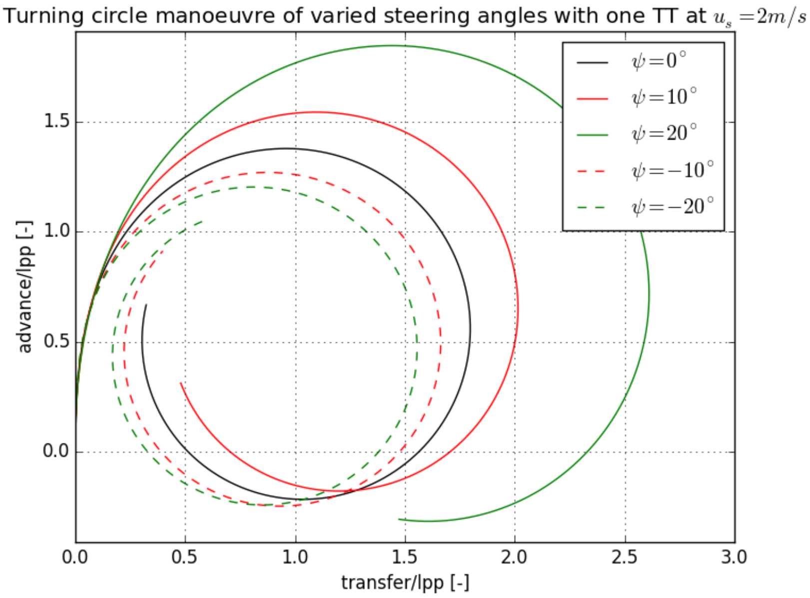

Tab. 7.7.: Parameters for turning circle manoeuvre (see fig. 7.17)

$u_s = 2$ m/s with one TT					
ψ [°]	-20	-10	0	10	20
Advance/Lpp [-]	1.19	1.26	1.37	1.54	1.84
Tactical Diameter/Lpp [-]	1.55	1.65	1.79	2.01	2.61
Steady β [°]	9.09	8.28	7.70	7.02	5.41

7.3.2 Variation of number of TT

Until now, only one TT has been taken into account, regarding to the study done by SINTEF that the interaction between two TTs are very small at the condition of zero ship speed. It is assumed that the HD for the second one can be taken over from the first one, which means, the HD related terms (see eq. 6.24 ~ eq. 6.26) will be doubled, if two TTs are in operation. The resistance of the ship due to increased number of TTs has to be updated. The operation point and corresponding revolution number of MP change subsequently.

The results are shown in the following figures and table. In this case, the azimuth angle ψ is set to be zero so that the inflow angle to MP is equal to the heading angle β. In comparison to one TT, the advance as well as the tactical diameter is getting smaller. However, the difference between 2 and 3 is less significant than the difference between 1 and 2 due to the increase of longitudinal velocity u.

Fig. 7.18.: Variation of number of TT at 2 m/s (predicted)

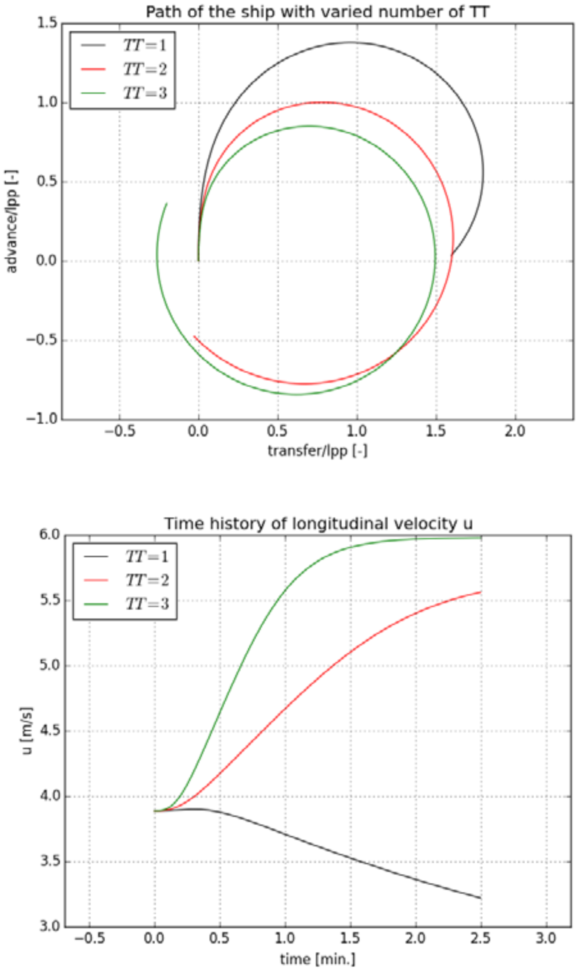

Tab. 7.8.: Parameters for turning circle manoeuvre (see fig. 7.18)

$\psi = 0$			
number of TT [-]	**1**	**2**	**3**
Advance/Lpp [-]	1.37	1.00	0.85
Tactical Diameter/Lpp [-]	1.79	1.60	1.49
β (max) [°]	7.70	4.74	3.94

7.3.3 Variation of ship speed

The extrapolated HD in tab. 7.6 are used for the prediction of turning circle at low velocities less than 2 m/s. In fig. 7.19 the turning manoeuvre at the velocities us = 1m/s and 0.5m/s from top to bottom is presented. The result shows that the effect of azimuth angle ψ on ship path is getting lost while reducing the ship speed. The reason is, that the increasing transverse force at ship low speed enlarges the difference to the MP.

Fig. 7.19.: Variation of ship speed at different azimuth angles ψ in the turning circle simulation of one TT (predicted)

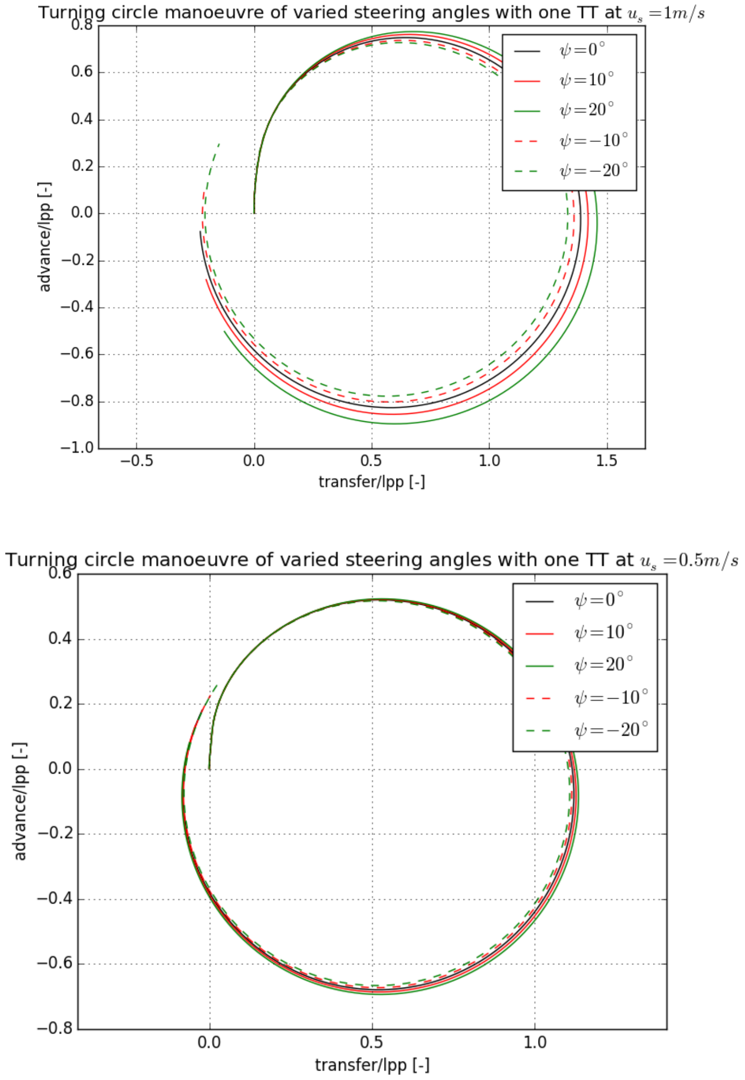

Tab. 7.9.: Parameters for turning circle manoeuvre (see fig. 7.19)

$\psi = 0^\circ$ with one TT		
u_s [m/s]	**1**	**0.5**
Advance/Lpp [-]	0.75	0.52
Tactical Diameter/Lpp [-]	1.39	1.12
Steady β [°]	4.73	4.71

7.3.4 Variation of revolution number of TT

As known in WP3.1.2, the force and torque derived from the TT have the square relation to the revolution number. It is assumed that the interaction related terms Y_{rrr}, Y_{rrv} and X_{uuu} have the same dependency. The result is shown in fig. 7.20. The production and reduction denote the percentage increment and decrement relative to the original rps, respectively.

Fig. 7.20.: Variation of rps in the turning circle simulation of one TT at $u_s = 2m/s$ and $\psi = -20°$ (green paths are predicted)

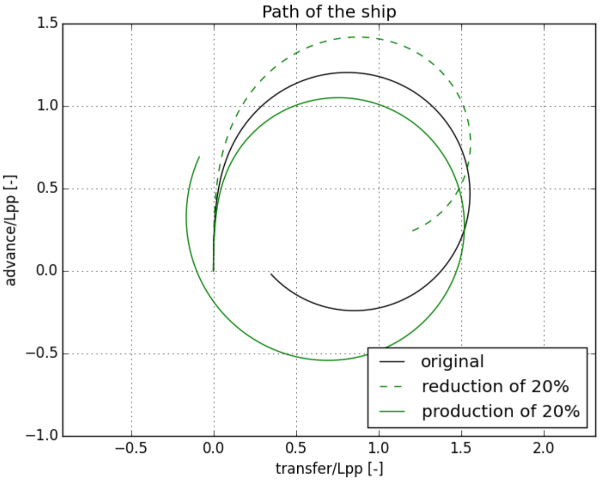

The accuracy of the results is based on the HD involved in the manoeuvring equations. The motion parameters like u', v' and r' should be chosen appropriately to reach the desired accuracy of the CFD-computation. In the presence of the working TT, large amplitude and small oscillation frequency ω' are preferred to cover the non-linearity's of the HD.

The development of slipstream during the ships turn plays an important role, which can be effected by the water line angle and the position of TT.

Some of experimental or CFD results at low velocities are still required to gain more information about the tendency of the HD as the function of the velocity. A non-linear relationship between them will be expected.

8 Conclusions and future work

The present work has fulfilled the requirements of the project Inter-SimPLex. A huge amount of numerical simulations were carried out for investigating off-design conditions for the azimuth thruster as well as ship manoeuvring in consideration of working tunnel thruster at ship low speed. This study includes following subjects:

Azimuth thruster:

- Investigation and analysis of critical cases with high dynamic loads
- Establishment of a prediction method

Here the azimuth thruster operates in inclined flow. A mathematical model has been developed for the prediction of loads in order to give relevant information. The prediction was made of the results provided by the RANSE simulation. The reliability of the calculations is very important. The prediction depends directly on the grid quality and the numerical settings such as turbulence model or the presence of the cavitating flow. Validations were made and some results were discussed in context of the physical phenomena.

Tunnel Thruster:

- Analysis of efficiency loss of tunnel thruster in dependency of ship speed and course angle
- Development of a calculating method for the performance of tunnel thruster in the turning circle manoeuvre

Tunnel thruster-hull interaction is dominated by the deflected slipstream from the bow thruster, which has strong influence on the pressure distribution on ship hull. A detailed study referred to the ship speed and course angle was carried out.

At the end turning circle manoeuvre at varied operation conditions including azimuth angle, number of tunnel thruster, ship speed and revolution number of tunnel thruster were achieved. The significant hydrodynamic derivatives in the manoeuvring equation for tunnel thruster at ship’s velocity of 2 m/s were identified. Due to the insufficient number of CFD results available for very low ship velocities, usage of these terms are still not common.

The computational effort of the simulation including the rotating propeller is very huge especially in case of low ship velocities; an improved method of replacing the fully modelled propeller is still required in the further work.

Bibliography

[1] Abdel-Maksoud, M. (2011). *Manövrierfähigkeit von Schiffen*. Hamburg, Germany: Hamburg University of Technology

[2] Abkowitz, M.A. (1964). *Lectures on Ship Hydrodynamics - Steering and Manoeuvrability*. Technical Report Hy-5. Lyngby, Denmark: Hydrodynamisk og aerodynamisk Laboratorium

[3] Akinturk, A., Islam, M. F., Veitch, B. and Liu, P. (2012). Performance of dynamic azimuthing podded propulsor. *International Shipbuilding Progress*, 59(1-2), pp. 83 – 106

[4] Amini, H. and Steen S. (2011). Experimental and Theoretical Analysis of Propeller Shaft Loads in Oblique Inflow. *Journal of Ship Research*, 55(4), pp. 1 -21,

[5] Amini, H., Sileo, L. and Steen, S. (2012). Numerical Calculation of the Propeller Shaft Loads in Oblique Inflow. *Journal of Marine Science and Technology*, 17(4), pp. 403 - 421

[6] ANSYS. Inc. (2013). *ANSYS CFX-Solver modeling guide*, release 15.0., Canonsburg, PA: Ansys Inc.

[7] Carlton, J. (2012). *Marine propellers and propulsion,* 3rd edition. Kidlington, Oxford, U.K.: Butterworth-Heinemann

[8] Crane, C. L., Eda, J. and Landsburg, A. (1989). *Controllability*. In: Lewis, E. V. (Ed.): *Principles of Naval Architecture - Vol. III - Motions in Waves and Controllability*., 2nd Rev., Jersey City: Society of Naval Architects and Marine Engineers

[9] English, J. W. and Steele, B. N. (1962). *The performance of lateral thrust units for ships as affected by forward speed and proximity of a wall*. Technical Report SH R28/62, Feltham, U.K.: National Physics Laboratory, Ship Division

[10] Ferziger, J. H. and Peric, M. (2002). *Computational method for fluid dynamics,* 3rd edition, Berlin, Germany: Springer-Verlag

[11] Huse, E. (1971). Propeller-Hull Vortex Cavitation. *Norw. Ship Model Exp. Tank Publ.*, No. 106 (May)

[12] Islam, M. F., Akinturk, A. and Veitch, B. (2016). Performance aspects of podded propulsor in dynamic operating conditions. *International Shipbuilding Progress*, 62(3-4), pp. 139 - 160

[13] Islam, M. F., Akinturk, A., Liu, P. and Veitch, B. (2007). Performance Characteristics of a Podded Propulsor During Dynamic Azimuthing. In: *Proc. of the 8th CMHSC 2007*, St John's, Canada, 8p

[14] ITTC (2008). *Model manufacture, propeller models terminology and nomenclature for propeller geometry*, 7.5-01-02-01. The International Towing Tank Conference – Recommended Procedures and Guidelines, Lyngby, Denmark: ITTC

[15] ITTC (2014). *Captive model test procedure*, 7.5-02-06-02. The International Towing Tank Conference - Recommended Procedures and Guidelines, Lyngby, Denmark: ITTC

[16] Keck, R.-E. (2012). A numerical investigation of nacelle anemometry for a HAWT using actuator disc and line models in CFX. *Renewable Energy*, 48(Dec.), pp 72 - 84

[17] Krasilnikov, V. (2017). *Algorithm for Preliminary Calculation of the Characteristics of a Tunnel Thruster*, Trondheim, Norway: SINTEF Ocean, not published

[18] Liu, P., Islam, M. and Veitch, B. (2009) Some Unsteady Propulsive Characteristics of a Podded Propeller Unit under Maneuvering Operation. In: *Proc. of the First International Symposium on Marine Propulsors smp'09*, Trondheim, Norway, 8p

[19] Mucha, P. and el Moctar, O. (2015). Revisiting mathematical models for manoeuvring prediction based on modified Taylor-series expansions. *Ship Technology Research*, 62(2), pp 81 - 96

[20] Neitzel, J. C., Pergande, M., Berger, S. and Abdel-Maksoud, M. (2015). Influence of the numerical propulsion modelling on the velocity distribution behind the propulsion device and maneuvering forces. In: Kinnas, S. A. (Ed.) *Proc. of the Fourth International Symposium on Marine Propulsors smp'15*, Austin, Texas, pp 361 - 370

[21] Stern, F., Kim, H. T., Patel, V. C. and Chen H.C. (1988). A viscous-flow approach to the computation of propeller-hull interaction. *Journal of Ship Research*, 32(4), pp 246 - 262

[22] Wolff, K. (1981). Ermittlung der Manövriereigenschaften fünf repräsentativer Schiffstypen mit Hilfe von CPMC-Modellversuchen. *Schriftenreihe Schiffbau*, 412(Dec), 161p, German

[23] Yongle, D., Baowei, S. and Peng, W. (2015). Numerical investigation of tip clearance effects on the performance of ducted propeller. *International Journal of Naval Architecture and Ocean Engineering*, 7(5), pp 795 - 804

A Geometric specifications of generic model thruster from MARINTEK

A.1. Housing and duct(all domensions in [mm])

Figure A.1.: Left: Top view drawing of the housing. Right: Half part of duct cross section

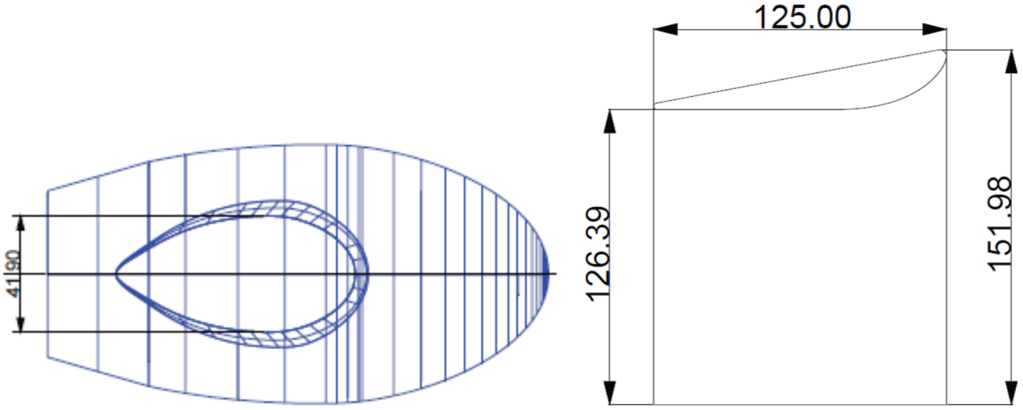

Figure A.2.: Side view of the housing.

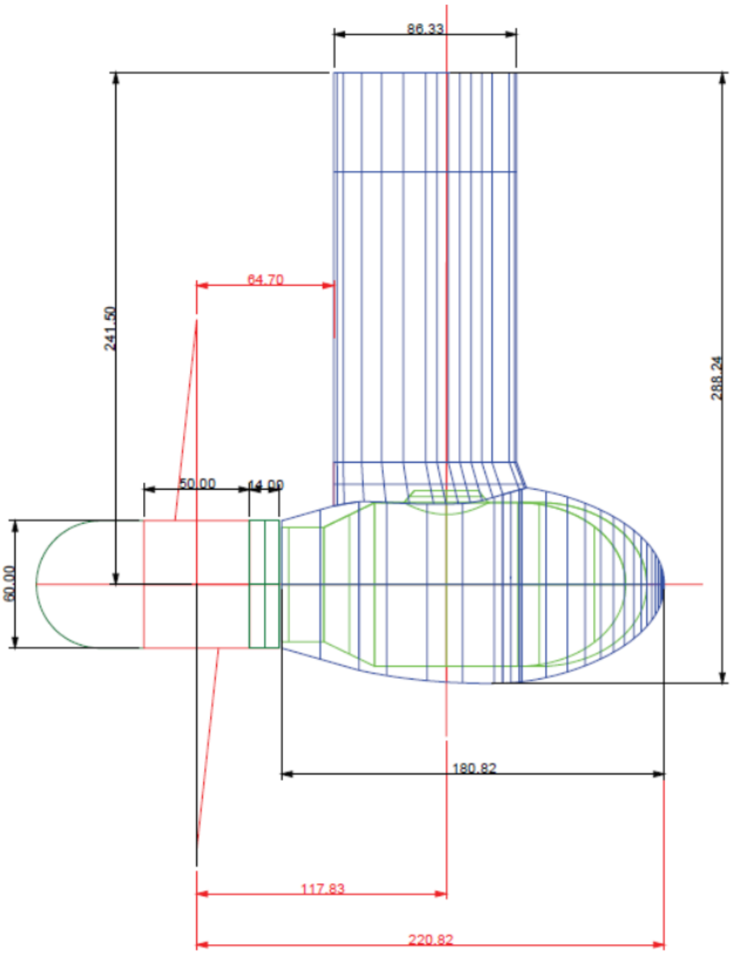

A.2. Propeller(all domensions in [mm])

Figure A.3.: Blade drawing.

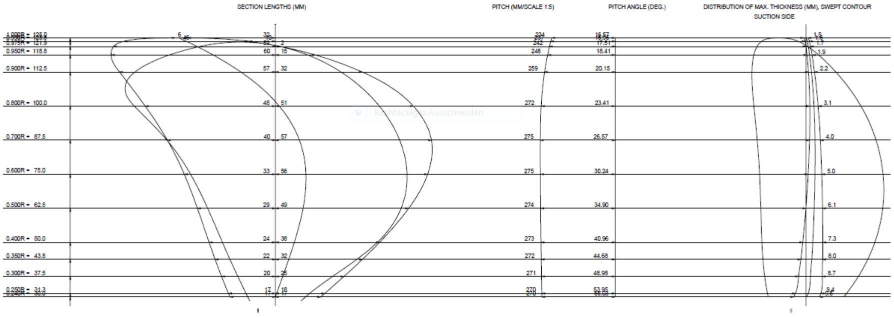

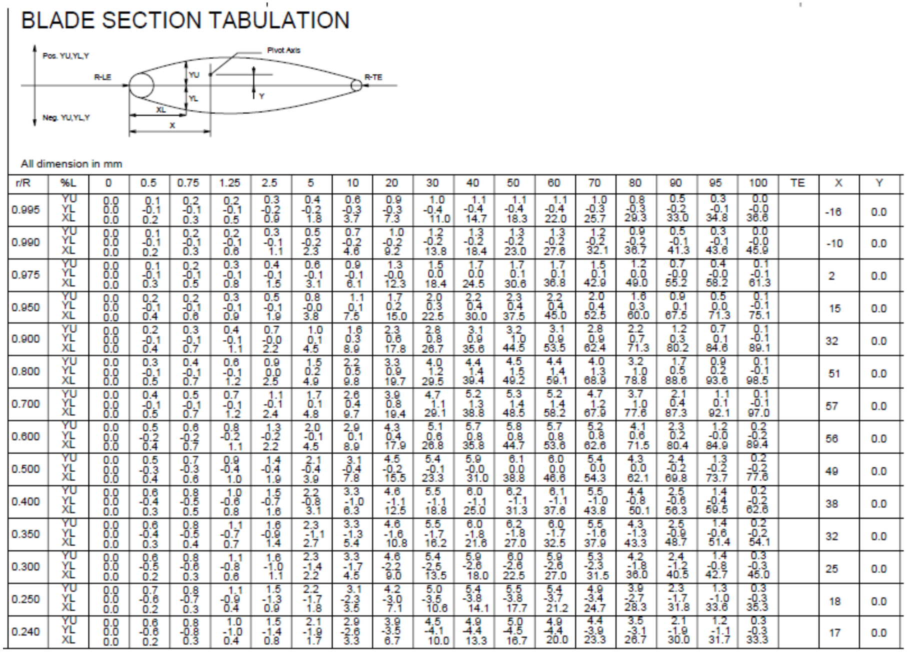

BLADE SECTION TABULATION

All dimension in mm

r/R	%L	0	0.5	0.75	1.25	2.5	5	10	20	30	40	50	60	70	80	90	95	100	TE	X	Y
0.995	YU YL XL	0.0 0.0 0.0	0.1 -0.1 0.2	0.2 -0.1 0.3	0.2 -0.1 0.5	0.3 -0.2 0.9	0.4 -0.2 1.8	0.6 -0.3 3.7	0.9 -0.3 7.3	1.0 -0.4 11.0	1.1 -0.4 14.7	1.1 -0.4 18.3	1.1 -0.4 22.0	1.0 -0.3 25.7	0.8 -0.3 29.3	0.5 -0.2 33.0	0.3 -0.1 34.8	0.0 -0.0 36.6		-16	0.0
0.990	YU YL XL	0.0 0.0 0.0	0.1 -0.1 0.2	0.2 -0.1 0.3	0.2 -0.1 0.6	0.3 -0.1 1.1	0.5 -0.2 2.3	0.7 -0.2 4.6	1.0 -0.2 9.2	1.2 -0.2 13.8	1.3 -0.2 18.4	1.3 -0.2 23.0	1.3 -0.2 27.6	1.2 -0.2 32.1	0.9 -0.2 36.7	0.5 -0.1 41.3	0.3 -0.1 43.6	0.0 -0.0 45.9		-10	0.0
0.975	YU YL XL	0.0 0.0 0.0	0.1 -0.1 0.3	0.2 -0.1 0.5	0.3 -0.1 0.8	0.4 -0.1 1.5	0.6 -0.1 3.1	0.9 -0.1 6.1	1.3 -0.0 12.3	1.5 0.0 18.4	1.7 0.0 24.5	1.7 0.1 30.6	1.7 0.1 36.8	1.5 0.1 42.9	1.2 0.0 49.0	0.7 -0.0 55.2	0.4 -0.0 58.2	0.1 -0.1 61.3		2	0.0
0.950	YU YL XL	0.0 0.0 0.0	0.2 -0.1 0.4	0.2 -0.1 0.6	0.3 -0.1 0.9	0.5 -0.1 1.9	0.8 -0.0 3.8	1.1 0.1 7.5	1.7 0.2 15.0	2.0 0.3 22.5	2.2 0.4 30.0	2.3 0.4 37.5	2.2 0.4 45.0	2.0 0.4 52.5	1.6 0.3 60.0	0.9 0.1 67.5	0.5 0.0 71.3	0.1 -0.1 75.1		15	0.0
0.900	YU YL XL	0.0 0.0 0.0	0.2 -0.1 0.4	0.3 -0.1 0.7	0.4 -0.1 1.1	0.7 -0.0 2.2	1.0 0.1 4.5	1.6 0.3 8.9	2.3 0.6 17.8	2.8 0.8 26.7	3.1 0.9 35.6	3.2 1.0 44.5	3.1 0.9 53.5	2.8 0.9 62.4	2.2 0.7 71.3	1.2 0.3 80.2	0.7 0.1 84.6	0.1 -0.1 89.1		32	0.0
0.800	YU YL XL	0.0 0.0 0.0	0.3 -0.1 0.5	0.4 -0.1 0.7	0.6 -0.1 1.2	0.9 0.0 2.5	1.5 0.2 4.9	2.2 0.5 9.8	3.3 0.9 19.7	4.0 1.2 29.5	4.4 1.4 39.4	4.5 1.5 49.2	4.4 1.4 59.1	4.0 1.3 68.9	3.2 1.0 78.8	1.7 0.5 88.6	0.9 0.2 93.6	0.1 -0.1 98.5		51	0.0
0.700	YU YL XL	0.0 0.0 0.0	0.4 -0.1 0.5	0.5 -0.1 0.7	0.7 -0.1 1.2	1.1 -0.1 2.4	1.7 0.1 4.8	2.6 0.4 9.7	3.9 0.8 19.4	4.7 1.1 29.1	5.2 1.3 38.8	5.3 1.4 48.5	5.2 1.4 58.2	4.7 1.2 67.9	3.7 1.0 77.6	2.1 0.4 87.3	1.1 0.1 92.1	0.1 -0.1 97.0		57	0.0
0.600	YU YL XL	0.0 0.0 0.0	0.5 -0.2 0.4	0.6 -0.2 0.7	0.8 -0.2 1.1	1.3 -0.2 2.2	2.0 -0.1 4.5	2.9 0.1 8.9	4.3 0.4 17.9	5.1 0.6 26.8	5.7 0.8 35.8	5.8 0.8 44.7	5.7 0.8 53.6	5.2 0.8 62.6	4.1 0.6 71.5	2.3 0.2 80.4	1.2 -0.0 84.9	0.2 -0.2 89.4		56	0.0
0.500	YU YL XL	0.0 0.0 0.0	0.5 -0.3 0.4	0.7 -0.3 0.6	0.9 -0.4 1.0	1.4 -0.4 1.9	2.1 -0.4 3.9	3.1 -0.4 7.8	4.5 -0.2 15.5	5.4 -0.1 23.3	5.9 -0.0 31.0	6.1 0.0 38.8	6.0 0.0 46.6	5.4 0.0 54.3	4.3 0.0 62.1	2.4 -0.2 69.8	1.3 -0.2 73.7	0.2 -0.2 77.6		49	0.0
0.400	YU YL XL	0.0 0.0 0.0	0.6 -0.4 0.3	0.8 -0.5 0.5	1.0 -0.6 0.8	1.5 -0.7 1.6	2.2 -0.8 3.1	3.3 -1.0 6.3	4.6 -1.1 12.5	5.5 -1.1 18.8	6.0 -1.1 25.0	6.2 -1.1 31.3	6.1 -1.1 37.6	5.5 -1.0 43.8	4.4 -0.8 50.1	2.5 -0.6 56.3	1.4 -0.4 59.5	0.2 -0.2 62.6		38	0.0
0.350	YU YL XL	0.0 0.0 0.0	0.6 -0.4 0.3	0.8 -0.5 0.4	1.1 -0.7 0.7	1.6 -0.9 1.4	2.3 -1.1 2.7	3.3 -1.3 5.4	4.6 -1.6 10.8	5.5 -1.7 16.2	6.0 -1.8 21.6	6.2 -1.8 27.0	6.0 -1.7 32.5	5.5 -1.6 37.9	4.3 -1.3 43.3	2.5 -0.9 48.7	1.4 -0.6 51.4	0.2 -0.2 54.1		32	0.0
0.300	YU YL XL	0.0 0.0 0.0	0.6 -0.5 0.2	0.8 -0.6 0.3	1.1 -0.8 0.6	1.6 -1.0 1.1	2.3 -1.4 2.2	3.3 -1.7 4.5	4.6 -2.2 9.0	5.4 -2.5 13.5	5.9 -2.6 18.0	6.0 -2.6 22.5	5.9 -2.6 27.0	5.3 -2.3 31.5	4.2 -1.8 36.0	2.4 -1.2 40.5	1.4 -0.8 42.7	0.3 -0.3 45.0		25	0.0
0.250	YU YL XL	0.0 0.0 0.0	0.7 -0.6 0.2	0.8 -0.7 0.3	1.1 -0.9 0.4	1.5 -1.3 0.9	2.2 -1.7 1.8	3.1 -2.3 3.5	4.2 -3.0 7.1	5.0 -3.5 10.6	5.4 -3.8 14.1	5.5 -3.8 17.7	5.4 -3.7 21.2	4.9 -3.4 24.7	3.9 -2.7 28.3	2.3 -1.7 31.8	1.3 -1.0 33.6	0.3 -0.3 35.3		18	0.0
0.240	YU YL XL	0.0 0.0 0.0	0.6 -0.6 0.2	0.8 -0.8 0.3	1.0 -1.0 0.4	1.5 -1.4 0.8	2.1 -1.9 1.7	2.9 -2.6 3.3	3.9 -3.5 6.7	4.5 -4.1 10.0	4.9 -4.4 13.3	5.0 -4.5 16.7	4.9 -4.4 20.0	4.4 -3.9 23.3	3.5 -3.1 26.7	2.1 -1.9 30.0	1.2 -1.1 31.7	0.3 -0.3 33.3		17	0.0

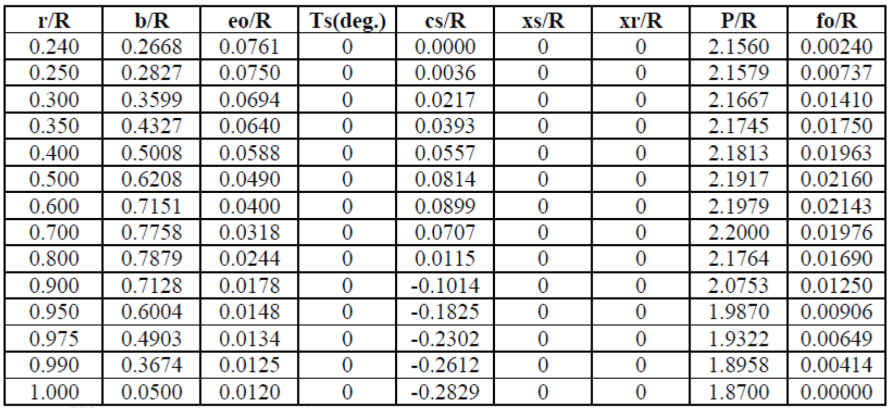

r/R	b/R	eo/R	Ts(deg.)	cs/R	xs/R	xr/R	P/R	fo/R
0.240	0.2668	0.0761	0	0.0000	0	0	2.1560	0.00240
0.250	0.2827	0.0750	0	0.0036	0	0	2.1579	0.00737
0.300	0.3599	0.0694	0	0.0217	0	0	2.1667	0.01410
0.350	0.4327	0.0640	0	0.0393	0	0	2.1745	0.01750
0.400	0.5008	0.0588	0	0.0557	0	0	2.1813	0.01963
0.500	0.6208	0.0490	0	0.0814	0	0	2.1917	0.02160
0.600	0.7151	0.0400	0	0.0899	0	0	2.1979	0.02143
0.700	0.7758	0.0318	0	0.0707	0	0	2.2000	0.01976
0.800	0.7879	0.0244	0	0.0115	0	0	2.1764	0.01690
0.900	0.7128	0.0178	0	-0.1014	0	0	2.0753	0.01250
0.950	0.6004	0.0148	0	-0.1825	0	0	1.9870	0.00906
0.975	0.4903	0.0134	0	-0.2302	0	0	1.9322	0.00649
0.990	0.3674	0.0125	0	-0.2612	0	0	1.8958	0.00414
1.000	0.0500	0.0120	0	-0.2829	0	0	1.8700	0.00000

! BRL passes through the middle point of the root section !
* b - blade section chord length;
* eo - maximum blade section thickness;
* Ts - blade section skew angle [deg.], positive to forward;
* cs - blade section skew, positive to forward (to leading edge);
* xs - blade section full rake (skew included), positive to forward;
* xr - blade section partial rake (skew excluded), positive to forward;
* P - blade section pitch;
* f - blade section maximum camber.

B Additional Tables and Diagrams of Simulations Results

B.1. case1: J=0, $\beta = 0°$

Setup	kt Propeller	10kq Propeller	kt Duct	kt Total	kside Duct	kside Total	10M Total
Experiment	0,3300	0,6000	0,3560	0,6340	0,0030	-0,0130	0,0150
2.7 M SST	0,3288	0,5955	0,3268	0,6101	0,0015	0,0035	0,0182
6 M SST	0,3269	0,5921	0,3350	0,6162	0,0016	0,0030	0,0222
20 M SST	0,3278	0,5936	0,3395	0,6214	0,0008	0,0030	0,0204
53 M SST	0,3308	0,5998	0,3427	0,6273	0,0008	0,0033	0,0176
20 M k-omega	0,3200	0,5996	0,3319	0,6089	0,0025	0,0053	0,0253
20 M BSL-EARSM	0,3283	0,5948	0,3388	0,6218	0,0034	0,0048	0,0235
20 M SAS-SST	0,3282	0,5946	0,3389	0,6213	0,0121	0,0176	-0,0280
27 M DES	0,3197	0,5940	0,3371	0,6136	0,0108	0,0142	-0,0206

Setup	kt Propeller	10kq Propeller	kt Duct	kt Total	kside Duct	kside Total	10M Total
Experiment	100,0	100,0	100,0	100,0	100,0	100,0	100,0
2.7 M SST	99,6	99,2	91,8	96,2	50,0	-26,8	121,0
6 M SST	99,1	98,7	94,1	97,2	51,9	-22,9	148,1
20 M SST	99,3	98,9	95,4	98,0	27,3	-23,2	136,1
53 M SST	100,2	100,0	96,3	98,9	27,8	-25,8	117,5
20 M k-omega	97,0	99,9	93,2	96,0	81,8	-41,1	168,7
20 M BSL-EARSM	99,5	99,1	95,2	98,1	112,9	-36,6	156,9
20 M SAS-SST	99,5	99,1	95,2	98,0	402,2	-135,3	-186,7
27 M DES	96,9	99,0	94,7	96,8	360,0	-109,1	-137,3

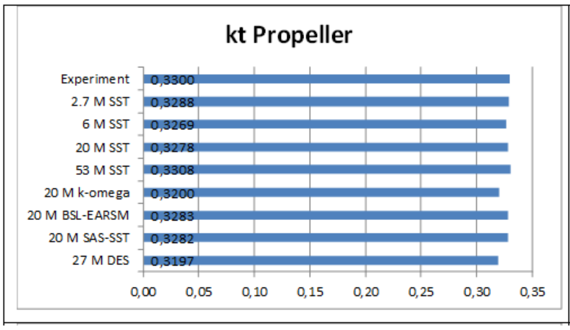

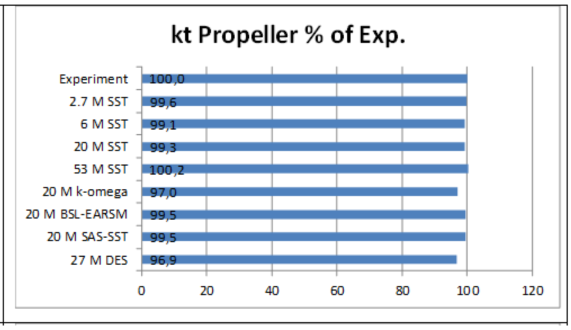

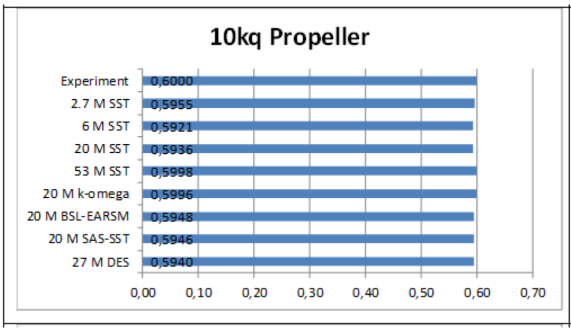

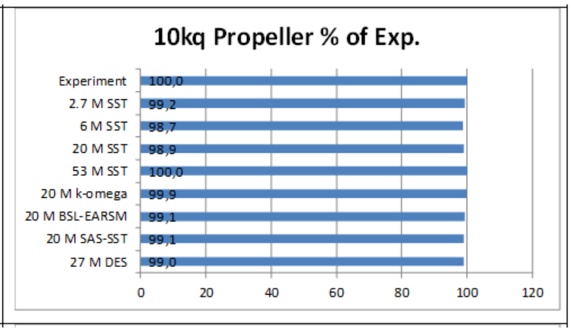

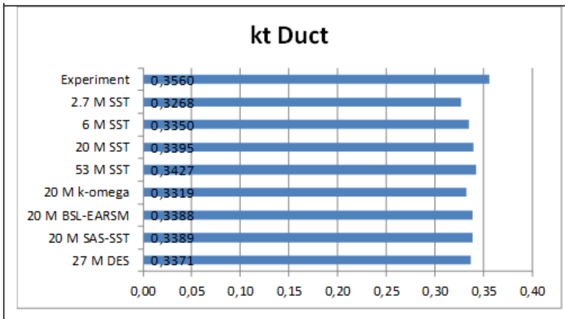

kt Duct

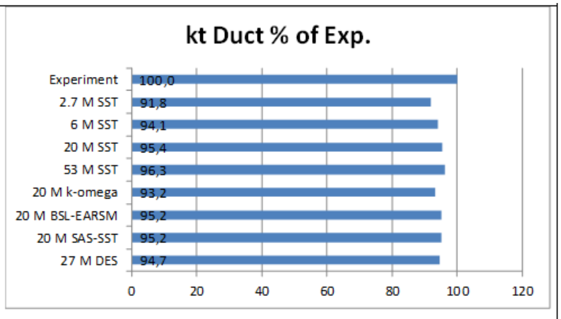

kt Duct % of Exp.

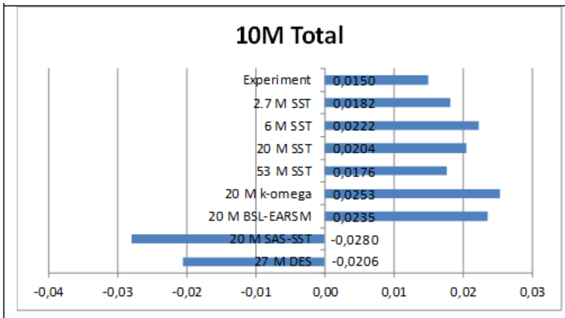

10M Total

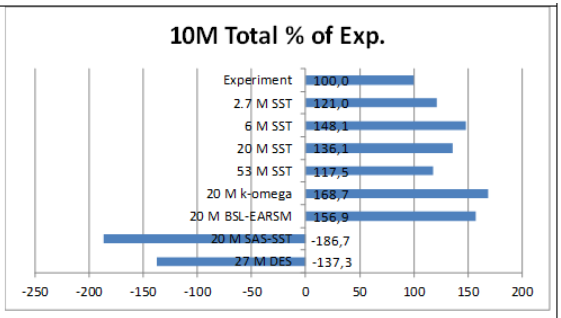

10M Total % of Exp.

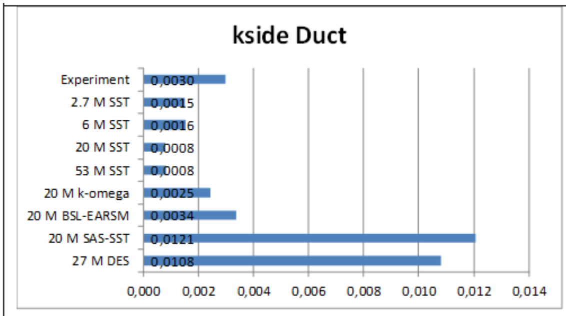

kside Duct

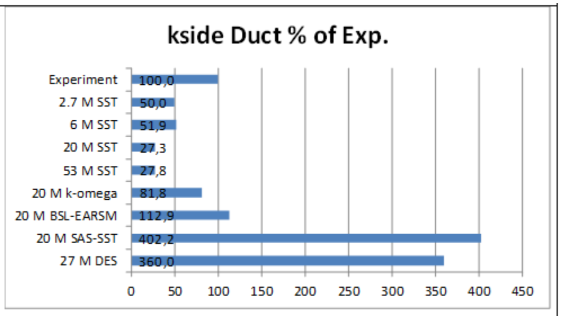

kside Duct % of Exp.

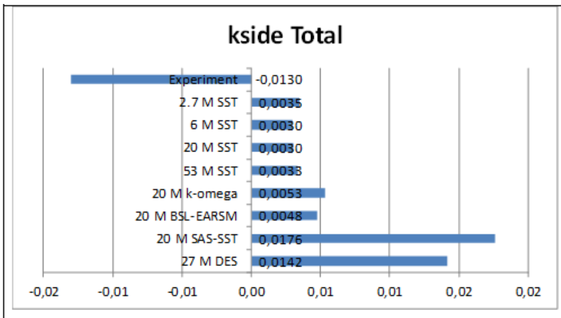

kside Total

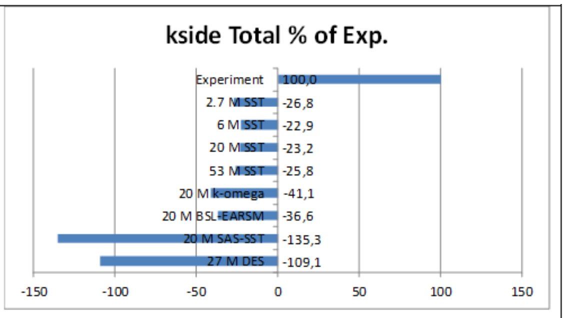

kside Total % of Exp.

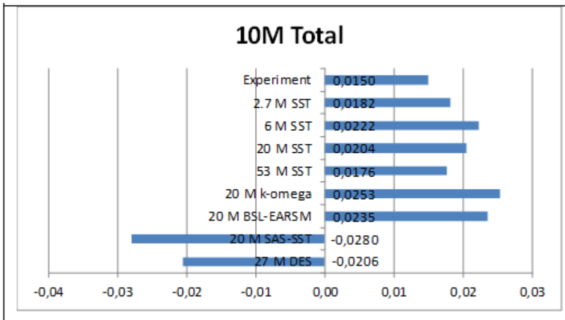

10M Total

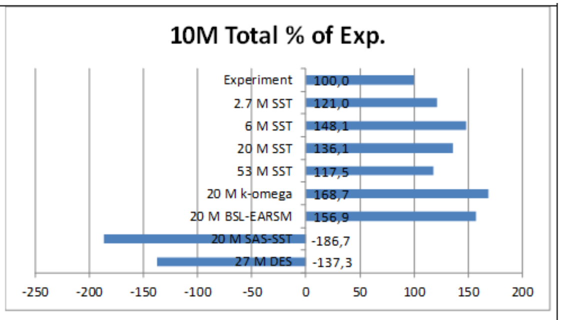

10M Total % of Exp.

B.2. case2: J=0.6, $\beta = 0°$

Setup	kt Propeller	10kq Propeller	kt Duct	kt Total	kside Duct	kside Total	10M Total
Experiment	0,2570	0,4930	0,0560	0,2760	0,0000	-0,0130	0,0200
2.7 M SST	0,2548	0,4882	0,0628	0,2828	0,0016	0,0045	0,0114
6 M SST	0,2573	0,4934	0,0652	0,2877	0,0021	0,0042	0,0139
20 M SST	0,2585	0,4964	0,0649	0,2904	0,0029	0,0040	0,0159
53 M SST	0,2590	0,4982	0,0651	0,2926	0,0027	0,0032	0,0187
20 M k-omega	0,2497	0,4991	0,0609	0,2827	0,0013	0,0033	0,0132
20 M BSL-EARSM	0,2589	0,4992	0,0636	0,2907	0,0027	0,0034	0,0104
20 M SAS-SST	0,2599	0,4980	0,0634	0,2879	0,0048	0,0073	0,0104
27 M DES	0,2508	0,4953	0,0605	0,2817	0,0027	0,0026	0,0135

Setup	kt Propeller	10kq Propeller	kt Duct	kt Total	kside Duct	kside Total	10M Total
Experiment	100,0	100,0	100,0	100,0	100,0	100,0	100,0
2.7 M SST	99,1	99,0	112,2	102,5	n. a.	-34,7	57,1
6 M SST	100,1	100,1	116,5	104,3	n. a.	-31,9	69,5
20 M SST	100,6	100,7	115,9	105,2	n. a.	-30,9	79,7
53 M SST	100,8	101,0	116,3	106,0	n. a.	-24,5	93,4
20 M k-omega	97,1	101,2	108,8	102,4	n. a.	-25,8	65,8
20 M BSL-EARSM	100,8	101,3	113,7	105,3	n. a.	-26,2	52,2
20 M SAS-SST	101,1	101,0	113,2	104,3	n. a.	-56,0	52,2
27 M DES	97,6	100,5	108,1	102,1	n. a.	-19,7	67,6

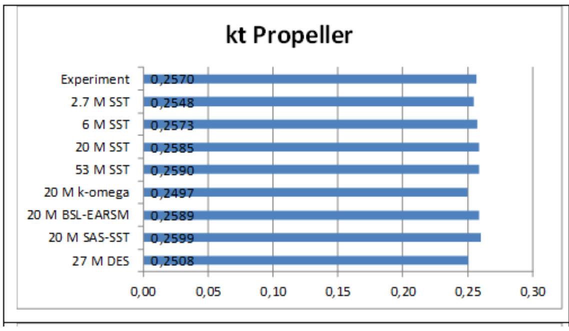

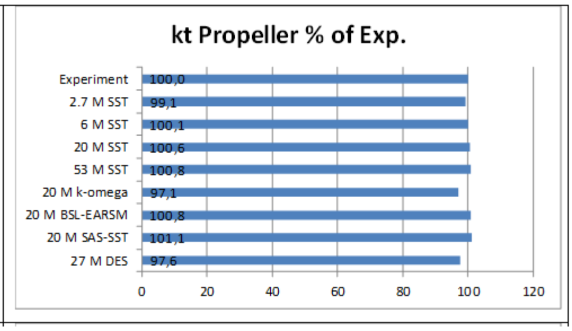

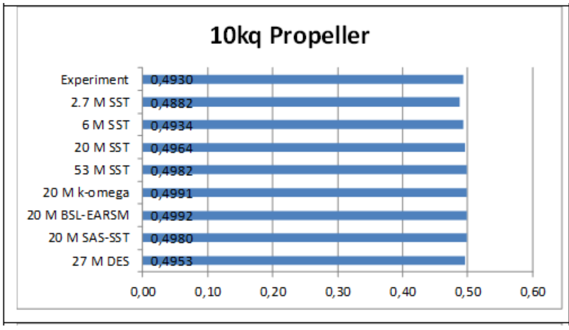

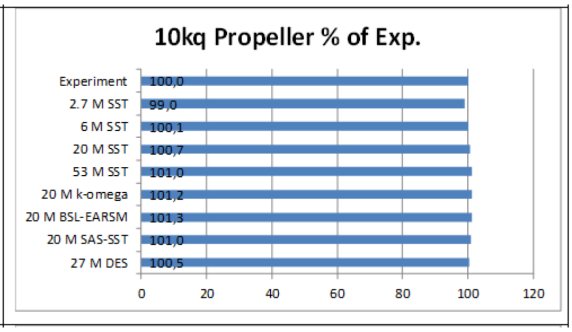

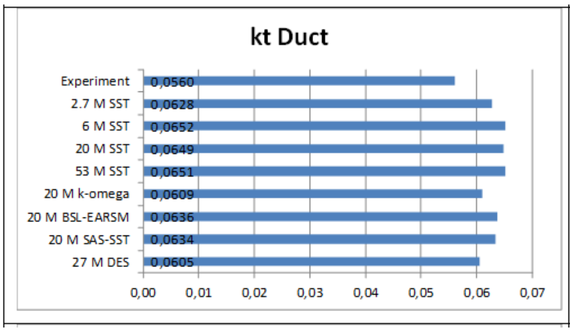
kt Duct
Experiment 0,0560
2.7 M SST 0,0628
6 M SST 0,0652
20 M SST 0,0649
53 M SST 0,0651
20 M k-omega 0,0609
20 M BSL-EARSM 0,0636
20 M SAS-SST 0,0634
27 M DES 0,0605
0,00 0,01 0,02 0,03 0,04 0,05 0,06 0,07

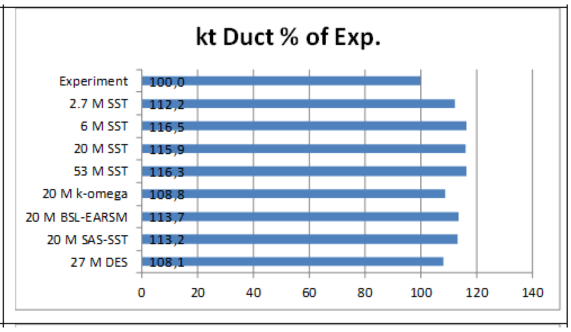
kt Duct % of Exp.
Experiment 100,0
2.7 M SST 112,2
6 M SST 116,5
20 M SST 115,9
53 M SST 116,3
20 M k-omega 108,8
20 M BSL-EARSM 113,7
20 M SAS-SST 113,2
27 M DES 108,1
0 20 40 60 80 100 120 140

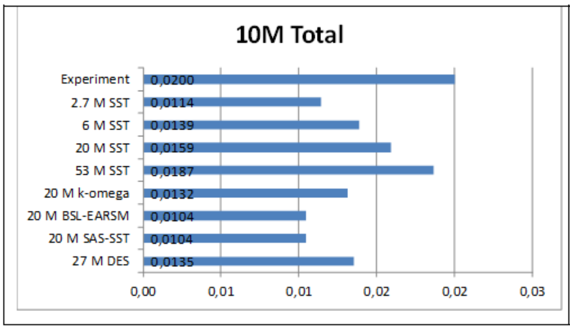
10M Total
Experiment 0,0200
2.7 M SST 0,0114
6 M SST 0,0139
20 M SST 0,0159
53 M SST 0,0187
20 M k-omega 0,0132
20 M BSL-EARSM 0,0104
20 M SAS-SST 0,0104
27 M DES 0,0135
0,00 0,01 0,01 0,02 0,02 0,03

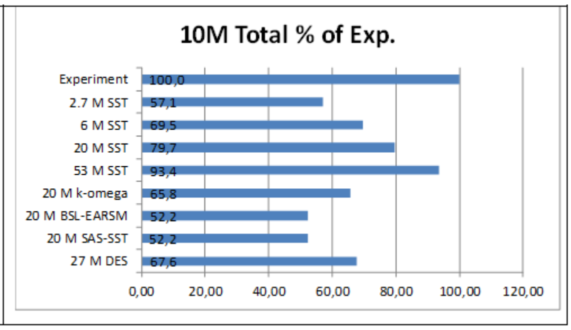
10M Total % of Exp.
Experiment 100,0
2.7 M SST 57,1
6 M SST 69,5
20 M SST 79,7
53 M SST 93,4
20 M k-omega 65,8
20 M BSL-EARSM 52,2
20 M SAS-SST 52,2
27 M DES 67,6
0,00 20,00 40,00 60,00 80,00 100,00 120,00

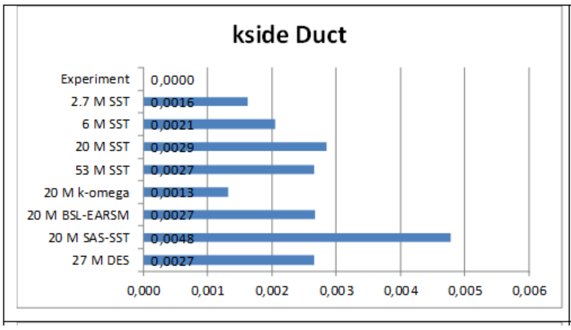
kside Duct
Experiment 0,0000
2.7 M SST 0,0016
6 M SST 0,0021
20 M SST 0,0029
53 M SST 0,0027
20 M k-omega 0,0013
20 M BSL-EARSM 0,0027
20 M SAS-SST 0,0048
27 M DES 0,0027
0,000 0,001 0,002 0,003 0,004 0,005 0,006

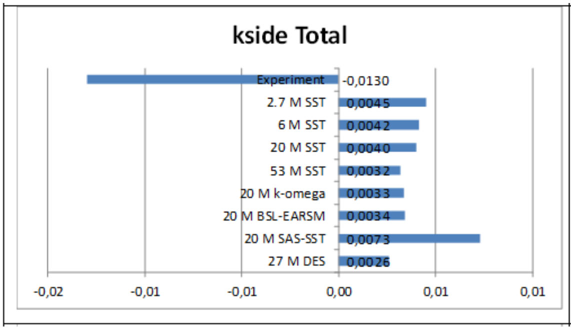
kside Total
Experiment -0,0130
2.7 M SST 0,0045
6 M SST 0,0042
20 M SST 0,0040
53 M SST 0,0032
20 M k-omega 0,0033
20 M BSL-EARSM 0,0034
20 M SAS-SST 0,0073
27 M DES 0,0026
-0,02 -0,01 -0,01 0,00 0,01 0,01

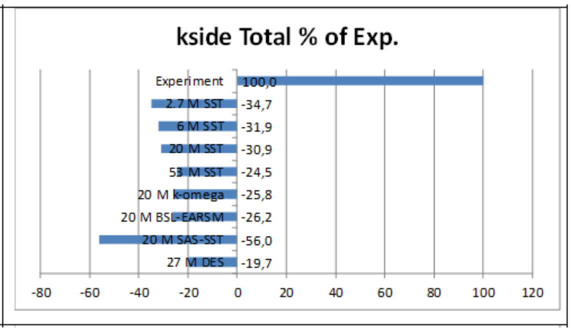
kside Total % of Exp.
Experiment 100,0
2.7 M SST -34,7
6 M SST -31,9
20 M SST -30,9
53 M SST -24,5
20 M k-omega -25,8
20 M BSL-EARSM -26,2
20 M SAS-SST -56,0
27 M DES -19,7
-80 -60 -40 -20 0 20 40 60 80 100 120

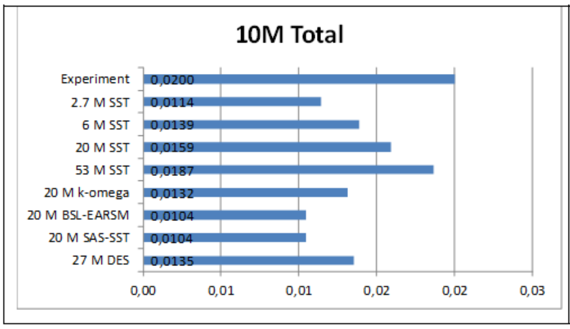
10M Total
Experiment 0,0200
2.7 M SST 0,0114
6 M SST 0,0139
20 M SST 0,0159
53 M SST 0,0187
20 M k-omega 0,0132
20 M BSL-EARSM 0,0104
20 M SAS-SST 0,0104
27 M DES 0,0135
0,00 0,01 0,01 0,02 0,02 0,03

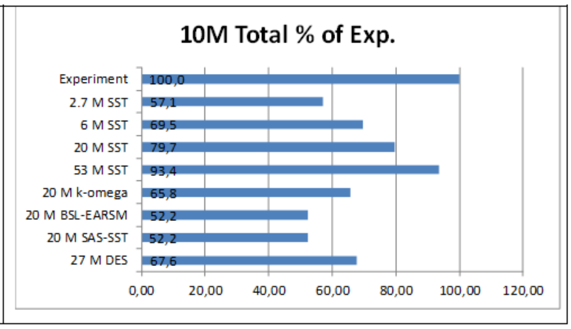
10M Total % of Exp.
Experiment 100,0
2.7 M SST 57,1
6 M SST 69,5
20 M SST 79,7
53 M SST 93,4
20 M k-omega 65,8
20 M BSL-EARSM 52,2
20 M SAS-SST 52,2
27 M DES 67,6
0,00 20,00 40,00 60,00 80,00 100,00 120,00

B.3. case3: J=0.6, $\beta = -35°$

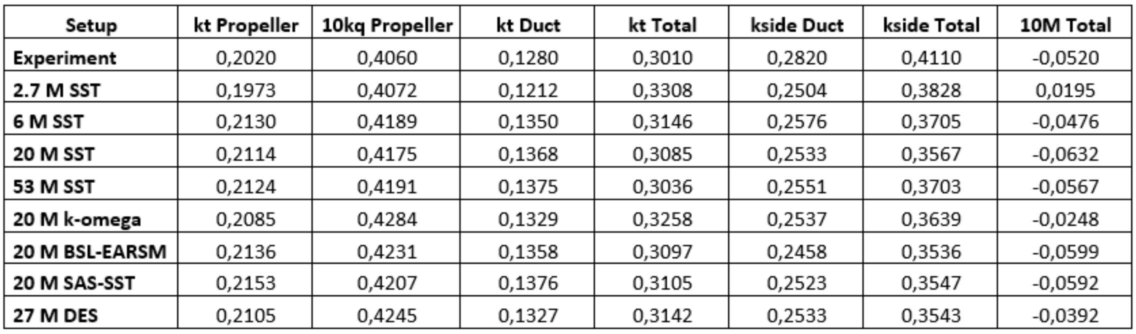

Setup	kt Propeller	10kq Propeller	kt Duct	kt Total	kside Duct	kside Total	10M Total
Experiment	0,2020	0,4060	0,1280	0,3010	0,2820	0,4110	-0,0520
2.7 M SST	0,1973	0,4072	0,1212	0,3308	0,2504	0,3828	0,0195
6 M SST	0,2130	0,4189	0,1350	0,3146	0,2576	0,3705	-0,0476
20 M SST	0,2114	0,4175	0,1368	0,3085	0,2533	0,3567	-0,0632
53 M SST	0,2124	0,4191	0,1375	0,3036	0,2551	0,3703	-0,0567
20 M k-omega	0,2085	0,4284	0,1329	0,3258	0,2537	0,3639	-0,0248
20 M BSL-EARSM	0,2136	0,4231	0,1358	0,3097	0,2458	0,3536	-0,0599
20 M SAS-SST	0,2153	0,4207	0,1376	0,3105	0,2523	0,3547	-0,0592
27 M DES	0,2105	0,4245	0,1327	0,3142	0,2533	0,3543	-0,0392

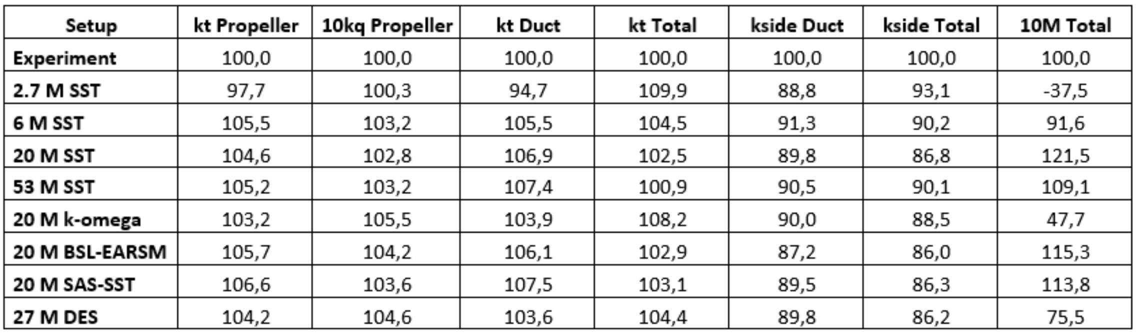

Setup	kt Propeller	10kq Propeller	kt Duct	kt Total	kside Duct	kside Total	10M Total
Experiment	100,0	100,0	100,0	100,0	100,0	100,0	100,0
2.7 M SST	97,7	100,3	94,7	109,9	88,8	93,1	-37,5
6 M SST	105,5	103,2	105,5	104,5	91,3	90,2	91,6
20 M SST	104,6	102,8	106,9	102,5	89,8	86,8	121,5
53 M SST	105,2	103,2	107,4	100,9	90,5	90,1	109,1
20 M k-omega	103,2	105,5	103,9	108,2	90,0	88,5	47,7
20 M BSL-EARSM	105,7	104,2	106,1	102,9	87,2	86,0	115,3
20 M SAS-SST	106,6	103,6	107,5	103,1	89,5	86,3	113,8
27 M DES	104,2	104,6	103,6	104,4	89,8	86,2	75,5

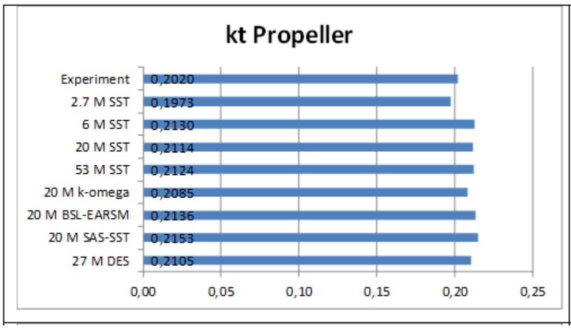

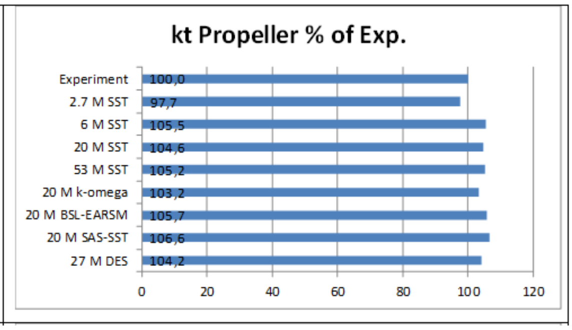

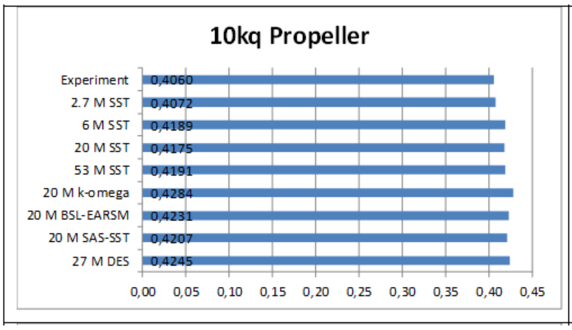

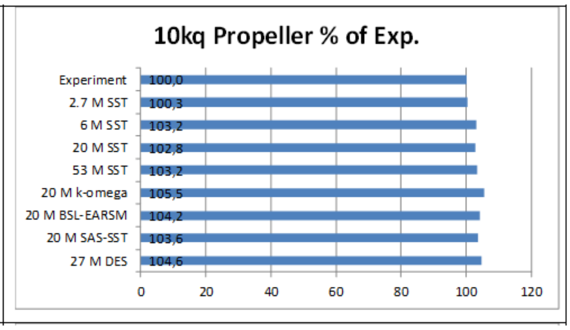

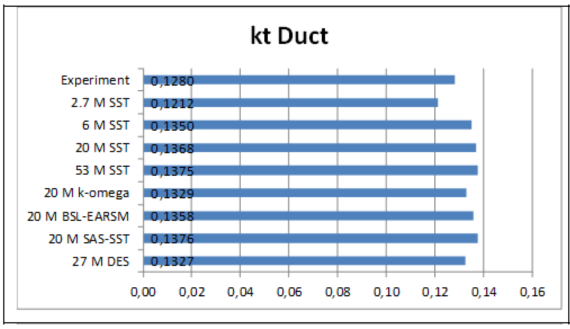
kt Duct
Experiment 0,1280
2.7 M SST 0,1212
6 M SST 0,1350
20 M SST 0,1368
53 M SST 0,1375
20 M k-omega 0,1329
20 M BSL-EARSM 0,1358
20 M SAS-SST 0,1376
27 M DES 0,1327
0,00 0,02 0,04 0,06 0,08 0,10 0,12 0,14 0,16

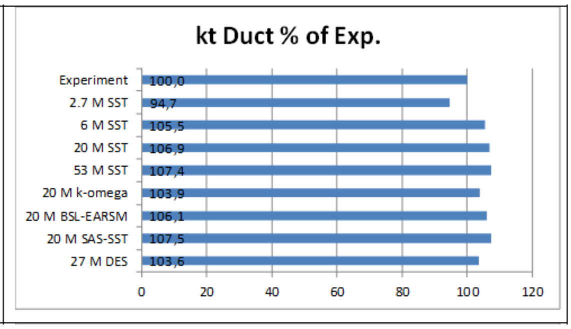
kt Duct % of Exp.
Experiment 100,0
2.7 M SST 94,7
6 M SST 105,5
20 M SST 106,9
53 M SST 107,4
20 M k-omega 103,9
20 M BSL-EARSM 106,1
20 M SAS-SST 107,5
27 M DES 103,6
0 20 40 60 80 100 120

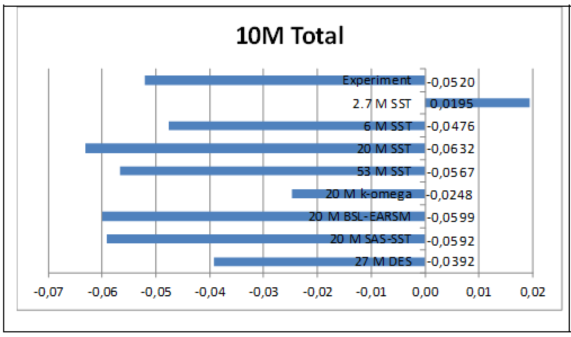
10M Total
Experiment -0,0520
2.7 M SST 0,0195
6 M SST -0,0476
20 M SST -0,0632
53 M SST -0,0567
20 M k-omega -0,0248
20 M BSL-EARSM -0,0599
20 M SAS-SST -0,0592
27 M DES -0,0392
-0,07 -0,06 -0,05 -0,04 -0,03 -0,02 -0,01 0,00 0,01 0,02

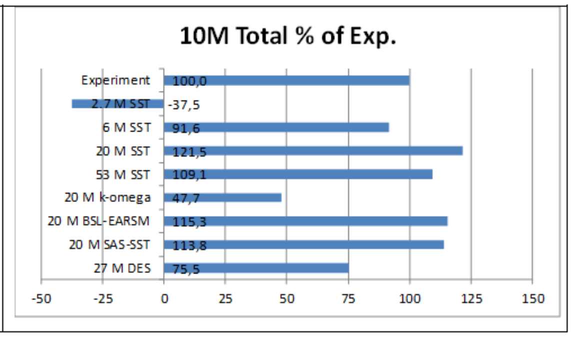
10M Total % of Exp.
Experiment 100,0
2.7 M SST -37,5
6 M SST 91,6
20 M SST 121,5
53 M SST 109,1
20 M k-omega 47,7
20 M BSL-EARSM 115,3
20 M SAS-SST 113,8
27 M DES 75,5
-50 -25 0 25 50 75 100 125 150

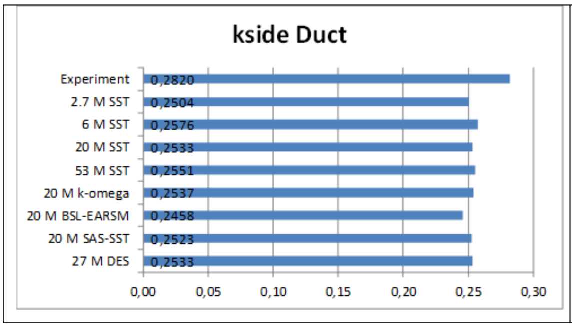
kside Duct
Experiment 0,2820
2.7 M SST 0,2504
6 M SST 0,2576
20 M SST 0,2533
53 M SST 0,2551
20 M k-omega 0,2537
20 M BSL-EARSM 0,2458
20 M SAS-SST 0,2523
27 M DES 0,2533
0,00 0,05 0,10 0,15 0,20 0,25 0,30

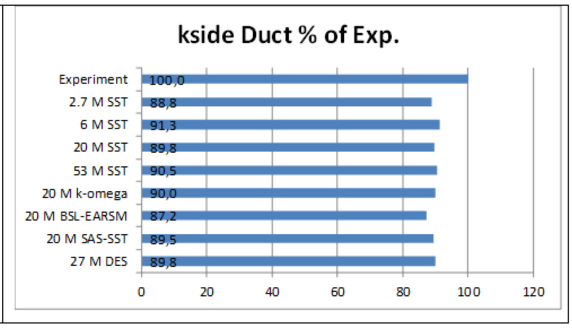
kside Duct % of Exp.
Experiment 100,0
2.7 M SST 88,8
6 M SST 91,3
20 M SST 89,8
53 M SST 90,5
20 M k-omega 90,0
20 M BSL-EARSM 87,2
20 M SAS-SST 89,5
27 M DES 89,8
0 20 40 60 80 100 120

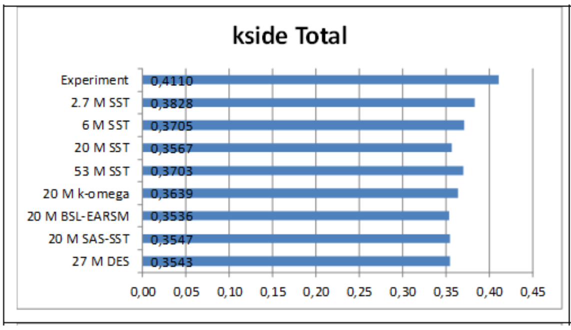
kside Total
Experiment 0,4110
2.7 M SST 0,3828
6 M SST 0,3705
20 M SST 0,3567
53 M SST 0,3703
20 M k-omega 0,3639
20 M BSL-EARSM 0,3536
20 M SAS-SST 0,3547
27 M DES 0,3543
0,00 0,05 0,10 0,15 0,20 0,25 0,30 0,35 0,40 0,45

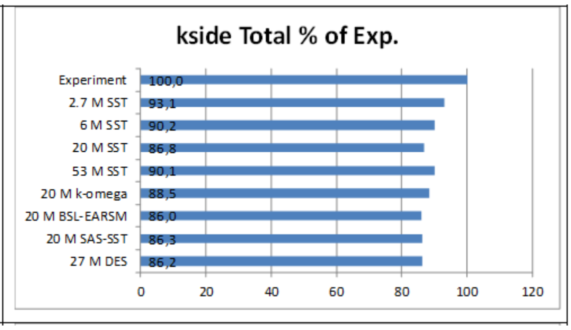
kside Total % of Exp.
Experiment 100,0
2.7 M SST 93,1
6 M SST 90,2
20 M SST 86,8
53 M SST 90,1
20 M k-omega 88,5
20 M BSL-EARSM 86,0
20 M SAS-SST 86,3
27 M DES 86,2
0 20 40 60 80 100 120

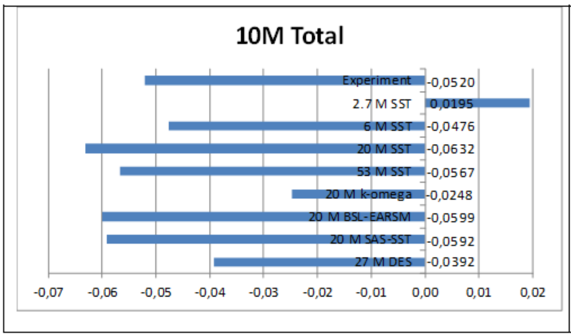
10M Total
Experiment -0,0520
2.7 M SST 0,0195
6 M SST -0,0476
20 M SST -0,0632
53 M SST -0,0567
20 M k-omega -0,0248
20 M BSL-EARSM -0,0599
20 M SAS-SST -0,0592
27 M DES -0,0392
-0,07 -0,06 -0,05 -0,04 -0,03 -0,02 -0,01 0,00 0,01 0,02

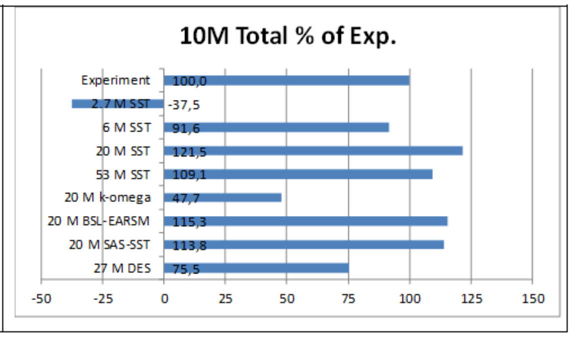
10M Total % of Exp.
Experiment 100,0
2.7 M SST -37,5
6 M SST 91,6
20 M SST 121,5
53 M SST 109,1
20 M k-omega 47,7
20 M BSL-EARSM 115,3
20 M SAS-SST 113,8
27 M DES 75,5
-50 -25 0 25 50 75 100 125 150

B.4. case4: J=0.6, $\beta = 35°$

Setup	kt Propeller	10kq Propeller	kt Duct	kt Total	kside Duct	kside Total	10M Total
Experiment	0,3000	0,5420	0,1640	0,4280	-0,3050	-0,4470	0,0080
2.7 M SST	0,2907	0,5645	0,1553	0,4638	-0,2562	-0,3801	-0,0072
6 M SST	0,2937	0,5489	0,1601	0,4256	-0,2497	-0,3373	0,0525
20 M SST	0,2949	0,5529	0,1684	0,4295	-0,2708	-0,3636	0,0689
53 M SST	0,2992	0,5601	0,1695	0,4312	-0,2692	-0,3646	0,0687
20 M k-omega	0,2816	0,5532	0,1606	0,4318	-0,2653	-0,3652	0,0459
20 M BSL-EARSM	0,2934	0,5530	0,1644	0,4242	-0,2648	-0,3520	0,0544
20 M SAS-SST	0,2962	0,5530	0,1686	0,4193	-0,2704	-0,3586	0,0794
27 M DES	0,2835	0,5474	0,1595	0,4232	-0,2638	-0,3668	0,0595

Setup	kt Propeller	10kq Propeller	kt Duct	kt Total	kside Duct	kside Total	10M Total
Experiment	100,0	100,0	100,0	100,0	100,0	100,0	100,0
2.7 M SST	96,9	104,1	94,7	108,4	84,0	85,0	-89,7
6 M SST	97,9	101,3	97,6	99,4	81,9	75,5	655,7
20 M SST	98,3	102,0	102,7	100,4	88,8	81,3	861,0
53 M SST	99,7	103,3	103,3	100,7	88,3	81,6	858,7
20 M k-omega	93,9	102,1	97,9	100,9	87,0	81,7	573,5
20 M BSL-EARSM	97,8	102,0	100,2	99,1	86,8	78,7	680,5
20 M SAS-SST	98,7	102,0	102,8	98,0	88,7	80,2	992,3
27 M DES	94,5	101,0	97,2	98,9	86,5	82,1	744,2

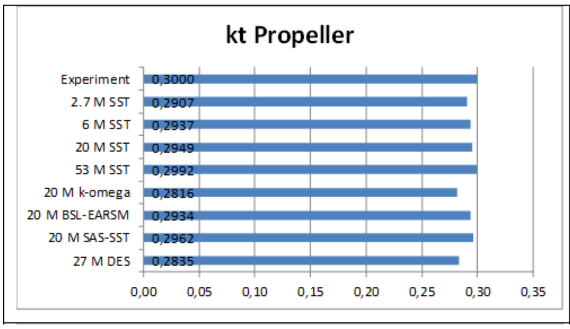

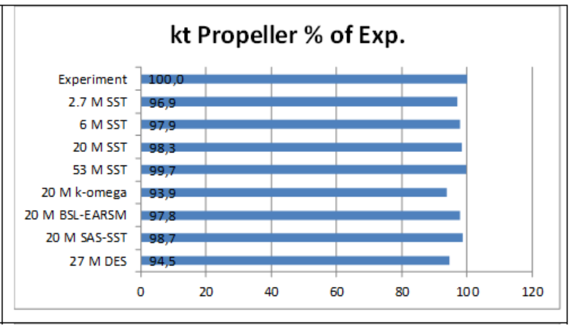

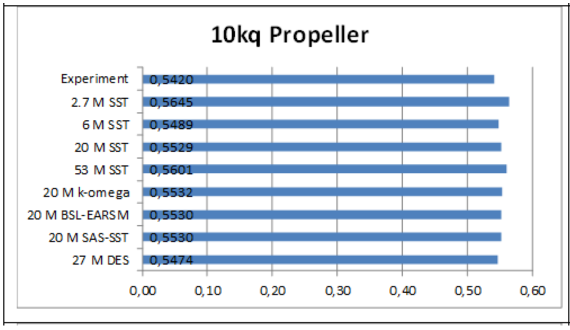

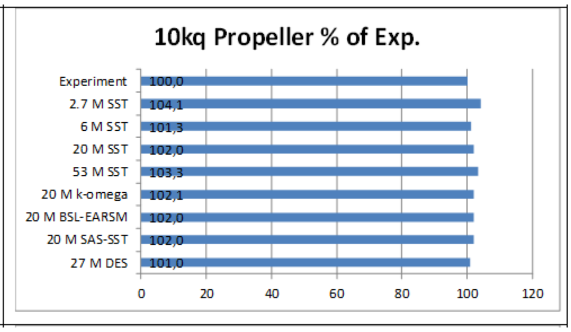

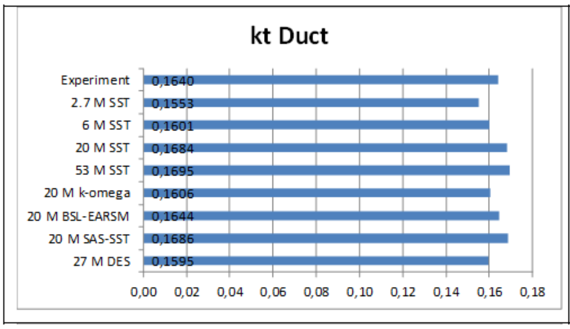
kt Duct
Experiment 0,1640
2.7 M SST 0,1553
6 M SST 0,1601
20 M SST 0,1684
53 M SST 0,1695
20 M k-omega 0,1606
20 M BSL-EARSM 0,1644
20 M SAS-SST 0,1686
27 M DES 0,1595
0,00 0,02 0,04 0,06 0,08 0,10 0,12 0,14 0,16 0,18

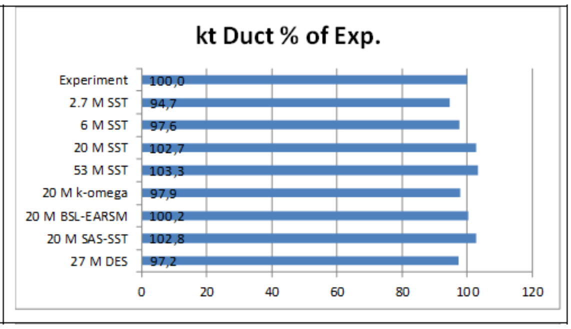
kt Duct % of Exp.
Experiment 100,0
2.7 M SST 94,7
6 M SST 97,6
20 M SST 102,7
53 M SST 103,3
20 M k-omega 97,9
20 M BSL-EARSM 100,2
20 M SAS-SST 102,8
27 M DES 97,2
0 20 40 60 80 100 120

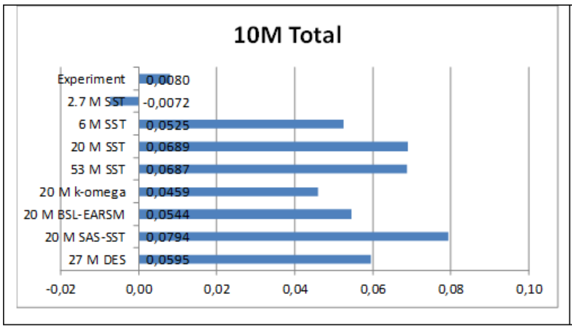
10M Total
Experiment 0,0080
2.7 M SST -0,0072
6 M SST 0,0525
20 M SST 0,0689
53 M SST 0,0687
20 M k-omega 0,0459
20 M BSL-EARSM 0,0544
20 M SAS-SST 0,0794
27 M DES 0,0595
-0,02 0,00 0,02 0,04 0,06 0,08 0,10

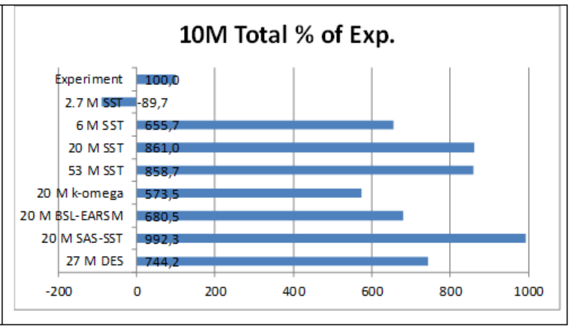
10M Total % of Exp.
Experiment 100,0
2.7 M SST -89,7
6 M SST 655,7
20 M SST 861,0
53 M SST 858,7
20 M k-omega 573,5
20 M BSL-EARSM 680,5
20 M SAS-SST 992,3
27 M DES 744,2
-200 0 200 400 600 800 1000

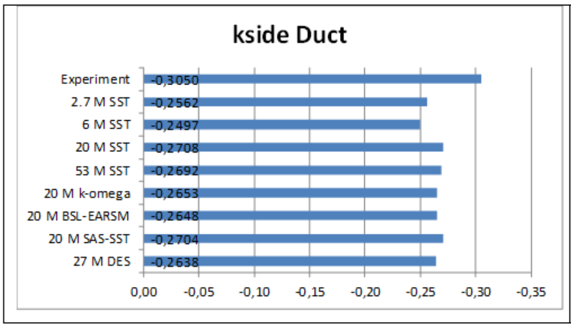
kside Duct
Experiment -0,3050
2.7 M SST -0,2562
6 M SST -0,2497
20 M SST -0,2708
53 M SST -0,2692
20 M k-omega -0,2653
20 M BSL-EARSM -0,2648
20 M SAS-SST -0,2704
27 M DES -0,2638
0,00 -0,05 -0,10 -0,15 -0,20 -0,25 -0,30 -0,35

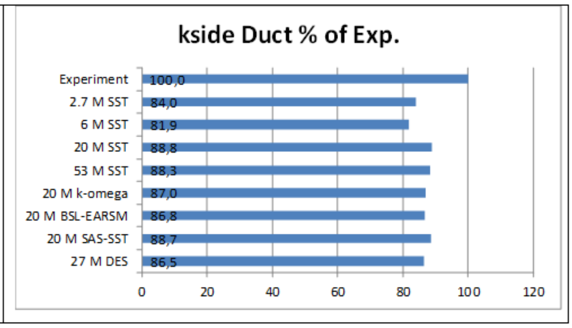
kside Duct % of Exp.
Experiment 100,0
2.7 M SST 84,0
6 M SST 81,9
20 M SST 88,8
53 M SST 88,3
20 M k-omega 87,0
20 M BSL-EARSM 86,8
20 M SAS-SST 88,7
27 M DES 86,5
0 20 40 60 80 100 120

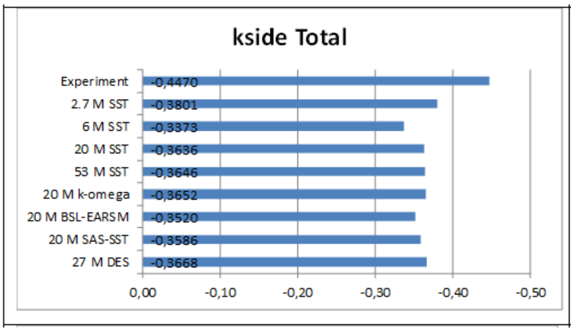
kside Total
Experiment -0,4470
2.7 M SST -0,3801
6 M SST -0,3373
20 M SST -0,3636
53 M SST -0,3646
20 M k-omega -0,3652
20 M BSL-EARSM -0,3520
20 M SAS-SST -0,3586
27 M DES -0,3668
0,00 -0,10 -0,20 -0,30 -0,40 -0,50

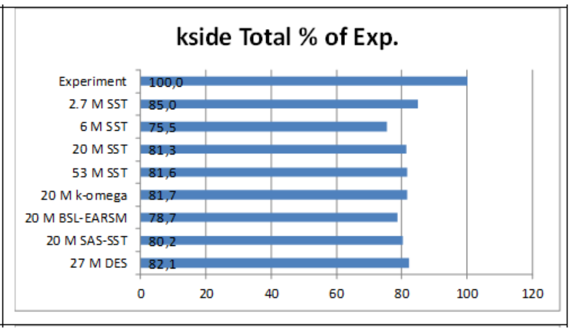
kside Total % of Exp.
Experiment 100,0
2.7 M SST 85,0
6 M SST 75,5
20 M SST 81,3
53 M SST 81,6
20 M k-omega 81,7
20 M BSL-EARSM 78,7
20 M SAS-SST 80,2
27 M DES 82,1
0 20 40 60 80 100 120

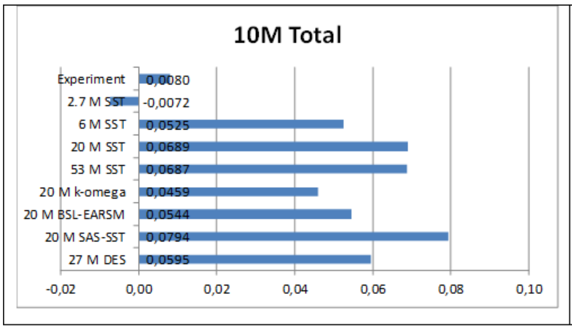
10M Total
Experiment 0,0080
2.7 M SST -0,0072
6 M SST 0,0525
20 M SST 0,0689
53 M SST 0,0687
20 M k-omega 0,0459
20 M BSL-EARSM 0,0544
20 M SAS-SST 0,0794
27 M DES 0,0595
-0,02 0,00 0,02 0,04 0,06 0,08 0,10

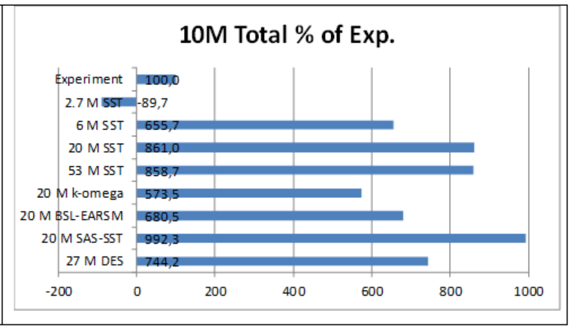
10M Total % of Exp.
Experiment 100,0
2.7 M SST -89,7
6 M SST 655,7
20 M SST 861,0
53 M SST 858,7
20 M k-omega 573,5
20 M BSL-EARSM 680,5
20 M SAS-SST 992,3
27 M DES 744,2
-200 0 200 400 600 800 1000

C Estimation of Y^+ for propeller

To estimate the Y^+ value, the Reynolds number should be firstly calculated, which is the function of chord length c, the velocity u composed of inflow and rotating velocity at radius r and the kinematic viscosity ν.

$$R_e = \frac{c \cdot u}{\nu} \tag{C.1}$$

The friction coefficient of plate is

$$c_f = \frac{0.075}{(\log_{10} Re - 2)^2} \tag{C.2}$$

The wall shear stress is obtained by using of Eq.[C.2]

$$\tau_w = \frac{1}{2} \cdot c_f \cdot \rho \cdot u^2 \tag{C.3}$$

The usage of Eq.[C.3] is to obtain the first cell spacing

$$y = \frac{y^+ \cdot \nu}{\sqrt{\frac{\tau_w}{\rho}}} \tag{C.4}$$

If y^+ is required to be 1, we obtain the Eq.[C.5] from Eq.[C.4]

$$y = \frac{1 \cdot \nu}{\sqrt{\frac{\tau_w}{\rho}}} \tag{C.5}$$

The Eq.[C.5] often overestimates the y^+. From the experience, four times less than y obtained by Eq.[C.5] should guarantee the y^+ value below 1.

D Geometric specifications of modified Kaplan propeller

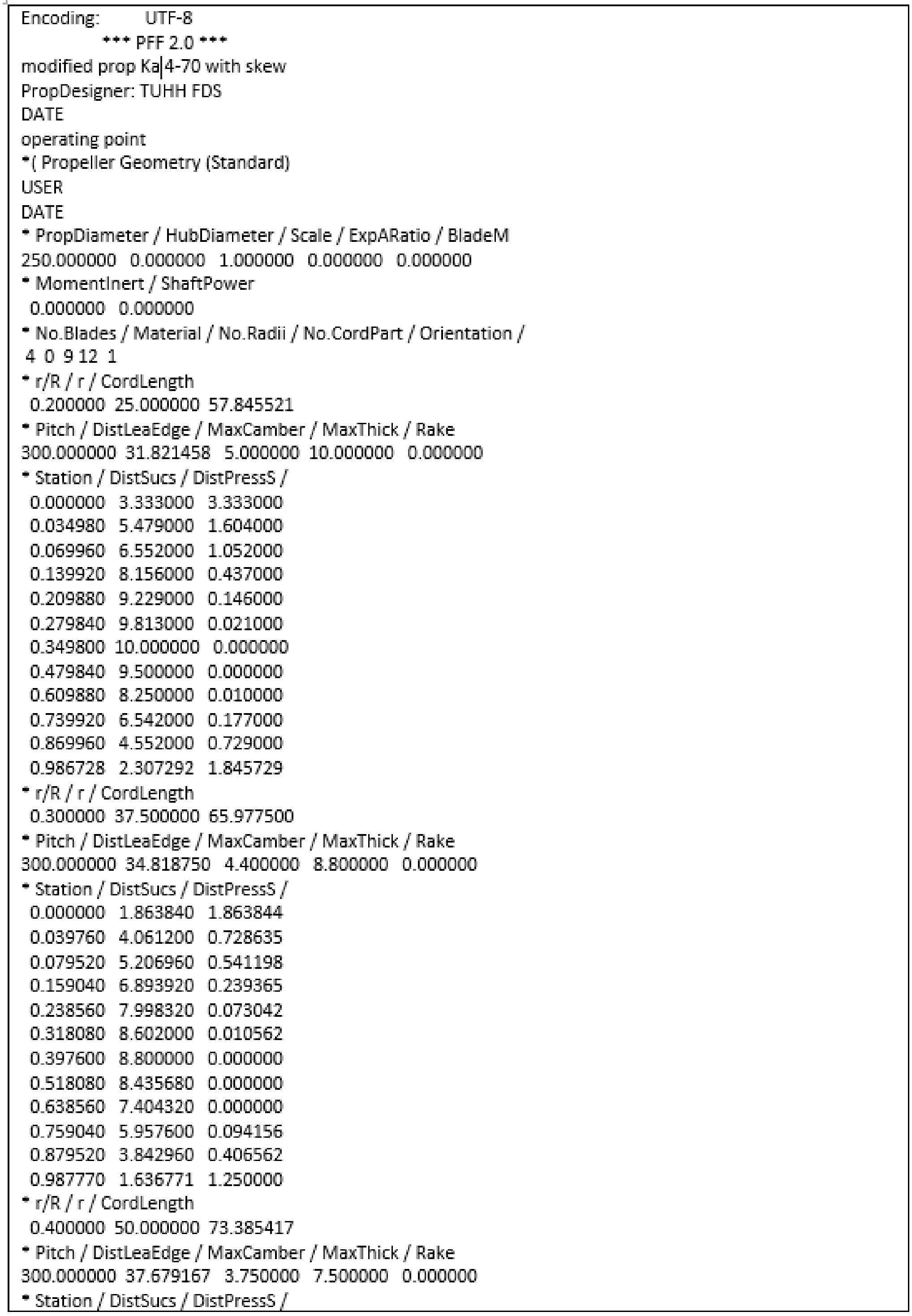

```
Encoding:        UTF-8
              *** PFF 2.0 ***
modified prop Ka4-70 with skew
PropDesigner: TUHH FDS
DATE
operating point
*( Propeller Geometry (Standard)
USER
DATE
* PropDiameter / HubDiameter / Scale / ExpARatio / BladeM
250.000000  0.000000  1.000000  0.000000  0.000000
* MomentInert / ShaftPower
 0.000000  0.000000
* No.Blades / Material / No.Radii / No.CordPart / Orientation /
 4  0  9 12  1
* r/R / r / CordLength
 0.200000  25.000000  57.845521
* Pitch / DistLeaEdge / MaxCamber / MaxThick / Rake
300.000000  31.821458   5.000000  10.000000   0.000000
* Station / DistSucs / DistPressS /
 0.000000   3.333000   3.333000
 0.034980   5.479000   1.604000
 0.069960   6.552000   1.052000
 0.139920   8.156000   0.437000
 0.209880   9.229000   0.146000
 0.279840   9.813000   0.021000
 0.349800  10.000000   0.000000
 0.479840   9.500000   0.000000
 0.609880   8.250000   0.010000
 0.739920   6.542000   0.177000
 0.869960   4.552000   0.729000
 0.986728   2.307292   1.845729
* r/R / r / CordLength
 0.300000  37.500000  65.977500
* Pitch / DistLeaEdge / MaxCamber / MaxThick / Rake
300.000000  34.818750   4.400000   8.800000   0.000000
* Station / DistSucs / DistPressS /
 0.000000   1.863840   1.863844
 0.039760   4.061200   0.728635
 0.079520   5.206960   0.541198
 0.159040   6.893920   0.239365
 0.238560   7.998320   0.073042
 0.318080   8.602000   0.010562
 0.397600   8.800000   0.000000
 0.518080   8.435680   0.000000
 0.638560   7.404320   0.000000
 0.759040   5.957600   0.094156
 0.879520   3.842960   0.406562
 0.987770   1.636771   1.250000
* r/R / r / CordLength
 0.400000  50.000000  73.385417
* Pitch / DistLeaEdge / MaxCamber / MaxThick / Rake
300.000000  37.679167   3.750000   7.500000   0.000000
* Station / DistSucs / DistPressS /
```

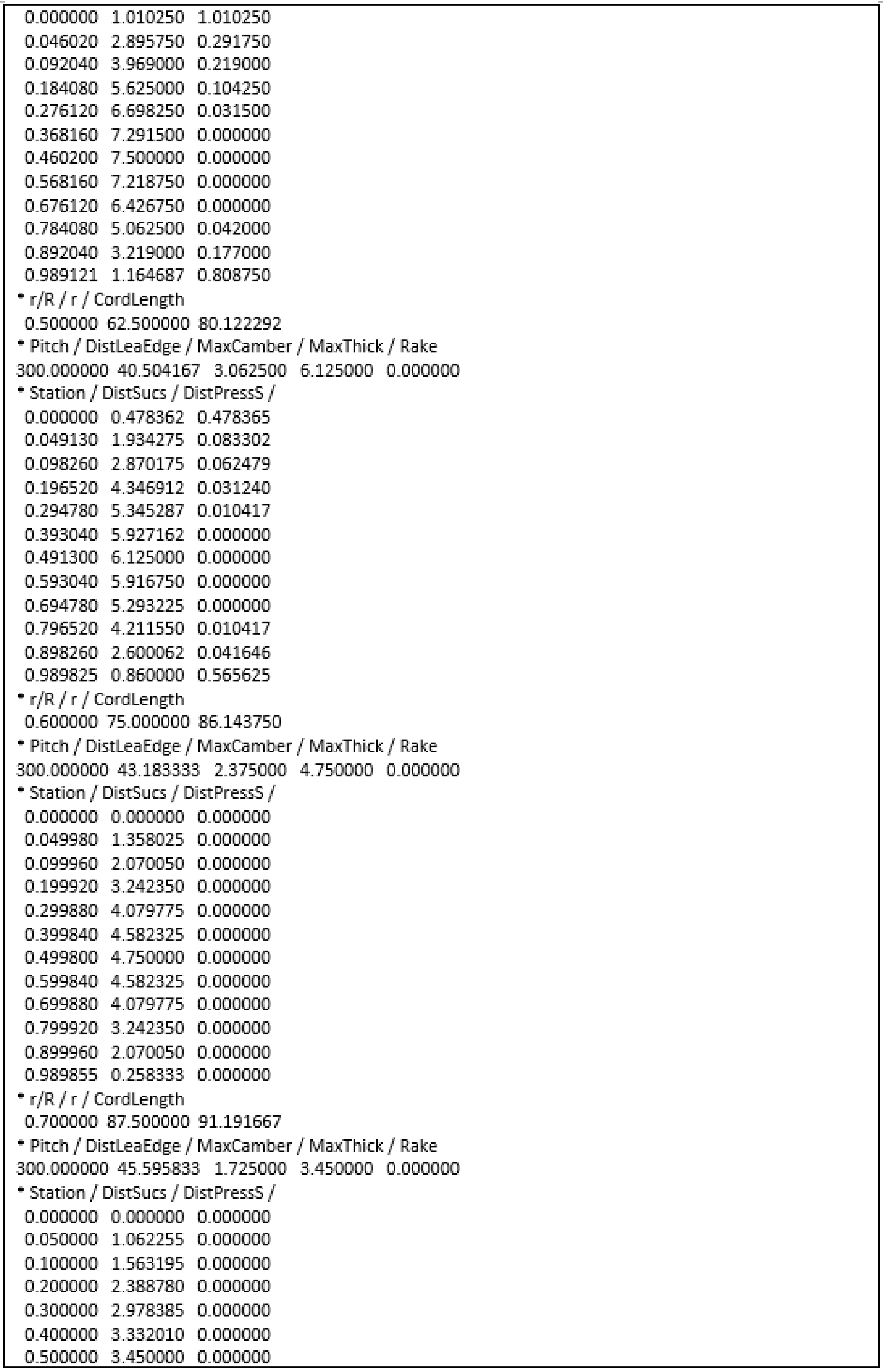

```
 0.000000  1.010250  1.010250
 0.046020  2.895750  0.291750
 0.092040  3.969000  0.219000
 0.184080  5.625000  0.104250
 0.276120  6.698250  0.031500
 0.368160  7.291500  0.000000
 0.460200  7.500000  0.000000
 0.568160  7.218750  0.000000
 0.676120  6.426750  0.000000
 0.784080  5.062500  0.042000
 0.892040  3.219000  0.177000
 0.989121  1.164687  0.808750
* r/R / r / CordLength
 0.500000 62.500000 80.122292
* Pitch / DistLeaEdge / MaxCamber / MaxThick / Rake
300.000000 40.504167  3.062500  6.125000  0.000000
* Station / DistSucs / DistPressS /
 0.000000  0.478362  0.478365
 0.049130  1.934275  0.083302
 0.098260  2.870175  0.062479
 0.196520  4.346912  0.031240
 0.294780  5.345287  0.010417
 0.393040  5.927162  0.000000
 0.491300  6.125000  0.000000
 0.593040  5.916750  0.000000
 0.694780  5.293225  0.000000
 0.796520  4.211550  0.010417
 0.898260  2.600062  0.041646
 0.989825  0.860000  0.565625
* r/R / r / CordLength
 0.600000 75.000000 86.143750
* Pitch / DistLeaEdge / MaxCamber / MaxThick / Rake
300.000000 43.183333  2.375000  4.750000  0.000000
* Station / DistSucs / DistPressS /
 0.000000  0.000000  0.000000
 0.049980  1.358025  0.000000
 0.099960  2.070050  0.000000
 0.199920  3.242350  0.000000
 0.299880  4.079775  0.000000
 0.399840  4.582325  0.000000
 0.499800  4.750000  0.000000
 0.599840  4.582325  0.000000
 0.699880  4.079775  0.000000
 0.799920  3.242350  0.000000
 0.899960  2.070050  0.000000
 0.989855  0.258333  0.000000
* r/R / r / CordLength
 0.700000 87.500000 91.191667
* Pitch / DistLeaEdge / MaxCamber / MaxThick / Rake
300.000000 45.595833  1.725000  3.450000  0.000000
* Station / DistSucs / DistPressS /
 0.000000  0.000000  0.000000
 0.050000  1.062255  0.000000
 0.100000  1.563195  0.000000
 0.200000  2.388780  0.000000
 0.300000  2.978385  0.000000
 0.400000  3.332010  0.000000
 0.500000  3.450000  0.000000
```

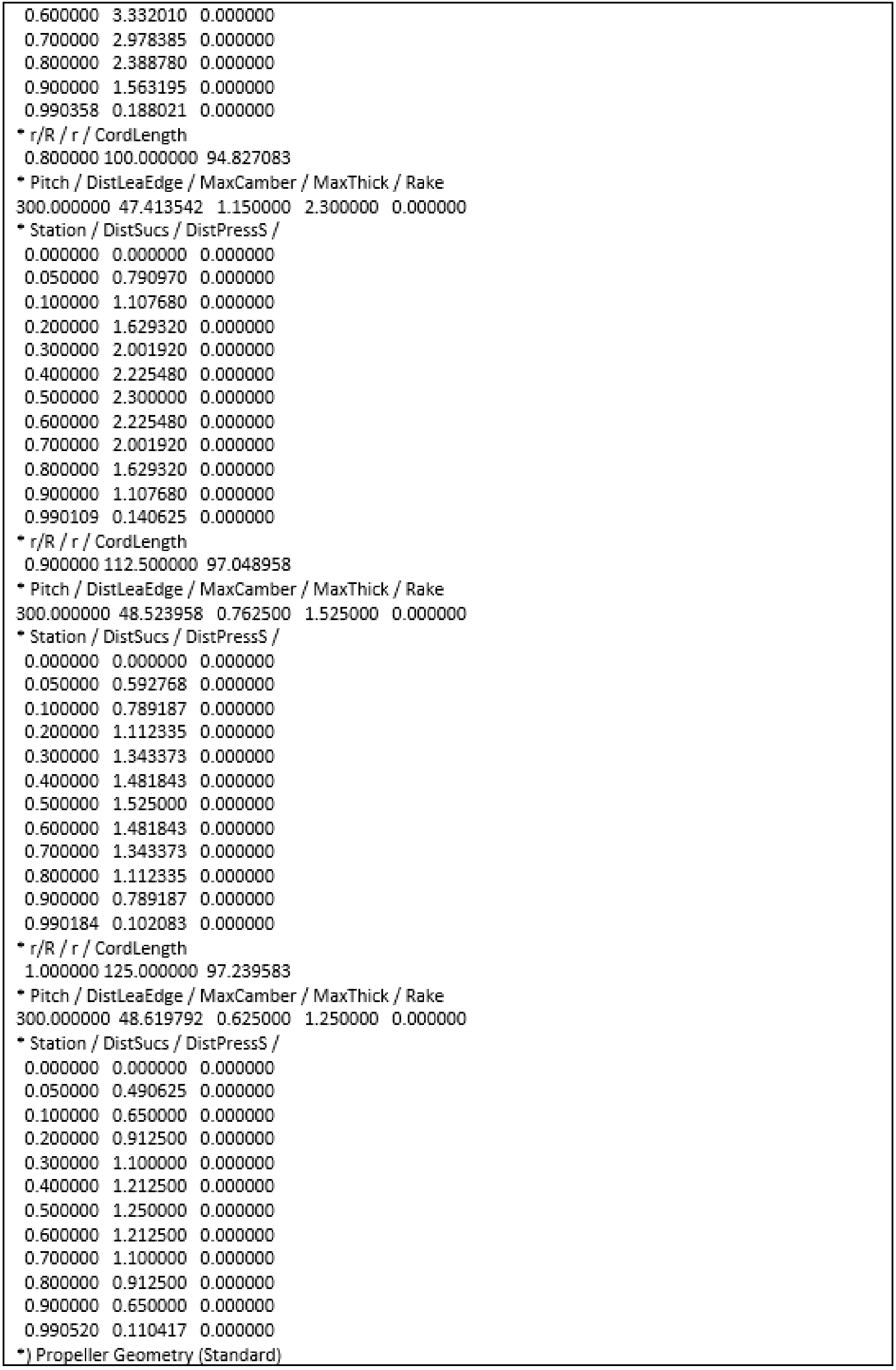

```
 0.600000  3.332010  0.000000
 0.700000  2.978385  0.000000
 0.800000  2.388780  0.000000
 0.900000  1.563195  0.000000
 0.990358  0.188021  0.000000
* r/R / r / CordLength
 0.800000 100.000000  94.827083
* Pitch / DistLeaEdge / MaxCamber / MaxThick / Rake
300.000000  47.413542   1.150000   2.300000   0.000000
* Station / DistSucs / DistPressS /
 0.000000  0.000000  0.000000
 0.050000  0.790970  0.000000
 0.100000  1.107680  0.000000
 0.200000  1.629320  0.000000
 0.300000  2.001920  0.000000
 0.400000  2.225480  0.000000
 0.500000  2.300000  0.000000
 0.600000  2.225480  0.000000
 0.700000  2.001920  0.000000
 0.800000  1.629320  0.000000
 0.900000  1.107680  0.000000
 0.990109  0.140625  0.000000
* r/R / r / CordLength
 0.900000 112.500000  97.048958
* Pitch / DistLeaEdge / MaxCamber / MaxThick / Rake
300.000000  48.523958   0.762500   1.525000   0.000000
* Station / DistSucs / DistPressS /
 0.000000  0.000000  0.000000
 0.050000  0.592768  0.000000
 0.100000  0.789187  0.000000
 0.200000  1.112335  0.000000
 0.300000  1.343373  0.000000
 0.400000  1.481843  0.000000
 0.500000  1.525000  0.000000
 0.600000  1.481843  0.000000
 0.700000  1.343373  0.000000
 0.800000  1.112335  0.000000
 0.900000  0.789187  0.000000
 0.990184  0.102083  0.000000
* r/R / r / CordLength
 1.000000 125.000000  97.239583
* Pitch / DistLeaEdge / MaxCamber / MaxThick / Rake
300.000000  48.619792   0.625000   1.250000   0.000000
* Station / DistSucs / DistPressS /
 0.000000  0.000000  0.000000
 0.050000  0.490625  0.000000
 0.100000  0.650000  0.000000
 0.200000  0.912500  0.000000
 0.300000  1.100000  0.000000
 0.400000  1.212500  0.000000
 0.500000  1.250000  0.000000
 0.600000  1.212500  0.000000
 0.700000  1.100000  0.000000
 0.800000  0.912500  0.000000
 0.900000  0.650000  0.000000
 0.990520  0.110417  0.000000
*) Propeller Geometry (Standard)
```

E Setting of control parameters in file named ”parameters.dat”

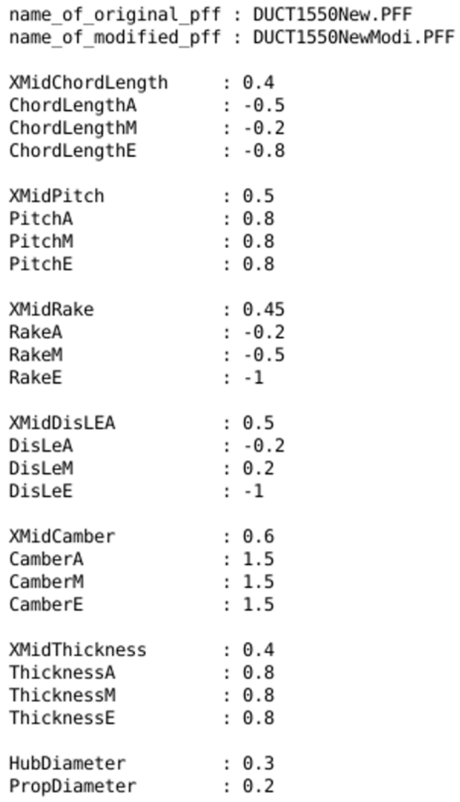

```
name_of_original_pff : DUCT1550New.PFF
name_of_modified_pff : DUCT1550NewModi.PFF

XMidChordLength     : 0.4
ChordLengthA        : -0.5
ChordLengthM        : -0.2
ChordLengthE        : -0.8

XMidPitch           : 0.5
PitchA              : 0.8
PitchM              : 0.8
PitchE              : 0.8

XMidRake            : 0.45
RakeA               : -0.2
RakeM               : -0.5
RakeE               : -1

XMidDisLEA          : 0.5
DisLeA              : -0.2
DisLeM              : 0.2
DisLeE              : -1

XMidCamber          : 0.6
CamberA             : 1.5
CamberM             : 1.5
CamberE             : 1.5

XMidThickness       : 0.4
ThicknessA          : 0.8
ThicknessM          : 0.8
ThicknessE          : 0.8

HubDiameter         : 0.3
PropDiameter        : 0.2
```

F Equation of Mesh Motion for Thruster

The initial position (x_0, y_0, z_0) is with respect to the stationary coordinate system. After first rotation about positive X-axis with the rotation rate of ω_1, one obtains the new position of (x_1, y_1, z_1)

$$\begin{pmatrix} x_1 \\ y_1 \\ z_1 \end{pmatrix} = \begin{pmatrix} 1 & 0 & 0 \\ 0 & cos(\omega_1 t) & -sin(\omega_1 t) \\ 0 & sin(\omega_1 t) & cos(\omega_1 t) \end{pmatrix} \begin{pmatrix} x_0 \\ y_0 \\ z_0 \end{pmatrix} \tag{F.1}$$

The second rotation is about positive Y-axis with the rotation rate of ω_2 from (x_1, y_1, z_1) to (x_2, y_2, z_2):

$$\begin{pmatrix} x_2 \\ y_2 \\ z_2 \end{pmatrix} = \begin{pmatrix} cos(\omega_2 t) & 0 & sin(\omega_2 t) \\ 0 & 1 & 0 \\ -sin(\omega_2 t) & 0 & cos(\omega_2 t) \end{pmatrix} \begin{pmatrix} x_1 \\ y_1 \\ z_1 \end{pmatrix} \tag{F.2}$$

The last rotation is about positive Z-axis with rotation rate of ω_2 from (x_2, y_2, z_2) to (x_3, y_3, z_3):

$$\begin{pmatrix} x_3 \\ y_3 \\ z_3 \end{pmatrix} = \begin{pmatrix} cos(\omega_3 t) & -sin(\omega_3 t) & 1 \\ sin(\omega_3 t) & cos(\omega_3 t) & 1 \\ 0 & 0 & 1 \end{pmatrix} \begin{pmatrix} x_2 \\ y_2 \\ z_2 \end{pmatrix} \tag{F.3}$$

Combining Eq.[F.3] with Eq.[F.1] and [F.2], the final coordinate with regard to stationary coordinate system is:

$$\begin{pmatrix} x_3 \\ y_3 \\ z_3 \end{pmatrix} = \begin{pmatrix} cos(\omega_3 t) & -sin(\omega_3 t) & 1 \\ sin(\omega_3 t) & cos(\omega_3 t) & 1 \\ 0 & 0 & 1 \end{pmatrix} \begin{pmatrix} cos(\omega_2 t) & 0 & sin(\omega_2 t) \\ 0 & 1 & 0 \\ -sin(\omega_2 t) & 0 & cos(\omega_2 t) \end{pmatrix} \begin{pmatrix} 1 & 0 & 0 \\ 0 & cos(\omega_1 t) & \text{-}sin(\omega_1 t) \\ 0 & sin(\omega_1 t) & cos(\omega_1 t) \end{pmatrix} \begin{pmatrix} x_0 \\ y_0 \\ z_0 \end{pmatrix} \tag{F.4}$$

Propeller is involved into the both rotation rates ω_1 and ω_3 (see Fig.[F.1]), but for the other parts like duct and housing the rotation rate of ω_1 is ignored (no rotation about X-axis). There is no rotation about Y-axis for all parts, so ω_2 is equal zero. The Eq.[F.4] can be simplified to Eq.[F.5] and Eq.[F.6] for duct and housing and rotating propeller, respectively.

$$\begin{pmatrix} x_3 \\ y_3 \\ z_3 \end{pmatrix} = \begin{pmatrix} cos(\omega_3 t) & -sin(\omega_3 t) & 1 \\ sin(\omega_3 t) & cos(\omega_3 t) & 1 \\ 0 & 0 & 1 \end{pmatrix} \begin{pmatrix} x_0 \\ y_0 \\ z_0 \end{pmatrix} \tag{F.5}$$

$$\begin{pmatrix} x_3 \\ y_3 \\ z_3 \end{pmatrix} = \begin{pmatrix} cos(\omega_3 t) & -sin(\omega_3 t) & 1 \\ sin(\omega_3 t) & cos(\omega_3 t) & 1 \\ 0 & 0 & 1 \end{pmatrix} \begin{pmatrix} 1 & 0 & 0 \\ 0 & cos(\omega_1 t) & -sin(\omega_1 t) \\ 0 & sin(\omega_1 t) & cos(\omega_1 t) \end{pmatrix} \begin{pmatrix} x_0 \\ y_0 \\ z_0 \end{pmatrix} \tag{F.6}$$

Note that, the sign of the rotation rate ω, namely ω_1, ω_2 and ω_3 can be different. For instance, if the thruster rotates to the port side, the sign of ω_3 is then negative.

Figure F.1.: Mesh motion related rotation axis

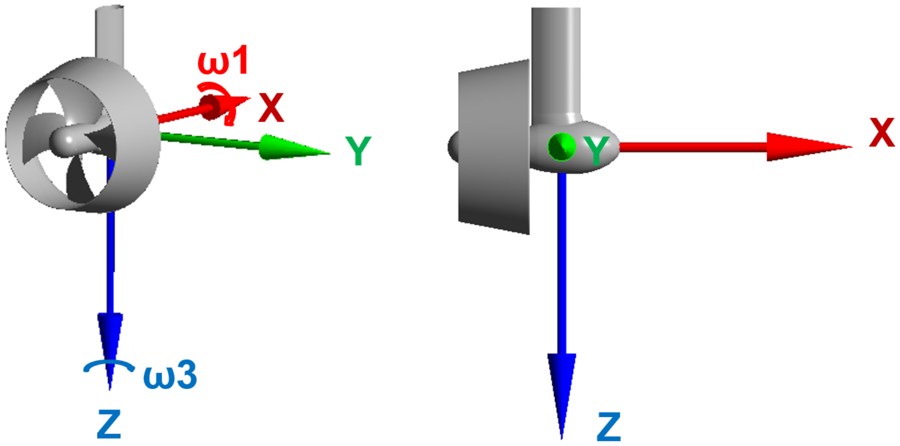

G Hydrodynamic Derivatives and Manoeuvring Model by Wolff

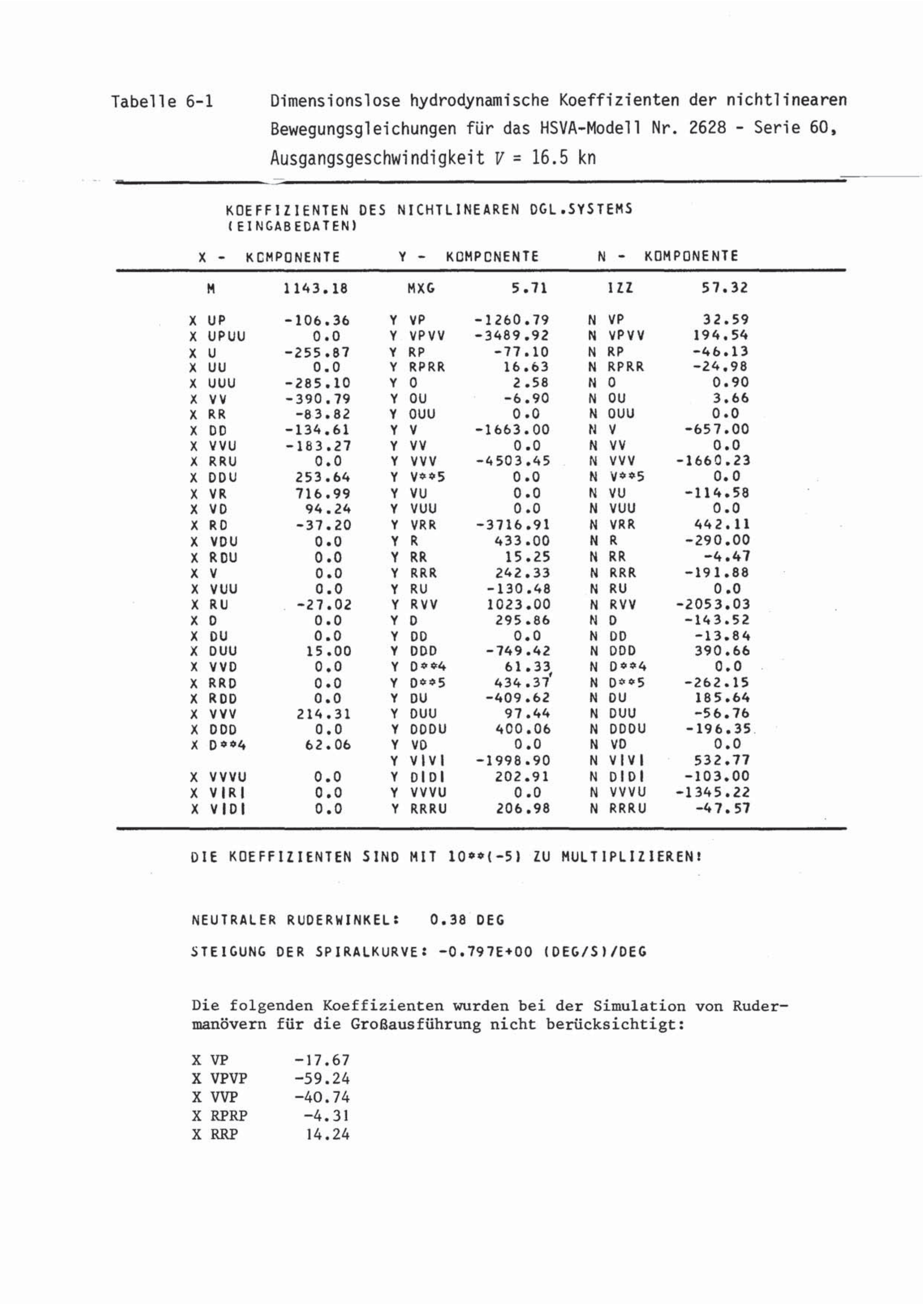

Tabelle 6-1 Dimensionslose hydrodynamische Koeffizienten der nichtlinearen Bewegungsgleichungen für das HSVA-Modell Nr. 2628 - Serie 60, Ausgangsgeschwindigkeit V = 16.5 kn

```
KOEFFIZIENTEN DES NICHTLINEAREN DGL.SYSTEMS
(EINGABEDATEN)

 X -  KOMPONENTE        Y -  KOMPONENTE        N -  KOMPONENTE
----------------------------------------------------------------------
   M        1143.18     MXG          5.71      IZZ          57.32

 X UP       -106.36     Y VP     -1260.79      N VP         32.59
 X UPUU        0.0      Y VPVV   -3489.92      N VPVV      194.54
 X U        -255.87     Y RP       -77.10      N RP        -46.13
 X UU          0.0      Y RPRR      16.63      N RPRR      -24.98
 X UUU      -285.10     Y 0          2.58      N 0           0.90
 X VV       -390.79     Y 0U        -6.90      N 0U          3.66
 X RR        -83.82     Y 0UU        0.0       N 0UU         0.0
 X DD       -134.61     Y V      -1663.00      N V        -657.00
 X VVU      -183.27     Y VV         0.0       N VV          0.0
 X RRU         0.0      Y VVV    -4503.45      N VVV     -1660.23
 X DDU       253.64     Y V**5       0.0       N V**5        0.0
 X VR        716.99     Y VU         0.0       N VU       -114.58
 X VD         94.24     Y VUU        0.0       N VUU         0.0
 X RD        -37.20     Y VRR    -3716.91      N VRR       442.11
 X VDU         0.0      Y R        433.00      N R        -290.00
 X RDU         0.0      Y RR        15.25      N RR         -4.47
 X V           0.0      Y RRR      242.33      N RRR      -191.88
 X VUU         0.0      Y RU      -130.48      N RU          0.0
 X RU        -27.02     Y RVV     1023.00      N RVV     -2053.03
 X D           0.0      Y D        295.86      N D        -143.52
 X DU          0.0      Y DD         0.0       N DD        -13.84
 X DUU        15.00     Y DDD     -749.42      N DDD       390.66
 X VVD         0.0      Y D**4      61.33      N D**4        0.0
 X RRD         0.0      Y D**5     434.37      N D**5     -262.15
 X RDD         0.0      Y DU      -409.62      N DU        185.64
 X VVV       214.31     Y DUU       97.44      N DUU       -56.76
 X DDD         0.0      Y DDDU     400.06      N DDDU     -196.35
 X D**4       62.06     Y VD         0.0       N VD          0.0
                        Y V|V|   -1998.90      N V|V|      532.77
 X VVVU        0.0      Y D|D|     202.91      N D|D|     -103.00
 X V|R|        0.0      Y VVVU       0.0       N VVVU    -1345.22
 X V|D|        0.0      Y RRRU     206.98      N RRRU      -47.57
----------------------------------------------------------------------

DIE KOEFFIZIENTEN SIND MIT 10**(-5) ZU MULTIPLIZIEREN!


NEUTRALER RUDERWINKEL:    0.38 DEG

STEIGUNG DER SPIRALKURVE: -0.797E+00 (DEG/S)/DEG
```

Die folgenden Koeffizienten wurden bei der Simulation von Rudermanövern für die Großausführung nicht berücksichtigt:

X VP	-17.67
X VPVP	-59.24
X VVP	-40.74
X RPRP	-4.31
X RRP	14.24

$$m\,(\dot{u} - v\,r - r^2\,x_G) = X \tag{1a}$$

$$m\,(\dot{v} + u\,r + \dot{r}\;x_G) = Y \tag{1b}$$

$$I_{zz}\dot{r} + m(ur + \dot{v})x_G = N \tag{1c}$$

$$\begin{aligned}
F = \;& F(u,v,r,\dot{u},\dot{v},\dot{r};\delta)\\
= \;& F_o\,u^2\\
& + F_u\,u\Delta u \quad + F_{uu}\,\Delta u^2 \quad + F_{uuu}\,\Delta u^3/u\\
& + F_{\dot{u}}\,\dot{u} \quad + F_{\dot{u}\dot{u}}\,\dot{u}^2/u^2 \quad + F_{\dot{u}\dot{u}\dot{u}}\,\dot{u}^3/u^4 \quad + F_{\dot{u}u}\,\dot{u}\Delta u/u \quad + F_{\dot{u}uu}\,\dot{u}\Delta u^2/u^2\\
& + F_v\,uv \quad + F_{vv}\,v^2 \quad + F_{vvv}\,v^3/u \quad + F_{vvvv}\,v^4/u^2 \quad + F_{vvvvv}\,v^5/u^3\\
& + F_{v|v|}\,v|v|\\
& + F_{\dot{v}}\,\dot{v} \quad + F_{\dot{v}\dot{v}}\,\dot{v}^2/u^2 \quad + F_{\dot{v}\dot{v}\dot{v}}\,\dot{v}^3/u^4 \quad + F_{\dot{v}v}\,\dot{v}v/u \quad + F_{\dot{v}vv}\,\dot{v}v^2/u^2\\
& + F_r\,ur \quad + F_{rr}\,r^2 \quad + F_{rrr}\,r^3/u \quad + F_{rrrr}\,r^4/u^2 \quad + F_{rrrrr}\,r^5/u^3\\
& + F_{r|r|}\,r|r|\\
& + F_{\dot{r}}\,\dot{r} \quad + F_{\dot{r}\dot{r}}\,\dot{r}^2/u^2 \quad + F_{\dot{r}\dot{r}\dot{r}}\,\dot{r}^3/u^4 \quad + F_{\dot{r}r}\,\dot{r}r/u \quad + F_{\dot{r}rr}\,\dot{r}r^2/u^2\\
& + F_\delta\,u^2\delta \quad + F_{\delta\delta}\,u^2\delta^2 \quad + F_{\delta\delta\delta}\,u^2\delta^3 \quad + F_{\delta\delta\delta\delta}\,u^2\delta^4 \quad + F_{\delta\delta\delta\delta\delta}\,u^2\delta^5\\
& + F_{\delta|\delta|}\,u^2\delta|\delta|\\
& + F_{vu}\,v\Delta u \quad + F_{vuu}\,v\Delta u^2/u \quad + F_{vvu}\,v^2\Delta u/u \quad + F_{vvvu}\,v^3\Delta u/u^2 \quad + F_{v|v|u}\,v|v|\Delta u/u\\
& + F_{ru}\,r\Delta u \quad + F_{ruu}\,r\Delta u^2/u \quad + F_{rru}\,r^2\Delta u/u \quad + F_{rrru}\,r^3\Delta u/u^2 \quad + F_{r|r|u}\,r|r|\Delta u/u\\
& + F_{\delta u}\,u\delta\Delta u \quad + F_{\delta uu}\,\delta\Delta u^2 \quad + F_{\delta\delta u}\,u\delta^2\Delta u \quad + F_{\delta\delta\delta u}\,u\delta^3\Delta u \quad + F_{\delta|\delta|u}\,u\delta|\delta|\Delta u\\
& + F_{vr}\,vr \quad + F_{vrr}\,vr^2/u \quad + F_{vrrr}\,vr^3/u^2 \quad + F_{vvr}\,v^2r/u \quad + F_{vvrr}\,v^2r^2/u^2\\
& + F_{vvvr}\,v^3r/u^2 \quad + F_{v|r|}\,v|r| \quad + F_{|v|r}\,|v|r\\
& + F_{v\delta}\,uv\delta \quad + F_{v\delta\delta}\,uv\delta^2 \quad + F_{vv\delta}\,v^2\delta \quad + F_{|v|\delta}\,u|v|\delta \quad + F_{v|\delta|}\,uv|\delta|\\
& + F_{r\delta}\,ur\delta \quad + F_{r\delta\delta}\,ur\delta^2 \quad + F_{rr\delta}\,r^2\delta \quad + F_{|r|}\,u|r|\delta \quad + F_{r|\delta|}\,ur|\delta|\\
& + F_{vru}\,vr\Delta u/u \quad + F_{v\delta u}\,v\delta\Delta u \quad + F_{r\delta u}\,r\delta\Delta u \quad + F_{vr\delta}\,vr\delta
\end{aligned} \tag{2}$$

Das Symbol Δu kennzeichnet die Änderung der Längsgeschwindigkeit $(u - U_o)$; der Index u steht für Δu.

H Definition of Non-Dimensional Hydrodynamic Derivatives

$m' = \frac{\text{mass}}{0.5\rho L_{pp}^3}$	$I'_{zz} = \frac{I_{zz}}{0.5\rho L_{pp}^5}$	
	u	
$X' = \frac{X}{0.5\rho U^2 L_{pp}^2}$	$Y' = \frac{Y}{0.5\rho U^2 L_{pp}^2}$	$N' = \frac{N}{0.5\rho U^2 L_{pp}^3}$
$X'_{u} = \frac{X_{u}}{0.5\rho U^1 L_{pp}^2}$	$Y'_{u} = \frac{Y_{u}}{0.5\rho U^1 L_{pp}^2}$	$N'_{u} = \frac{N_{u}}{0.5\rho U^1 L_{pp}^3}$
$X'_{uu} = \frac{X_{uu}}{0.5\rho U^0 L_{pp}^2}$	$Y'_{uu} = \frac{Y_{uu}}{0.5\rho U^0 L_{pp}^2}$	$N'_{uu} = \frac{N_{uu}}{0.5\rho U^0 L_{pp}^3}$
$X'_{uuu} = \frac{X_{uuu}}{0.5\rho U^{-1} L_{pp}^2}$	$Y'_{uuu} = \frac{Y_{uuu}}{0.5\rho U^{-1} L_{pp}^2}$	$N'_{uuu} = \frac{N_{uuu}}{0.5\rho U^{-1} L_{pp}^3}$
$X'_{\dot{u}} = \frac{X_{\dot{u}}}{0.5\rho U^0 L_{pp}^3}$	$Y'_{\dot{u}} = \frac{Y_{\dot{u}}}{0.5\rho U^0 L_{pp}^3}$	$N'_{\dot{u}} = \frac{N_{\dot{u}}}{0.5\rho U^0 L_{pp}^4}$
$X'_{\dot{u}u} = \frac{X_{\dot{u}u}}{0.5\rho U^{-1} L_{pp}^3}$	$Y'_{\dot{u}u} = \frac{Y_{\dot{u}u}}{0.5\rho U^{-1} L_{pp}^3}$	$N'_{\dot{u}u} = \frac{N_{\dot{u}u}}{0.5\rho U^{-1} L_{pp}^4}$
$X'_{\dot{u}uu} = \frac{X_{\dot{u}uu}}{0.5\rho U^{-2} L_{pp}^3}$	$Y'_{\dot{u}uu} = \frac{Y_{\dot{u}uu}}{0.5\rho U^{-2} L_{pp}^3}$	$N'_{\dot{u}uu} = \frac{N_{\dot{u}uu}}{0.5\rho U^{-2} L_{pp}^4}$
	v	
$X'_{v} = \frac{X_{v}}{0.5\rho U^1 L_{pp}^2}$	$Y'_{v} = \frac{Y_{v}}{0.5\rho U^1 L_{pp}^2}$	$N'_{v} = \frac{N_{v}}{0.5\rho U^1 L_{pp}^3}$
$X'_{vv} = \frac{X_{vv}}{0.5\rho U^0 L_{pp}^2}$	$Y'_{vv} = \frac{Y_{vv}}{0.5\rho U^0 L_{pp}^2}$	$N'_{vv} = \frac{N_{vv}}{0.5\rho U^0 L_{pp}^3}$
$X'_{vvv} = \frac{X_{vvv}}{0.5\rho U^{-1} L_{pp}^2}$	$Y'_{vvv} = \frac{Y_{vvv}}{0.5\rho U^{-1} L_{pp}^2}$	$N'_{vvv} = \frac{N_{vvv}}{0.5\rho U^{-1} L_{pp}^3}$
$X'_{\dot{v}} = \frac{X_{\dot{v}}}{0.5\rho U^0 L_{pp}^3}$	$Y'_{\dot{v}} = \frac{Y_{\dot{v}}}{0.5\rho U^0 L_{pp}^3}$	$N'_{\dot{v}} = \frac{N_{\dot{v}}}{0.5\rho U^0 L_{pp}^4}$
$X'_{\dot{v}v} = \frac{X_{\dot{v}v}}{0.5\rho U^{-1} L_{pp}^3}$	$Y'_{\dot{v}v} = \frac{Y_{\dot{v}v}}{0.5\rho U^{-1} L_{pp}^3}$	$N'_{\dot{v}v} = \frac{N_{\dot{v}v}}{0.5\rho U^{-1} L_{pp}^4}$
$X'_{\dot{v}vv} = \frac{X_{\dot{v}vv}}{0.5\rho U^{-2} L_{pp}^3}$	$Y'_{\dot{v}vv} = \frac{Y_{\dot{v}vv}}{0.5\rho U^{-2} L_{pp}^3}$	$N'_{\dot{v}vv} = \frac{N_{\dot{v}vv}}{0.5\rho U^{-2} L_{pp}^4}$
	r	
$X'_{r} = \frac{X_{r}}{0.5\rho U^1 L_{pp}^3}$	$Y'_{r} = \frac{Y_{r}}{0.5\rho U^1 L_{pp}^3}$	$N'_{r} = \frac{N_{r}}{0.5\rho U^1 L_{pp}^4}$
$X'_{rr} = \frac{X_{rr}}{0.5\rho U^0 L_{pp}^4}$	$Y'_{rr} = \frac{Y_{rr}}{0.5\rho U^0 L_{pp}^4}$	$N'_{rr} = \frac{N_{rr}}{0.5\rho U^0 L_{pp}^5}$
$X'_{rrr} = \frac{X_{rrr}}{0.5\rho U^{-1} L_{pp}^5}$	$Y'_{rrr} = \frac{Y_{rrr}}{0.5\rho U^{-1} L_{pp}^5}$	$N'_{rrr} = \frac{N_{rrr}}{0.5\rho U^{-1} L_{pp}^6}$
$X'_{\dot{r}} = \frac{X_{\dot{r}}}{0.5\rho U^0 L_{pp}^4}$	$Y'_{\dot{r}} = \frac{Y_{\dot{r}}}{0.5\rho U^0 L_{pp}^4}$	$N'_{\dot{r}} = \frac{N_{\dot{r}}}{0.5\rho U^0 L_{pp}^5}$
$X'_{\dot{r}r} = \frac{X_{\dot{r}r}}{0.5\rho U^{-1} L_{pp}^5}$	$Y'_{\dot{r}r} = \frac{Y_{\dot{r}r}}{0.5\rho U^{-1} L_{pp}^5}$	$N'_{\dot{r}r} = \frac{N_{\dot{r}r}}{0.5\rho U^{-1} L_{pp}^6}$
$X'_{\dot{r}rr} = \frac{X_{\dot{r}rr}}{0.5\rho U^{-2} L_{pp}^6}$	$Y'_{\dot{r}rr} = \frac{Y_{\dot{r}rr}}{0.5\rho U^{-2} L_{pp}^6}$	$N'_{\dot{r}rr} = \frac{N_{\dot{r}rr}}{0.5\rho U^{-2} L_{pp}^7}$
	rv	
$X'_{rv} = \frac{X_{rv}}{0.5\rho U^0 L_{pp}^3}$	$Y'_{rv} = \frac{Y_{rv}}{0.5\rho U^0 L_{pp}^3}$	$N'_{rv} = \frac{N_{rv}}{0.5\rho U^0 L_{pp}^4}$
$X'_{rrv} = \frac{X_{rrv}}{0.5\rho U^{-1} L_{pp}^4}$	$Y'_{rrv} = \frac{Y_{rrv}}{0.5\rho U^{-1} L_{pp}^4}$	$N'_{rrv} = \frac{N_{rrv}}{0.5\rho U^{-1} L_{pp}^5}$
$X'_{vvr} = \frac{X_{vvr}}{0.5\rho U^{-1} L_{pp}^3}$	$Y'_{vvr} = \frac{Y_{vvr}}{0.5\rho U^{-1} L_{pp}^3}$	$N'_{vvr} = \frac{N_{vvr}}{0.5\rho U^{-1} L_{pp}^4}$
	rvu	
$X'_{vu} = \frac{X_{vu}}{0.5\rho U^0 L_{pp}^2}$	$Y'_{vu} = \frac{Y_{vu}}{0.5\rho U^0 L_{pp}^2}$	$N'_{vu} = \frac{N_{vu}}{0.5\rho U^0 L_{pp}^3}$
$X'_{vuu} = \frac{X_{vuu}}{0.5\rho U^{-1} L_{pp}^2}$	$Y'_{vuu} = \frac{Y_{vuu}}{0.5\rho U^{-1} L_{pp}^2}$	$N'_{vuu} = \frac{N_{vuu}}{0.5\rho U^{-1} L_{pp}^3}$
$X'_{ru} = \frac{X_{ru}}{0.5\rho U^0 L_{pp}^3}$	$Y'_{ru} = \frac{Y_{ru}}{0.5\rho U^0 L_{pp}^3}$	$N'_{ru} = \frac{N_{ru}}{0.5\rho U^0 L_{pp}^4}$
$X'_{ruu} = \frac{X_{ruu}}{0.5\rho U^{-1} L_{pp}^3}$	$Y'_{ruu} = \frac{Y_{ruu}}{0.5\rho U^{-1} L_{pp}^3}$	$N'_{ruu} = \frac{N_{ruu}}{0.5\rho U^{-1} L_{pp}^4}$
$X'_{rvu} = \frac{X_{rvu}}{0.5\rho U^{-1} L_{pp}^3}$	$Y'_{rvu} = \frac{Y_{rvu}}{0.5\rho U^{-1} L_{pp}^3}$	$N'_{rvu} = \frac{N_{rvu}}{0.5\rho U^{-1} L_{pp}^4}$
$X'_{vvu} = \frac{X_{vvu}}{0.5\rho U^{-1} L_{pp}^2}$	$Y'_{vvu} = \frac{Y_{vvu}}{0.5\rho U^{-1} L_{pp}^2}$	$N'_{vvu} = \frac{N_{vvu}}{0.5\rho U^{-1} L_{pp}^3}$
$X'_{rru} = \frac{X_{rru}}{0.5\rho U^{-1} L_{pp}^4}$	$Y'_{rru} = \frac{Y_{rru}}{0.5\rho U^{-1} L_{pp}^4}$	$N'_{rru} = \frac{N_{rru}}{0.5\rho U^{-1} L_{pp}^5}$

I Reduction of Hydrodynamic Derivatives of Ship w/o Bow Thruster

Figure I.1.: Comparison of time history of forces X, Y and moment N during one period of dynamic tests between original (blue)-, regression(red)- and reduction(green) cuve. From top to bottom: Surge, sway, yaw and combined sway-yaw

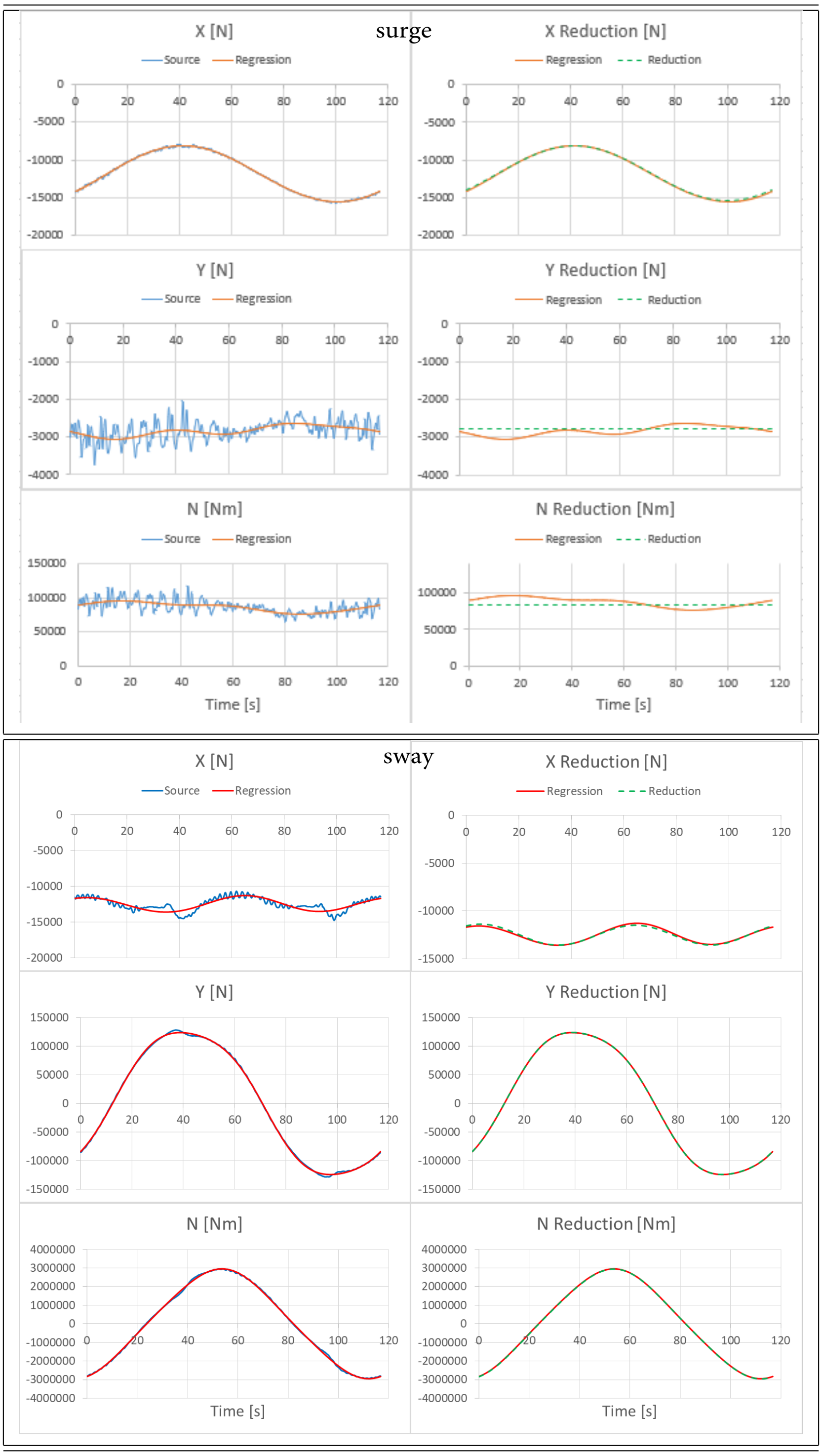

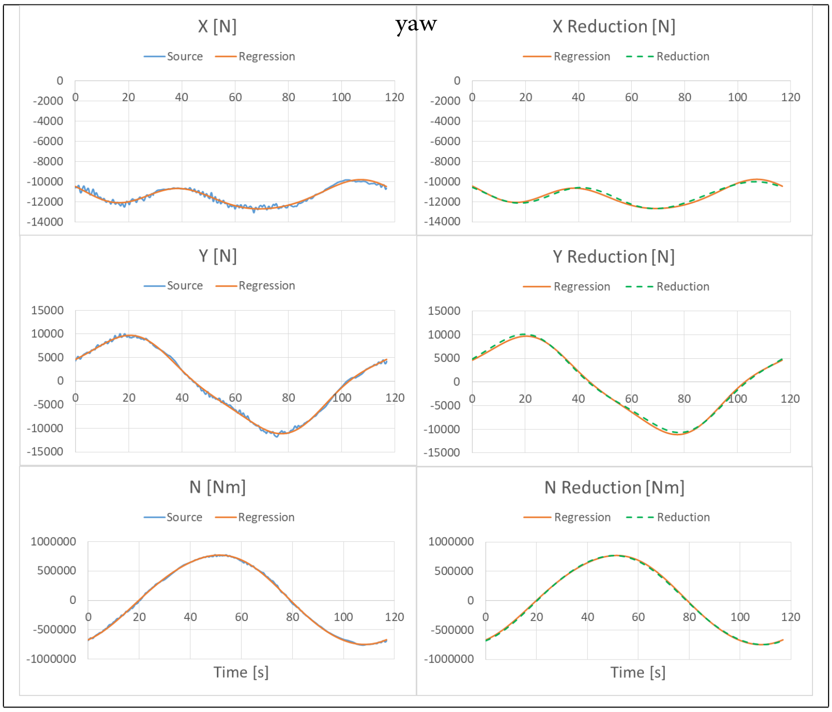
yaw
X [N]
Source
Regression
0
-2000
-4000
-6000
-8000
-10000
-12000
-14000
0
20
40
60
80
100
120
X Reduction [N]
Regression
Reduction
Y [N]
Source
Regression
15000
10000
5000
0
-5000
-10000
-15000
Y Reduction [N]
Regression
Reduction
N [Nm]
Source
Regression
1000000
500000
0
-500000
-1000000
Time [s]
N Reduction [Nm]
Regression
Reduction
Time [s]

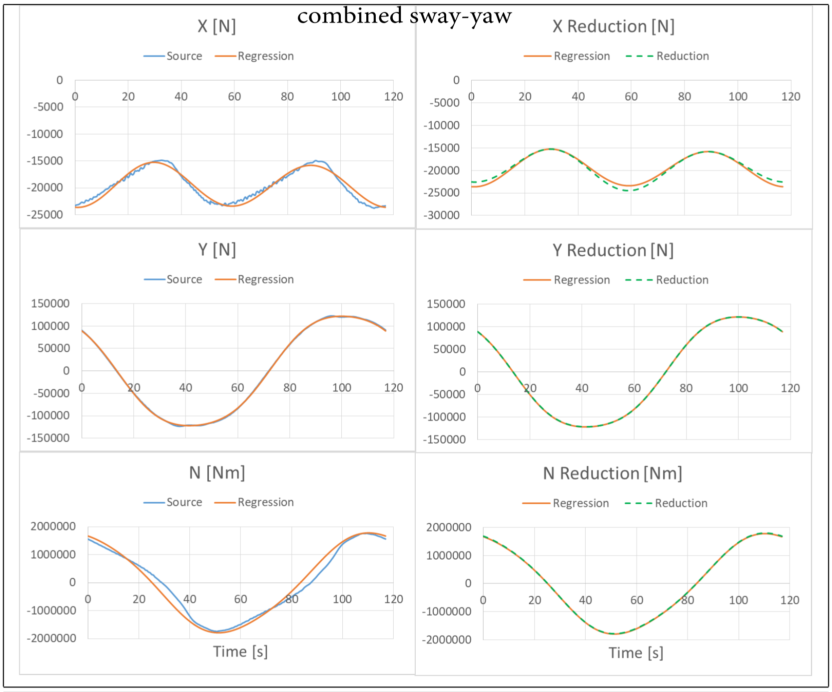
combined sway-yaw
X [N]
Source
Regression
0
-5000
-10000
-15000
-20000
-25000
0
20
40
60
80
100
120
X Reduction [N]
Regression
Reduction
-30000
Y [N]
Source
Regression
150000
100000
50000
0
-50000
-100000
-150000
Y Reduction [N]
Regression
Reduction
N [Nm]
Source
Regression
2000000
1000000
0
-1000000
-2000000
Time [s]
N Reduction [Nm]
Regression
Reduction
Time [s]

J Distribution of Forces and Moment as Function of Velocities

Figure J.1.: Distribution of forces X, Y and moment N during one period of dynamic tests. From top to bottom: surge, sway and yaw

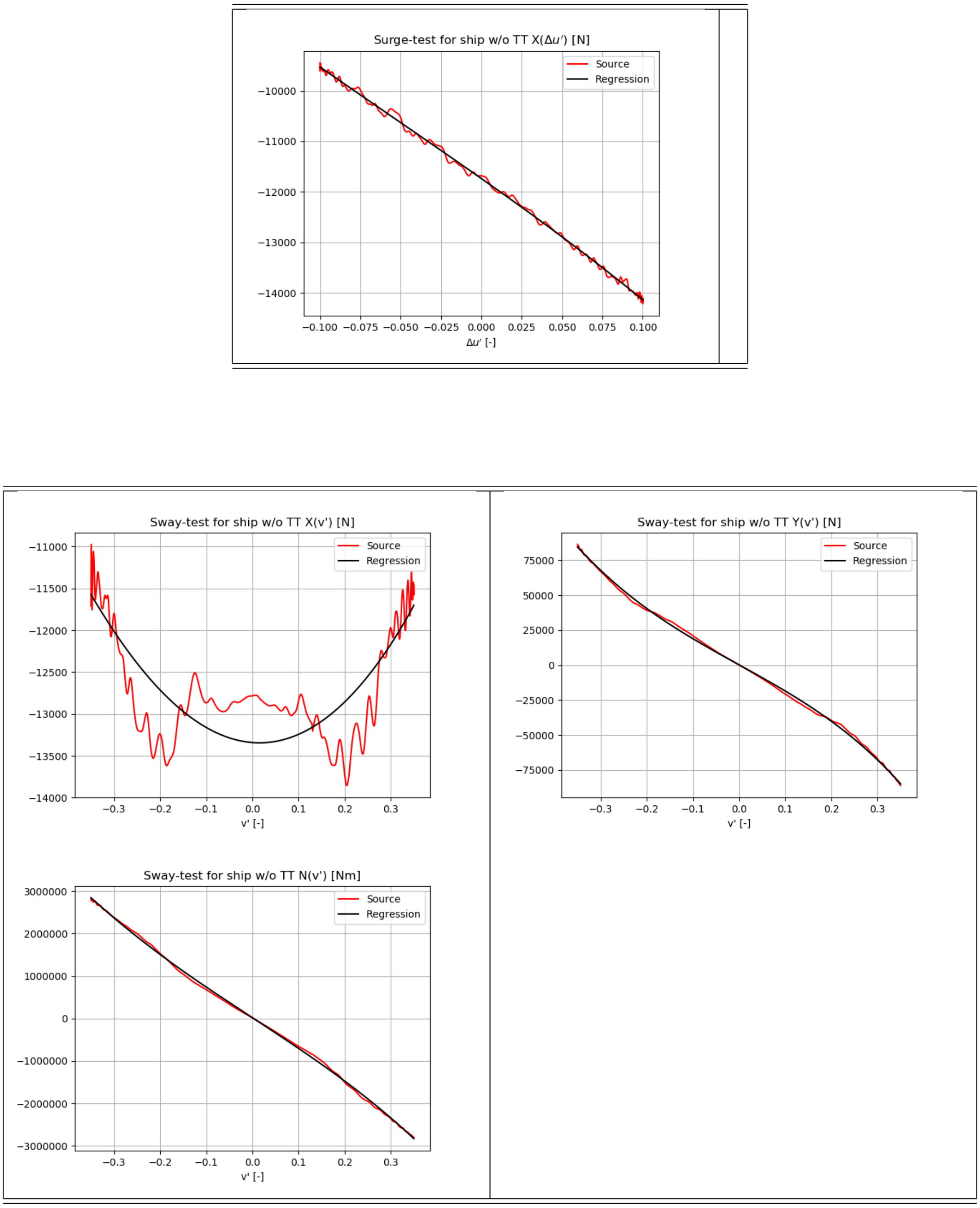

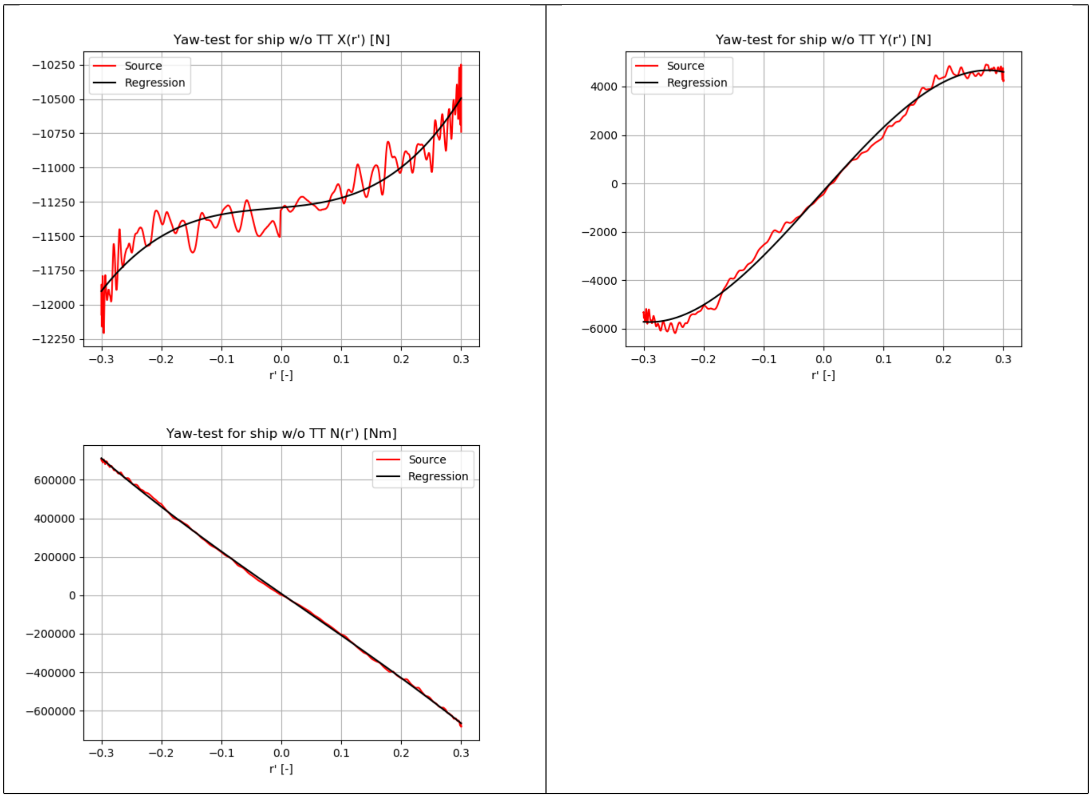
Yaw-test for ship w/o TT X(r') [N]
Source
Regression
−10250
−10500
−10750
−11000
−11250
−11500
−11750
−12000
−12250
−0.3
−0.2
−0.1
0.0
0.1
0.2
0.3
r' [-]
Yaw-test for ship w/o TT Y(r') [N]
Source
Regression
4000
2000
0
−2000
−4000
−6000
−0.3
−0.2
−0.1
0.0
0.1
0.2
0.3
r' [-]
Yaw-test for ship w/o TT N(r') [Nm]
Source
Regression
600000
400000
200000
0
−200000
−400000
−600000
−0.3
−0.2
−0.1
0.0
0.1
0.2
0.3
r' [-]